

**CHARGE TRANSPORT IN ORGANIC AND ORGANOMETALLIC MOLECULES: DEVICE DESIGN,
FABRICATION, AND TESTING**

Robert Charles Bruce

A dissertation submitted to the faculty at the University of North Carolina at Chapel Hill in partial fulfillment of the requirements for the degree of Doctor of Philosophy in the Department of Chemistry.

Chapel Hill
2015

Approved by:

Wei You

Andrew M. Moran

James F. Cahoon

Jillian L. Dempsey

Scott C. Warren

© 2015
Robert Charles Bruce
ALL RIGHTS RESERVED

ABSTRACT

Robert Charles Bruce: Charge Transport in Organic and Organometallic Molecules:
Device Design, Fabrication, and Testing
(Under the direction of Wei You)

Molecular electronics (ME) represents a frontier for electronics. Designing electronic devices at the single molecule level would lead to extremely high density devices, and the organic materials typically used in ME can bring switchable properties and enable formation of transistors at the single molecule level. While promising, potential issues arise from incorporating these organic-based materials and their unique properties into electronic devices. Solutions exist to generate electrical devices with organic materials, but understanding the impacts of these fabrication processes is necessary for their use in practical application settings.

The focus of this work is studying unique organic and organometallic materials in molecular electronic device architectures designed toward use in practical electronic settings. Spin-active organometallic complexes – a cobalt bis(dioxylylene) based valence tautomer (CoVT), and multi[(porphinato)metal] oligomer wires – are used to build molecular wires and studied in ME settings designed through self-assembly approaches. While the CoVT molecule is shown to actually lose its valence tautomerism when tethered to a surface, the porphyrin wires show metal center dependence on charge transport properties, enabling them to be used in potentially switchable ME and spintronic devices.

Alongside this, a variety of soft lithographic techniques are utilized and the effects of their fabrication processes on device output analyzed. Nanotransfer printing (nTP) is tested with basic monolayers, showing in phenylenedithiols lower tunneling attenuation than seen through

other electrically identical architectures. We explain the force effects from nTP to be a possible cause and use this as a case study in highlighting the impact architecture can have on monolayer properties. Despite this, porphyrin wires in nTP junctions exhibit near identical electrical properties compared to single molecule measurements, highlighting the technique's ability to exhibit the electrical properties of more specialized and complex molecules.

Other soft lithographic techniques were also highlighted toward designing macroscopically accessible junctions. Nanoindentation, a kinetically-controlled transfer printing (KTP) process, and transfer of graphene *via* polymer layer are all studied. As a whole, these processes highlight the effects and limitations that are inherent to designing molecular electronic devices, and we discuss the needs for fabrication processes to enable practical electronic and spintronic devices from organic-based materials.

Dedicated to all the teachers
that helped me grow and pushed me,
and whose job I'm convinced will be ten times harder
than anything I will ever do.

ACKNOWLEDGEMENTS

First, I need to thank my advisor, Wei You. Wei, I'm so appreciative for letting me be a part of your group. You gave me every opportunity to succeed, let me learn and work on so many diverse things, and opened any door that needed it. I don't know if I'll ever meet a professor who cared so much about his students. Thank you so much.

I'd also like to thank my amazing sub-groupmates, Travis, Josh, Jeremy, and Elizabeth. The past five years have been an amazing experience, and I can't imagine asking for better people to work with and learn from. I don't think being a part of or simply watching random arguments will ever be so much fun. I'd be remiss if I left out a thanks for the rest of the You group as well, thank you for all of the research talks, BBQs, and board game nights. I'm sorry if I drove you guys nuts with XPS talks, but I hope something positive rubbed off of my nerdy obsessions.

There are so many other people that I could probably write a whole thesis-length document thanking, I hope it suffices for me to say thank you to the amazing people that have supported me over the past five years – my fellow classmates, the young adult group (and others) from UPC, choir members, and so many other people. It's been a blessing to get to know you all and experience Chapel Hill with you; you are an inseparable part of the work in this thesis.

And finally, thank you to my family for all your love and support, and most importantly, bringing bagels when you visited. Seriously though, I love you guys, and I'm looking forward to where the next chapter of all our lives takes us.

TABLE OF CONTENTS

| | |
|--|-----------|
| LIST OF FIGURES | xiv |
| LIST OF TABLES | xx |
| LIST OF EQUATIONS..... | xxi |
| LIST OF ABBREVIATIONS AND SYMBOLS | xxii |
| CHAPTER 1: <i>Introduction to Molecular Electronics and Spintronics</i> | 1 |
| 1.1 Background | 1 |
| 1.2 Organic Materials for Electronic Applications | 4 |
| 1.2.1 Recent Interests in Organic Electronics | 4 |
| 1.2.2 Properties of Organics for Electronic Applications | 6 |
| 1.3 Molecular Electronics | 9 |
| 1.3.1 Synthetic Control of Molecular Electronic Properties | 9 |
| 1.3.2 Switchable Properties in Molecular Electronics | 11 |
| 1.4 Organic Spintronics | 12 |
| 1.4.1 Basics of Spintronics- Spin Valve | 13 |
| 1.4.2 Basics of Organic Spintronics | 16 |
| 1.4.3 Organic Magnetoresistance | 16 |
| 1.4.4 Magnetic Properties from Organic Molecules..... | 19 |

| | | |
|--|---|-----------|
| 1.4.5 | Interface Considerations in Organic Spintronics | 21 |
| 1.4.6 | Spintronics from Controlling Spin State in Organic-Based Molecules | 24 |
| 1.5 | Designing Devices with Organic-Based Materials | 26 |
| 1.5.1 | Techniques for Designing Molecular Electronic Devices..... | 27 |
| 1.5.2 | Soft Lithography and Transfer Printing in Molecular Electronics | 29 |
| 1.6 | Research Overview | 30 |
| 1.7 | References | 32 |
| CHAPTER 2: <i>Adapting Spintronic Organometallic Molecules to Molecular Electronic Settings</i> | | 38 |
| 2.1 | Background | 38 |
| 2.1.1 | History of Magnetism in Metals | 38 |
| 2.1.2 | Magnetic Properties in Organic Molecules | 43 |
| 2.2 | Study of Iron Spin Crossover Films | 45 |
| 2.2.1 | Spin Crossover | 45 |
| 2.2.2 | Experimental- FeSCO Film Growth and Study | 48 |
| 2.2.3 | Results and Discussion- FeSCO | 49 |
| 2.3 | Study of Valence Tautomers Designed as Molecular Wires | 52 |
| 2.3.1 | Valence Tautomerism for Spintronic Devices..... | 52 |
| 2.3.2 | Experimental- CoVT Wire Growth and Study | 57 |
| 2.3.3 | Results and Discussion- CoVT Wire Growth and Study | 59 |

| | | |
|---|---|-----------|
| 2.4 | Conclusions..... | 70 |
| 2.5 | Appendix | 72 |
| 2.5.1 | XPS Spectra for Various CoVT Wire Components..... | 72 |
| 2.6 | References | 79 |
| CHAPTER 3: <i>Studying Phenylenedithiol Monolayers in Nanotransfer Printed</i> | | |
| | <i>Molecular Junctions</i> | 82 |
| 3.1 | Background | 82 |
| 3.1.1 | Electrical Characterization of Molecular Junctions | 82 |
| 3.1.2 | Nanotransfer Printing | 85 |
| 3.1.3 | Alkanethiols in Nanotransfer Printed Junctions | 86 |
| 3.1.4 | Phenylenedithiol Self-Assembled Monolayers..... | 89 |
| 3.1.5 | Overview | 91 |
| 3.2 | Experimental | 92 |
| 3.2.1 | Materials | 92 |
| 3.2.2 | Gold Substrate and Self-Assembled Monolayer Preparation | 92 |
| 3.2.3 | Nanotransfer Printing | 93 |
| 3.2.4 | Atomic Force Microscopy | 93 |
| 3.2.5 | X-Ray Photoelectron Spectroscopy | 94 |
| 3.3 | Results and Discussion | 94 |
| 3.3.1 | ETMS Deprotection Effects on Monolayers | 94 |

| | | |
|--|---|------------|
| 3.3.2 | Phenylenedithiol Monolayer Characterization | 100 |
| 3.3.3 | nTP Characterization of Phenylenedithiol Monolayers | 104 |
| 3.3.4 | Influence of Device Architecture on Measured ME Properties..... | 109 |
| 3.4 | Conclusions..... | 112 |
| 3.5 | Appendix | 114 |
| 3.5.1 | Synthetic Procedures..... | 114 |
| 3.5.2 | NMR Spectra for Synthesized Compounds..... | 117 |
| 3.6 | References | 121 |
| CHAPTER 4: <i>Studies of Multi[(Porphinato)Metal] Oligomer Wires in Molecular Electronic Devices</i>..... | | 124 |
| 4.1 | Background | 124 |
| 4.1.1 | Organic Heterocycles for Spintronic Effects..... | 124 |
| 4.1.2 | Spintronic Effects from Porphyrin Metal Centers | 126 |
| 4.1.3 | Molecular Electronic Studies of Porphyrin Wires | 128 |
| 4.1.4 | Overview | 129 |
| 4.2 | Methods..... | 129 |
| 4.2.1 | Materials | 129 |
| 4.2.2 | Gold Substrate and Self-Assembled Monolayer Preparation..... | 130 |
| 4.2.3 | Nanotransfer Printing | 130 |
| 4.2.4 | Atomic Force Microscopy..... | 131 |

| | | |
|---|---|------------|
| 4.2.5 | Photoelectron Spectroscopy | 131 |
| 4.2.6 | Cyclic Voltammetry | 132 |
| 4.3 | Results and Discussion | 132 |
| 4.3.1 | Carbodithioate Linkers in Porphyrin Monolayers | 132 |
| 4.3.2 | Deprotection Effects on Metal Binding Groups | 138 |
| 4.3.3 | Thioacetyl Linkers in Porphyrin Monolayers | 143 |
| 4.3.4 | Picturing Porphyrin Wires on a Surface | 145 |
| 4.3.5 | Changing Porphyrin Metal Centers | 150 |
| 4.3.6 | Nanotransfer Printed Porphyrin Oligomer Wire Devices | 154 |
| 4.3.7 | UPS Measurements of Porphyrin Monolayers | 160 |
| 4.4 | Conclusions | 166 |
| 4.5 | Appendix | 168 |
| 4.5.1 | Synthetic Schemes | 168 |
| 4.5.2 | XPS Spectra | 175 |
| 4.5.3 | UPS Spectra | 189 |
| 4.6 | References | 192 |
| CHAPTER 5: <i>Large Area Junctions from Soft Lithography for Macroscopically Accessible Molecular Electronic Devices</i> | | 195 |
| 5.1 | Background | 195 |
| 5.1.1 | Limitations of Fabrication Techniques in Molecular Electronic | 195 |

| | | |
|--|---|------------|
| 5.1.2 | Overview | 196 |
| 5.2 | Methods | 197 |
| 5.2.1 | General | 197 |
| 5.2.2 | Atomic Force Microscopy | 197 |
| 5.2.3 | Kinetic Controlled Transfer Printing (KTP)..... | 198 |
| 5.2.4 | Electron Beam Lithography..... | 198 |
| 5.2.5 | Oxygen Plasma Cleaning | 199 |
| 5.2.6 | Graphene Transfer and Device Fabrication..... | 199 |
| 5.2.7 | Raman Spectroscopy | 200 |
| 5.2.8 | PEDOT:PSS Devices | 200 |
| 5.3 | Results and Discussion | 200 |
| 5.3.1 | Nanoindentation of 200 nm nTP Features..... | 200 |
| 5.3.2 | Kinetic Controlled Transfer Printing | 203 |
| 5.3.3 | Graphene as a Molecular Electronic Buffer Layer | 214 |
| 5.3.4 | Evaluation of Macroscopic Fabrication Techniques..... | 220 |
| 5.4 | Conclusions..... | 224 |
| 5.5 | Appendix | 227 |
| 5.6 | References | 228 |
| CHAPTER 6: <i>Summary of Conclusions and Recommendations for Future Work</i>..... | | 230 |
| 6.1 | Summary of Conclusions | 230 |

| | | |
|------------|--|------------|
| 6.1.1 | Adapting Spintronic Molecules to Molecular Electronic Settings | 231 |
| 6.1.2 | Studying Phenylenedithiol Monolayers in nTP Molecular Junctions..... | 232 |
| 6.1.3 | Studies of Porphyrin Oligomer Wires in Molecular Electronic Devices | 233 |
| 6.1.4 | Large Area Junctions from Soft Lithography for Macroscopic ME Junctions | 234 |
| 6.2 | Recommendations for Future Work | 237 |
| 6.2.1 | Thermally Stable Metal Binding Groups | 237 |
| 6.2.2 | Silicon Substrates for Analyzing Monolayer Properties | 238 |
| 6.2.3 | Solvent Assisted Transfer Printing | 239 |
| 6.2.4 | Metal Effects in Porphyrin Nanowires..... | 242 |
| 6.3 | Methods..... | 244 |
| 6.3.1 | Solvent Assisted Transfer Printing | 244 |
| 6.4 | References | 246 |

LIST OF FIGURES

| | |
|---|----|
| Figure 1.1 – Moore’s Law | 3 |
| Figure 1.2 – Amdahl’s Law | 3 |
| Figure 1.3 – Champion Solar Cell Efficiencies Based on Solar Cell Type..... | 5 |
| Figure 1.4 – Solution Processible Techniques for Large Scale OPV Production. | 6 |
| Figure 1.5 – Examples of Post-Synthesis Switchable Properties in Organic Systems..... | 8 |
| Figure 1.6 – Altering Charge Transport Mechanisms in Molecular Wires..... | 10 |
| Figure 1.7 – Conductance Switching in Molecular Wires | 11 |
| Figure 1.8 – Spin Valve..... | 13 |
| Figure 1.9 – Organic Magnetoresistance (OMAR) in PEDOT/C ₆₀ /Al devices..... | 17 |
| Figure 1.10 – Coulomb Blockade | 18 |
| Figure 1.11 – Organic Radicals for Spin Polarized Transport | 20 |
| Figure 1.12 – Engineering Spintronic Effects at Zinc Methyl Phenalenyl (ZMP) Interfaces | 23 |
| Figure 1.13 – Organic Magnetic Effects | 25 |
| Figure 1.14 – Molecular Electronic Junctions..... | 27 |
| Figure 1.15 – Molecular Electronics Devices Prepared with Buffer Layers..... | 28 |
| Figure 2.1 – Magnetism in Manganese-Doped Carbon Nanotubes (CNTs) | 42 |
| Figure 2.2 – Levitating Frog in a 20 Tesla Magnet | 43 |
| Figure 2.3 – Possible Electron Configurations for d-shell in Fe ²⁺ Complex..... | 46 |
| Figure 2.4 – SQUID Magnetometry of Powder FeSCO | 49 |
| Figure 2.5 – FeSCO Color Change as a Function of Temperature..... | 50 |
| Figure 2.6 – FeSCO Fe 2p XPS Spectra at Variable Temperature..... | 51 |

| | |
|---|----|
| Figure 2.7 – Cobalt bis(dioxylylene) Molecule [CoVT] and its Valence Tautomer Transition..... | 54 |
| Figure 2.8 – Effects on Valence Tautomerism from Different Ligands | 56 |
| Figure 2.9 – Attaching CoVT to a Surface..... | 57 |
| Figure 2.10 – CoVT Ligand Test on a Surface..... | 59 |
| Figure 2.11 – XPS Characterization of CoVT on a Surface..... | 60 |
| Figure 2.12 – Steric Hindrance in CoVT Wires | 63 |
| Figure 2.13 – Polymerization of CoVT and Linker Group | 64 |
| Figure 2.14 – Cross Sectional AFM of CoVT Multilayers on Gold..... | 66 |
| Figure 2.15 – CoVT Monomer Wires at Variable Temperature | 68 |
| Figure 2.16 – CoVT Crystals on Au/SiO _x Substrates | 69 |
| Figure 2.17 – Pyridine-dodecane-thiol Seed Monolayer XPS Spectra | 72 |
| Figure 2.18 – CNCoVT XPS Spectra | 73 |
| Figure 2.19 – CNCoVT/ bipy XPS Spectra..... | 74 |
| Figure 2.20 – CNCoVT/ bipy/ CNCoVT XPS Spectra..... | 75 |
| Figure 2.21 – CNCoVT/ DipyE XPS Spectra | 76 |
| Figure 2.22 – BrCoVT (110K) XPS Spectra..... | 77 |
| Figure 2.23 – BrCoVT (210K) XPS Spectra..... | 78 |
| Figure 3.1 – Nanotransfer Printing | 86 |
| Figure 3.2 – Octanethiol Self-Assembled Monolayer on Gold | 87 |
| Figure 3.3 – Alkanedithiol Monolayers Measured in Nanotransfer Printed Junctions..... | 88 |
| Figure 3.4 – Phenylenedithiol Calculated Rotation Energy | 89 |
| Figure 3.5 – Oligo- <i>para</i> -phenylenedithiols | 95 |

| | |
|---|-----|
| Figure 3.6 – qphDSH Monolayer Quality Based on TBAF Conditions | 96 |
| Figure 3.7 – Proposed Kinetics of ETMS Protection and Effects of Deprotectant Concentration..... | 99 |
| Figure 3.8 – XPS Spectra for Phenylenedithiol Monolayers | 101 |
| Figure 3.9 – Nanotransfer Printed Junctions with Phenylenedithiols | 104 |
| Figure 3.10 – Deprotected DS-ETMS Electrical Properties | 105 |
| Figure 3.11 – Phenylenedithiol nTP Characterization | 106 |
| Figure 3.12 – Electrical Measurements for Oligo- <i>para</i> -phenylenedithiol Devices..... | 108 |
| Figure 3.13 – Synthetic Route for ETMS-protected Phenylenedithiols | 114 |
| Figure 3.14 – H-NMR for Synthesized qphD-SETMS..... | 117 |
| Figure 3.15 – ^{13}C -NMR for Synthesized qphD-SETMS..... | 118 |
| Figure 3.16 – H-NMR for Synthesized tphD-SETMS..... | 119 |
| Figure 3.17 – ^{13}C -NMR for Synthesized tphD-SETMS | 120 |
| Figure 4.1 – Zinc Porphyrin Wires in STM-Break Junction | 128 |
| Figure 4.2 – PZn-CS ₂ Structure | 132 |
| Figure 4.3 – PZn ₁ -CS ₂ Monolayers on Gold Substrates | 135 |
| Figure 4.4 – PZn ₁ -CS ₂ Concentration Dependence | 137 |
| Figure 4.5 – XPS of Alkanecarbodithioate Monolayer..... | 138 |
| Figure 4.6 – XPS of Benzenecarbodithioate with ETMS Protection..... | 140 |
| Figure 4.7 – XPS of Benzenecarbodithioate Without Protection Group | 141 |
| Figure 4.8 – Phenylthioacetate Monolayers on Gold..... | 142 |
| Figure 4.9 – PZn-SAc Monolayers Prepared on Gold | 144 |
| Figure 4.10 – DFT Calculated Orientation for PZn ₁ -CS ₂ | 146 |
| Figure 4.11 – Model of Porphyrin Wires on a Surface | 148 |

| | |
|---|-----|
| Figure 4.12 – PZn ₁ -SAC Nanotransfer Printed Electrodes | 150 |
| Figure 4.13 – XPS of Metal Centers for Different PM ₁ -SAC Species | 151 |
| Figure 4.14 – AFM of nTP Pads on PCu ₃ -SAC from Different Solvents..... | 152 |
| Figure 4.15 – Copper and Nickel Porphyrin Monomer Monolayers | 153 |
| Figure 4.16 – nTP Junction with PM _n -SAC Monolayer | 154 |
| Figure 4.17 – Measured Electrical Devices for PZn-SAC Series..... | 156 |
| Figure 4.18 – Histograms for PM ₁ -SAC nTP Junctions | 157 |
| Figure 4.19 – Length Dependent Resistance for PM _n -SAC Junctions | 158 |
| Figure 4.20 – Cyclic Voltammetry Data for Porphyrin Wires | 160 |
| Figure 4.21 – UPS of Porphyrin Monomers..... | 161 |
| Figure 4.22 – Multibarrier Model for Molecules with Metal Binding Groups | 164 |
| Figure 4.24 – XPS- PZn ₁ CS ₂ - 0.1 mM, 1:4 PZn:TBAF | 175 |
| Figure 4.25 – XPS- PZn ₁ CS ₂ - 1 mM | 176 |
| Figure 4.26 – XPS- PZn ₁ CS ₂ - 10 mM | 176 |
| Figure 4.27 – XPS- PZn ₁ CS ₂ - 1:2 molecule: TBAF | 177 |
| Figure 4.28 – XPS- PZn ₁ CS ₂ - 1:4 molecule: TBAF | 177 |
| Figure 4.29 – XPS- PZn ₁ CS ₂ - 1:16 molecule: TBAF | 178 |
| Figure 4.30 – XPS- PZn ₁ CS ₂ - Excess TBAF | 178 |
| Figure 4.31 – XPS- C ₁₀ CS ₂ | 179 |
| Figure 4.32 – XPS- PhCS ₂ -ETMS- 1:2 molecule: TBAF | 179 |
| Figure 4.33 – XPS- PhCS ₂ -ETMS- 1:8 molecule: TBAF | 180 |
| Figure 4.34 – XPS- PhCS ₂ -ETMS- Excess TBAF | 180 |
| Figure 4.35 – XPS- PhCS ₂ -H- Without TBAF | 181 |

| | |
|---|-----|
| Figure 4.36 – XPS- PhCS ₂ -H- With TBAF | 181 |
| Figure 4.37 – XPS- PhSAc- 1 mM | 182 |
| Figure 4.38 – XPS- PZn ₁ -SAc | 183 |
| Figure 4.39 – XPS- PZn ₂ -SAc | 183 |
| Figure 4.40 – XPS- PZn ₃ -SAc | 184 |
| Figure 4.41 – XPS- PCu ₁ -SAc DCM | 184 |
| Figure 4.42 – XPS- PCu ₂ -SAc DCM | 185 |
| Figure 4.43 – XPS- PCu ₃ -SAc DCM | 186 |
| Figure 4.44 – XPS- PNi ₁ -SAc | 187 |
| Figure 4.45 – XPS- PNi ₂ -SAc | 187 |
| Figure 4.46 – XPS- PNi ₃ -SAc | 188 |
| Figure 4.47 – XPS- PFe ₁ -SAc | 188 |
| Figure 4.48 – UPS of Porphyrin Monomers..... | 189 |
| Figure 4.49 – UPS- Cutoff Region | 190 |
| Figure 4.50 – UPS- High Kinetic Energy Region | 191 |
| Figure 5.1 – Nanoindentation on Different Photoresist Formulations..... | 201 |
| Figure 5.2 – Kinetic Controlled Transfer Printing (KTP) Process | 204 |
| Figure 5.3 – KTP Crossbars on a Au/SiO _x Substrate | 205 |
| Figure 5.4 – KTP Device Architecture..... | 206 |
| Figure 5.5 – E-beam Exposure Test on 1 μm thick PMMA..... | 208 |
| Figure 5.6 – KTP Features Imaged through PMMA | 209 |
| Figure 5.7 – Graphene Transfer Process | 215 |
| Figure 5.8 – Raman of Graphene Films | 216 |

| | |
|---|-----|
| Figure 5.9 – Heatless Graphene Transfer | 217 |
| Figure 5.10 – E-beam Patterned Graphene..... | 219 |
| Figure 5.11 – Large Area Junctions Prepared with PEDOT:PSS Buffer Layer | 221 |
| Figure 5.12 – XPS Evidence of Heat Effects in Decanedithiol | 222 |
| Figure 5.13 – XPS- DDT Monolayer | 227 |
| Figure 5.14 – XPS- DDT after Heat Exposure | 227 |
| Figure 5.15 – XPS- DDT after O ₂ Plasma Exposure | 227 |
| Figure 6.1 – Solvent Assisted Transfer Printing (SATP)..... | 240 |
| Figure 6.2 – Sample SATP Transfer Substrate..... | 241 |
| Figure 6.3 – Spin Coupling from Porphyrin Metal Centers | 242 |

LIST OF TABLES

| | |
|---|-----|
| Table 2-1 – Atomic Concentrations for CoVT Monomers from Routes 1 and 2 | 61 |
| Table 3-1 – XPS Measured Monolayer Height for qphDSH Monolayers | 97 |
| Table 3-2 – Estimated Heights of Oligo- <i>para</i> -phenylenedithiol Monolayers by XPS..... | 100 |
| Table 3-3 – XPS S 2p Fit Peak Parameters for Oligo- <i>para</i> -phenylenedithiol Monolayers | 103 |
| Table 4-1 – XPS Measured Heights for PZn ₁ -CS ₂ Monolayers | 135 |
| Table 4-2 – XPS Measured Heights for PZn-SAc Series..... | 144 |
| Table 4-3 – S 2p Peak Ratios for Various PM _n -SAc Monolayers | 147 |
| Table 4-4 – PCu-SAc Thicknesses on Gold From Different Solvents | 153 |
| Table 4-5 – Statistics Derived from UPS Spectra..... | 162 |
| Table 5-1 – Exposures and Control Regions for PEDOT:PSS on PMMA Devices..... | 212 |

LIST OF EQUATIONS

| | |
|------------|-----|
| (1-1)..... | 14 |
| (1-2)..... | 15 |
| (1-3)..... | 15 |
| (2-1)..... | 39 |
| (2-2)..... | 39 |
| (2-3)..... | 40 |
| (2-4)..... | 40 |
| (2-5)..... | 40 |
| (2-6)..... | 40 |
| (2-7)..... | 50 |
| (3-1)..... | 88 |
| (3-2)..... | 97 |
| (4-2)..... | 162 |

LIST OF ABBREVIATIONS AND SYMBOLS

| | |
|-----------------------|---|
| Å | angstrom |
| β | tunneling decay parameter |
| Ω | ohm |
| Δ_0 | field splitting |
| μ | magnetic moment |
| $\chi_{\text{para}}T$ | magnetic susceptibility |
| ϕ | tunneling barrier height |
| AFM | atomic force microscopy |
| BIPO | bis-tetramethyl-piperidyl-oxyl-butadiin |
| bipy | 1,4-bipyridine |
| BJ | break junction |
| bphDSH | bis- <i>para</i> -phenylenedithiol |
| BrCoVT | CoVT with bromopyridine ligand |
| °C | degrees Celsius |
| cAFM | conductive-atomic force microscopy |
| CoVT | cobalt valence tautomer [Co(dioxolene) ₂ (4-X-py) ₂] |
| CMR | colossal magnetoresistance |
| CNCoVT | CoVT with cyanopyridine ligand |
| CNT | carbon nanotube |
| CV | cyclic voltammetry |
| DCM | dichloromethane |
| DDT | 1,10-decanedithiol |

| | |
|----------|---|
| DEAP | diethoxyacetophenone |
| DFT | density functional theory |
| DipyE | 1,2-di(4,pyridyl)ethylene |
| DMSO | dimethyl sulfoxide |
| DOS | density of states |
| DXP | N,N'-bis(2,6-dimethylphenyl)-perylene-3,4,9,10-tetracarboxylic diimide |
| E_F | Fermi energy |
| EGaIn | eutectic gallium-indium |
| ETMS | ethyltrimethylsilane |
| FeSCO | iron spin crossover [Fe[(H ₂ Bpz ₂) ₂ bpy]] |
| G | conductance |
| GMR | giant magnetoresistance |
| HMDS | hexamethyldisilazane |
| HOMO | highest occupied molecular orbital |
| hr | hour |
| I | current |
| IPA | isopropanol |
| IR | infrared |
| J_{ij} | exchange parameter |
| K | degrees Kelvin |
| KTP | kinetically-controlled transfer printing |
| LbL | layer-by-layer |
| LIESST | light induced excited spin state trapping |

| | |
|------------------|--|
| ME | molecular electronics |
| MIBK | methyl isobutyl ketone |
| mins | minutes |
| MOF | metal organic framework |
| mphDSH | mono- <i>para</i> -phenylenedithiol |
| MR | magnetoresistance |
| N | newtons |
| NMR | nuclear magnetic resonance |
| nCoVT | CoVT with no ligand |
| nTP | nanotransfer printing |
| OLED | organic light emitting diode |
| OMAR | organic magnetoresistance |
| OPE | oligo(phenylene ethynylene) |
| OPI | oligophenyleneimine |
| OSV | organic spin valve |
| <i>pb</i> -RAIRS | <i>p</i> -polarized backside reflection absorption infrared spectroscopy |
| Pc | phthalocyanine |
| PCBM | [6,6]-phenyl C61 butyric acid methyl ester |
| PDMS | polydimethylsiloxane |
| PECVD | plasma enhanced-chemical vapor deposition |
| PEDOT | poly(3,4-ethylenedioxythiophene) |
| PET | polyethylene terephthalate |
| PFPE | perfluoropolyether |

| | |
|---------------------|--|
| PMMA | poly(methyl methacrylate) |
| PR | photoresist |
| PSS | polystyrene sulfonate |
| PV | photovoltaic |
| PVAc | poly(vinyl acetate) |
| QD | quantum dot |
| qphDSH | quater- <i>para</i> -phenylenedithiol |
| rGO | reduced graphene oxide |
| RSF | relative sensitivity factor |
| s | second(s) |
| SAc | thioacetate |
| SAM | self-assembled monolayer |
| SATP | solvent-assisted transfer printing |
| SCO | spin crossover |
| SEM | scanning electron microscope |
| SiO _x | silicon oxide |
| SQUID | semiconducting quantum interference device |
| STM | scanning tunneling microscopy |
| T_g | glass transition temperature |
| TBAF | tetrabutylammonium fluoride |
| TBA-PF ₆ | tetrabutylammonium hexaphosphate |
| TCNE | tetracyanoethylene |
| TCNQ | tetracyanoquinodimethane |

| | |
|--------|---|
| TEMPO | [2,2,6,6-tetramethylpiperidin-1-yl]oxyl |
| THF | tetrahydrofuran |
| TMR | tunneling magnetoresistance |
| tphDSH | ter- <i>para</i> -phenylenedithiol |
| TTF | tetrathifulvalene |
| μCP | microcontact printing |
| UPS | ultraviolet photoelectron spectroscopy |
| UV | ultraviolet |
| V | volt |
| XPS | x-ray photoelectron spectroscopy |
| ZMP | zinc methyl phenalenyl |

CHAPTER 1:

INTRODUCTION TO MOLECULAR ELECTRONICS AND ORGANIC SPINTRONICS

1.1 Background

The early 21st century has proven to be an extraordinarily exciting time for technological advances. It is easy to take for granted that the things we may be used to in our day to day lives – such as the Internet, online communication, GPS navigation – simply weren't present as little as twenty or thirty years ago. The rate of technological advancement and innovation is so high that each new generation experiences a seemingly new world from the last, thinking that new inventions the previous generation had to adapt to are normal, and there are no indications this trend will change anytime in the foreseeable future.

One of the most direct points of evidence for the high rate of technology increase comes in the form of the computer. Twenty or thirty years ago it would be sensible to ask if a person owned a computer; now a more sensible question is how many computers they own, or even how many they have with them at any point in time. Such a change in question comes from the technological advancements that have come in computer technology and the scaling down of computer components to make modern phones just as powerful as desktop consoles from the late 20th century.

Size is actually a relevant quantitative method by which both industry and the lay audience judges the advancement of computer technology, and a relationship often cited in this discussion is known as Moore's Law (Figure 1.1). The "Law" was originally stated in 1965 by

Gordon E. Moore, co-founder of Intel, and was based on an empirical observation about the decreasing size of transistors in computer chips.¹ Simply put, transistors drive the processing capability of computers, and increasing the number of transistors concurrently increases the ability of the processor and the device incorporating them. Moore observed that the density of transistors that were being fabricated on an integrated circuit doubled approximately every two years and predicted that this trend would continue. 50 years later, many innovations – such as the more recent implementations of 3-dimensional transistor architecture, high-dielectric constant materials like hafnium and zirconium, and multi-core processors – have enabled this trend to extend beyond several predicted fundamental limits of silicon-based transistor technology. Transistors now are mass-produced at 22 nm sizes, with sub-10 nm transistors on the horizon.

While the size decreases and subsequent increase in computer capability are undeniable, a few undesired consequences in this silicon-based electronics regime have emerged. For example, some properties such as clock speed and actions/clock have leveled off in recent years. The innovation of multi-core processing has increased computational capability, but as observed by computer architect Gene Amdahl is what has been referred to as Amdahl's Law, there is a diminishing return to the benefits of multi-cores as more cores are added (Figure 1.2). Different opinions exist on the matter, but some estimations state that the cost to go beyond 16 cores – both in terms of hardware as well as software production to account for the increased processor complexity – will outweigh any commercial benefits.

The point of this discussion isn't to imply, as has been stated multiple times along the life of Moore's Law, that computers and transistor technology are anywhere near stagnating. History has proven that innovations continue to overcome assumed limits and roadblocks, and the creativity and innovation behind recent advancements will no doubt be extended in one form or

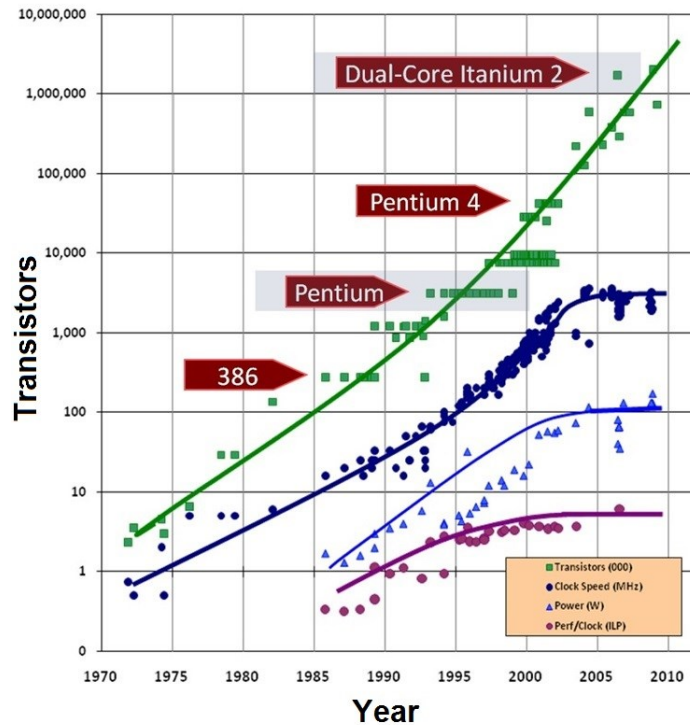


Figure 1.1 – Moore's Law

Graphical representation of Moore's Law, depicting the logarithmic growth of the number transistors in a processor over time (green squares), as well as the power (blue triangles), clock speed (purple circles) and performances per clock (perf/clock; maroon circles) of the same transistors.²

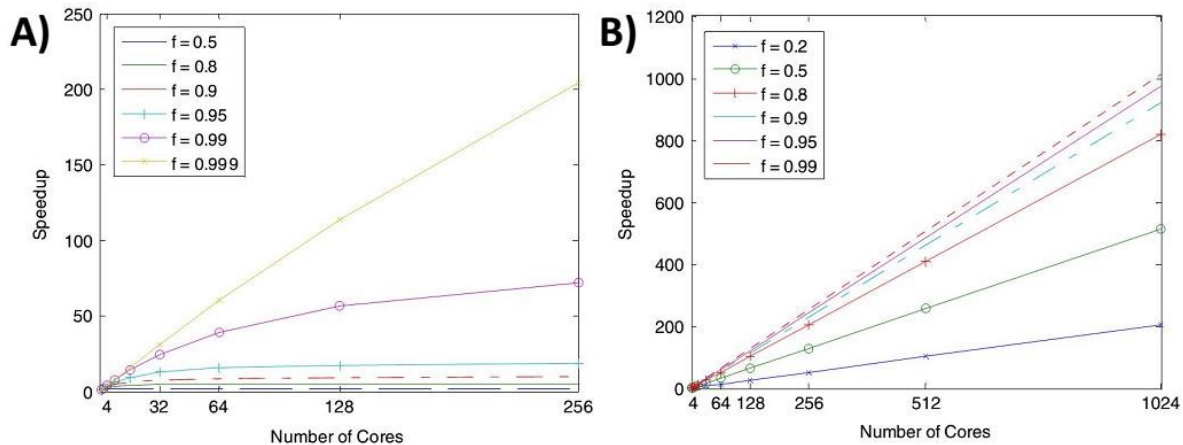


Figure 1.2 – Amdahl's Law

Calculations of various modifications of Amdahl's Law, comparing the speedup (enhanced performance / original performance) of a processor based on number of cores and the portion of a workload that can be parallelized across multiple cores (f), assuming **A)** fixed-size speedup and **B)** fixed-time speedup. Reprinted from Ref. 3, Copyright 2010, with permission from Elsevier.

another. The point of this discussion is also not to simply execute the common ‘here is a problem, here is a solution’ setup. The reality is that the silicon-based technologies that have been the staple of late 20th century/ early 21st century electronics have enormous amounts of talent and time invested in them to continue and push the technology forward. History has shown that if researchers and industry were to decide to stay in the same regime, no doubt at least for the foreseeable future more advances could be made.

The goal of this discussion and subsequent work in this thesis is to suggest and highlight an alternative to the present path of silicon-based technology in computer technology and the like, one that involves unique processes but is not orthogonal to present technologies, can be innovative yet inexpensive in its execution, and bears its own disadvantages and limits but can potentially overcome the pitfalls becoming present in simple scaling of silicon-based transistors.

1.2 Organic Materials for Electronic Applications

1.2.1 Recent Interests in Organic Electronics

In 2000, the Nobel Prize in chemistry was awarded to the group of Alan Heeger, Alan MacDiarmid, and Hideki Shirakawa for “the discovery and development of conductive polymers”.⁴ While it has been many years since the first examples of organics being used in photovoltaics (PVs) and electronics – one of the first reports comes from 1958 when David Kearns and Melvin Calvin used magnesium phthalocyanine disks coated with tetramethyl *p*-phenylenediamine for photovoltaic cells⁵ – the much more recent Nobel Prize highlights the focus and excitement that has been given to organic materials and their conductive properties. In fact, recent discoveries and advances have accelerated organic electronics into a variety of electronic applications. Organic light emitting diodes (OLEDs), motivated by the highly tunable bandgaps in organic materials, are currently being mass produced in televisions and other visual

displays.⁶ Organic solar cells are experiencing fast paced growth with efficiencies high enough or near high enough for commercialization (Figure 1.3).⁷ Most relevant to the work to be presented here, organics have also become an attractive option for transistor and switch type applications relevant to computer technology.

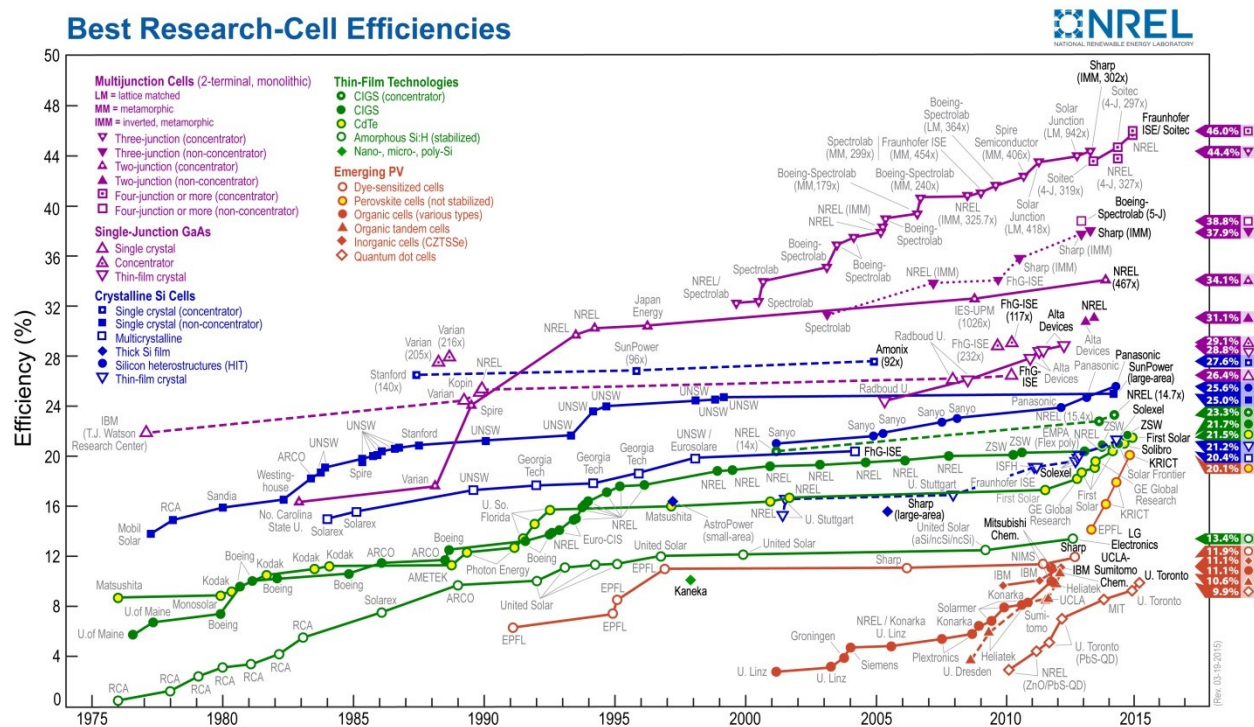


Figure 1.3 – Champion Solar Cell Efficiencies Based on Solar Cell Type

Plot showing champion solar cell efficiencies for a number of classes of solar cells, as compiled by the National Renewable Energy Laboratory (NREL). Organic solar cells and their rising efficiency are represented in the ‘emerging PV’ category by the filled red data points.⁷

1.2.2 Properties of Organics for Electronic Applications

There are strong advantages to utilizing organic materials in transistors as well as other electronic applications. Many facile processes have been developed for the deposition of organics, from the basics of spin-casting and solution soaking to more complex patterning methods. Solution processibility of many organics allows for mass-producible deposition methods such as flow-coating and ink-jet printing.⁸ Taking advantage of the self-assembly properties of organics can lead to easy-to-produce assemblies. For example, pentathiophene derivatives are found to assemble into micron sized conductive islands when prepared in Langmuir-Blodgett films.⁹ Many of these processes can be low cost, accomplished by relatively basic equipment and requiring little more than the active material and solvent or surfactant.

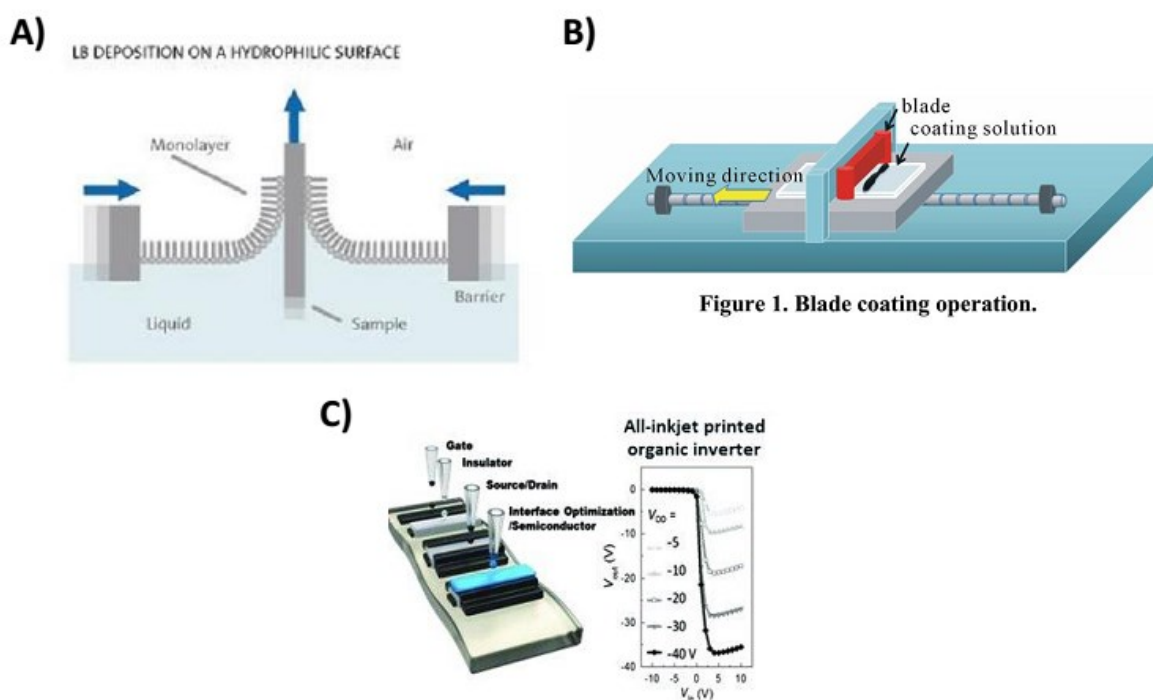


Figure 1.4 – Solution Processible Techniques for Large Scale OPV Production.

Representation of several solution processible techniques for mass production of organic photovoltaics. **A)** Formation of Langmuir-Blodgett films from a solution.¹⁰ **B)** Blade coating of organic PV (OPV) films from solution.¹¹ Copyright 2013, Scientific Research Publishing. **C)** Representation of fabrication process and output of ink-jet printed OPV.¹² Copyright © 2013, Wiley-VCH Verlag GmbH & Co. KGaA.

Another advantage is the functionalizability of organic materials. Sometimes simple chemical reactions and design principles can modify organic materials and dramatically change their properties. In one study, attaching a tetrathiafulvalene (TTF) moiety onto different positions along a oligo(phenylene ethynylene) (OPE) backbone significantly alters the bandgap and conductance of molecular wires.¹³ Using linear or bent OPE backbones can also change the delocalization of charges along a wire.¹⁴ Controlling the rotation of phenyl rings synthetically highlights that conductance can be tuned synthetically.¹⁵ These represent just a few examples of the capability shown in organic systems.

Even more impressive than these, the most dynamic organic systems contain functional groups or configurations that can be switched post-synthesis. Photochromic compounds can have conjugation established or broken, which will have large impacts on the conductivity of the molecular unit.¹⁶ Temperature can be designed to switch between polymorphic states in tetraacetate.¹⁷ Exposure to specific chemicals (or hydrogen, in the case of pH changes) can also affect conjugation and thereby conductivity,¹⁸ and magnetic or electric fields can be used to alter spin states or electric polarizations and thereby conductivity (Figure 1.5).¹⁹ It should be stated that some silicon systems can be altered, the main way being chemical or physical doping, but *in-situ* alteration of their properties like those described here are rare.

Furthermore, organics lend themselves well to biological applications. Organic based plastics and polymers have long been used to encapsulate inorganic systems in biological settings.²⁰ The biocompatibility of many conductive organics creates the possibility for fully biodegradable systems for a wide range of uses.²¹ Utilizing another important property of organic films and materials – their flexibility – electronics have been designed to conform to the shapes

of various appendages and organs, enabling their use in external limbs and studying diseases and events such as heart disease and strokes.^{22,23}

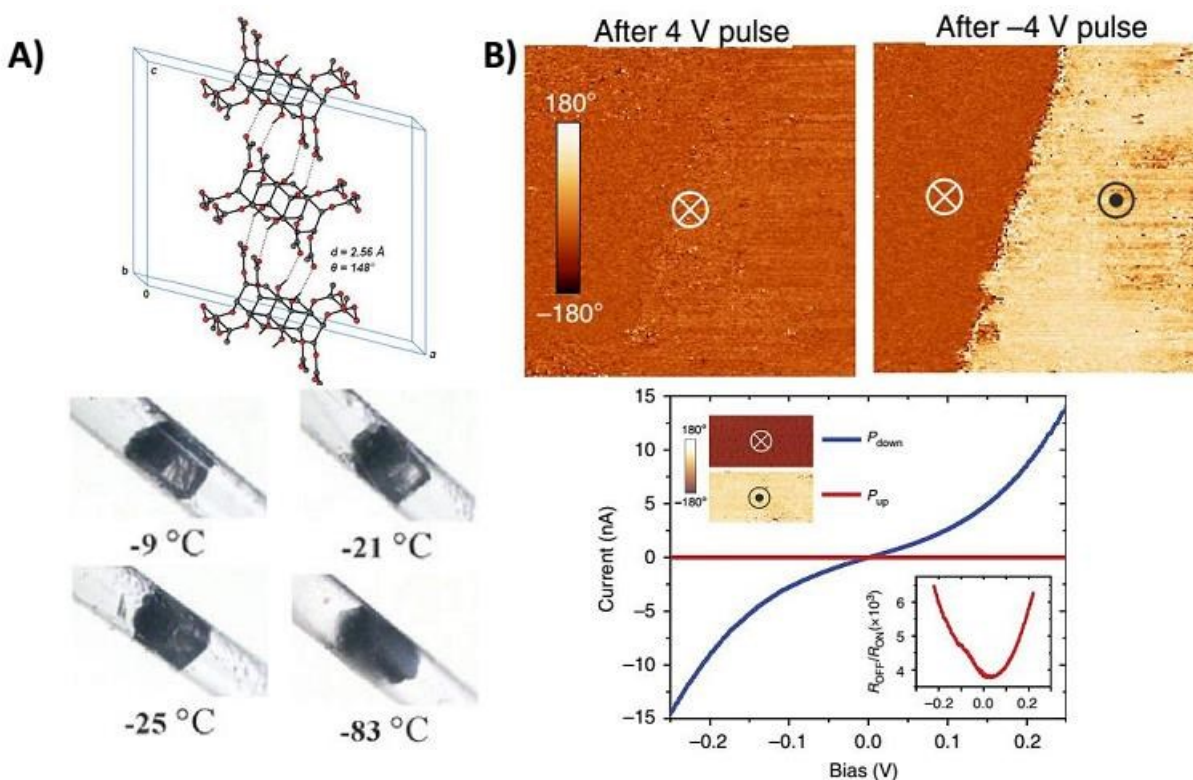


Figure 1.5 – Examples of Post-Synthesis Switchable Properties in Organic Systems

Examples of post-synthesis switch properties in organic systems. **A)** Molecular packing in polyacene films at 18°C , and visual representation of its polymorphism at different temperatures. Reproduced from Ref. 17 with permission of The Royal Society of Chemistry. **B)** Graphene/NH₃/BaTiO₃/LSMO samples, measured by piezoresistance force microscopy, showing the appearance of different electric field polarizations at different biases. The current-voltage plot underneath shows different resistances can be measured for upward (red) and downward (blue) polarizations in the sample.¹⁹ Reprinted by permission from Macmillan Publishers Ltd: Nature, Ref. 19, Copyright 2014.

The largest disadvantage to organics in these applications is their susceptibility to degradation in ambient conditions. Though the Kearns and Calvin PV cell that represented the first of its field required an oxidized organic film for its function, a large number of organic PVs (OPVs) and other organic electronics quickly lose their functionality in oxygen. Many of these

effects are removed by studying systems in vacuum or inert environment (nitrogen, argon), but these conditions are difficult to extend to practical use. Encapsulation methods have been developed to mitigate these effects, such as depositing inorganic oxides²⁴ or polymer layers.²⁵ Especially with the former, care must be taken such that the encapsulating material doesn't penetrate or otherwise impede function of the active layer.

Despite this disadvantage, constant advancements such as encapsulation continue to push organic materials to relevancy in electronics. Especially as we consider the capability to make devices on the single molecule level as will be described in the next section, a bright future is evident from applications incorporating these materials.

1.3 Molecular Electronics

Beyond bulk materials and films, a frontier of electronic devices exists at the single molecule level. Even considering the presumably soon advent of sub-10 nm transistors, molecular electronics (ME) – which is generally referred to here as utilizing organic-based molecules in single or few number of molecule junctions for electronic applications – promises a huge jump in transistor density due to devices potentially existing within a single molecule. Though more than this, molecular electronics is an exciting field because of the unique properties that can exist in single or few number of molecule junctions. When properly executed, the synthetic control that can be had on organic molecules can be used to directly realize dramatic property changes in molecular electronic systems.

1.3.1 Synthetic Control of Molecular Electronic Properties

Whereas thick films of materials will typically have a range of inter- and intramolecular charge transport mechanisms occurring simultaneously, transport pathways in ME systems tend to be easier to understand and manipulate. Molecular length in single molecule wires can directly

control the charge transport through finite regimes such as tunneling and charge hopping, as seen by controlling the number of repeat units in OPE chains.²⁶ Functional groups can also significantly modify the charge transport properties of similar length wires. Synthetically inserting parallel transport pathways through a molecular wire can lead to quantum interference, either constructive or destructive, with these effects sometimes being altered with different functional groups on a common backbone.²⁷ Due to quantized energy levels present in many organics, bias dependent current effects can be realized. Negative differential resistance and other similar alterations in the current profile of molecular electronic systems can manifest as transport becomes resonant under certain biases.²⁸ In addition, organic systems can be designed to rectify current based on the direction of injection electrons (holes). Often this control comes from asymmetric systems, created in some cases through physical separations of n-type and p-type regions,²⁹ other times by incorporating asymmetric regions on molecular wires.^{30,31}

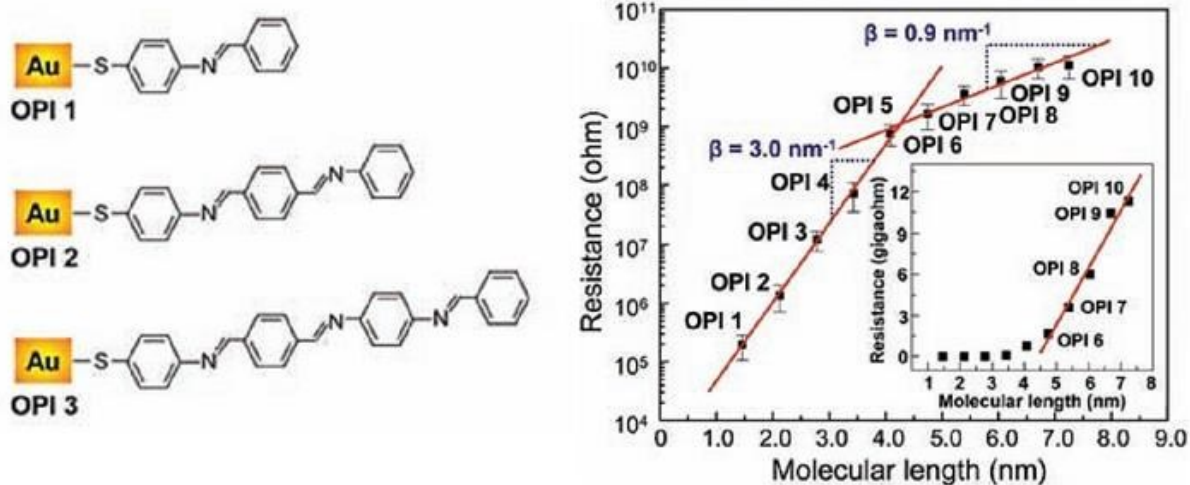


Figure 1.6 – Altering Charge Transport Mechanisms in Molecular Wires

Representation of oligophenyleneimine (OPI) wires, which can be grown to specific lengths *via* a click chemistry process, and their electrical properties when measured *via* conductive-atomic force microscopy (cAFM). A shift from tunneling to charge hopping is exhibited in changing resistance trends of shorter OPI wires to longer. From Ref. 32. Reprinted with permission from AAAS.

1.3.2 Switchable Properties in Molecular Electronics

Perhaps even more powerful than the effects already described, a wide range of hysteretic and switchable properties can be realized in molecular electronic devices for potential use in single molecule transistors. These properties can start at the thin film level, such as in metal organic frameworks (MOFs) containing 7,7,8,8-tetracyanoquinodimethane (TCNQ) that can have tunable electrical properties with different TCNQ infiltration,³³ and C₆₀ films on silicon oxide substrates that have hysteretic current based on previously applied bias due to remnant charges at the C₆₀/ silicon oxide interface.³⁴

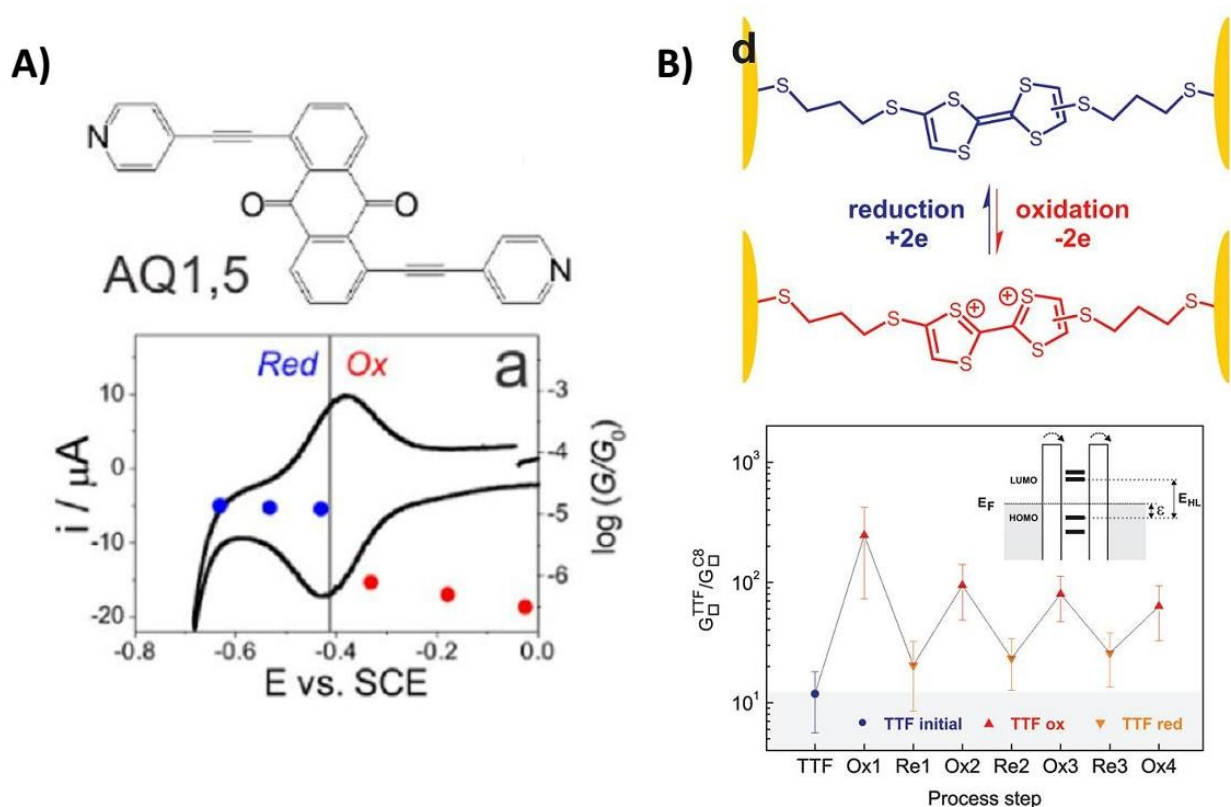


Figure 1.7 – Conductance Switching in Molecular Wires

A) Anthraquinone-based molecular wires in STM-BJ setup, where oxidizing/reducing the anthraquinone core correlates with over an order magnitude change in the conductance of the wire. Reprinted with permission from Ref. 35. Copyright 2014 American Chemical Society. **B)** A TTF derivative in STM-BJ setup where oxidation/ reduction of the wire changes the ratio of the conductance relative to a junction with just C8 molecules present ($G^{\text{TTF}}/G^{\text{C8}}$). Reprinted with permission from Ref. 36. Copyright 2010 American Chemical Society.

Because of their simplified transport pathways, molecular wires can amplify these effects from switchable events. Utilizing the oxidation/reduction of an anthraquinone core, molecular wires in a scanning tunneling microscopy (STM) setup can exhibit over an order of magnitude alteration in current.³⁵ Redox reactions affecting TTF units in molecular wires were also shown to affect current and sheet resistance in connected networks of gold nanoparticles (Figure 1.7).³⁶ Similar to redox switching, controlling the charges on zwitterions attached to a surface is expected to be able to modulate current.³³ Organic fluorescent logic gates were designed to be able to respond to multiple stimuli – glutamate, zinc, and pH – and form molecular logic ‘AND’ gates that influence the fluorescence output based on the inputs.³⁷ Utilizing in-situ chemical reactions *via* sources such as ultraviolet (UV) light to affect conjugation in molecular wires will affect coupling of molecular units and therefore the current that can pass through them.^{16,38} In addition, physical mechanisms can be used to control output through molecular wires. Mechanically stretching a junction can affect conjugation and affect current through the junctions.^{39–41} Altogether, a host of switches manifesting from control of the properties of organic molecular wires have been realized, highlighting the power and promise of organic-based molecules in this setup.

1.4 Organic Spintronics

Much effort has been placed on using electrons and modulating their output for switch type properties in molecular electronics. However, manipulating a particular property of electrons – their angular momentum or spin – can be equally as powerful. Such manipulation leads to a discussion of spintronics – the utilization of spin as a degree of freedom in electronic devices.

1.4.1 Basics of Spintronics- Spin Valve

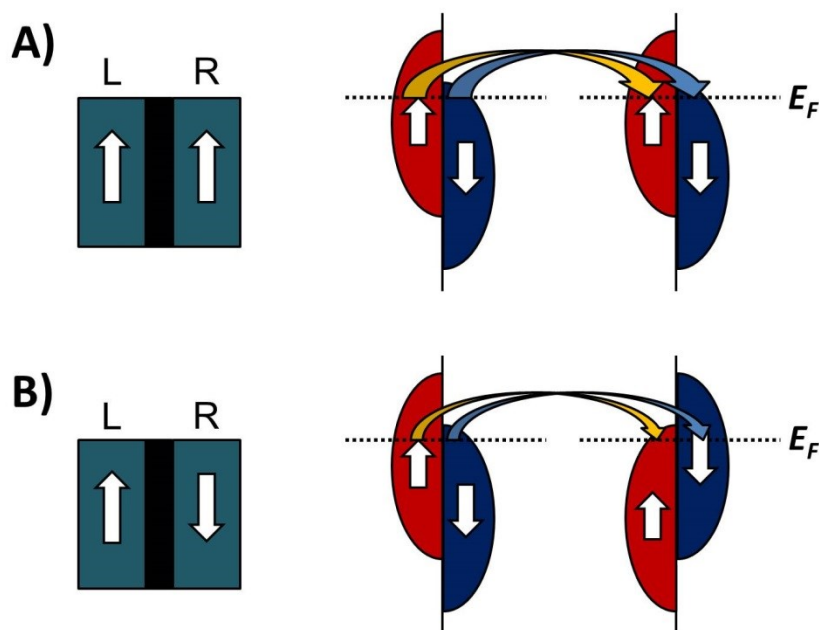


Figure 1.8 – Spin Valve

Pictorial representation of a spin valve, with a tunneling spacer separating two magnetic electrodes (represented by ‘L’ and ‘R’ for ‘left’ and ‘right’). **A)** Electrodes with parallel magnetization, leading to matching of spin DOS in this system at Fermi level (E_F) and high current through the device. **B)** Electrodes with anti-parallel magnetization, leading to mismatch of spin DOS in this system at E_F and low current through the device.

The basic premise of spintronics involves manipulating the density of states (DOS) in molecules to allow or disallow transport of electrons based on their spin state. In the most basic execution, the spin DOS of an injector electrode, which is symmetric between electron spins in many systems in absence of a magnetic field, is manipulated by a magnetic field to be made asymmetric. This change results in one electron spin becoming a majority spin and a net non-zero spin being injected into the spintronic system. The spintronic device will have a receptor molecule or electrode that preferentially allows transport of a particular spin, often due to its own asymmetric spin DOS. Depending on the injected spins and receptor spin DOS, two outcomes

are possible. If the majority spin transported through the device is also the majority DOS in the acceptor, a large number of electrons are allowed to be transported through the junction, signifying the low resistance/ high current state of the device. Mismatch of majority spin and receptor spin DOS will result in the inability of electrons to transport through the device. Electrons will be scattered at the receptor interface, and a high resistance/ low current state will ensue.

The ideas presented in this basic picture are the functioning principles behind the spin valve (Figure 1.8). The spin valve has three parts: two metals, typically from a class of metal known as a ferromagnet which, up to its Curie temperature – the temperature at which it loses its ability to sustain a remnant magnetism upon removal of the magnetic field – maintains spin DOS after it has been manipulated *via* magnetic field; and an insulating (non-magnetic) tunnel barrier. The two metals are influenced by a magnetic field to change their spin state, ideally having different coercive fields to manipulate their spin states independently of the other metal. As magnetic field switches the magnetizations of the electrodes, the resistance of the overall junction will change as the electrodes have parallel or anti-parallel magnetizations. Electrons tunneling through the tunnel barrier will maintain their spin state, allowing for the electrodes and their magnetic properties to be the only comparison that influences the resistance. The effect of magnetic field due to change in resistance as a function of magnetic field is represented by the magnetoresistance (MR) of the device:

$$MR = \frac{R(B) - R_0}{R_0} \quad (1-1)$$

In the case of tunneling through a non-magnetic spacer where only the electrodes impact the resistance properties, the MR is referred to as tunneling magnetoresistance (TMR). MR in general can be a positive or negative value, and the same is true with TMR. In the case of TMR,

the sign can be either due to the properties (specifically the DOS) of the metals used. While the magnetizations of the metals will always be aligned if a large enough magnetic field is applied, due to the nature of tunneling, the electrons at the Fermi level (E_F) will be the highest energy electrons and have the largest probability of transporting through a tunnel junction.

Magnetization doesn't always correspond with DOS at E_F , so it is possible to have two metals that have aligned magnetic states but either aligned or mismatched DOS. Because of this, it is possible to have positive or negative TMR in a spin valve. Knowing the DOS of the metals allows us to estimate a TMR value *via* Julliere's model⁴²:

$$TMR = \frac{G_{\perp} - G_{\parallel}}{G_{\parallel}} = \frac{2P_L P_R}{1 - P_L P_R} \quad (1-2)$$

$$P_L = \frac{n_L^{\uparrow} - n_L^{\downarrow}}{n_L^{\uparrow} + n_L^{\downarrow}} \quad P_R = \frac{n_R^{\uparrow} - n_R^{\downarrow}}{n_R^{\uparrow} + n_R^{\downarrow}} \quad (1-3)$$

where G , the conductance of either the parallel (\parallel) magnetization condition or the anti-parallel (\perp) magnetization condition can be described by the spin polarization (P) of the two metal electrodes at E_F (labeled here as 'L' for left electrode and 'R' for right electrode). The spin polarization is determined *via* the DOS at E_F is determined by the ratio of spin 'up' electrons (n^{\uparrow}) to the spin 'down' electrons (n^{\downarrow}). The designation of 'up' and 'down' is arbitrary, as we are referring simply to two angular momenta with no distinct directionality (other than the fact that they are opposite to one another). The common notation is to consider the 'up' electrons to be the majority carriers, and the 'down' electrons as minority carriers. The equations (1-2) and (1-3) above are valid regardless of these denotations.

This basic spin valve has proven to be extremely useful and, to a certain degree, is still the basis of magnetic memory. Even larger MR effects than expected *via* Julliere's TMR model can be obtained in unique systems based on the spin valve. The most classic example of this is

known as giant magnetoresistance (GMR), which was first seen in layered stacks of chromium and iron.⁴³ Other effects, such as colossal magnetoresistance (CMR), an even larger MR effect than GMR when perovskite cells are used as a spacer, have been seen as well.⁴⁴ This highlights the fact that many possibilities that can be built off this basic spin valve picture and can lead to many unique effects.

1.4.2 Basics of Organic Spintronics

The field of organic spintronics mostly focuses on creating unique effects in spintronic devices by replacing the tunneling spacer from the spin valve with an organic layer. At its core, this modification allows for one large advantage: organics and organic-based materials typically have higher spin delocalization lengths than their inorganic counterparts. Spin-orbit coupling interactions that would lead to spin-flipping events occur more frequently with larger atomic mass, scaling by a factor of Z^4 . The low atomic mass from carbon instantly reduces these effects, increasing spin diffusion length from the order of 10^0 nm in typical metals to as high as 10^2 nm in organic materials.⁴⁵ Spin-orbit coupling will still ultimately reduce MR effects in longer organic systems,⁴⁶ but modifying the structure of device architectures, such as taking rubrene thin films and restricting them into nanowires,⁴⁷ have been able to further the spin diffusion length improvements in certain systems. This allows for injection and transport of electron spin for finite lengths through organic materials, allowing for the spacer in the spin valve picture to become an active component in the spintronic device.

1.4.3 Organic Magnetoresistance

Simply injecting and transporting spins through an active layer bears unique consequences on the MR properties of a spintronic device. The effects of transporting electron spin through films of non-magnetic organic materials has been studied and expressed through an effect known as organic magnetoresistance (OMAR). In this setup, the injected spins can interact

with one another, leading to formation and spin interaction of singlet/ triplet polarons, paired polarons, bipolarons, and singlet/triplet excitons.⁴⁸ Due to these effects, ultimately the observed MR effect is no longer dependent solely on the DOS of the metals. OMAR is not a fully understood effect, possessing positive or negative signs depending on the properties and composition of the active layer as well as the conditions under which it is measured. One particular interesting study showed that tuning the composition of a polymer-fullerene blend can alter the presence of excitons, free charge carriers, and polarons, which thereby affects the shape and sign of the OMAR effect.⁴⁸ Some experiments have shown that hyperfine coupling plays a role in the effect, where films of C₆₀ without hydrogen groups do not exhibit OMAR but [6,6]-phenyl C61 butyric acid methyl ester (PCBM) molecules with hydrogen do.⁴⁹ The aforementioned bipolaron formation in OMAR has been used to create models that, thus far, have yielded some of the best models of OMAR in the literature.⁵⁰

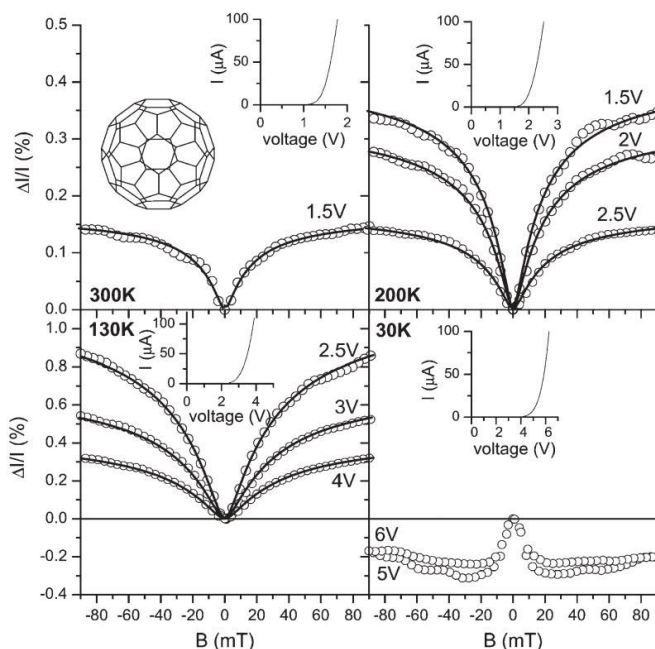


Figure 1.9 – Organic Magnetoresistance (OMAR) in PEDOT/C₆₀/Al devices

Different temperatures and biases for OMAR measurement lead to different magnitudes as well as different signs and trends of MR behavior. Reproduced from Ref. 51 with permission of the Royal Society of Chemistry.

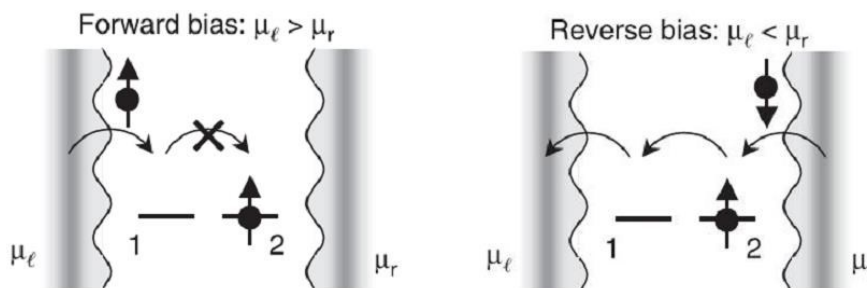


Figure 1.10 – Coulomb Blockade

As presented in this image involving quantum dots (QDs), Coulomb blockades limit the spins that can transport through a limited transport site system, as with QDs or molecular wires. The image on the left shows that when an electron is introduced into the system on site 1, if it has the same spin as site 2, the electron cannot transport due to Pauli exclusion, and it will also scatter any other spin up electrons on site 1, effectively stopping the flow of current. In this two-QD system, the reverse bias allows for some current to flow since spin up electrons are forbidden before injection, but while they cannot transport, they also are not trapped along the wire. From *Science* **2013**, 341, 257-260. Reprinted with permission from AAAS.

One element of OMAR that has been expressed and experimentally verified is the formation of spin blockades in localized regions of organic layers. Due to Pauli exclusion principle, two electrons with same spin cannot occupy the same orbital. At least a slight inhibition on charge transport will be seen since we no longer have spin randomized currents in these spintronic scenarios, allowing for blockades to form, as well as a lower probability of spin flipping events due to the organic materials being used. In the case of systems where the charge transport is restricted to a wire, this effect can be extremely augmented since there would be no alternate pathways for current to travel, creating a (spin) Coulomb blockade that results in very large MR effects (Figure 1.10). For example, restricting charge transport along long wires of perylene-based DXP molecules in a zeolite backbone, designed such that charge transport could not tunnel between electrodes but had to undergo charge hopping between perylene units, yields MR effects up to 2000% in sub-100 nm films.⁵² It should be noted here that the literature typically refers to OMAR in the case of thin films and not in the case of these wires, but the

same principles in OMAR apply to the wire case.⁵³ Overall, this discussion and observation of OMAR expresses that organic films can already be manipulated to yield MR effects much larger than the tunneling based MR effects typical in spin valves.

1.4.4 Magnetic Properties from Organic Molecules

Even beyond this, specialized organic molecules can possess inherent magnetic properties, allowing for injected spin to be manipulated within the ‘spacer’ of the spintronic device. Spin interactions have yielded ferromagnetic properties in specialized organic systems, such as films of bis-tetramethyl-piperidyl-oxyl-butadiin (BIPO).⁵⁴ Ferromagnetic properties have also manifested in vanadium tetracyanoethylene complexes ($V[TCNE]_x$), due to antiferromagnetic coupling between the V^{2+} unpaired 3d electrons and the $TCNE^-$ unpaired π^* electron, allowing a ferromagnetic system with a Curie temperature well above room temperature.⁵⁵ Interestingly, ferromagnetism has been expressed from non-magnetic Teflon substrates that have been cut or torn. It is expected in these systems that dangling carbon bonds, generated by the break, interact constructively to yield the magnetic signal. Exposure to hydrogen environments removes this magnetic signal, along with a theoretic analysis, giving further evidence to this dangling bond hypothesis.⁵⁶

Taking advantage of similar magnetic properties in organics, multiple reports have suggested the capability of organic systems to manipulate spin current such that they exhibit inherent spin polarized transport. A few mechanisms exist to suggest how this can be possible. Chiral polymers represent a unique test bed as transport through these molecules results in a system similar to a magnetic coil. Magnetic coils are known from basic electricity and magnetism principles to generate a magnetic field when current is passed through. The magnetic field can then align the spin state of electrons transported through them, an effect which is realized in chiral systems. DNA oligomers⁵⁷ and short chiral polymers⁵⁸ have been shown to

exhibit over 80% spin polarization, detected by a variety of methods including optical analysis, cyclic voltammetry, and magnetoresistance measurements in a device, where in all cases a magnetic field is only used for spin detection.

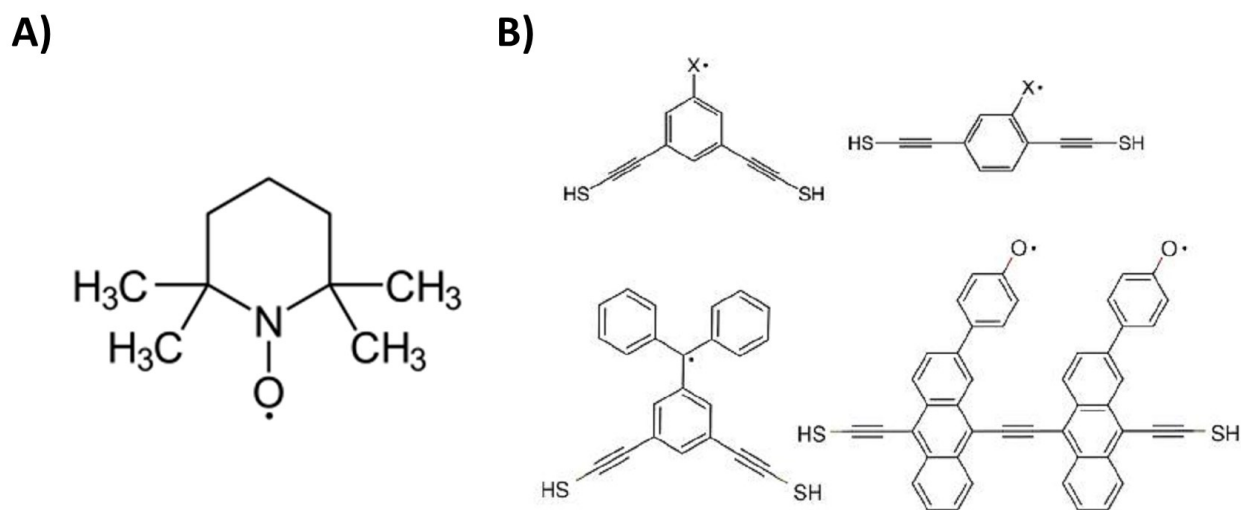


Figure 1.11 – Organic Radicals for Spin Polarized Transport

A) Representation of TEMPO ([2,2,6,6-tetramethylpiperidin-1-yl]oxyl). **B)** Several radical-based molecular wires computationally showing spin-polarized transport states by Herrmann *et al.* Reprinted with permission from Ref. 59. Copyright 2010 American Chemical Society.

A number of organic molecules, such as TEMPO ([2,2,6,6-tetramethylpiperidin-1-yl]oxyl), are known to possess long-lived radicals, existing even in ambient conditions in certain circumstances. Theoretical studies have suggested these radicals will contribute magnetic field effects on electrons transporting through organic systems, thereby providing a method similar to the chiral molecules where spin polarization is generated (Figure 1.11).⁵⁹ Unfortunately, the instability of these radicals prevents many molecules from sustaining them in functional device architectures. Certain systems provide exceptions to this rule, such as films of zinc methyl phenalenyl (ZMP) which can sustain an injected electron from ferromagnetic metal at the

molecule-metal interface for switchable MR properties.⁶⁰ Finished devices including this molecule have expressed 25% MR in finished devices. Ultimately, a bonafide synthetic approach to radical insertion and utilization for spin polarized transport has not yet been developed.

It should be stated that other specialized molecular systems have been theoretically predicted to exhibit spin polarized transport. The design principles, such as coupling metal centers to conjugated sheets²⁸ or the effect of paramagnetic metal centers to phthalocyanines and porphyrins⁶¹ provide evidence toward systems that may have strong spin interaction. The difficulty in these systems are twofold – many of the experimentally predicted systems are difficult to be synthesized, and the spin polarized DOS predicted from many of these calculations would be difficult to realize outside of the low temperature, high magnetic field (3 Tesla and higher) conditions assumed in the calculation. The porphyrin molecules studied in this work, while slightly different from the fused porphyrin rings used in Cho *et al.*, attempt to use this metal center- conjugated organic system approach for inherent spin transport properties.

1.4.5 Interface Considerations in Organic Spintronics

It should be noted that the MR effects in the chiral systems described above, which show high spin polarized transport through the organic molecule, ultimately yield low-MR effects (<10%) when a second electrode is attached. This highlights the fact that electrodes and interfaces can play a significant role in spin scattering effects, potentially leading to the augmentation or destruction of spintronic effects. One of the potential negatives of using organic molecules in spintronic devices comes from an effect known as “conductivity mismatch”.⁶² Conductivity mismatch comes from the fact that organic materials are significantly higher resistance materials than the metals typically used to inject electrons into them. In a basic spin transport model, we assume majority and minority carriers will transport independently from one another, a fact which is untrue but helps us describe the mismatch scenario easily. The transport

of spins through the organic is the rate limiting step in this problem, not the injection of the electrons, and since majority and minority carriers transport equally ‘slowly’, a limited number of majority and minority carriers can transport through the junction at a time. Therefore, even if a large spin polarization exists in a metal, the majority carriers do not transport quickly enough through the organic film to allow the polarization to be realized in the second electrode, and the measured spin polarization at the second electrode (as well as resulting MR effect) will be significantly lower.

One notable solution to get around the conductivity mismatch problem is to utilize a tunnel barrier for electron injection into the organic active layer. Tunneling preserves the spin of electrons, and given that it is an even higher resistance transport mechanism than transport through an organic medium (assuming the organic isn’t purely insulating), the rate limiting step for transport now becomes the tunneling barrier. While the overall resistance of the device will be raised, the spin polarization will be preserved through the organic layer, allowing for organic materials to be effectively used in spintronic settings.

This design principle has been applied in numerous situations to create organic spin valves (OSVs).^{63,64} A proof of concept study involving pentacene definitively shows the impact of the tunnel barrier. On its own, pentacene is a highly conductive organic molecule, but when used on its own in an OSV setting, no MR is seen. Only when the pentacene is subjected to an oxygen plasma is any spin valve behavior readily seen. Hong *et al.*¹⁸ show *via* depth profiling that the plasma only oxidizes the top layer of the pentacene, forming a quinone layer to act as a tunnel barrier to resolve the conductivity mismatch. Consequently, MR was observed in the plasma exposed device, thereby showing that the quinone layer (the tunnel barrier) resolved the conductivity mismatch problem.

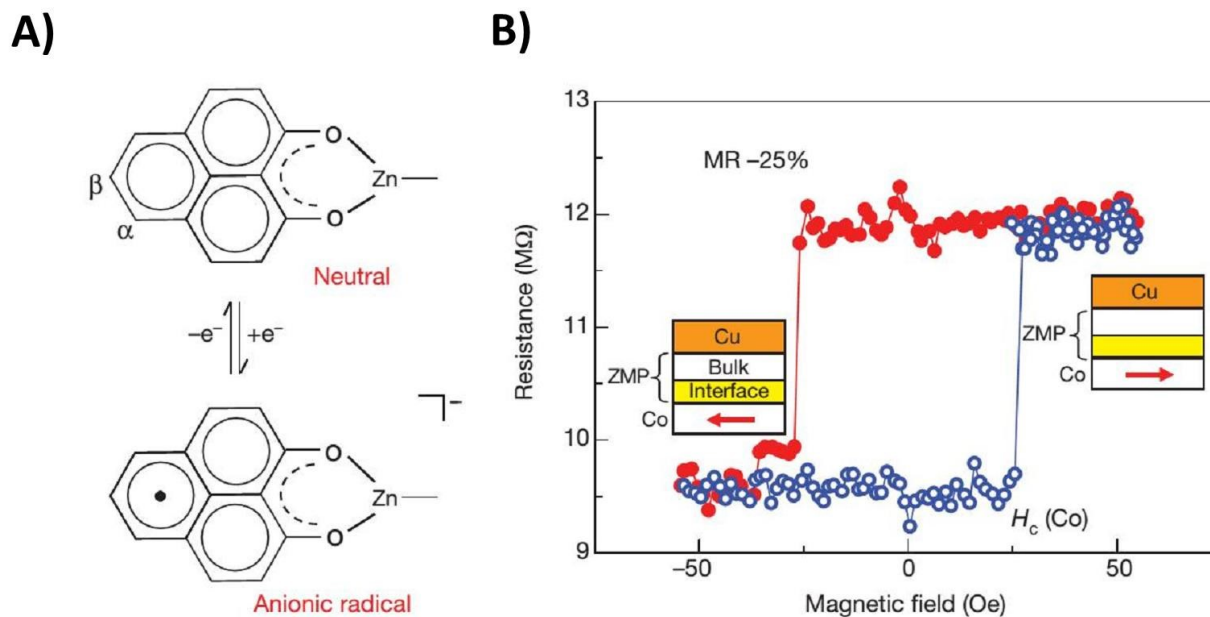


Figure 1.12 – Engineering Spintronic Effects at Zinc Methyl Phenalenyl (ZMP) Interfaces

A) Reduction of neutral ZMP leads to an unpaired electron in the conjugated network. **B)** Device MR output, showing that the presence/ absence of this unpaired electron can influence a spintronic effect at the interface.

Reprinted by permission from Macmillan Publishers Ltd: *Nature*, Ref. 60, Copyright 2013.

Several studies have demonstrated that specific interface effects can be used to effectively design organic spintronic systems with good output, even without these tunnel barriers for spin injection. So-called “spinterfaces” can be generated between organic layer and metal electrode to have realistic impacts on the output of an organic spintronic device. In the case of C_{60} films on iron, it was discovered that the 3d states of the iron layer antiferromagnetically coupled with the C_{60} and ultimately reduced the spin moment in the metal by 6%.⁶⁵ Such an outcome would weaken the spin polarized injection and the MR of a resulting device. More constructive “spinterfaces” can be generated by introducing interlayers in organic systems, such as lithium fluoride films in bathophenanthroline monolayers which will anti-ferromagnetically couple with the monolayer to control the sign and magnitude of MR in

finished devices.⁶⁶ In addition, as mentioned previously, films of ZMP can be reduced at an interface due to electron exchange with an electrode, producing an anionic radical in the ZMP molecule (Figure 1.12).⁶⁰ This unpaired radical will change the magnetic properties and interactions of the molecule at the interface, and is experimentally shown to yield 25% MR in finished devices.

1.4.6 Spintronics from Controlling Spin State in Organic-Based Molecules

Much of organic spintronics focuses around the injection and extraction of electron spin in an organic layer, manipulating the spin state of current in the active layer and obtaining switchable properties from this. However, included in this topic of spintronics are systems where changing the spin state of the organic layer changes the properties of the molecule and, potentially, the current passed through it. Electronically labile molecules with redox active metal centers are typical candidates for these effects. Specifically, d-valence metals such as cobalt, iron, manganese, rhodium, iridium, and copper have been seen in various organic-based molecules to change spin states, a change that can also change some of the other properties of the system.⁶⁷

A basic example of these metal center based effects on spin is known as spin crossover (SCO). In this instance, external stimuli such as light or temperature alter the valence d-shell from a high-spin to a low-spin state, or vice versa. This change represents a change in the DOS of the system, which can manifest in resistance change through the molecule. In fact, such control can be realized in individual molecules deposited onto a surface and studied *via* STM-break junction (STM-BJ).⁶⁸ Applying different biases to cause the spin flip directly correlated to different measured current through the molecules, providing a method to use SCO in molecular systems for switching and potential memory applications.

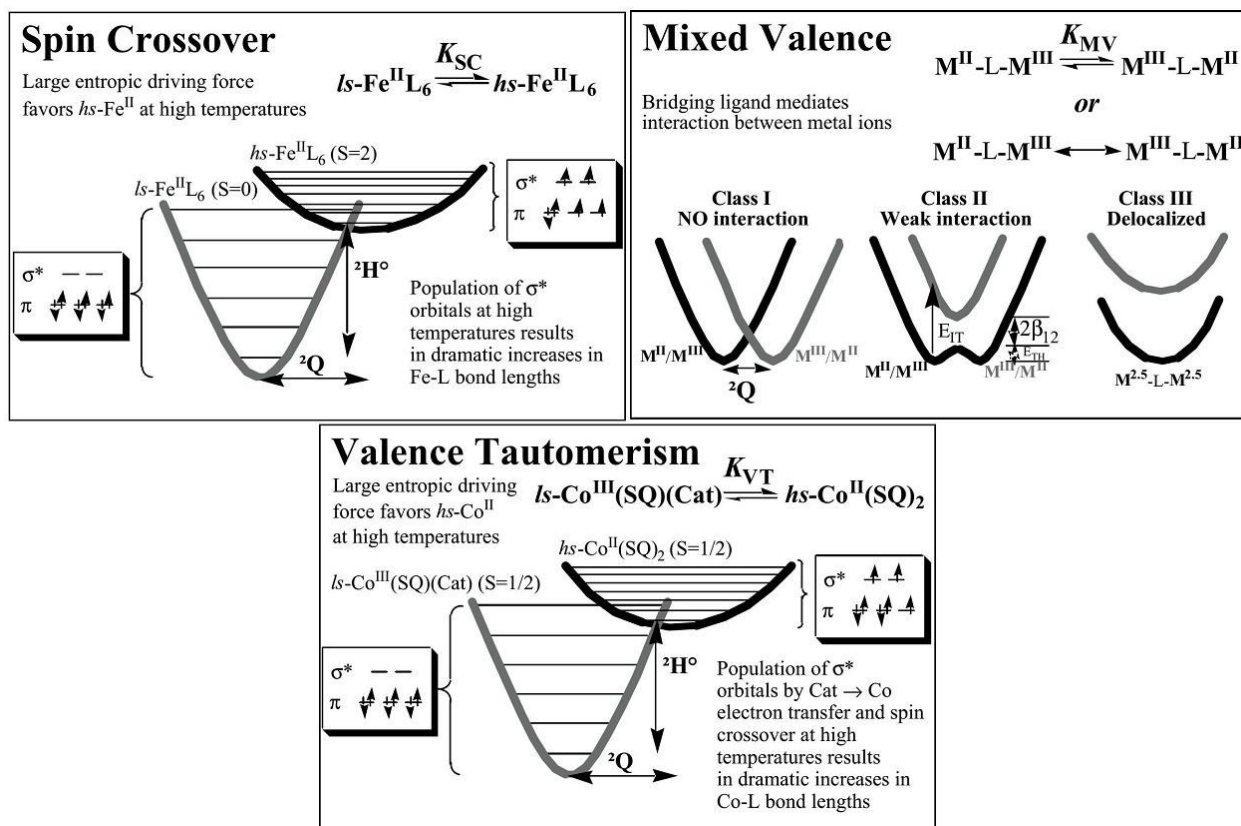


Figure 1.13 – Organic Magnetic Effects

Diagrams representing the basics of spin crossover, mixed valency, and valence tautomerism. Images designed by David Schultz (NC State).

Another example is a mixed-valence system where, similar to SCO metal centers, the oxidation state of the metals can change. Unlike the previous case, mixed valence systems involve interacting metal centers, allowing oxidation states to coexist *via* electronic coupling across a bridging ligand. Because of such coupling between metal centers, stark effect on charge transport or, relevant to this discussion, spin transport can occur, and the presence of Coulomb blockades as discussed in OMAR can appear. Theoretical studies suggest mixed valence $\text{Fe}^{\text{II}}\text{-Fe}^{\text{III}}$ dimers can exhibit this effect,⁶⁹ generating antiferromagnetic coupling between the iron centers and a Coulomb blockade transport regime. This blockade could be lifted by oxidizing the dimer, highlighting the power of such a switch if it were to be experimentally realized.

A more complex scenario occurs in a class of molecules known as valence tautomers (VTs). While undergoing the same low-spin to high-spin transition as SCO molecules, the transition in VTs is due to an intramolecular electron exchange between metal and ligand, oxidizing or reducing the metal and correspondingly changing its spin state. Cobalt metal centers are strong VT candidates because of this; their neutral d_7 valence shell lends itself to a high-spin configuration, whereas removing an electron from the d-shell would lend well to a low-spin configuration where all electrons could be paired.⁷⁰ Such a switch would change both the magnetic properties of the VT as well as the current properties, with external switches such as light, heat, magnetic field or electrical field allowing for such a switch.

1.5 Designing Devices with Organic-Based Materials

The various examples described above show that adapting organic molecules for electronic and spintronic applications can have many advantages. The potential for switches, transistors, and molecular magnets, can all be realized through the design and implementation of organic-based molecular devices. As may also be apparent, one of the largest challenges with molecular electronics/ spintronics and the implementation of these promising effects in functional devices is actually fabricating devices with single/ few numbers of molecules. Many of the examples above describe thick organic films which can often utilize the same fabrication techniques – such as metal evaporation and sputtering to attach electrodes – as their inorganic counterparts. Adapting these processes by using metals such as copper or lead that have exceedingly low interactions with substrates helps mitigate metal penetration and subsequent device short circuiting.⁷¹ Despite this, pinholes and defects are common to certain systems, and metal penetration can lead to poor interfaces and, in some cases, erroneous results. Moreover, many of the effects offered by these organic based materials – switching events, spin

polarization, and electronic/ spintronic coupling – have been seen or are expected to be most pronounced in monolayers, wires, or single/few number of molecule devices, where these defects, pinholes, and other fragilities will be most pronounced. Altogether, reproducing organic devices with inorganic fabrication processes is not always a perfect process. For both the efforts of scaling down device size and for seeing potentially more dramatic properties from out systems, especially at the single molecule level, special consideration must be made in device fabrication in order to realize the effects, especially in a practical setting.

1.5.1 Techniques for Designing Molecular Electronic Devices

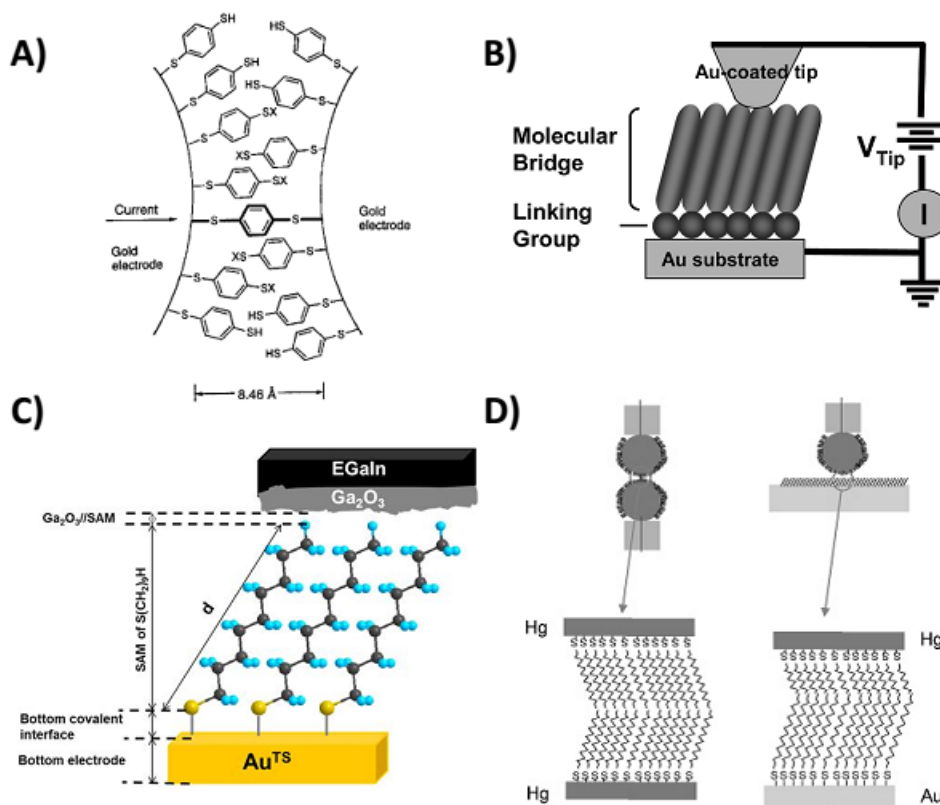


Figure 1.14 – Molecular Electronic Junctions

Several examples for forming direct contact to an organic monolayer, including **A)** break junctions (Reprinted with permission from Ref. 72. Copyright 2004 American Chemical Society), **B)** conductive-atomic force microscopy (cAFM) (Reprinted with permission from Ref. 73. Copyright 2011 American Chemical Society), **C)** gallium-indium drop junctions (EGaIn) (Reprinted with permission from Ref. 74. Copyright 2014 American Chemical Society), **D)** Hg-drop electrodes (Reprinted with permission from Ref. 72. Copyright 2004 American Chemical Society).

Much effort has been devoted to designing molecular junctions to realize the unique electrical and magnetic properties of organic based molecules. A host of techniques such as break junctions,⁷² atomic force microscopy with conductive cantilevers,⁷³ mercury-drop electrodes, and gallium-indium drop junctions (EGaIn)⁷⁴ have been used to analytically study organic systems, incorporating them into non-destructive electrical junctions and seeing the desired effects (Figure 1.14). However, these techniques are purely analytic and, at present, restricted in their possible use due to requiring either dangerous materials or highly specialized equipment for their implementation.

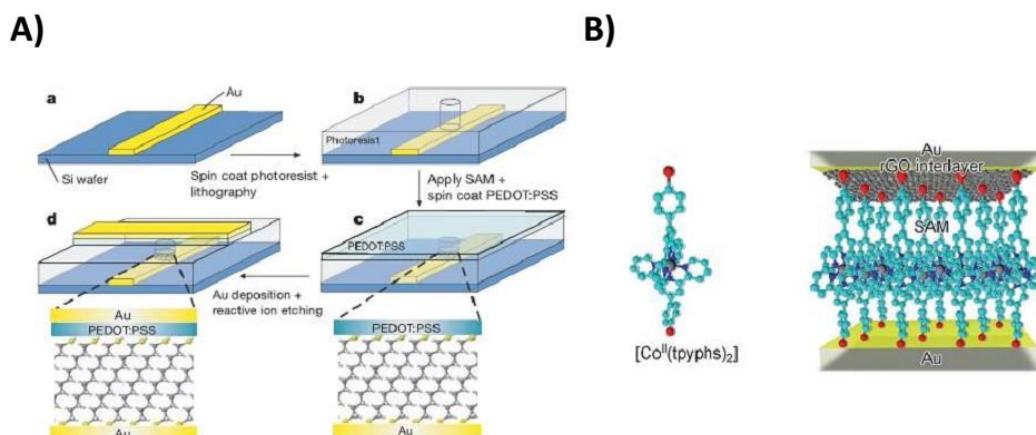


Figure 1.15 – Molecular Electronics Devices Prepared with Buffer Layers.

A) Devices incorporating solution processable PEDOT:PSS as a buffer layer. Reprinted by permission from Macmillan Publishers Ltd: *Nature*, Ref. 75, Copyright 2006. **B)** Device architecture incorporating solution processable reduced graphene oxide (rGO) for transparent electrodes.⁷⁶ Copyright © 2013, Wiley-VCH Verlag GmbH & KGaA.

Techniques to get beyond these limitations have been pursued, a large subset involving depositing buffer layers onto organic thin films or monolayers. These buffers, which include PEDOT:PSS⁷⁵ and single-sheet graphene⁷⁶ or graphene derivatives⁷⁷ can withstand many of the fabrication techniques used in the semiconductor industry. Unfortunately, buffer layers introduce additional interfaces in these devices, which, as described previously, may limit the ability to

interact metal and molecule directly at interfaces to exhibit unique effects in certain systems. For full realization of the effects organic materials can bring into the electronic/spintronic realm, the interface must be preserved and carefully tuned, and adding buffer layers only reduces the possibilities and benefits that exist from this exercise. Utilizing techniques that allow electrode deposition directly onto our systems without destroying them will offer the largest possible benefit toward dynamic single molecule systems.

1.5.2 *Soft Lithography and Transfer Printing in Molecular Electronics*

A recent focus for designing molecular electronic architectures with chemically bound metal contacts falls under the general title of soft lithography. The basic premise of these techniques involves some form of a transfer substrate, often times a polymer, that brings a metallic electrode into ‘soft’ contact (i.e. physical contact at ambient conditions) with an organic layer. The transfer layer may be sacrificial, as is typical in transferring plasma-enhanced chemical vapor deposition (PECVD) grown graphene where a poly(methyl methacrylate) (PMMA) layer or other polymer layer is dissolved to expose the graphene,⁷⁸ or it may be reusable in the case of a transfer process such as developed by John Rogers’ group.⁷⁹ In either case, the technique usually relies on standard lithographic patterning of metal contacts on robust films and materials – polymers or silicon wafers are typical – and transferring these metals and materials using soft lithographic techniques onto the more ‘fragile’ organic monolayers and films.

The advantage here is obvious – deposition of a metal contact directly onto an arbitrary substrate without fear of thermally penetrating metal into the film. Transfer printed methods have been shown to transfer features of various shapes and sizes onto organic monolayers, sustaining the films such that their charge transport properties could be measured.⁸⁰ If used in conjunction with metal binding groups on the target substrate, a chemical bond can form the metal-molecule

interface and allow for strong coupling that can potentially lead to strong electron (hole) injection and effects such as the “spinterface” effects described previously. It should be noted that there is evidence of size limitations and effects of even these soft lithographic processes due to the more frail nature and other properties of certain organic systems.⁸¹ This fact will motivate studies throughout this work in analyzing the effects of different architectures and fabrication techniques on organic systems.

1.6 Research Overview

The goal of this work is to design and study unique organic-based molecules in single (or few number of) molecule device settings to study their electrical and spin transport properties, with a sub-goal of facilitating their use to practical electronic applications *via* facile and scalable lithographic processes. These goals necessitate two research focuses – incorporating the molecules into settings for single molecule studies, and analyzing the architectures and processes used to incorporate these molecules into electrical devices to understand their impacts. As will be expressed, understanding the consequences of device processing and architecture is paramount if a true understanding of the organic molecules incorporated into them is to be achieved. Using the understanding of these device architectures, interesting effects in these unique molecules can be isolated and interpreted.

This work will present several sets of molecules, some basic, some with interesting transport and spin properties, toward incorporation into molecular junctions *via* soft lithographic techniques. Chapter 2 will show work with organometallic compounds possessing unique single molecule spin transitions – an iron spin crossover (FeSCO) compound, and a cobalt bis(dioxyene) valence tautomer complex (CoVT. Establishing techniques to study spin properties with the FeSCO, the CoVT is used to attempt to form a single molecule wire to study

its spin properties. Chapter 3 will introduce a basic molecular unit – phenylenedithiols – that is used to study the impacts of a particular soft lithographic process, nanotransfer printing (nTP), on aromatic compounds. Chapter 4 will then build off the knowledge of nTP, using the technique to study molecular wires from multi[(porphinato)metal] oligomers. Special focus is given here on forming molecular wires with the complex oligomers used and, once nTP is utilized in making electrical junctions, the effects of metal center on transport properties through the wire. Chapter 5 will expand on soft lithographic techniques to attempt at forming macroscopically accessible molecular junctions for temperature dependent and spin measurements through the molecular wires as well as toward the sub-goal of practical applicability. Finally, Chapter 6 will suggest modifications based off the findings of this work toward designing more robust molecular systems to overcome fabrication limitations of the junctions designed here. Such recommendations can help take the interesting molecules and results found in this work and potentially facilitate their use toward both future academic research and industrial applicability.

1.7 References

- (1) Schaller, R. R. *IEEE Spectr.* **1997**, *34*, 52–59.
- (2) Hruska, J. Moore's Law is dead, long live Moore's Law
<http://www.extremetech.com/extreme/203490-moores-law-is-dead-long-live-moores-law>.
- (3) Sun, X.-H.; Chen, Y. *J. Parallel Distrib. Comput.* **2010**, *70*, 183–188.
- (4) Royal Swedish Academy of Sciences The Nobel Prize in Chemistry 2000
http://www.nobelprize.org/nobel_prizes/chemistry/laureates/2000/press.html.
- (5) Kearns, D.; Calvin, M. *J. Chem. Phys.* **1958**, *29*, 950.
- (6) Barrietos, M. C. LG unveils 2015 OLED TV line-up, home appliances, and G Flex 2
<http://www.gadgets magazine.com.ph/events/ces-2015-lg-unveils-2015-oled-tv-line-up-home-appliances-and-g-flex-2.html>.
- (7) National Renewable Energy Laboratory Best Research-Cell Efficiencies
<http://www.nrel.gov/ncpv/>.
- (8) Teichler, A.; Perelaer, J.; Schubert, U. S. *J. Mater. Chem. C* **2013**, *1*, 1910–1925.
- (9) Hendriksen, B. L. M.; Martin, F.; Qi, Y.; Mauldin, C.; Vukmirovic, N.; Ren, J.; Wormeester, H.; Katan, A. J.; Altoe, V.; Aloni, S.; Fréchet, J. M. J.; Wang, L.-W.; Salmeron, M. *Nano Lett.* **2011**, *11*, 4107–12.
- (10) Biolin Scientific Langmuir, Langmuir-Blodgett and Langmuir-Schaefer Technologies
<http://www.biolinscientific.com/ksvnima/technologies/?card=KT1>.
- (11) Chen, K.; Yeh, H.; Chen, H.; Liu, T.; Huang, S.; Wu, P.; Tiu, C. *Adv. Chem. Eng. Sci.* **2013**, *3*, 105–111.
- (12) Chung, S.; Jang, M.; Ji, S.-B.; Im, H.; Seong, N.; Ha, J.; Kwon, S.-K.; Kim, Y.-H.; Yang, H.; Hong, Y. *Adv. Mater.* **2013**, *25*, 4773–4777.
- (13) Wei, Z.; Li, T.; Jennum, K.; Santella, M.; Bovet, N.; Hu, W.; Nielsen, M. B.; Bjørnholm, T.; Solomon, G. C.; Laursen, B. W.; Nørgaard, K. *Langmuir* **2012**, *28*, 4016–4023.
- (14) Terao, J.; Wadahama, A.; Matono, A.; Tada, T.; Watanabe, S.; Seki, S.; Fujihara, T.; Tsuji, Y. *Nat. Commun.* **2013**, *4*, 1691.
- (15) Venkataraman, L.; Klare, J. E.; Nuckolls, C.; Hybertsen, M. S.; Steigerwald, M. L. *Nature* **2006**, *442*, 904–907.

- (16) Jia, C.; Wang, J.; Yao, C.; Cao, Y.; Zhong, Y.; Liu, Z.; Liu, Z.; Guo, X. *Angew. Chem. Int. Ed.* **2013**, *52*, 8666–8670.
- (17) Mehta, G.; Sen, S. *Chem. Commun.* **2009**, 5981–5983.
- (18) Hong, J.-Y.; Chang, Y.-M.; Chuang, C.-H.; Li, K.-S.; Jhang, Y.-C.; Shiu, H.-W.; Chen, C.-H.; Chiang, W.-C.; Lin, M.-T. *J. Phys. Chem. C* **2012**, *116*, 21157–21161.
- (19) Lu, H.; Lipatov, A.; Ryu, S.; Kim, D. J.; Lee, H.; Zhuravlev, M. Y.; Eom, C. B.; Tsymbal, E. Y.; Sinitiskii, A.; Gruverman, A. *Nat. Commun.* **2014**, *5*, 5518.
- (20) Tseung, A. C. C.; King, W. J.; Wan, B. Y. C. *Med. Biol. Eng.* **1971**, *9*, 175–184.
- (21) Bettinger, C. J.; Bao, Z. *Polym. Int.* **2010**, *59*, 563–567.
- (22) Liao, C.; Zhang, M.; Yao, M. Y.; Huy, T.; Li, L.; Yan, F. *Adv. Mater.* **2014**, Early View.
- (23) Xu, L.; Gutbrod, S. R.; Bonifas, A. P.; Su, Y.; Sulkin, M. S.; Lu, N.; Chung, H.-J.; Jang, K.-I.; Liu, Z.; Ying, M.; Lu, C.; Webb, R. C.; Kim, J.-S.; Laughner, J. I.; Cheng, H.; Liu, Y.; Ameen, A.; Jeong, J.-W.; Kim, G.-T.; Huang, Y.; Efimov, I. R.; Rogers, J. A. *Nat. Commun.* **2014**, *5*, 3329.
- (24) Sarkar, S.; Culp, J. H.; Whyland, J. T.; Garvan, M.; Misra, V. *Org. Electron.* **2010**, *11*, 1896–1900.
- (25) Logothetidis, S.; Laskarakis, a.; Georgiou, D.; Amberg-Schwab, S.; Weber, U.; Noller, K.; Schmidt, M.; Küçükpinar-Niarchos, E.; Lohwasser, W. *Eur. Phys. J. Appl. Phys.* **2010**, *51*, 33203.
- (26) Lu, Q.; Liu, K.; Zhang, H.; Du, Z.; Wang, X.; Wang, F. *ACS Nano* **2009**, *3*, 3861–3868.
- (27) Vazquez, H.; Skouta, R.; Schneebeli, S.; Kamenetska, M.; Breslow, R.; Venkataraman, L.; Hybertsen, M. S. *Nat. Nanotechnol.* **2012**, *7*, 663–667.
- (28) Chen, Y.; Hsu, S.; Kaun, C.; Lin, M. *J. Phys. Chem. C* **2014**, *118*, 21199–21203.
- (29) Cayre, O. J.; Chang, S. T.; Velez, O. D. *J. Am. Chem. Soc.* **2007**, *129*, 10801–10806.
- (30) Díez-Pérez, I.; Hihath, J.; Lee, Y.; Yu, L.; Adamska, L.; Kozhushner, M. A.; Oleynik, I. I.; Tao, N. *Nat. Chem.* **2009**, *1*, 635–641.
- (31) Ho, G.; Heath, J. R.; Kondratenko, M.; Perepichka, D. F.; Arseneault, K.; Pézolet, M.; Bryce, M. R. *Chem. Eur. J.* **2005**, *11*, 2914–2922.
- (32) Ho Choi, S.; Kim, B.; Frisbie, C. D. *Science* **2008**, *320*, 1482–1486.

- (33) Siemeling, U.; Memczak, H.; Bruhn, C.; Vogel, F.; Träger, F.; Baio, J. E.; Weidner, T. *Dalton Trans.* **2012**, 41, 2986–2994.
- (34) Siebeneicher, P.; Kleemann, H.; Leo, K.; Lüssem, B. *Appl. Phys. Lett.* **2012**, 100, 193301.
- (35) Baghernejd, M.; Zhao, X.; Oronso, K. B.; Fueg, M.; Moreno-Garcia, P.; Rudnev, A. V.; Kaliginedi, V.; Vesztergom, S.; Huang, C.; Hong, W.; Broekmann, P.; Wandlowski, T.; Thygesen, K. S.; Bryce, M. R. *J. Am. Chem. Soc.* **2014**, 136, 17922–17925.
- (36) Liao, J.; Agustsson, J. S.; Wu, S.; Schönenberger, C.; Calame, M.; Leroux, Y.; Mayor, M.; Jeannin, O.; Ran, Y.-F.; Liu, S.-X.; Decurtins, S. *Nano Lett.* **2010**, 10, 759–764.
- (37) Hettie, K. S.; Klockow, J. L.; Glass, T. E. *J. Am. Chem. Soc.* **2014**, 136, 4877–4880.
- (38) Perrin, M. L.; Frisenda, R.; Koole, M.; Seldenthuis, J. S.; Gil, J. A. C.; Valkenier, H.; Hummelen, J. C.; Renaud, N.; Grozema, F. C.; Thijssen, J. M.; Dulić, D.; van der Zant, H. S. J. *Nat. Nanotechnol.* **2014**, 9, 830–834.
- (39) Franco, I.; Solomon, G. C.; Schatz, G. C.; Ratner, M. A. *J. Am. Chem. Soc.* **2011**, 133, 15714–15720.
- (40) Kiguchi, M.; Ohto, T.; Fujii, S.; Sugiyasu, K.; Nakajima, S.; Takeuchi, M.; Nakamura, H. *J. Am. Chem. Soc.* **2014**, 136, 7327–7332.
- (41) Su, T. A.; Widawsky, J. R.; Li, H.; Klausen, R. S.; Leighton, J. L.; Steigerwald, M. L.; Venkataraman, L.; Nuckolls, C. *J. Am. Chem. Soc.* **2013**, 135, 18331–18334.
- (42) Julliere, M. *Phys. Lett. A* **1975**, 54, 225–226.
- (43) Baibich, M. N.; Broto, J. M.; Fert, A.; Nguyen Van Dau, F.; Petroff, F. *Phys. Rev. Lett.* **1988**, 61, 2472–2475.
- (44) Ramirez, A. P. *J. Phys. Condens. Matter* **1997**, 9, 8171–8199.
- (45) Zhang, X.; Mizukami, S.; Kubota, T.; Ma, Q.; Oogane, M.; Naganuma, H.; Ando, Y.; Miyazaki, T. *Nat. Commun.* **2013**, 4, 1392.
- (46) Tran, T. L. A.; Le, T. Q.; Sanderink, J. G. M.; van der Wiel, W. G.; de Jong, M. P. *Adv. Funct. Mater.* **2012**, 22, 1180–1189.
- (47) Alam, K. M.; Bodepudi, S. C.; Starko-Bowes, R.; Pramanik, S. *Appl. Phys. Lett.* **2012**, 101, 192403.
- (48) Janssen, P.; Cox, M.; Wouters, S. H. W.; Kemerink, M.; Wienk, M. M.; Koopmans, B. *Nat. Commun.* **2013**, 4, 2286.

- (49) Nguyen, T. D.; Sheng, Y.; Wohlgenannt, M.; Anthopoulos, T. D. *Synth. Met.* **2007**, *157*, 930–934.
- (50) Wohlgenannt, M.; Bobbert, P. A.; Koopmans, B.; Bloom, F. L. In *Organic Spintronics*; 2010; pp. 67–136.
- (51) Nguyen, T. D.; Sheng, Y.; Rybicki, J.; Veeraraghavan, G.; Wohlgenannt, M. *J. Mater. Chem.* **2007**, *17*, 1995–2001.
- (52) Mahato, R. N.; Lülfi, H.; Siekman, M. H.; Kersten, S. P.; Bobbert, P. A.; de Jong, M. P.; De Cola, L.; van der Wiel, W. G. *Science* **2013**, *341*, 257–260.
- (53) Kersten, S. P.; Meskers, S. C. J.; Bobbert, P. A. *Phys. Rev. B* **2012**, *86*, 045210.
- (54) Korshak, Y. V.; Medvedera, T. V.; Ovchinnikov, A. A.; Spector, V. N. *Nature* **1987**, *326*, 370–372.
- (55) Li, B.; Kao, C.-Y.; Lu, Y.; Yoo, J.-W.; Prigodin, V. N.; Epstein, A. J. *Appl. Phys. Lett.* **2011**, *99*, 153503.
- (56) Ma, Y. W.; Lu, Y. H.; Yi, J. B.; Feng, Y. P.; Herng, T. S.; Liu, X.; Gao, D. Q.; Xue, D. S.; Xue, J. M.; Ouyang, J. Y.; Ding, J. *Nat. Commun.* **2012**, *3*, 727.
- (57) Xie, Z.; Markus, T. Z.; Cohen, S. R.; Vager, Z.; Gutierrez, R.; Naaman, R. *Nano Lett.* **2011**, *11*, 4652–4655.
- (58) Mondal, P. C.; Kantor-Uriel, N.; Mathew, S. P.; Tassinari, F.; Fontanesi, C.; Naaman, R. *Adv. Mater.* **2015**, *27*, 1924–1927.
- (59) Herrmann, C.; Solomon, G. C.; Ratner, M. A. *J. Am. Chem. Soc.* **2010**, *132*, 3682–3684.
- (60) Raman, K. V.; Kamerbeek, A. M.; Mukherjee, A.; Atodiresei, N.; Sen, T. K.; Lazić, P.; Caciuc, V.; Michel, R.; Stalke, D.; Mandal, S. K.; Blügel, S.; Münzenberg, M.; Moodera, J. S. *Nature* **2013**, *493*, 509–513.
- (61) Cho, W. J.; Cho, Y.; Min, S. K.; Kim, W. Y.; Kim, K. S. *J. Am. Chem. Soc.* **2011**, *133*, 9364–9369.
- (62) Schmidt, G.; Ferrand, D.; Molenkamp, L.; Filip, A.; van Wees, B. *Phys. Rev. B* **2000**, *62*, R4790–R4793.
- (63) Gobbi, M.; Golmar, F.; Llopis, R.; Casanova, F.; Hueso, L. E. *Adv. Mater.* **2011**, *23*, 1609–1613.
- (64) Sun, D.; Ehrenfreund, E.; Valy Vardeny, Z. *Chem. Commun.* **2014**, *50*, 1781–1793.

- (65) Tran, T. L. A.; Cakır, D.; Wong, P. K. J.; Preobrajenski, A. B.; Brocks, G.; van der Wiel, W. G.; de Jong, M. P. *ACS Appl. Mater. Interfaces* **2013**, *5*, 837–841.
- (66) Ciudad, D.; Gobbi, M.; Kinane, C. J.; Eich, M.; Moodera, J. S.; Hueso, L. E. *Adv. Mater.* **2014**, *26*, 7561–7567.
- (67) Miyamachi, T.; Gruber, M.; Davesne, V.; Bowen, M.; Boukari, S.; Joly, L.; Scheurer, F.; Rogez, G.; Yamada, T. K.; Ohresser, P.; Beaurepaire, E.; Wulfhekel, W. *Nat. Commun.* **2012**, *3*, 938.
- (68) Pronschinske, A.; Chen, Y.; Lewis, G. F.; Shultz, D. a; Calzolari, A.; Nardelli, M. B.; Dougherty, D. B. *Nano Lett.* **2013**, *13*, 1429–1434.
- (69) Soncini, A.; Mallah, T.; Chibotaru, L. F. *J. Am. Chem. Soc.* **2010**, *132*, 8106–8114.
- (70) Adams, D. M.; Hendrickson, D. N. *J. Am. Chem. Soc.* **1996**, *118*, 11515–11528.
- (71) Lu, P.; Shi, Z.; Walker, A. V *Langmuir* **2011**, *27*, 13022–13028.
- (72) McCreery, R. L. *Chem. Mater.* **2004**, *16*, 4477–4496.
- (73) Kim, B.; Choi, S. H.; Zhu, X.-Y.; Frisbie, C. D. *J. Am. Chem. Soc.* **2011**, *133*, 19864–19877.
- (74) Baghbanzadeh, M.; Simeone, F. C.; Bowers, C. M.; Liao, K.; Thuo, M.; Baghbanzadeh, M.; Miller, M. S.; Carmichael, T. B.; Whitesides, G. M. *J. Am. Chem. Soc.* **2014**, *136*, 16919–16925.
- (75) Akkerman, H. B.; Blom, P. W. M.; de Leeuw, D. M.; de Boer, B. *Nature* **2006**, *441*, 69–72.
- (76) Seo, S.; Min, M.; Lee, S. M.; Lee, H. *Nat. Commun.* **2013**, *4*, 1920.
- (77) Seo, S.; Min, M.; Lee, J.; Lee, T.; Choi, S.-Y.; Lee, H. *Angew. Chem. Int. Ed.* **2012**, *51*, 108–112.
- (78) Liang, X.; Sperling, B. A.; Calizo, I.; Cheng, G.; Hacker, C. A.; Zhang, Q.; Obeng, Y.; Yan, K.; Peng, H.; Li, Q.; Zhu, X.; Yuan, H.; Walker, A. R. H.; Liu, Z.; Peng, L.-M.; Richter, C. A. *ACS Nano* **2011**, *5*, 9144–9153.
- (79) Menard, E.; Bilhaut, L.; Zaumseil, J.; Rogers, J. A. *Langmuir* **2004**, *20*, 6871–6878.
- (80) Niskala, J. R.; Rice, W. C.; Bruce, R. C.; Merkel, T. J.; Tsui, F.; You, W. *J. Am. Chem. Soc.* **2012**, *134*, 12072–12082.

- (81) Jeong, H.; Kim, D.; Kim, P.; Rae Cho, M.; Hwang, W.-T.; Jang, Y.; Cho, K.; Min, M.; Xiang, D.; Daniel Park, Y.; Jeong, H.; Lee, T. *Nanotechnology* **2015**, *26*, 025601.

CHAPTER 2:

ADAPTING SPINTRONIC ORGANOMETALLIC MOLECULES TO MOLECULAR ELECTRONIC SETTINGS

Robert C. Bruce,^a Daniel E. Stasiw,^b Alex Pronschinske,^c Geoff Lewis,^b Yifeng Chen,^c Arrigo Calcolari,^{de} Marco Buongiorno-Nardelli,^e Daniel B. Dougherty,^c David A. Schultz,^b Wei You^a

(a) Dept. of Chemistry, University of North Carolina- Chapel Hill, Chapel Hill, NC

(b) Dept. of Chemistry, North Carolina State University, Raleigh, NC

(c) Dept. of Physics, North Carolina State University, Raleigh, NC

(d) CNR-NANO, Istituto Nanoscienze, Centro S3 I-41125, Modena, Italy

(e) Dept. of Physics and Dept. of Chemistry, University of North Texas, Denton, TX

2.1 Background

2.1.1 History of Magnetism in Metals

The fact that electrons have possessed quantized angular momenta has been known for many years. Classical experiments, such as the Stern-Gerlach experiment, have provided experimental observations of this property. In this experiment, silver atoms were ejected from a furnace and onto a detector, passing through a magnetic field perpendicular to the direction of atom movement along the way. The d₉-silver atoms possess one unpaired electron, allowing for ease in evaluating of the magnetic properties of the paramagnetic atom. The results of the experiment showed that the silver atom beam separated into two distinct beams, equally and oppositely affected by the magnetic field, with no atoms on the detector between the beams. This observation corroborates experimental results from other phenomena (ex. doublet spectral lines in hydrogen atom from spin-orbit interactions) and confirms the presence of a quantization of

angular momentum that could only be described by the unpaired electron on the silver atom.

Ultimately, these showed that electrons possessed two angular momenta, or spins, of equal and opposite magnitude.¹

Most uses of electrical currents ignore the effects of electron spin in their execution. The effects of spin can be observed in currents, such as the spin Hall effect leading to accumulation of spin on the lateral boundaries of a current-carrying sample,² but practically these effects bear little consequence on moving current (the current flowing through an electrical outlet is effectively spin randomized), it only matters whether or not electrons of any spin are transported. New avenues are opened when electron spin is incorporated, and even the simple picture of current on versus current off can be manipulated in spintronic settings.

The basis for almost all, if not all, the magnetic effects in spintronics comes from energy splitting of angular momenta in a magnetic field:

$$\Delta E = -\mu \cdot B \quad (2-1)$$

where μ is the magnetic moment and B is the applied magnetic field. Since electron spin will inherently contribute a magnetic moment, any application of a field will create an energy split where one spin state will become more energetically favorable than another. To give a more numerical description to this splitting, we define μ by visualizing an electron as a charge moving circularly around a nucleus as predicted in the Bohr atomic picture. The basic definition for magnetic moment defines it as:

$$\mu = IA \quad (2-2)$$

where I is current and A is area of the current. In the Bohr atomic picture, A is a circle defined by $A = \pi r^2$. The circulating current, I , is given by:

$$I = \frac{-e}{T} = \frac{ev}{2\pi r} \quad (2-3)$$

where the period, T , is simply expanded to represent the electron moving around the nucleus. If we remember that the electron and its energy (and therefore momentum) are quantized as per basic quantum mechanics principles, we can apply the definition:

$$L = mvr = \frac{nh}{2\pi} \quad (2-4)$$

where L is angular momentum, h is Planck constant, and n represents an integer quantization of that energy. Using the equations above, we can combine them to obtain the magnetic moment for a $n = 1$ system:

$$\mu = \frac{eh}{4\pi m} = \mu_B \quad (2-5)$$

We plug in known values for the charge and mass of an electron and we obtain the quantity known as the Bohn magneton ($\mu_B = 9.27 \times 10^{-24} \text{ Am}^2$). This number is interesting, coming from a now known to be erroneous picture of the atom, yet still representing a quantized magnetic moment that small scale magnetic systems are scaled to.³ It also gives credence to the idea that consequential magnetic effects, especially those at the single molecule level, can come simply by considering the spin on an electron.

This single electron picture, while useful, quickly becomes complicated when we consider electron-electron interactions. These exchange interactions differ between systems, enabling spin alignment or spin anti-alignment under different circumstances. A basic equation to express this interaction is given by the Heisenberg-Dirac-Van Vleck (HDVV) Hamiltonian:

$$\hat{H}_{ij} = -2J_{ij}\hat{S}_i\hat{S}_j \quad (2-6)$$

where \hat{S}_i and \hat{S}_j are the spin operators for two charged species and J_{ij} is the exchange parameter.

In this basic relationship, the magnitudes of the spins are proportional to the magnetic effect, and the exchange parameter term accounts for all interactions to determine ground state spin preference. Using the exchange parameter in this manner can make it difficult to fully dissect, but it still allows us to comment on two general but widespread classes of interaction – ferromagnetic coupling, where $J_{ij} > 0$ and it is energetically preferable for the spins to align; and antiferromagnetic coupling, where $J_{ij} < 0$ and it is energetically preferable for the spins to be anti-aligned. Again, more complex interactions, such as superexchange and double exchange can very easily make this picture complicated.⁴ However, what this model expresses is that different spin interactions exist, some where spins will align with each other, others where spins will anti-align.

In metals, both types of coupling are well represented. Ferromagnetic coupling leads to a few classes of magnetic materials, paramagnets and ferromagnets being the most common of them. Both have the same property where spins will align in a magnetic field. The difference is that the spin state becomes randomized in paramagnetic species when the magnetic field is removed, whereas ferromagnets will retain a remnant magnetization (Figure 2.1). The remnant magnetization, alongside hysteresis of spin flipping, allows ferromagnets to be useful for magnetic memory. Over time, thermal fluctuations will cause spin randomization in ferromagnets, with each ferromagnet possessing a characteristic Curie temperature (T_C) above which they lose their remnant magnetization, instead becoming what are known as superparamagnets. Superparamagnets can become ferromagnetic when $T > T_C$, however any previous spin state from a previous ferromagnetic state is still lost.

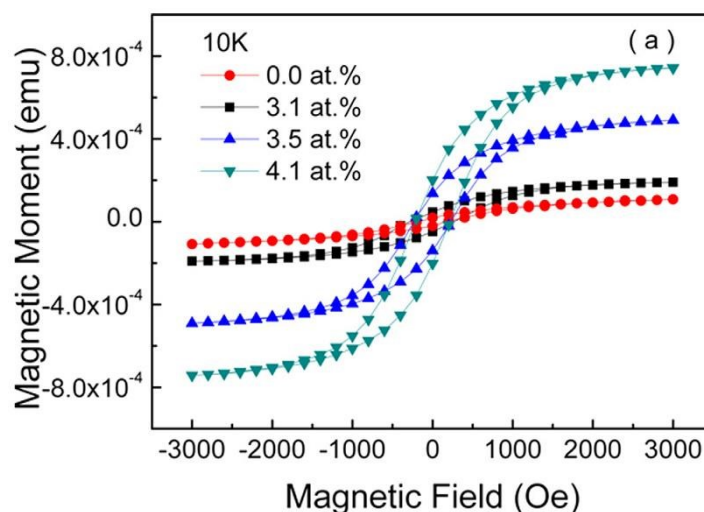


Figure 2.1 – Magnetism in Manganese-Doped Carbon Nanotubes (CNTs)

Ferromagnetism expressed in manganese doped CNTs (“%” refer to percent Mn doping), measured at low temperature (10 K), as shown through hysteresis of magnetic signal and remnant magnetization at 0 Oe fields. Reprinted with permission from Ref. 5. Copyright 2012, AIP Publishing LLC.

Antiferromagnetic coupling can lead to antiferromagnets, where spins are spin anti-aligned with each other throughout a sample. Antiferromagnetism can be common in some transition metals, specifically oxides of those metals. As with ferromagnets, antiferromagnets can lose their magnetic properties due to thermal fluctuation above the Néel temperature (T_N). One of the interesting uses of antiferromagnets is that they can pin the magnetism at a ferromagnetic interface, creating larger coercive fields for spin flipping. Apart from this, they will ultimately resist the effects of magnetic field, acting essentially as strong diamagnets and can be repelled from a magnetic field.

These basic magnetic effects have been widely utilized in a variety of applications. Magnetic memory builds off of spin valve configurations where two ferromagnets, separated by an insulating tunnel barrier, control the resistance of a device based on their spin alignment or anti-alignment,⁶ seeing sometimes exceptionally large MR effects in specialized systems.⁷ Diamagnetism and its repulsion to magnetic field can lead to levitation of any number of

materials.⁸ Sensors, magnetic resonance imaging (MRI), and some revered characterization techniques in chemistry such as nuclear magnetic resonance (NMR) are among the many other uses of the principles discussed above.



Figure 2.2 – Levitating Frog in a 20 Tesla Magnet

Levitation of a diamagnetic frog in the bore of a strong magnet, exhibiting the general ability to levitate diamagnetic materials due to their repulsion to a magnetic field.⁸ © European Physical Society. Reproduced by permission of IOP Publishing. All rights reserved.

2.1.2 Magnetic Properties in Organic Molecules

The magnetic principles discussed above are very widely seen throughout metallic materials. When we begin to talk about possibly including organic materials into the discussion, however, we have to deal with a few immediate consequences. Ferromagnetism, antiferromagnetism, and many other magnetic effects rely on the ability of spin states to interact with one another. Electrons are much more localized in organic systems, preventing long-range order in many instances that are needed for powerful magnets. Lower mobilities and higher resistances present in many organics also prevent these long-range interactions. Further, many organic materials have lower energy and more tightly bound valence electrons, mitigating the

freedom of unpaired electrons to interact in unique spin coupling events. Overall, the magnetic properties of organic materials are much weaker than their inorganic counterparts.

One powerful method to induce magnetic properties in organic molecules is to use metals and their strong magnetic properties in conjunction with organic complexes. Simply doping organic systems with metals can present magnetic properties, such as doping manganese electrochemically into single wall carbon nanotubes (SWCNTs).⁵ More powerful than this approach involves synthetically incorporating metals into organic compounds. In the case of metal-phthalocyanines (Pc), synthesizing phthalocyanines with different d-valence metals (Mn, Fe, Ni, Cu) generates different magnetic properties. The power in this approach comes from the ability to switch the properties of the metal centers, thereby changing the magnetic properties observed in the Pc molecules. In one example, lithium doping is used to effectively reduce the metals, changing their oxidation state and changing the overall magnetic properties. In particular, CuPc molecules on a surface could have their magnetism quenched by lithium doping, whereas NiPc molecules can recover their magnetic properties.⁹

Perhaps the biggest advantage of this approach of combining magnetic centers with organic ‘housing’ is it gives us the potential to isolate and sustain single spin states.¹⁰ Treating an organic complex as a sort of quantum well can trap spins, even utilizing quantum mechanical principles to further split energy gaps between spin states. Single spins are easy to flip due to low spin coupling, but if we want to apply single molecules to low energy-cost applications, that ease to controllably flip spin is desirable, so long as we can maintain the spin for long times after the flipping. Other benefits can be generated, such as influence on spin transport and possible inherent spin-polarization of current.¹¹ Due to only one or few spins being present in these small systems, there are no (or very few) exchange interactions to provide thermal stability to many of

these systems. Sustaining these effects at room temperature is and will be a challenge. Despite this, proof of concept has been provided that single molecule magnets with controllable magnetic properties can be designed and tuned,^{12,13} and work to further these and similar systems is needed and desired to help realize these properties for applications such as single molecule transistors in practical and scalable settings.

In this chapter, we will focus on this approach of using metals in organometallic systems to observe their magnetic properties with the goal of adapting these systems for single or few number of molecule type of applications. In particular, two systems have been studied – an iron-based spin crossover (FeSCO) complex, and a cobalt dioxylyene based valence tautomer (CoVT). The FeSCO is utilized in monolayer formation as a test bed for observing magnetic properties *via* x-ray photoelectron spectroscopy (XPS). The CoVT is tested as a molecular wire to see if its tautomer properties can be observed in a practical molecular electronic architecture.

2.2 Study of Iron Spin Crossover Films²⁴

2.2.1 Spin Crossover

Spin crossover (SCO) refers to a phenomenon where the spin state of a complex changes due to an external stimulus. Metal complexes, most specifically complexes with d-valence metals, can exhibit SCO due to the ability to dramatically change the valence shell orbital splitting and the distribution of orbital filling. In these instances, changing the degeneracies and splittings leads to a change in the number of unpaired electrons and, ultimately, the spin state of the complex (see Figure 2.3). Different stimuli have been reported to induce this effect, the most notable being heat and light, the latter representing an effect known as light induced excited spin state trapping (LIESST).¹⁴

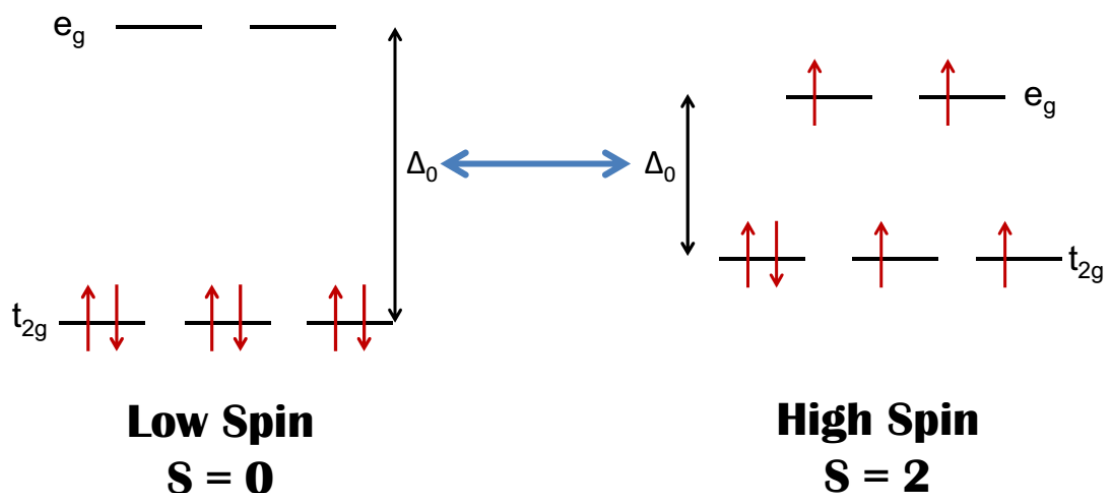


Figure 2.3 – Possible Electron Configurations for d-shell in Fe^{2+} Complex

Electron configurations for the d_6 -valence shell in Fe^{2+} , assuming octahedral field splitting, for different strengths of the field (Δ_0). Large Δ_0 leads to a low spin configuration where only the t_{2g} orbitals are filled by the six d-electrons, leading to pairing of all electrons and a diamagnetic spin state ($S = 0$). Transitioning to low Δ_0 leads to electrons filling the t_{2g} and e_g as if they were degenerate (high spin), leaving four unpaired electrons and resulting in an $S = 2$ magnetic state.

SCO has been reported in a number of literature studies. Matsuda and Tajima report films of $[\text{Fe}(\text{dpp})_2](\text{BF}_4)_2$ ($\text{dpp} = 2,6\text{-di}(\text{pyrazolyl})\text{pyridine}$) that exhibit a temperature influenced transition around 260 K, optically visible and detectable by SQUID (semiconducting quantum interference device) magnetometry.¹⁵ Layer-by-layer (LbL) approaches have developed 3-dimensional coordination polymers of $\text{Fe}(\text{pyrazine})\{\text{M}(\text{CN})_4\}$ ($\text{M} = \text{Ni}, \text{Pd}, \text{Pt}$), which show SCO around 280 K.¹⁶ Toward single molecule magnet applications, systems with more individually accessible molecules have also been developed. Iron SCOs with phenanthroline and dihydrobis(pyrazolyl)borate ligands are able to be formed in bilayer form by sublimation on gold, and an STM tip is able to bias the sample into switching from LS to HS at low temperature,¹⁷ and isolated iron SCOs with just phenanthroline ligands observe the same effect.¹⁸ The latter study is especially interesting as the SCO effect results in a change in current

through the system, corroborating theoretical studies¹⁹ and establishing an easily identifiable output that can be measured in a finished device architecture.

The transition common throughout these iron SCO systems is the change from an $S = 0$, LS state to an $S = 2$, HS state. One of the interesting ways that we could show the crossover effect is to utilize this change from paired to unpaired electrons and look at spectroscopic effects of this. Specifically, in XPS, electrons ejected from core energy shells can interact with valence shells and have effects on the measured spectrum. Fe 2p subshells naturally have a doublet due to the inherent angular momentum of the p-orbital ($L = 1$), which results in two peaks corresponding to the same electron energy level due to spin-orbit coupling. In addition to this, the Fe 2p shell can also possess satellite, or shake-up, peaks where the ejected electron interacts with the valence shell, reducing the kinetic energy of the ejected electron and producing a second doublet in the XPS spectrum. Interestingly, this shake-up peak is only present in the paramagnetic state ($S > 0$) and not in the diamagnetic state ($S = 0$), indicating the unpaired electron plays a role in the interaction that leads to this satellite peak.²⁰ Satellite peaks can yield information about the inter-electronic coupling and charge-transfer entities of complexes as well.²¹ Here though, we are predominantly interested in using the shake-up peaks as a fingerprint of the LS to HS transition and, ultimately, verify the SCO properties of an iron SCO.

2.2.2 Experimental- FeSCO Film Growth and Study

$\text{Fe}[(\text{H}_2\text{Bpz}_2)_2\text{bpy}]$ was synthesized by literature procedure in an air-free Schlenk line.²² The synthesis yielded a purple powder that, when tested *via* SQUID magnetometry, observed a SCO event around 160 K. The solid was deposited onto a film onto a Au(111) substrate by vacuum sublimation to thicknesses of around 50 nm at rates typically in the range of 0.2 – 1.0 Å/s. These films visually exhibited SCO as well, experiencing a visual color change from purple to dark green when dipped in liquid- N_2 . When cooled in the XPS change, a visual color change could be seen inside the chamber as well, the LS state appearing more of a black color through the XPS window.

XPS was carried out in a commercial Kratos Axis Ultra DLD system with base pressure $\sim 2 \times 10^{-9}$ Torr. A monochromatic Al $K\alpha$ source (KE = 1486.6 eV) was used for XPS characterization. The beam was used with 10 mA emission and 15 kV bias on the anode. No external charge neutralization was used in the experiment. XPS was done at two temperatures- room temperature (~ 300 K) and 115 K to capture the spectra from the HS and LS states, respectively. Temperature was measured by a thermal couple on the substrate holder inside the XPS. It is possible the reported numbers vary slightly from the measured value due to lack of perfect thermal conductivity through the glass/mica substrate and possible local heating effects from XPS. 115 K was chosen as it was the base temperature attainable by flowing liquid- N_2 through the substrate holder during the experiment. High resolution scans were taken of the Fe 2p core shell, averaging 2 sweeps per temperature with a dwell time of 500.0 ms and 0.1 eV step at each temperature.

First principles density functional theory (DFT) calculations were carried out using the QUANTUM-ESPRESSO software package.²³ A plane wave basis set of 28 Ry (280 Ry) cutoff for kinetic energy (charge) was used with ultrasoft pseudopotentials of the PBE exchange-

correlation functional type in the generalized gradient approximation (GGA). The intermolecular van der Waals interactions were taken into account by the London dispersion force model. The low-spin molecular configurations are obtained by spin unrestricted calculations, while the high-spin states have been constructed by constraining the number of unpaired electrons on each molecule to be four. Since the singlet lowest and multiplet high-spin configurations are the lowest energy states for the corresponding spin multiplicities, they are correctly calculated by DFT.

2.2.3 Results and Discussion- FeSCO

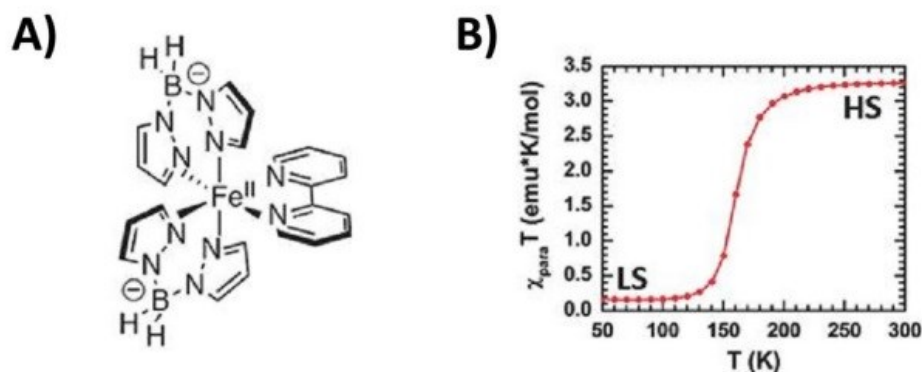


Figure 2.4 – SQUID Magnetometry of Powder FeSCO

A) Chemical structure of $\text{Fe}[(\text{H}_2\text{Bpz}_2)_2\text{bpy}]$ (FeSCO). **B)** Temperature dependence of magnetic properties of FeSCO powder, indicating LS to HS transition, centered around 160 K..²⁴ Reproduced by permission of The Royal Society of Chemistry.

The SCO properties of the synthesized FeSCO were characterized by SQUID magnetometry. Figure 2.4 shows the temperature dependence of the magnetic properties. A transition, centered around 160 K, highlights the presence of the LS to HS transition. The $\chi_{\text{para}}T$ value in Figure 2.4B for the high spin state is approximately 3. Using Curie's law for paramagnets, we can extract the approximate spin state of at the higher temperatures:

$$\chi_{para}T = \frac{Ng^2\mu_B^2S(S+1)}{3k_B} = 0.125 g^2S(S+1) \frac{emu * K}{mol} \quad (2-7)$$

where g is the Landé factor which for electrons is approximately 2, k_B is Boltzmann's constant, and S is the spin state. Solving the above expression for $\chi_{para}T = 3$, we obtain $S = 2$, which matches the ideal field splitting picture given in Figure 2.3. The actual field splitting may be slightly different as the picture shown above assumes octahedral splitting; either way, we see a shift from $S = 0$ in LS state to $S = 2$ in HS state for the FeSCO powder. The temperature at which this transition occurs is ultimately the “bulk” spin crossover value, where cooperative effects are governed by crystal packing, but it provides a strong baseline for the temperature of the transition expected in the sublimated thin films.

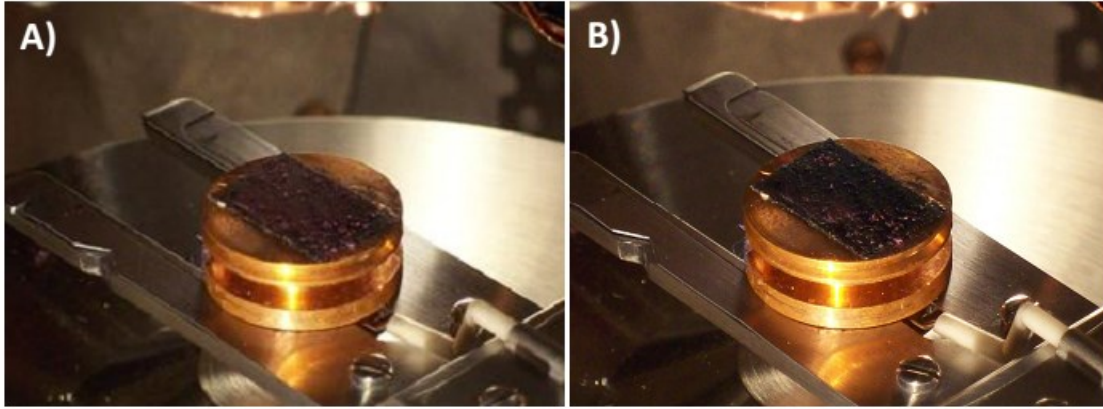


Figure 2.5 – FeSCO Color Change as a Function of Temperature

FeSCO films, seen through the window into an XPS chamber, on a substrate holder at **A)** 300 K and **B)** 115 K.

Thin film samples to measure the SCO properties *via* XPS were prepared by depositing approximately 50 nm films on Au(111)/mica. Figure 2.5 shows the visual impacts of cooling the FeSCO substrates inside the XPS. At room temperature (RT), the films appeared purple through the XPS window. When cooled to the base temperature of 115 K, the film visually appears

darker, which corresponds with the visual changes seen outside of the XPS chamber that corresponded to HS to LS transition. Some purple was still present, but this indicates that at least a significant portion of the FeSCO sample transitioned to LS state at the lower temperature.

XPS spectra were obtained at 115 K and 300 K. Special focus was given to the Fe 2p core shell, as these spectra have satellite peaks that can be used to identify HS or LS properties. Figure 2.6A shows that this change is visible spectroscopically at the high and low temperatures. Main peaks at 711 eV ($2p_{3/2}$) and 724 eV ($2p_{1/2}$) are close to iron spectra for the Fe^{2+} oxidation state in other SCO compounds.²⁵ Satellite peaks appear approximately 716 eV ($2p_{3/2}$) and 729 eV ($2p_{1/2}$) at 300 K, but become strongly diminished at 115 K. Such a diminishing at low temperature indicates the change from HS to LS. Computational models confirm the assessment of shakeup peaks – high spin state is shown to express satellite peaks, whereas low spin states will not. Overall, this XPS experiment shows that the spin properties of transition metals, specifically spin transitions from diamagnetic to paramagnetic spin states, are able to be observed by XPS.

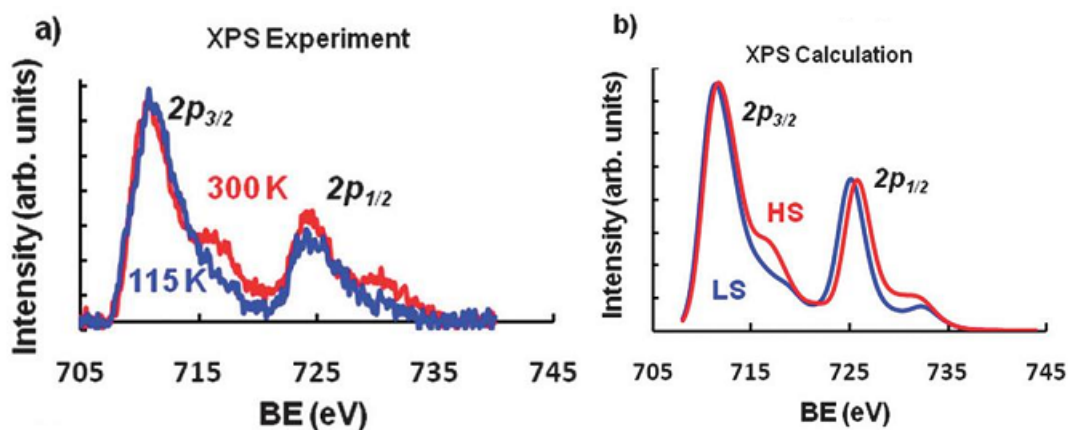


Figure 2.6 – FeSCO Fe 2p XPS Spectra at Variable Temperature

A) Experimental high resolution XPS spectra of Fe 2p core shell of FeSCO at 115 K and 300 K. **B)** Computational spectra for same conditions, performed by Marco Buongiorno-Nardelli.²⁴ Reproduced by permission of The Royal Society of Chemistry.

2.3 Study of Valence Tautomers Designed as Molecular Wires

2.3.1 Valence Tautomerism for Spintronic Devices

Valence tautomerism (VT) is similar to the spin crossover effect discussed above in that it involves changing the spin of the metal center in the compound incorporating it. The difference between the two effects is that VT incorporates an exchange of radicals between metal center and ligand to create these effects. In particular systems, such as cobalt metal center VTs, this exchange can switch the spin state of the metal center from diamagnetic to paramagnetic, highlighting the spintronic capabilities of the effect.²⁶

VT molecules often involve ligands that alternate between states of possessing or lacking free radicals. The promise of this approach in changing molecular properties is shown in zinc methyl phenalenyl (ZMP) molecules, which exhibit different spintronic properties in states with free radicals at the surface versus states without free radicals,²⁷ as well as theoretical studies of the effects of radicals on spin transport.²⁸ As discussed previously, sustaining free radicals is a synthetic challenge, and their reactivity in ambient conditions prevents many ligands from being useful for VT effects. However, proper choice of ligands that can sustain these radicals, such as 1,2,3-benzotriazinyl ligands,²⁹ can enable air and moisture stable spin transitions. Once these needs have been met, extremely strong electronic coupling between metal and ligand can be realized to enable these VT effects.³⁰

An important question to consider is what architecture would be best to utilize VT for practical device architectures. A wide range of options exist to deposit VT molecules on a surface to exploit their properties. As described with the FeSCO, film deposition is a strong possibility. Even simpler than the vapor deposition used for that system is solution processable film formation, using processes such as spin-casting or drop casting, or more complex methods such as ink-jet printing.³¹ The difficulty with these processes is that they often don't form self-

assembled and reproducible substrates. The FeSCO system forms very reliable monolayers and bilayers, but even the bilayer has a complex surface of spin interactions that would need to be accounted for and understood to utilize it for molecular devices.²² Moreover, many of these methods can yield varieties of results. Spun-cast films can have different domains and different orderings of molecules, often times across the same substrate.³² Molecules such as TIPS-pentacene highlight the fact that dramatically different film properties including detrimental mobility drops can be easily and, sometimes accidentally, obtained.³³ Such properties could make understanding of properties of the molecule (such as spin transport through the film) non-trivial. The best architectures for such an understanding would involve reliable and reproducible molecular interactions, orientations, and charge transport pathways. Moreover, adaptability to permanent devices and eventual application use would be also desirable.

A promising form for small and even specialized molecules to take to fulfill these requirements is the molecular wire. Attaching a monolayer to a gold surface *via* substrate binding group has been shown to work with varieties of molecules to create vertically standing systems for reproducible electrical analysis.³⁴ The simplest approach for creating molecules for this wire setting is to synthesize molecules with metal binding groups and attach them to a surface. However, there are limitations with this process. First, an immediate requirement is solubility of molecules, a factor that rules out many large molecules that could be of interest. Second, even if molecules are soluble, there is no assurance that a metal binding group will attach in methods that enable vertically standing and accessible molecules. As will be discussed in a later chapter, metal binding modes can be complicated, and the self-assembly obtained from basic molecules such as alkanethiols are not always seen in larger molecules.

Growing wires off of a surface provides an alternative approach that can get around some of these pitfalls. Recent literature has provided numerous examples of polymerizations off of a surface, one promising example being polymer brushes that can be grown to hundreds of nanometers in length.^{35,36} In these reactions, a ‘seed’ monolayer is placed, then an initiation step begins growth of a polymer chain. Often, these are one pot reactions involving catalyst and monomer such that the reaction can proceed autonomously until either the catalyst degrades, the monomer or reactive species are depleted, or the reaction is quenched. Such processes have been shown to be patternable *via* standard lithography as well as adaptable to different substrates depending on the chemical units used.³⁵ The downfall to this method, however, is that it is limited in the scope of molecules that can be grown in this method. In the case of ligand exchange reactions, which as described in a moment will be used with this system, the reaction is not catalyst driven, allowing the polymerization to occur in solution, leading to various lengths of molecular units attaching to the growth on the surface. The ability to controllably form a homogenous surface may not be possible because of this.

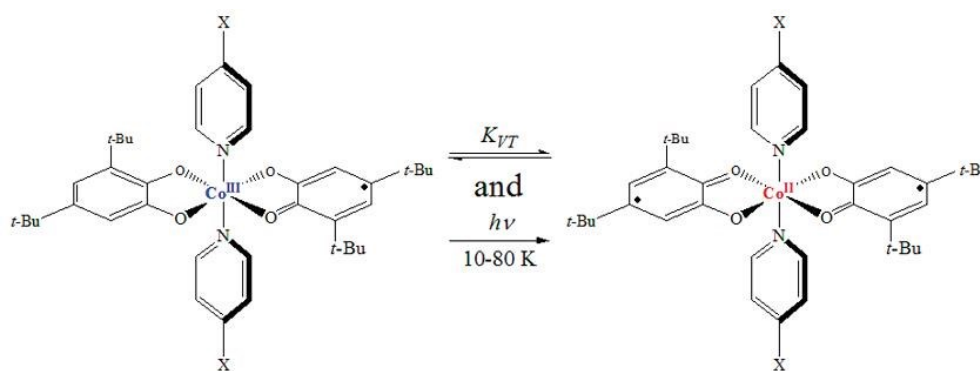


Figure 2.7 – Cobalt bis(dioxylylene) Molecule [CoVT] and its Valence Tautomer Transition

Molecular configurations for CoVT before and after VT transition, induced by temperature and light (at low T). Intramolecular charge transfer between the cobalt metal center and dioxylylene ligand enables oxidation change in the metal center, a change in the spin state of the molecule, and a slight rearrangement in molecular geometry. Reprinted with permission from Ref. 37. Copyright 2010 American Chemical Society.

In the case of the CoVT molecule, a less automated, more manual approach can be used to grow wires from the surface. For this, a layer-by-layer (LbL) growth process would be well suited for the molecular wire. The LbL process follows a basic procedure: a ‘seed’ monomer is attached to a surface of interest, often a simple molecule known to pack well and form high density monolayers. Then the wire is formed by inclusion of ‘core’ groups that attach to the surface group, alternated with intermediate linkers to enable the multilayer growth. While this process is slower than a continuous reaction, reliable and nearly identical layers can be grown to a wide variety of lengths.³⁸ In certain cases, changes in charge transport properties are seen as the LbL extends the chain length.³⁹ As long as the metal binding group isn’t affected, in principle this approach can design wires as far as the materials and patience of the researcher to do this alternating soak allow.

Long wires are not required for LbL wires to yield interesting spintronic results. As theoretical studies have shown, having just three metal centers may be sufficient for spin polarization and other effects.¹¹ Radicals can be incorporated directly onto the ‘seed’ monolayer in some instances using this approach,⁴⁰ and Coulomb blockades can be generated by just one repeat unit in a LbL wire.⁴¹ The ability to make long wires still gives us the potential to augment any spin effects, moving charge transport out of a potentially direct tunneling regime and allowing Coulomb blockades from spin interaction to have dramatic effects on resistances in electronic junctions.

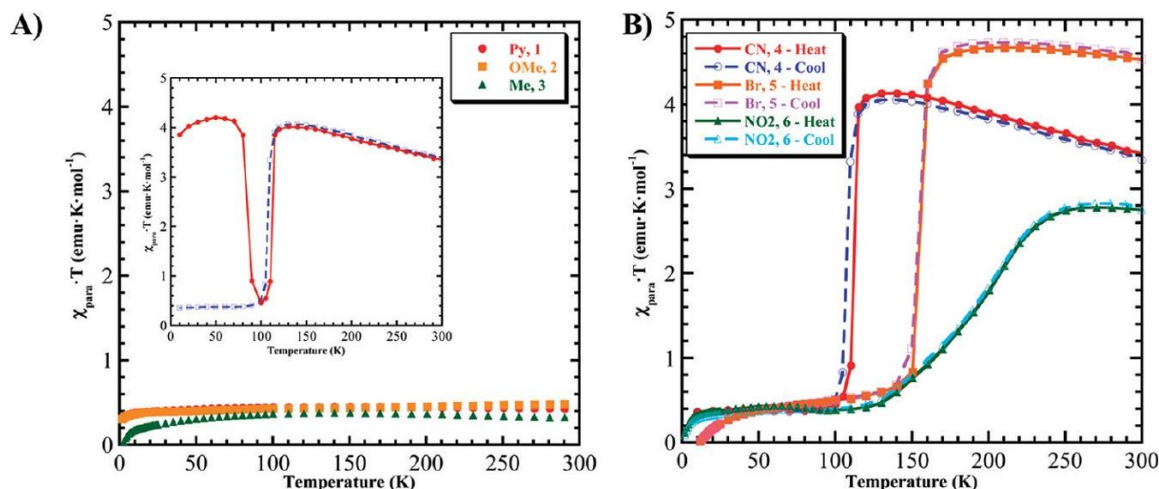


Figure 2.8 – Effects on Valence Tautomerism from Different Ligands

A) Variable-temperature magnetic susceptibility for cobalt bis(dioxylylene) molecules with 4-(X)pyridine ligands, where X = H (1), OMe (2), Me (3). No VT transition is seen in these molecules. **B)** Magnetic properties of similar molecules with X = CN (4), Br (5), NO₂ (6). VT transition is evident from change in $\chi_{\text{para}} \cdot T$ versus temperature. Inset: first heating and cooling cycle for (4). Reprinted with permission from Ref. 37. Copyright 2010 American Chemical Society.

The goal of this section is to incorporate the CoVT molecule into a molecular wire. Ligand exchange was done with the pyridine-based ligands of the molecule to attach it to a similar pyridine unit on a surface. In particular, a pyridine unit with a long alkane chain was used to decouple the metal center from the substrate, allowing for any spintronic effects from the wire to only come from the cobalt metal center(s). Several linker groups were used to try to build multilayers of the molecule. XPS experiments examined multilayer growth, comparing molecular ratios to see the effects of molecule addition at each step of the LbL growth. It was also known from previous studies of CoVT molecules that the non-dioxylylene ligand could affect the temperature of the VT transition or even influence its presence in the compound. As shown with the FeSCO, XPS at variable temperature could examine the satellite peaks that would be expected to be present for paramagnetic spin states in the metal center and absent for diamagnetic states. Therefore, the FeSCO experiment was replicated with CoVT on a surface.

2.3.2 Experimental- CoVT Wire Growth and Study

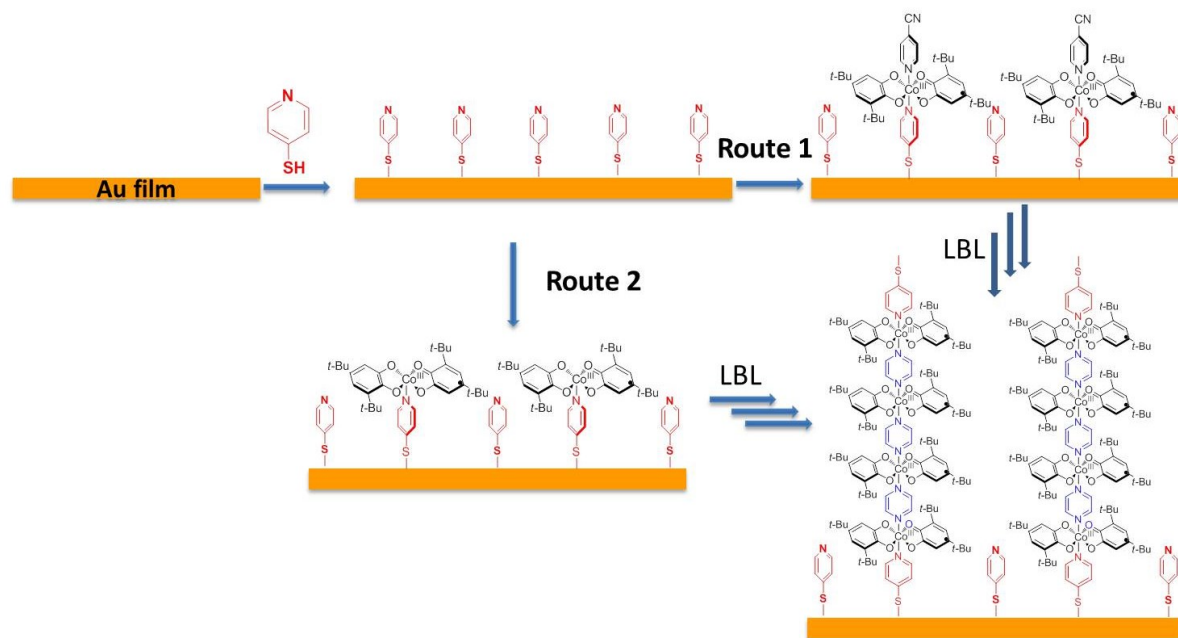


Figure 2.9 – Attaching CoVT to a Surface

Two routes for growing CoVT wires on a surface, utilizing a ligand exchange process (Route 1) and utilizing a tetramer of CoVT molecules without ligand (Route 2) to attach molecules to a seed monolayer, then using a LbL approach with pyridine based ligands to form a multilayer. CNCoVT molecules used for growth in this figure.

Silicon oxide (SiOx) substrates with evaporated titanium and gold are utilized for growth of CoVT wires. SiOx (Si <100> with 1 μm thick oxide, Addison Engineering) was cleaned in RCA (2:1:1 H₂O, NH₄OH, H₂O₂) for 15 mins, rinsed in copious amounts of H₂O and ethanol, blown dry *via* N₂ stream, and placed in UV-ozone for 20 mins. Metal films were prepared by thermal evaporation under vacuum ($P_{\text{deposition}} \leq 3 \times 10^{-6}$ mbar) utilizing evaporation boats from RD Mathis and evaporation materials from KJ Lesker. Titanium was evaporated as an adhesion layer, 5 nm @ 1 Å/s. Gold was subsequently evaporated (without breaking vacuum), 40 nm @ 1 Å/s for first 5 nm then 10 Å/s for the remainder. This procedure with slow first few nanometers and faster deposition for the remainder were found to produce the smoothest films.

‘Seed’ monolayers for the CoVT molecule were prepared by solution soak of 3-(pyridine-4-yl)-dodecane-1-thiol to bind to gold. The pyridine-dodecane-thiol was synthesized and attached to gold by solution soaking in 1 mM ethanol solutions overnight, sonicating in a fresh ethanol solution, then blowing dry in nitrogen.

CoVT molecules were attached to this seed layer by one of two routes (Figure 2.9). Route 1 incorporates a VT molecule including pyridine based ligands, synthesized as described in Schmidt et al.³⁷ In this route, ligand exchange of the pyridine based ligands (X = Br, CN) of the CoVT was required for attachment to the substrate surface. This process was accomplished *via* solution soaking under N₂ inert environment in 1 mM dichloromethane (DCM) solutions for 24-48 hrs, leading to replacement of one of the pyridine ligands. Substrates were sonicated in fresh DCM to remove physisorbed molecules and dried with N₂ stream. Route 2 involved a VT-based tetramer without pyridine ligands (nCoVT, for ‘naked’-CoVT) that was expected to separate into individual nCoVT units upon attachment to the seed monolayer. nCoVT attachment was accomplished in similar manner (1 mM solution in DCM for 24-48 hrs, sonication in DCM, dry with N₂). After establishing the CoVT core in both routes, multilayers of the CoVT molecules were attached in a LbL approach by alternating soaks of a pyridine-based linker group and another CoVT molecule. Two linkers – 1,4-bipyridine [bipy] and 1,2-di(4,pyridyl)ethylene [DipyE] – were used, attached *via* 1 mM soaks for 24 hrs, followed by CoVT soak as described with the seed attachment. As proposed, the final product would include a thiol-pyridine ligand for binding to a top contact. The length of the multilayer is referred to by the number of core CoVT units in the final chain, as shown in Figure 2.9.

XPS was done in the same setup as section 2.2.2. Survey scans were done with 100.0 ms dwell times with 1 eV steps, averaging two sweeps. High resolution scans were obtained for

several core shells: C 1s (250.0 ms dwell time, 0.1 eV step, 1 sweep), Co 2p (800.0 ms dwell time, 0.1 eV step, 2 sweeps), N 1s (800.0 ms dwell time, 0.1 eV step, 2 sweeps), O 1s (331.5 ms dwell time, 0.1 eV step, 2 sweeps), Br 3d (425.5 ms dwell time, 0.1 eV step, 2 sweeps), S 2p (800.0 ms dwell time, 0.1 eV step, 1 sweep), Au 4f (458.0 ms dwell time, 0.1 eV step, 1 sweep). All binding energies were shifted so C 1s = 184.5 eV, the expected aliphatic carbon peak. Backgrounds were subtracted using a Shirley background subtraction formula. Peaks were then assigned using a Gaussian-Lorentzian hybrid function. In the case of elements with spin-orbit coupling (all but the s-orbital signals in this study), doublet peaks were assigned based on literature splittings.

2.3.3 Results and Discussion- CoVT Wire Growth and Study

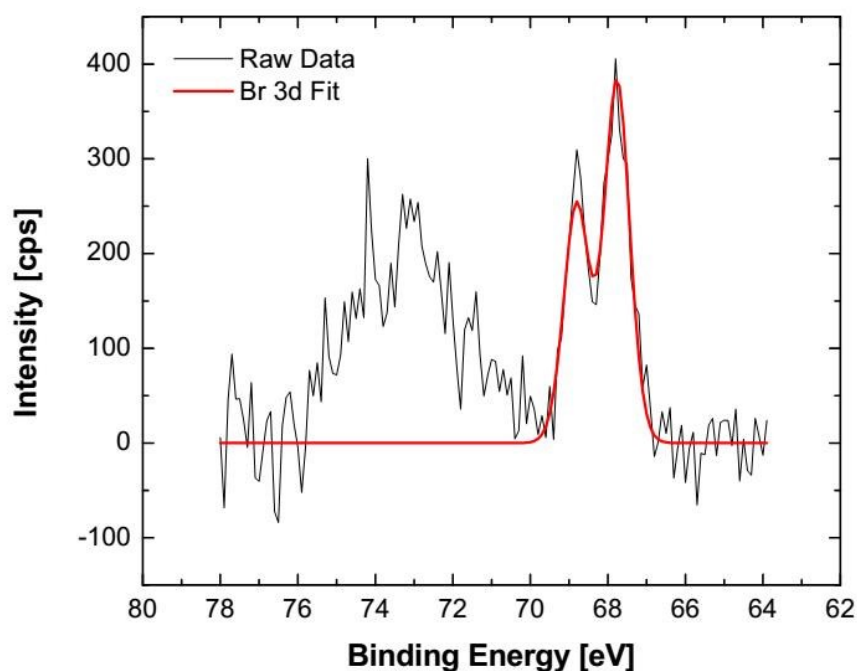


Figure 2.10 – CoVT Ligand Test on a Surface

XPS Br 3d spectra of BrCoVT ($X = \text{Br}$) molecules ligand exchanged on a gold surface. Br 3d serves as a fingerprint of the ligand still being present on the substrate in XPS. The peak around 73 eV binding energy is too high to be bromine, and likely comes from a heavy metal contaminant.

The first check that must be done is to confirm whether the ligand exchange process to attach CoVT molecules onto a gold substrate. Figure 2.10 shows XPS spectra for a CoVT molecule with a bromo-pyridine ligand (BrCoVT) that has been ligand exchanged onto the pyridine-dodecane-thiol monolayer. The bromine provides a fingerprint that can be used to identify that the top ligand of the CoVT molecule has been unaffected by the molecule attachment. As the figure shows, a strong bromine signal is present that cannot be explained by any other source than the CoVT molecule ligand exchanging to become attached to the substrate. The sonication and cleaning steps should prevent the physisorption of CoVT molecules, and test soaks on a bare gold surface (without seed monolayer) show no presence of VT molecules. Along with the Co 2p spectra shown in Figure 2.11, it is evident that as anticipated by Route 1, a CoVT monomer is confirmed to be able to ligand exchange onto the seed monolayer and begin the wire growth.

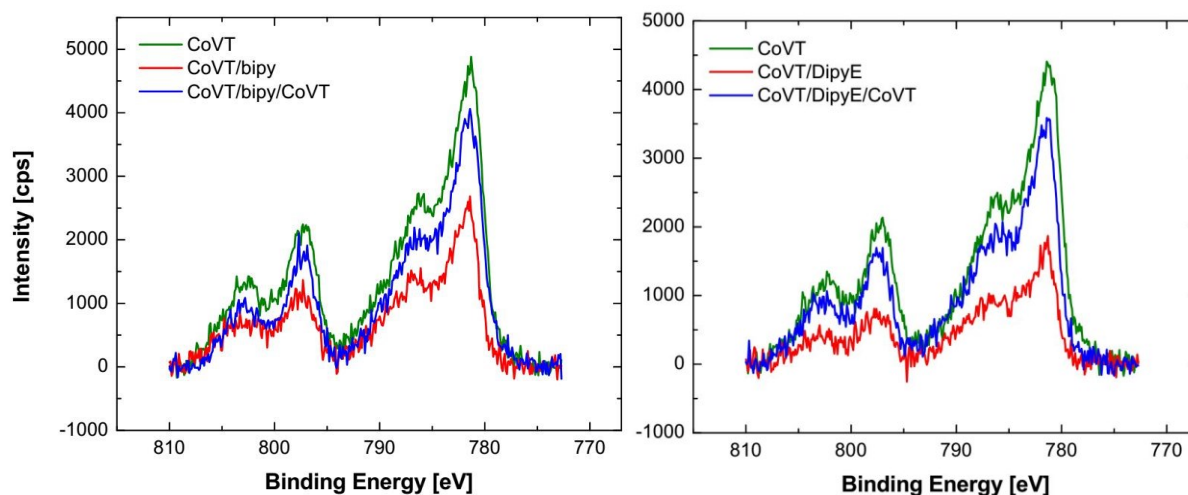


Figure 2.11 – XPS Characterization of CoVT on a Surface

Co 2p XPS spectra of CNCoVT growth on a surface for bipy (left) and DipyE (right) linker groups. Spectra are taken after pyridine-dodecane-thiol linkers and solution soaks in CoVT (green), CoVT/ linker (red), and CoVT/ linker/ CoVT (blue).

Table 2-1 shows that Route 2 is also suitable for monomer growth into a wire. XPS spectra were integrated and compared, and by taking into account the relative sensitivity factors (RSFs) of each elemental signal, we obtain atomic concentration percentages for each element in the signal. The peak included in the table represents the main peak for each signal; p- and d-orbitals contain typically contain a doublet due to spin orbit coupling at a characteristic splitting, and cobalt and sulfur possess a doublet not listed in the table though is accounted for in the integrated area. Oxygen and other trace elements are omitted in this comparison; the goal is to compare elements that could identify key components of the wire, such as the metal binding group (sulfur), the CoVT ligand (nitrogen), and the CoVT unit itself (cobalt). Carbon was included in the analysis; however, background carbon in the XPS prevents this from being quantitatively useful in comparing elemental concentrations.

Table 2-1 – Atomic Concentrations for CoVT Monomers from Routes 1 and 2

| XPS Peak | XPS Peak Information | | CoVT Wire- Route 1 | | CoVT Wire- Route 2 | |
|----------|----------------------|-------|--------------------|----------------|--------------------|----------------|
| | Binding Energy (eV)* | RSF | Raw Area | Atomic Conc. % | Raw Area | Atomic Conc. % |
| C 1s | 285.0 | 0.278 | 11679.4 | 79.86 | 10925.7 | 79.12 |
| S 2p | 161.9 | 0.668 | 2725.6 | 8.03 | 2729.5 | 8.52 |
| Co 2p | 781.5 | 3.59 | 13765.7 | 6.21 | 11762.5 | 5.62 |
| N 1s | 400.9 | 0.477 | 1536.5 | 5.91 | 1655.5 | 6.74 |

* Represents the main peak for each element; integrated area accounts for area from all peaks

Suitability for Route 2 is established through the near identical percentages in atomic concentration between Route 1 and Route 2. Having established that Route 1 generates valid monomer CoVT wires, the near identical results means utilizing nCoVT also generates wires.

To further analyze the elemental analysis, it should be pointed out the trend of sulfur > nitrogen > cobalt in atomic percentages. The cobalt being the smallest perhaps is unsurprising, as a simple explanation would be that not all of the seed molecules have CoVT molecules attached to them. A consequence of the CoVT molecule is the size of the dioxylyene ligands, which will likely prevent good packing of the molecules. It should also be pointed out that even the most well-packed monolayers in alkanethiols are expected to tilt on a surface.³⁴ As such, the seed monolayer is expected to have a tilt. The monolayer is built off of a relatively long carbon chain, so the monolayer may approach the 30° tilt from alkanes, though the tilt is likely higher due to lower packing in this seed monolayer from the pyridine head. The bulky side chain comes into play again as the CoVT group is expected to bind parallel to the seed monolayer, and any tilt could be reflected in tilt of the wire as a whole. This could cause steric hindrance effects of the dioxylyene ligands with the seed monolayer, which and as shown in Figure 2.12, could potentially inhibit attachment of the CoVT. These factors are expected to prevent one-to-one attachment of CoVT to seed. Raw atomic concentrations from Co 2p and S 2p values indicate around 75% of seed monolayer has molecule bound. Due to larger attenuation of the sulfur signal than cobalt through a mostly carbon based layer,⁴² this ratio will favor the sulfur even more. Still, this indicates a finite percentage of the seed has CoVT bound to it.

Another assessment needs to be made reflecting the higher atomic ratio of sulfur to both cobalt and nitrogen. Sulfur is expected to be in at most a 1:1 ratio with nitrogen on the surface, as the only source for it should be the seed monolayer while nitrogen could come from the

monolayer or the ligand on the VT. The higher sulfur ratio expresses that more sulfur than standing monolayer has been deposited, possibly from a breakdown of the monolayer in certain places. Despite this, sonication and cleaning steps still imply that CoVT appears to be chemically bound to the substrate, which should only come from ligand exchange onto the chemically bound seed monolayer. Even if the coverage of monolayer on the surface is not perfect, we should still expect this CoVT monomer to be a fitting substrate to continue growing a multilayer.

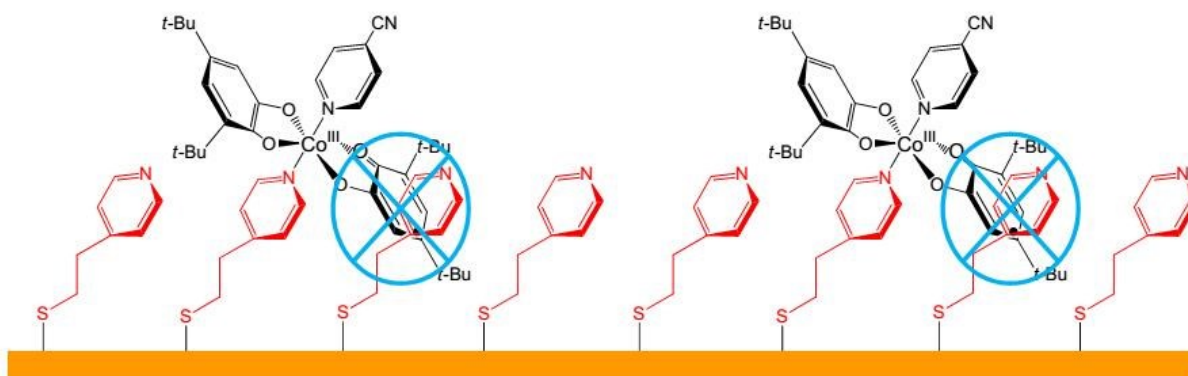


Figure 2.12 – Steric Hindrance in CoVT Wires

Two-dimensional pictorial description of possible steric hindrance effects in attaching CoVT to seed monolayer. Accounting for tilts in monolayer, the dioxylene ligands may physically hinder the attachment of CoVT molecules.

Figure 2.11 above also shows XPS Co 2p spectra for attempted growth of a CNCoVT multilayer on a gold surface. After growth of the monomer, a linker group (either bipy or DipyE) is soaked onto the surface, then a second soak in CoVT is done to attach a second CoVT group. However, as the XPS spectra show, the CoVT spectra experience a sharp drop in Co 2p signal after the linker group is introduced. The subsequent second soak of the substrate in CoVT solution recovers some of the lost cobalt signal, but never as high as the original monolayer soak. Similar results are obtained for nCoVT attachment *via* Route 2. As before, attenuation of ejected core shell electrons is expected, and if a multilayer is being grown, the cobalt electrons from the

first layer would be attenuated even more as the multilayer is being grown. However, the linker group is too short to see the rather large 50-60% (bipy ligand) and 60-70% (DipyE) reduction in Co 2p signal seen upon linker addition. This short distance, coupled with the fact that the anticipated tilt of the monolayer would further reduce the length through which these electrons would travel, would not explain the severe drop in Co 2p intensity. A much more likely explanation is that the CoVT is being removed from the surface during the linker soak and the CoVT monomer is being recovered during the second CoVT soak.



Figure 2.13 – Polymerization of CoVT and Linker Group

Refluxing CoVT and bipy in DCM leads to the formation of an insoluble precipitate, indicative of a high molecular weight polymer being formed by the reaction.

The first question needing to be addressed is whether or not the ligand exchange process works as designed. Proof of the ability to attach the ligand to CoVT is done by a solution reaction of the CoVT with bipy in DCM. The molecules are simply refluxed for 2 hrs to test their reaction ability. Figure 2.13 shows an image of the solid formed in the resulting reaction vessel.

The liquid remaining after reaction only showed indication of CoVT monomer and bipy ligand *via* mass spectrometry, so focus was placed on the precipitate of the reaction. Formation of a solid is strong indication that a polymerization has taken place. Characterization of the molecule was unable to be done as it was insoluble in any attempted solvent. The best conclusion is that the insoluble precipitate represents a high molecular weight polymer, indicating the ligand attachment and subsequent multilayer growth should be possible.

The conclusion left then from both the surface wire growth and the solution polymerization is that ligand exchange is occurring when bipy and DipyE is soaked with CoVT on a seed monolayer. However, the ligand being exchanged – at least in part – is likely the pyridine group from the seed monolayer instead of the top ligand, knocking the CoVT off of the surface instead of enabling growth of the wire. Control solutions in ethanol do not remove the monomer, indicating it must be the linker group removing the CoVT from the surface, not the solvent. It was expected that the steric hindrance might work in favor of molecular wire growth in this instance, where the seed monolayer and the bulky dioxyethylene ligands might prevent access to reacting with the surface bound portion of the wire, though clearly this was not the case.

In spite of seeing a large portion of CoVT being removed from the surface, one final test of the ability to form multilayers using this ligand exchange approach was tried *via* multiple solution soaks to form a surface bound CoVT oligomer/polymer. Using other molecules, such an approach has achieved long (tens of nanometers) wires in a decent homogenous manner even after a 30 layer growth.⁴³ Therefore, 15, 30, and 40 iterations of CoVT and bipy linker soakings were done to attempt at growing these wires.

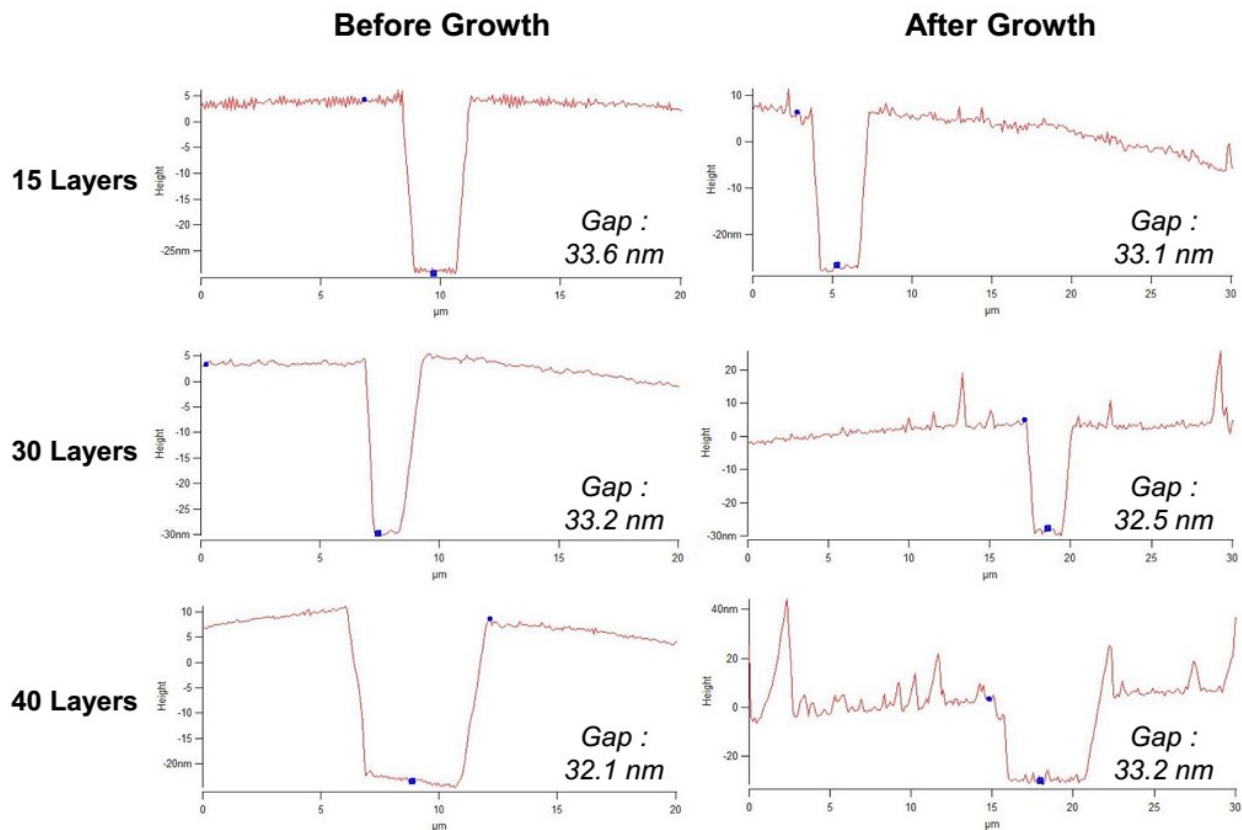


Figure 2.14 – Cross Sectional AFM of CoVT Multilayers on Gold

AFM measured across predefined gaps in Au/SiO_x substrates before and after CNCoVT multilayer formation (15-, 30-, and 40-layer growth). The “gap” refers to the height difference between the top of the substrate to the bottom of the gap, as determined by the height difference between the blue points on each AFM image. Gaps did not change appreciably, indicating lack of layer type growth. Higher number of layers involved in wire growth did lead to higher peaks across the surface, indicating possible multilayer growth in small regions, but clearly do not represent layered growth.

Figure 2.14 shows cross sections of atomic force microscopy (AFM) spectra for each sample. The dip in the middle was defined when the gold substrate was formed as an internal reference for height difference, representing a region where no Ti/Au was evaporated. The height gap was measured before and after wire growth to account for the possibility for any layer growth. Unfortunately, layer growth was not seen, as indicated by nearly identical gaps in the height before and after the solution soaks, and in fact any growth on the surface is seen only as

spotty and inhomogeneous peaks across the substrate. It should be stated that the roughness and heights seen do appear to become larger for the samples with longer solution soaks. Height spikes as large as 15 nm are seen in the 30 layer sample, and as high as 40 nm in the 40 layer sample. However, even if such roughness is due to multilayer growth, the film quality may reflect what was seen in the monolayer to bilayer study that the linker group knocks off a finite percentage of the CoVT upon its addition. This possibility, and the resulting inhomogeneity across the substrate, makes the LbL monolayer impractical for device fabrication.

Despite the inability to build reliable LbL monolayers, the possibility still existed to use the CoVT monomer in a molecular device setting as the VT transition could still result in changes in transport properties. As discussed previously, changing ligands was known to affect the VT properties of the molecule, and the question to be addressed was whether or not attaching the CoVT *via* the seed monomer altered the VT transition. To examine this, the variable temperature experiment done with the FeSCO molecule was replicated for CoVT.

As shown in Figure 2.8, BrCoVT molecules have a VT transition in the solid form at 150 K. Within the temperature limitations of the XPS system, this temperature should be obtainable with a decently sized temperature window of almost 50 K to account for any temperature shift in the transition, making the X = Br ligand ideal for this test. However, as shown in Figure 2.15, even with this modest window to account for shifts in the VT transition, no reduction in satellite peak intensity was seen down to 110 K compared to higher temperature (210 K). All other elemental signals and markers in XPS were identical, further suggesting no change was seen. This may not be a full indication that all VT properties are lost, but it is indication that any such transition is at a temperature possibly too impractical to electrically evaluate the transport properties and any potential Coulomb blockade properties.

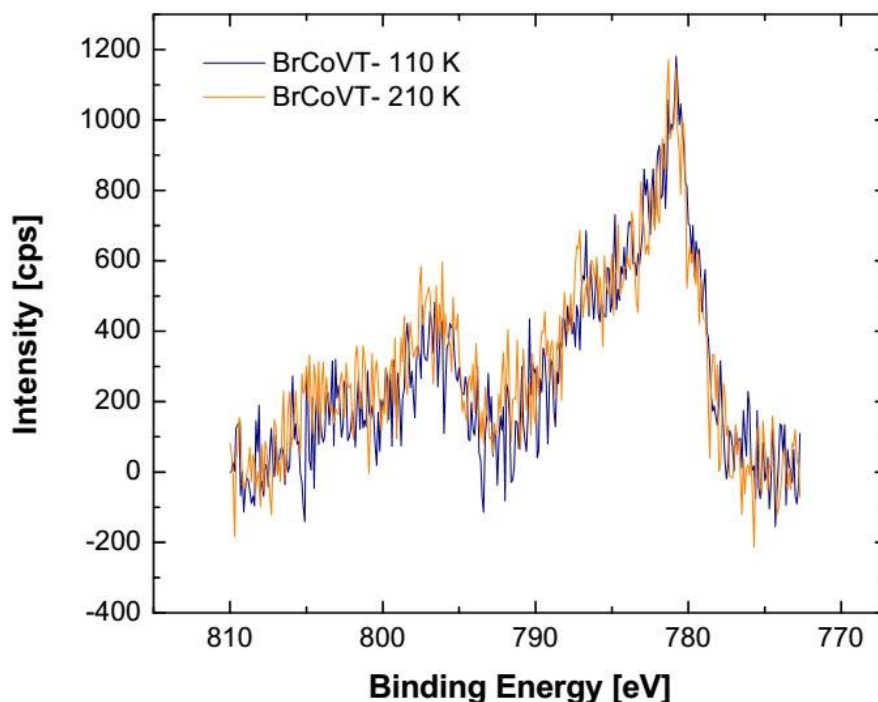


Figure 2.15 – CoVT Monomer Wires at Variable Temperature

XPS Co 2p core shell spectra taken at 110 K and 210 K for X = Br CoVT. Spectra show no difference in either the main peaks or the satellite peaks.

At this point, it is apparent the advantages of the CoVT are lost using this ligand exchange approach. A good accomplishment has been made in the ability to attach these molecules to a surface, but without the ability to grow a reliable multilayer into a molecular wire, and without any VT properties in the wire monomer with liquid-N₂ cooling, the spintronic capability of the wire system is significantly lower than originally envisioned. This is not to say that the VT properties could not be realized in different junctions. As shown in Figure 2.16, crystalline regions can be formed from the molecules after drop casting a CoVT solution onto a substrate, and in principle these crystals could be aligned in electrical junctions to realize their VT properties. Such a process would be highly manual and/or require different processing to align crystals. Furthermore, the transport properties of these junctions would be much more

complex than the single molecule wires attempted to be designed in this work. In light of no straightforward methods to accomplish single molecule measurements, the CoVT appears invalid, at least with this approach, for use in highly reproducible molecular electronic junctions.

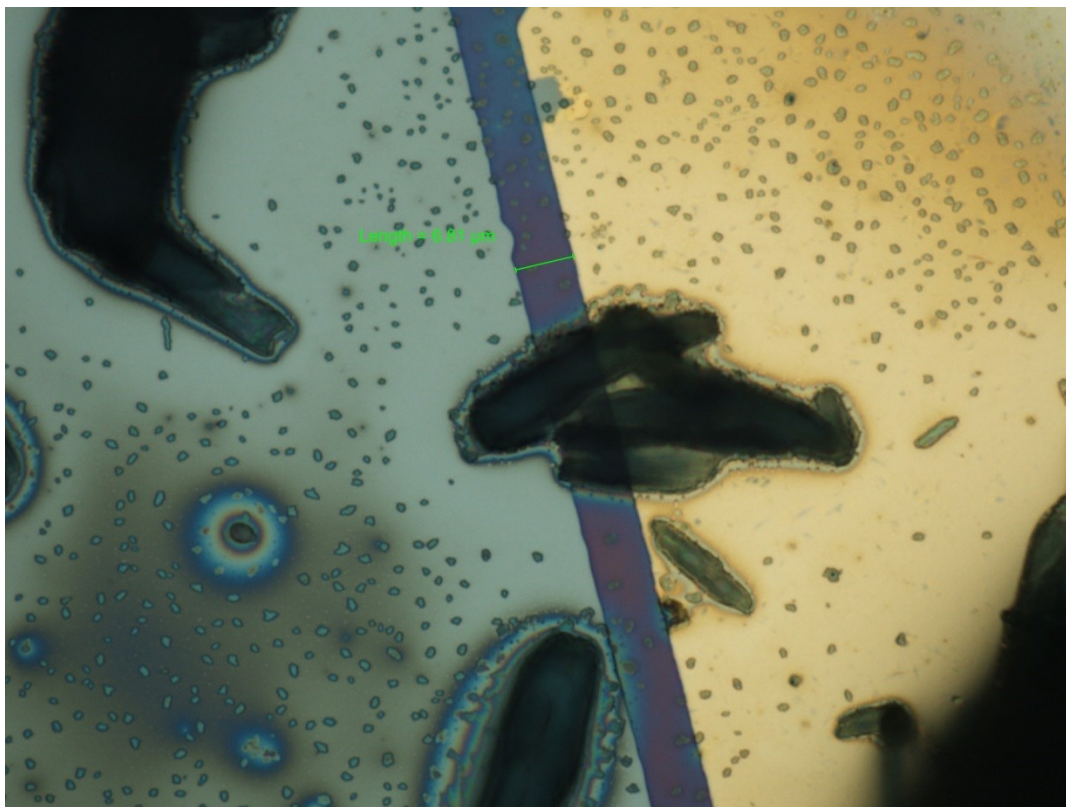


Figure 2.16 – CoVT Crystals on Au/SiO_x Substrates

CNCoVT crystals formed from drop cast solutions in DCM. Crystals were formed on predefined gold substrates on SiO_x with approximately 7 μm gaps between source and drain electrodes, and manually moved to make electrical connection between source and drain.

2.4 Conclusions

This chapter highlights work with several molecules exhibiting spintronic properties arising from spin transitions in the metal center of the molecule, transitioning from a diamagnetic state to a paramagnetic state *via* external stimuli (light or temperature). This work focused on an XPS method to characterize the VT properties as well as a synthetic route to attempt to grow a molecular wire from molecules with spin transitions and create an architecture that could exhibit spin state transitions and potentially function as a switch where the resistance could be externally changed.

Iron SCO's with pyridine based ligands were studied in XPS to show their crossover properties. Thin films of the molecules exhibit changes in satellite peaks of the Fe 2p spectra as a function of temperature, corresponding with the change from diamagnetic LS state to the paramagnetic HS state. It was expected that such effect could be used to indicate a similar diamagnetic to paramagnetic transition in CoVT molecules.

Cobalt bis(dioxylylene) based molecules with VT properties were utilized in a LbL approach to attempt to attach them to a gold surface *via* a pyridine-alkanethiol based 'seed' monolayer and grow wires using alternating solution soaks. Strong evidence is given that CoVT monomers could be grown using a ligand exchange approach with the pyridine group of the seed monolayer to attach CoVT to the surface. However, this ligand exchange is limited in that there was no ligand site selectivity with subsequent soaks, and attempts to further grow the chain by attaching a linker group resulted in removal of CoVT from the surface. Small percentages of wires may be grown into multilayers as shown by 15, 30, and 40 layer syntheses on a gold surface, but at best this growth is inhomogeneous. Furthermore, evidence is shown that even though CoVT could be ligand exchanged as a monomer, no VT properties were seen in the XPS setup *via* liquid-N₂ cooling.

While this ligand exchange approach did not sustain the VT properties of the molecules in this study, the approach is still interesting, and it could be tuned to different systems to both attach unique molecules to surfaces. If proper tuning of ligands is used, future work could potentially grow multilayers of molecules to take advantage of unique properties such as SCO and VT for dynamic electronic or spintronic properties across a molecular wire.

2.5 Appendix

2.5.1 XPS Spectra for Various CoVT Wire Components

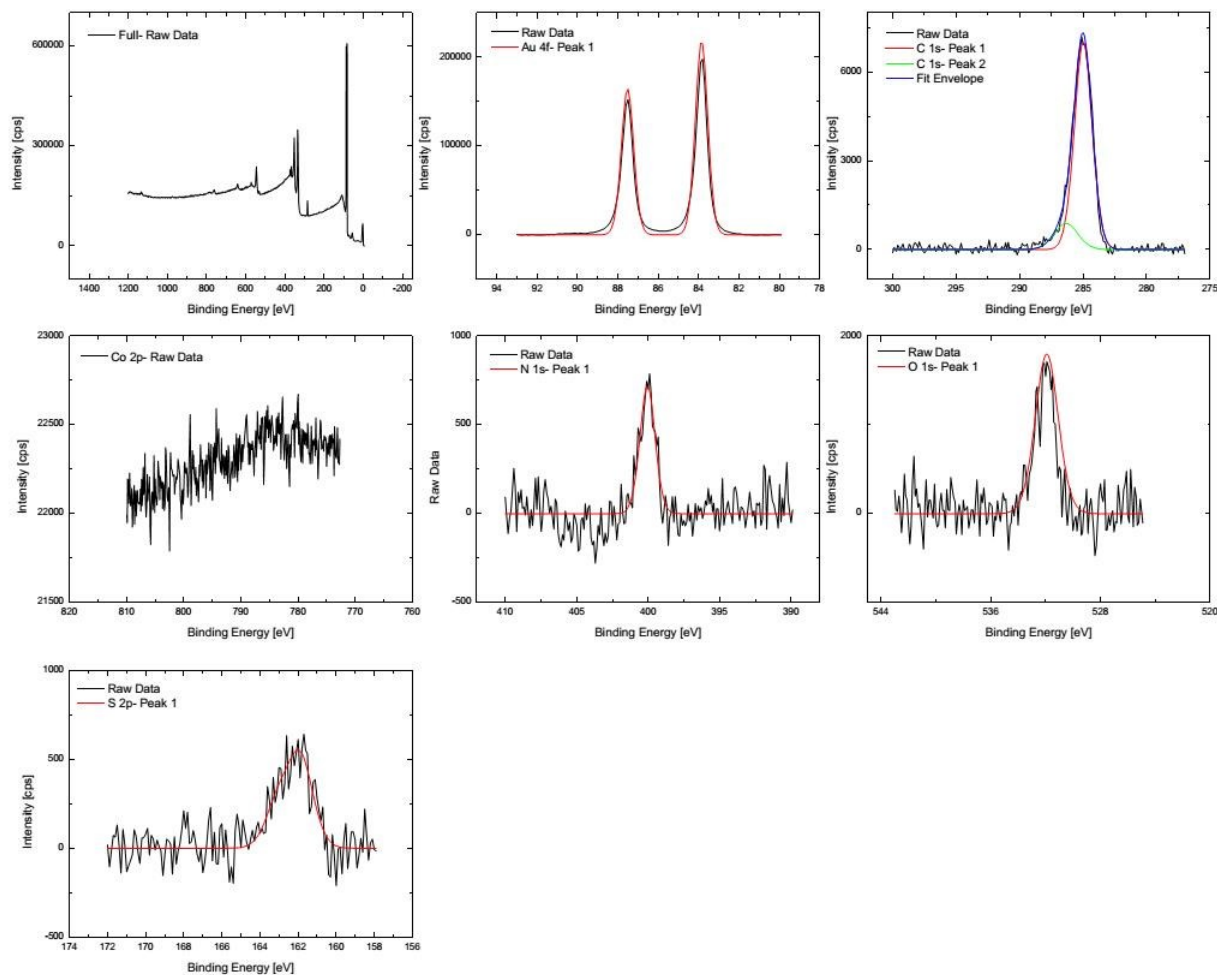


Figure 2.17 – Pyridine-dodecane-thiol Seed Monolayer XPS Spectra

XPS spectra for pyridine-dodecane-thiol seed layers, measured at RT. Full spectrum; Au 4f, with one doublet fitted; C 1s with two singlets fitted; Co 2p, with no discernable peaks; N 1s, with one singlet fitted; O 1s, with one singlet fitted; and S 2p, with one doublet fitted. Fit peaks are defined by Gaussian-Lorentzian functions. Fit envelopes are given as sums of fit peaks when more than one is given to evaluate the overall fit compared to raw data.

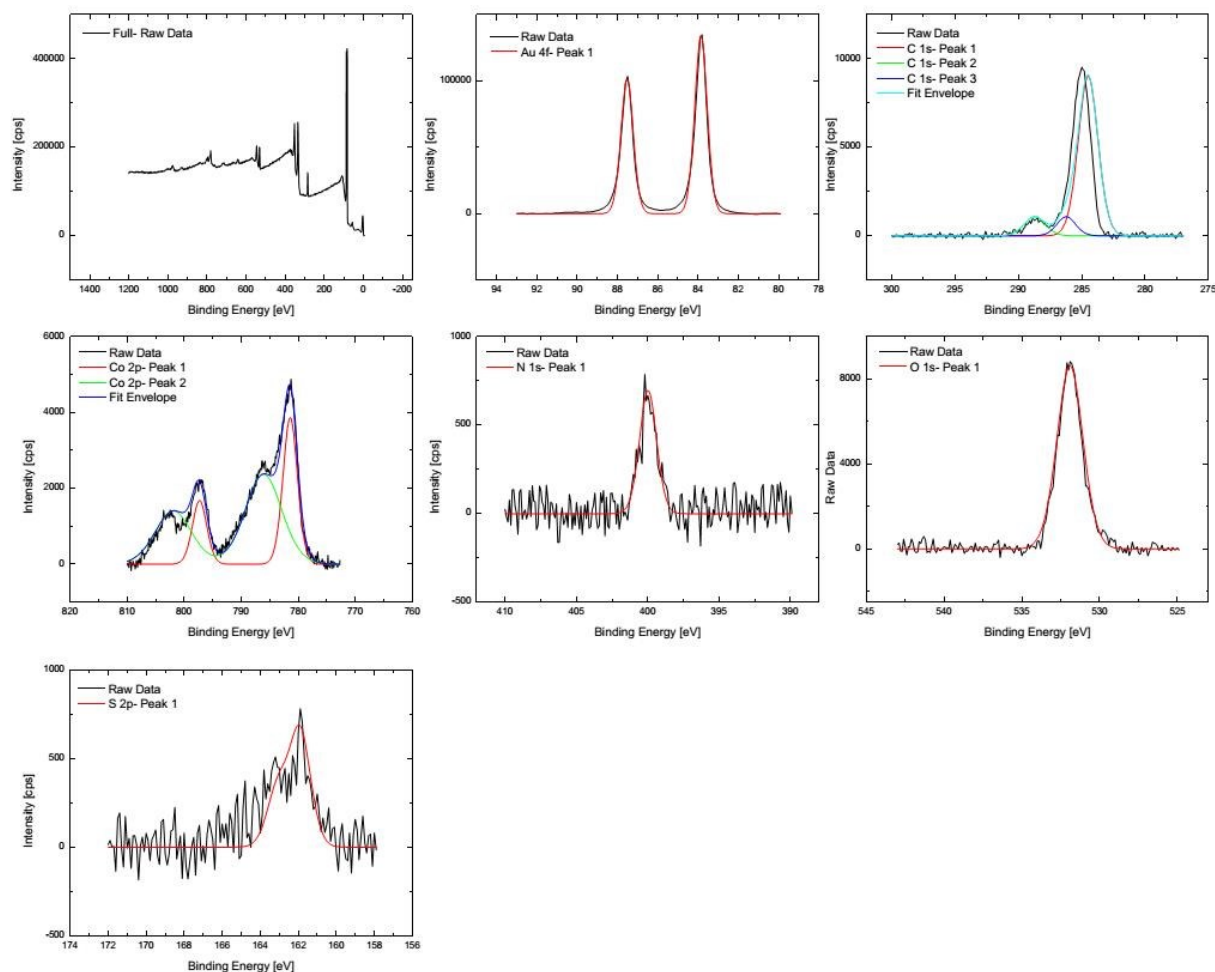


Figure 2.18 – CNCovT XPS Spectra

XPS spectra for CNCovT layers, measured at RT. Full spectrum; Au 4f, with one doublet fitted; C 1s with three singlets fitted; Co 2p, with two doublets (one for satellite peaks) fitted; N 1s, with one singlet fitted; O 1s, with one singlet fitted; and S 2p, with one doublet fitted. Fit peaks are defined by Gaussian-Lorentzian functions. Fit envelopes are given as sums of fit peaks when more than one is given to evaluate the overall fit compared to raw data.

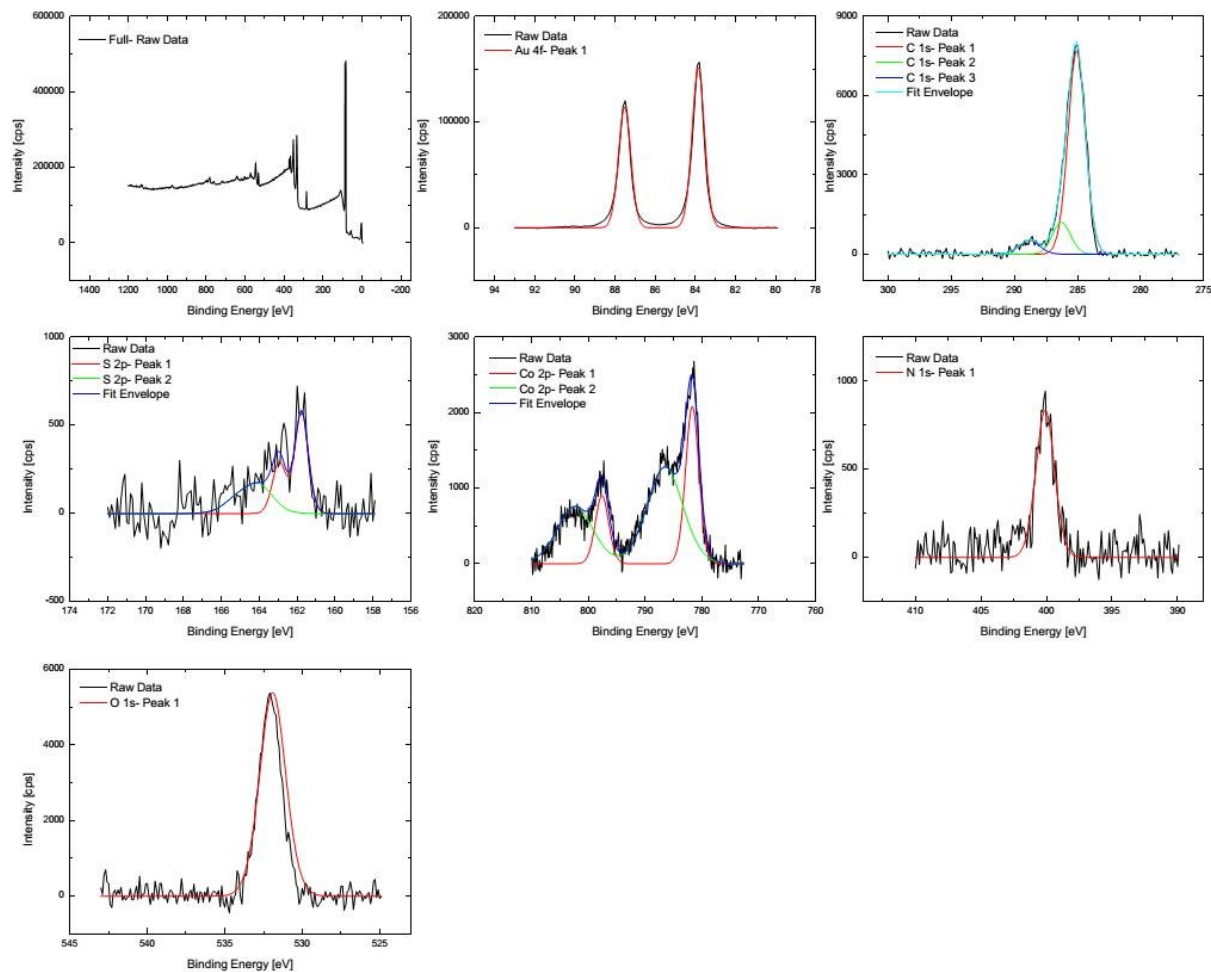


Figure 2.19 – CNCovT/ bipy XPS Spectra

XPS spectra for CNCovT/ bipy layers, measured at RT. Full spectrum; Au 4f, with one doublet fitted; C 1s with three singlets fitted; S 2p, with two doublets fitted; Co 2p, with two doublets (one for satellite peaks) fitted; N 1s, with one singlet fitted; and O 1s, with one singlet fitted. Fit peaks are defined by Gaussian-Lorentzian functions. Fit envelopes are given as sums of fit peaks when more than one is given to evaluate the overall fit compared to raw data.

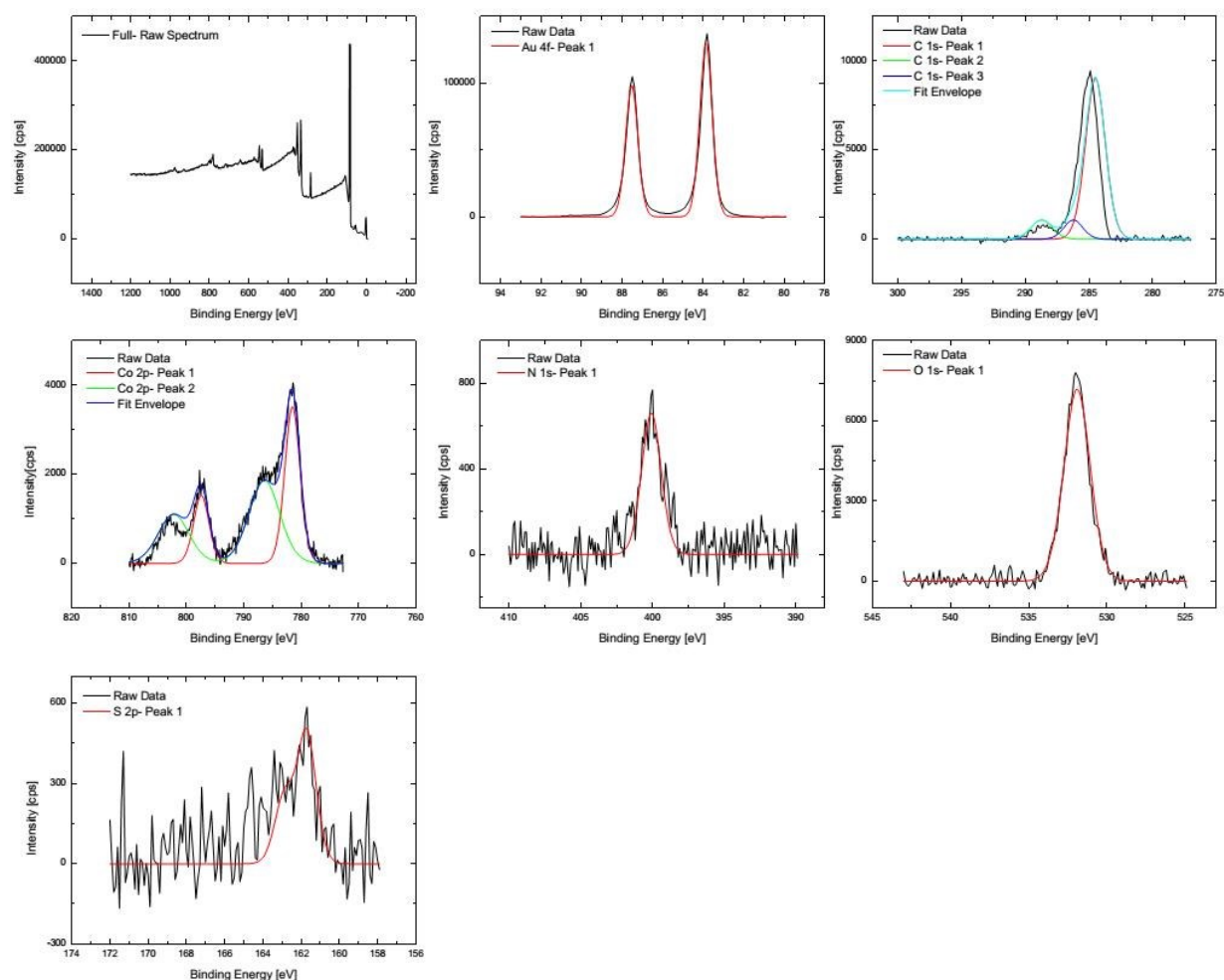


Figure 2.20 – CNCovT/ bipy/ CNCovT XPS Spectra

XPS spectra for CNCovT/ bipy/ CNCovT layers, measured at RT. Full spectrum; Au 4f, with one doublet fitted; C 1s with three singlets fitted; Co 2p, with two doublets (one for satellite peaks) fitted; N 1s, with one singlet fitted; O 1s, with one singlet fitted; and S 2p, with one doublet fitted. Fit peaks are defined by Gaussian-Lorentzian functions. Fit envelopes are given as sums of fit peaks when more than one is given to evaluate the overall fit compared to raw data.

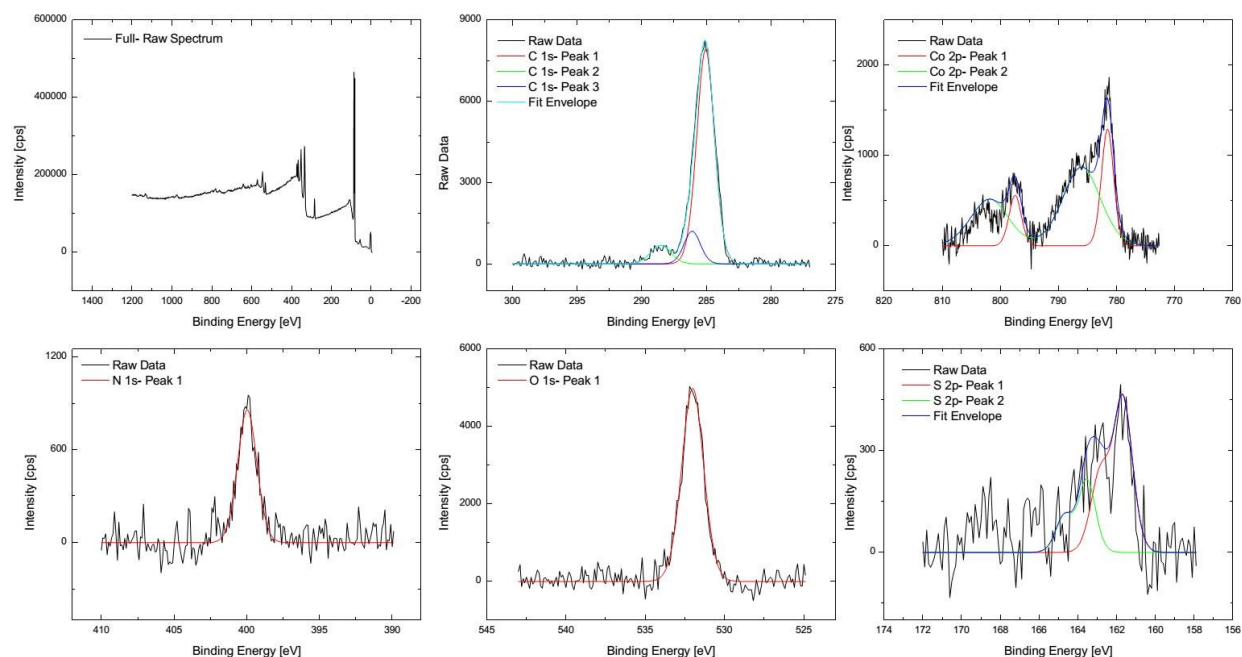


Figure 2.21 – CNCoVT/ DipyE XPS Spectra

XPS spectra for CNCoVT/ DipyE layers, measured at RT. Full spectrum; C 1s with three singlets fitted; Co 2p, with two doublets (one for satellite peaks) fitted; N 1s, with one singlet fitted; O 1s, with one singlet fitted; and S 2p, with two doublets fitted. Fit peaks are defined by Gaussian-Lorentzian functions. Fit envelopes are given as sums of fit peaks when more than one is given to evaluate the overall fit compared to raw data.

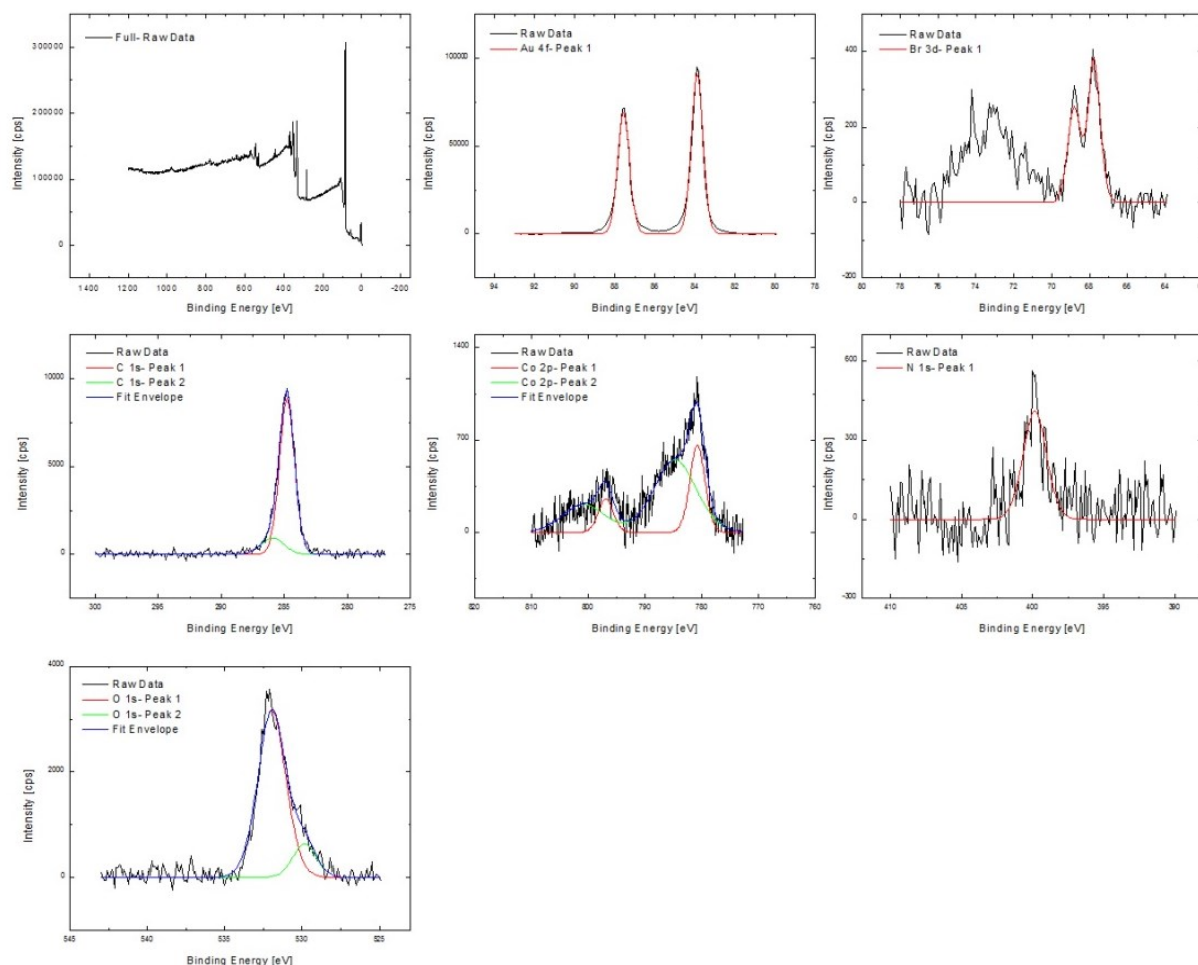


Figure 2.22 – BrCoVT (110K) XPS Spectra

XPS spectra for BrCoVT monomers, measured at 110 K. Full spectrum; Au 4f, with one doublet fitted; Br 3d, with one doublet fitted (other peak is too low for bromine, may be heavy metal); C 1s, with two singlets fitted; Co 2p, with two doublets (one for satellite peaks) fitted; N 1s, with one singlet fitted; and O 1s, with two singlets fitted. Fit peaks are defined by Gaussian-Lorentzian functions. Fit envelopes are given as sums of fit peaks when more than one is given to evaluate the overall fit compared to raw data.

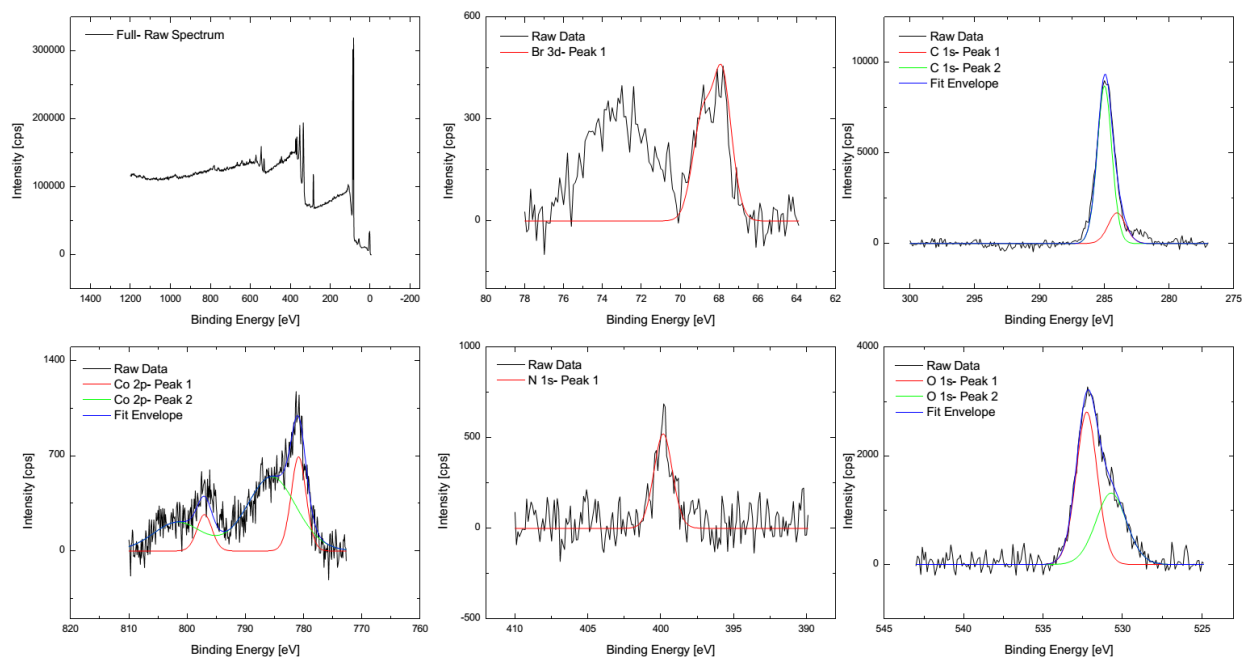


Figure 2.23 – BrCoVT (210K) XPS Spectra

XPS spectra for BrCoVT monomers, measured at 210 K. Full spectrum, Br 3d, with one doublet fitted (other peak is too low for bromine, may be heavy metal); C 1s, with two singlets fitted; Co 2p, with two doublets (one for satellite peaks) fitted; N 1s, with one singlet fitted; and O 1s, with two singlets fitted. Fit peaks are defined by Gaussian-Lorentzian functions. Fit envelopes are given as sums of fits when more than one is given to evaluate the overall fit compared to raw data.

2.6 References

- (1) Batelaan, H.; Gay, T. J.; Schwendiman, J. J. *Phys. Rev. Lett.* **1997**, *79*, 4517–4521.
- (2) Hirsch, J. E. *Phys. Rev. Lett.* **1999**, *83*, 1834–1837.
- (3) Billas, I. M. L.; Chatelain, A.; de Heer, W. A. *Science* **1994**, *265*, 1682–1684.
- (4) Barbara, P. F.; Meyer, T. J.; Ratner, M. A. *J. Phys. Chem.* **1996**, *100*, 13148–13168.
- (5) Soo Park, C.; Zhan Jin, X.; Nam Yun, K.; Ran Park, Y.; Shon, Y.; Min, N.-K.; Jin Lee, C. *Appl. Phys. Lett.* **2012**, *100*, 192409.
- (6) Julliere, M. *Phys. Lett. A* **1975**, *54*, 225–226.
- (7) Yuasa, S.; Nagahama, T.; Fukushima, A.; Suzuki, Y.; Ando, K. *Nat. Mater.* **2004**, *3*, 868–871.
- (8) Berry, M. V.; Geim, A. K. *Eur. J. Phys.* **1997**, *18*, 307–313.
- (9) Stepanow, S.; Rizzini, A. L.; Krull, C.; Kavich, J.; Cezar, J. C.; Yakhou-harris, F.; Sheverdyeva, P. M.; Moras, P.; Carbone, C.; Ceballos, G.; Mugarza, A.; Gambardella, P. *J. Am. Chem. Soc.* **2014**, *136*, 5451–5459.
- (10) Dei, A.; Gatteschi, D. *Angew. Chem. Int. Ed.* **2011**, *50*, 11852–11858.
- (11) Cho, W. J.; Cho, Y.; Min, S. K.; Kim, W. Y.; Kim, K. S. *J. Am. Chem. Soc.* **2011**, *133*, 9364–9369.
- (12) King, D. M.; Tuna, F.; McMaster, J.; Lewis, W.; Blake, A. J.; McInnes, E. J. L.; Liddle, S. T. *Angew. Chem. Int. Ed.* **2013**, *52*, 4921–4924.
- (13) Busche, C.; Vilà-Nadal, L.; Yan, J.; Miras, H. N.; Long, D.-L.; Georgiev, V. P.; Asenov, A.; Pedersen, R. H.; Gadegaard, N.; Mirza, M. M.; Paul, D. J.; Poblet, J. M.; Cronin, L. *Nature* **2014**, *515*, 545–549.
- (14) Matsumoto, T.; Newton, G. N.; Shiga, T.; Hayami, S.; Matsui, Y.; Okamoto, H.; Kumai, R.; Murakami, Y.; Oshio, H. *Nat. Commun.* **2014**, *5*, 3865.
- (15) Matsuda, M.; Tajima, H. *Chem. Lett.* **2007**, *36*, 700–701.
- (16) Cobo, S.; Molnár, G.; Real, J. A.; Bousseksou, A. *Angew. Chem. Int. Ed.* **2006**, *45*, 5786–5789.
- (17) Gopakumar, T. G.; Matino, F.; Naggert, H.; Bannwarth, A.; Tuczek, F.; Berndt, R. *Angew. Chem. Int. Ed.* **2012**, *51*, 6262–6266.

- (18) Miyamachi, T.; Gruber, M.; Davesne, V.; Bowen, M.; Boukari, S.; Joly, L.; Scheurer, F.; Rogez, G.; Yamada, T. K.; Ohresser, P.; Beaurepaire, E.; Wulfhekel, W. *Nat. Commun.* **2012**, *3*, 938.
- (19) Aravena, D.; Ruiz, E. *J. Am. Chem. Soc.* **2011**, *134*, 777–779.
- (20) Bocquet, A. E.; Mizokawa, T.; Saitoh, T.; Namatame, H.; Fujimori, A. *Phys. Rev. B* **1992**, *46*, 3771–3784.
- (21) Burger, K.; Furlani, C.; Mattoño, G. *J. Electron Spectrosc. Relat. Phenomena* **1980**, *21*, 249–256.
- (22) Pronschinske, A.; Chen, Y.; Lewis, G. F.; Shultz, D. a; Calzolari, A.; Nardelli, M. B.; Dougherty, D. B. *Nano Lett.* **2013**, *13*, 1429–1434.
- (23) Giannozzi, P.; Baroni, S.; Bonini, N.; Calandra, M.; Car, R.; Cavazzoni, C.; Ceresoli, D.; Chiarotti, G. L.; Cococcioni, M.; Dabo, I.; Dal Corso, A.; de Gironcoli, S.; Fabris, S.; Fratesi, G.; Gebauer, R.; Gerstmann, U.; Gougoussis, C.; Kokalj, A.; Lazzeri, M.; Martin-Samos, L.; Marzari, N.; Mauri, F.; Mazzarello, R.; Paolini, S.; Pasquarello, A.; Paulatto, L.; Sbraccia, C.; Scandolo, S.; Sclauzero, G.; Seitsonen, A. P.; Smogunov, A.; Umari, P.; Wentzcovitch, R. M. *J. Phys. Condens. Matter* **2009**, *21*, 395502.
- (24) Pronschinske, A.; Bruce, R. C.; Lewis, G.; Chen, Y.; Calzolari, A.; Buongiorno-Nardelli, M.; Shultz, D. A.; You, W.; Dougherty, D. B. *Chem. Commun.* **2013**, *49*, 10446–10452. – Reproduced by permission of the Royal Society of Chemistry.
- (25) Burger, K.; Ebel, H. *Inorganica Chim. Acta* **1981**, *53*, L105–L107.
- (26) Calzolari, A.; Chen, Y.; Lewis, F.; Dougherty, D. B.; Shultz, D.; Buongiorno-Nardelli, M. *J. Phys. Chem. B* **2012**, *116*, 13141–13148.
- (27) Raman, K. V.; Kamerbeek, A. M.; Mukherjee, A.; Atodiresei, N.; Sen, T. K.; Lazić, P.; Caciuc, V.; Michel, R.; Stalke, D.; Mandal, S. K.; Blügel, S.; Münzenberg, M.; Moodera, J. S. *Nature* **2013**, *493*, 509–513.
- (28) Herrmann, C.; Solomon, G. C.; Ratner, M. A. *J. Am. Chem. Soc.* **2010**, *132*, 3682–3684.
- (29) Constantinides, C. P.; Berezin, A. A.; Zissimou, G. A.; Manoli, M.; Leitun, G. M.; Bendikov, M.; Probert, M. R.; Rawson, J. M.; Koutentis, P. A. *J. Am. Chem. Soc.* **2014**, *136*, 11906–11909.
- (30) Jeon, I.-R.; Park, J. G.; Xiao, D. J.; Harris, T. D. *J. Am. Chem. Soc.* **2013**, *135*, 16845–16848.
- (31) Chung, S.; Jang, M.; Ji, S.-B.; Im, H.; Seong, N.; Ha, J.; Kwon, S.-K.; Kim, Y.-H.; Yang, H.; Hong, Y. *Adv. Mater.* **2013**, *25*, 4773–4777.

- (32) Kurta, R. P.; Grodd, L.; Mikayelyan, E.; Gorobtsov, O. Y.; Zaluzhnyy, I. A.; Fratoddi, I.; Venditti, I.; Russo, V.; Sprung, M.; Vartanyants, I. A.; Grigorian, S. *Phys. Chem. Chem. Phys.* **2015**, *17*, 7404–7410.
- (33) Wong, C. Y.; Cotts, B. L.; Wu, H.; Ginsberg, N. S. *Nat. Commun.* **2015**, *6*, 5946.
- (34) Love, J. C.; Estroff, L. A.; Kriebel, J. K.; Nuzzo, R. G.; Whitesides, G. M. *Chem. Rev.* **2005**, *105*, 1103–1169.
- (35) Steenackers, M.; Gigler, A. M.; Zhang, N.; Deubel, F.; Seifert, M.; Hess, L. H.; Lim, C. H. Y. X.; Loh, K. P.; Garrido, J. A.; Jordan, R.; Stutzmann, M.; Sharp, I. D. *J. Am. Chem. Soc.* **2011**, *133*, 10490–10498.
- (36) Onses, M. S.; Ramirez-Hernandez, A.; Hur, S.-M.; Sutanto, E.; Williamson, L.; Alleyne, A. G.; Nealey, P. F.; de Pablo, J. J.; Rogers, J. A. *ACS Nano* **2014**, *8*, 6606–6613.
- (37) Schmidt, R. D.; Shultz, D. A.; Martin, J. D.; Boyle, P. D. *J. Am. Chem. Soc.* **2010**, *132*, 6261–6273.
- (38) Tuccitto, N.; Ferri, V.; Cavazzini, M.; Quici, S.; Zhavnerko, G.; Licciardello, A.; Rampi, M. A. *Nat. Mater.* **2009**, *8*, 41–46.
- (39) Ho Choi, S.; Kim, B.; Frisbie, C. D. *Science* **2008**, *320*, 1482–1486.
- (40) Mas-Torrent, M.; Crivillers, N.; Rovira, C.; Veciana, J. *Chem. Rev.* **2012**, *112*, 2506–2527.
- (41) Park, J.; Pasupathy, A. N.; Goldsmith, J. I. *Nature* **2002**, *417*, 722–725.
- (42) Cumpson, P. J.; Seah, M. P. *Surf. Interface Anal.* **1997**, *25*, 430–446.
- (43) Lin, C.; Kagan, C. R. *J. Am. Chem. Soc.* **2003**, *125*, 336–337.

CHAPTER 3:

STUDYING PHENYLENEDITHIOL MONOLAYERS IN NANOTRANSFER PRINTED MOLECULAR JUNCTIONS

Robert C. Bruce, Samuel B. Anderson, Wei You

3.1 Background

3.1.1 Electrical Characterization of Molecular Junctions

With recent advances in molecular electronics (ME), scaling down electronic systems to the single molecule level for use in practical electronic devices is a realistic proposition. A wide set of interesting effects that have been and are expected to be observed offer the potential for single molecule transistors and unique functionality in electrical devices.¹⁻³ Processes also exist to orient these systems to access single molecules. Self-assembled monolayers (SAMs) have been realized for a number of molecules, allowing for facile arrangement of molecules and large numbers of devices to potentially be made across the same substrate.⁴ This opens up the possibility of creating a high density of functioning electrical devices, all potentially down to the single molecule scale, a proposition that would dramatically impact modern electronics.

The reason that studies of molecular electronic junctions are still ongoing is that while techniques exist for facile deposition of molecules, such as self-assembly, making electrical contact to these systems is difficult. Typical processing of inorganic electronics involves evaporation of metals and sometimes harsh chemical conditions for lithographic patterning. Materials like silicon and GaAs have proven fitting for these processes, but many of the organic

systems that can form facile molecular substrates are not thermally or chemically stable enough to withstand direct evaporation or standard lithographic processes.⁵ At best, a tradeoff exists between ease of molecule deposition and ease of reliability of top contact deposition. Short organic monolayers, such as alkanethiols, have been shown to form non-shortened electrical junctions only around 1% of the time with evaporated metal electrodes.⁶ Long molecular chains have been shown to be more reliable with direct metal evaporation, but these systems are limited, and most chains cannot reach a length or density to fulfill this. We can utilize spun-cast organic films to be able to withstand evaporated metals, but this gives up much of the proposition of single molecule devices, not to mention that charge transport through films would be more complex than transport through a single wire.⁷

Even with long molecular chains or films of organic materials, or even with the 1% of self-assembled monolayer devices that survive direct metal evaporation processes, metal penetration is still a stumbling block toward reliable junction fabrication. In the case of monolayers, inconsistent results appear to be made from the 1%, indicating even the non-shortened devices are unreliable.⁸ In the case of films of organic materials, metal penetration effects can arise, leading to questionable interfaces and inconsistent transport properties across devices. In one classic example, spun-cast films of tris(8-hydroxyquinolato)aluminum (Alq_3) had ferromagnetic electrodes evaporated directly on top with hopes of designing a spin valve through the organic based material. Spin valve properties were seen in preliminary studies, but it was later discovered through the lack of temperature dependence in the transport that the evaporated electrodes were directly tunneling between each other and not transporting electrons through the Alq_3 film as originally expected. Given the thickness of the film, direct tunneling should not have been possible, indicating that the evaporated metal had penetrated into the organic film and

led to erroneous results.^{9,10} Such effects exist throughout the fields of organic electronics and ME and highlight the need for care when designing electronic junctions.

A much more promising approach than restricting organic electronics and ME is to evaporation techniques is to adapt new ones. As discussed previously (see Section 1.5.1), many different processes specific to organic and ME have been established. Analytic techniques can make temporary contacts,^{11,12} but represent forming only temporary junctions, often times with dangerous chemicals and advanced equipment. Buffer layers, such as PEDOT:PSS, can be spun-cast and allow for direct metal evaporation in fabricating large area junctions,¹³ but they replace a chemically bound top contact with a physical contact and interfaces that could interrupt or convolute charge or spin transport. The ideal device architecture, both for device stability and for realizing unique electronic properties in single molecule junctions, would involve chemically bound metal contacts on both sides of the junction.

One of the most promising methods for transfer of a metal contact directly onto an organic layer is soft lithography.¹⁴ In this process, all patterning and deposition of metal contacts are done on dummy substrates, such as silicon oxide or polymers, that can withstand these processes. The patterned metal films are then transferred onto an organic film by a polymer or other type of transfer material. Multiple iterations exist, but the most typical utilize elastomeric properties in these polymers to make good contact across an organic monolayer or other transfer substrate. Through this process, the interface between organic and electrode is simplified, and the possibility for a direct metal contact that does not destroy or penetrate an organic monolayer can be realized.

Soft lithographic processes are represented in multiple processes and can transfer varieties of materials. Carbon nanotube (CNT) arrays have been developed to transfer metal

nanodots onto arbitrary substrates.¹⁵ Perfluoropolyether (PFPE) backing layers are often used to transfer PECVD grown graphene and MoS₂ monolayers from a metal foil onto arbitrary substrates.^{16,17} Organic molecules have been transferred through these processes as well, as shown through microcontact printing (μ CP).¹⁸ These processes can involve removal of all material from a polymer layer so it can be reused,¹⁹ or sacrificial polymer layers that are destroyed after transfer.²⁰ Moreover, these processes can be adapted for repeatability on a mass production scale.²¹ Overall, soft lithographic processes provide a method for patternable and reproducible electrode formation on organic films and monolayers, which in the case of this study is extremely useful for realizing molecular dependent effects.

3.1.2 Nanotransfer Printing

One specific iteration of soft lithography that has been utilized to print metal electrodes onto organic monolayers is nTP.²² Figure 3.1 outlines the basic procedure for the process. First, a liquid polymer is cross-linked on an elastomeric stamp on a patterned substrate. This step defines the eventual final transferred electrode size. The figure shows patterning on a PFPE mold, though in principle it could be patterned on a silicon substrate or any other patternable layer. Also, other polymers can be used for this process, such as poly(dimethylsiloxane) (PDMS).²³ Once the elastomeric stamp has been formed, metal can be evaporated directly onto the stamp. Due to the patterning, raised features on the stamp will provide the features to be transferred onto the organic layer. Finally, the metal contacts are brought in contact with the desired substrate – in this case an organic monolayer – and the stamp is peeled away, leaving the metal pad exposed on the organic layer.

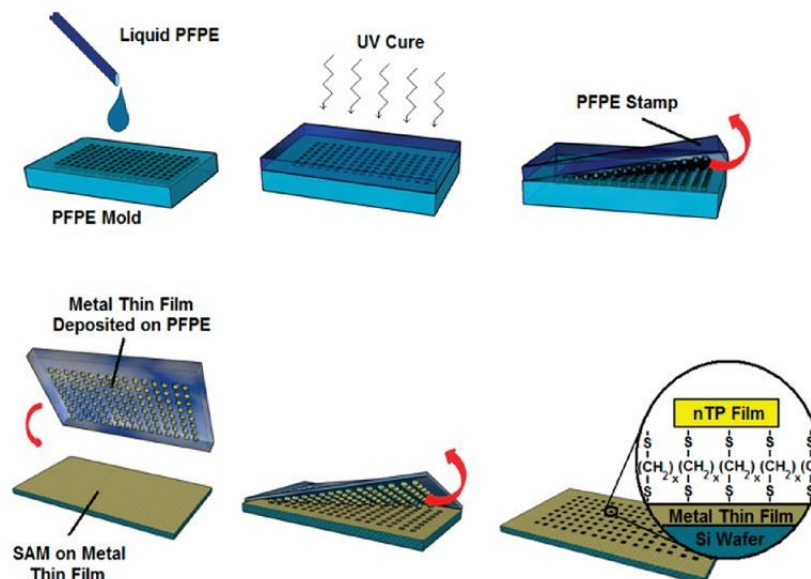


Figure 3.1 – Nanotransfer Printing

Procedure for nanotransfer printing. Liquid PFPE is cured on a mold into a patterned elastomeric stamp. The patterned stamp then has metal evaporated onto it, and the metal can be transferred onto a monolayer on another substrate. Removing the stamp exposes the metal features on the monolayer. Reprinted with permission from Ref. 22. Copyright 2009 American Chemical Society.

This process is non-destructive to the organic monolayer, providing just a physical force on the substrate, and can be used to transfer large numbers of electrodes of nanoscale size across a substrate. The advantages of the technique follow the advantages hoped to be seen in techniques for use with molecular electronic materials- large number of devices made on a small scale, reproducible across multiple substrates, and generates direct metal-molecule interfaces in a non-destructive manner.

3.1.3 Alkanethiols in Nanotransfer Printed Junctions

An ideal test bed for the nTP technique and its applicability with organic monolayers is alkanethiols. Thiols can chemically interact with a host of metal surfaces,²⁴ enabling formation of SAMs. The thiol to metal bond is relatively weak insofar as organic to metal bonds are concerned; however, this actually works to our advantage as this allows for ease of attachment

and detachment in solution to naturally form a well-packed and ordered monolayer on a gold film. While an ‘ideal’ monolayer, this picture of an ideal SAM across a substrate is somewhat erroneous, and even the most well-packed layer is known to possess grain boundaries and defects. Figure 3.2 shows an example of an octanethiol monolayer, highlighting that these defects can exist up to the order of a nanometer.²⁵ Longer monolayers are expected to pack better in the alkanethiols series. Practical organic systems should reasonably be expected to have nanoscale defects, so if nTP cannot work on these SAMs, they should not be expected to work on the single molecule scale under most conditions.

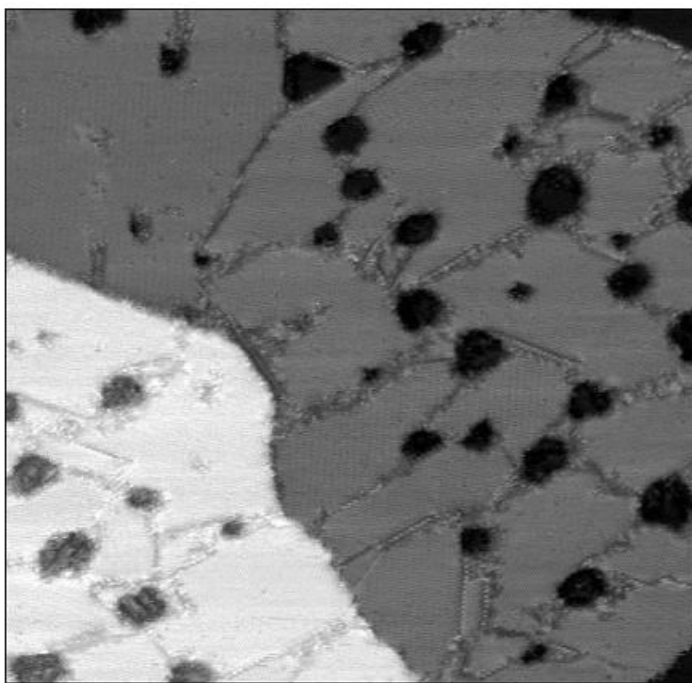


Figure 3.2 – Octanethiol Self-Assembled Monolayer on Gold

STM of octanethiol monolayer on atomically flat Au/mica, formed from soak in 0.1 mM solutions in ethanol for 2.5 hrs. Lighter colors across most of substrate represent plateaus of gold. Darker circles represent defects in the alkane film. Image is 970 Å × 945 Å. Reprinted with permission from Ref. 25. Copyright 2012 American Chemical Society.

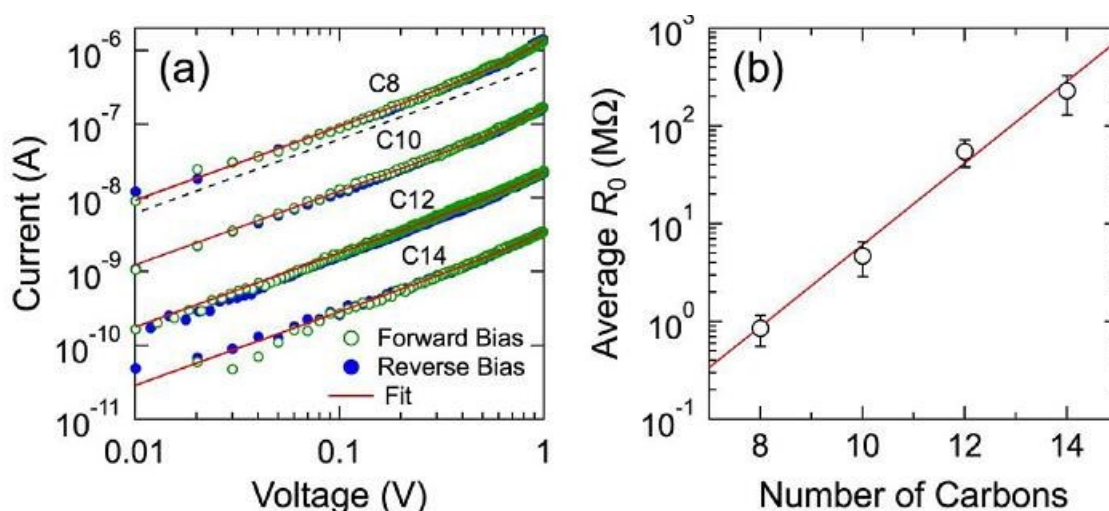


Figure 3.3 – Alkanedithiol Monolayers Measured in Nanotransfer Printed Junctions

Characteristic I-V behavior for 200 nm diameter nTP contacts versus molecular length in Au-alkanedithiol SAM-Au junctions. **A)** Representative curves for alkanes of various carbon chain length (C_x , where x = number of carbons). **B)** Average zero-bias resistance versus molecular length. Red line is a linear fit to the semilog plot. Reprinted with permission from Ref. 26. Copyright 2012 American Chemical Society.

Despite potential sources of failure, alkanethiols can be electrically characterized and yield molecular dependent results. Figure 3.3 shows results of electrically characterized 200 nm diameter nTP junctions. These molecules are expected to exhibit direct tunneling due to the insulating nature of the wires. Resistance in these devices would be expected to increase exponentially in this transport regime, as expressed by Equation (3-1):

$$R = R_0 \exp(-\beta * L) \quad (3-1)$$

Here, R is resistance; R_0 is the inherent resistance from the junction, characterization method, or other inherent property of the junction; L is length of the junction (in this case, the length of the molecule); and β is the tunneling decay parameter, which is supposed to be a property of the molecule but is functionally a property of the molecule in a particular junction. For tunneling systems, the resistance should increase as a function of molecular length, a trend seen when C_x -

dithiols are characterized in nTP junctions, where $x = 8, 10, 12, 14$. Using Equation (3-1), the β for the alkanedithiol system measured in nTP junctions can be extrapolated, yielding $\beta = 1.16 \pm 0.10 \text{ \AA}^{-1}$, which is similar to previously obtained values measured in different molecular junctions.²⁷

The biggest question that remains is whether or not the technique is adaptable to different molecular systems than the alkanes studied above, or, most relevantly, if there are any consequences to the adaptation. While the alkanedithiol system proves molecular dependent transport can be seen, proof needs to be seen that different systems with transport properties other than direct tunneling can also have their electrical properties exhibited in nTP devices.

3.1.4 Phenylenedithiol Self-Assembled Monolayers

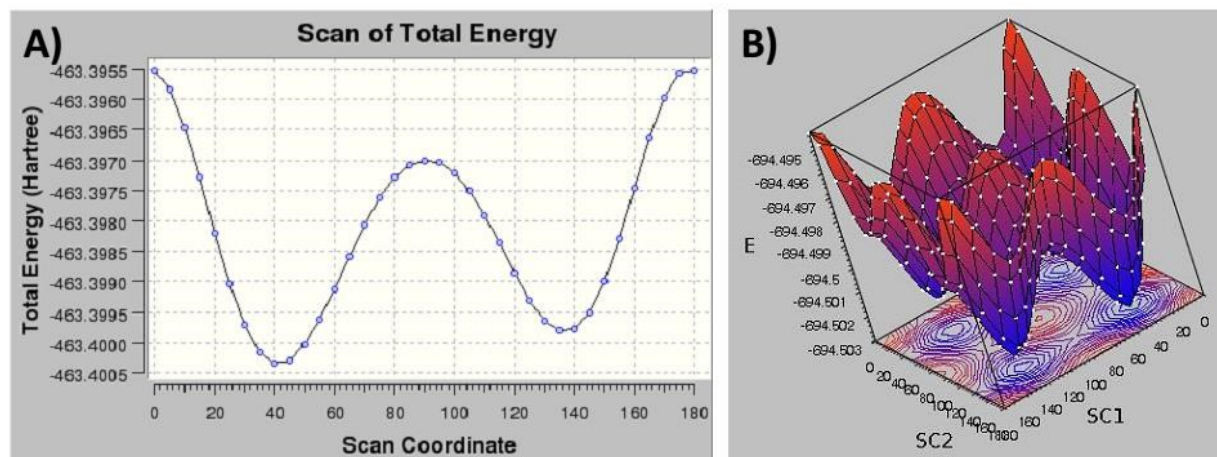


Figure 3.4 – Phenylenedithiol Calculated Rotation Energy

Density functional theory (DFT) calculated energies for rotation angle between phenyl rings in phenylenedithiols, for **A**) biphenylenedithiol (scan coordinate refers to angle between rings) and **B**) *p*-terphenylenedithiol (SC1 refers to rotation between phenyl rings 1 and 2, SC2 refers to rotation between phenyl rings 2 and 3). Images by Shubin Liu.

Phenylenethiols and phenylenedithiols represent a relatively basic ME system, made up of phenyl rings rotated approximately 40° relative to each other (Figure 3.4), presenting low conjugation between rings and ultimately presenting a resistive system in comparison to other

organic systems. Relevant to this study, phenylenedithiols represent a finite step away from the alkanedithiols already studied in nTP junctions and a step toward the organic conjugated systems that exhibit unique charge and spin properties. First, the physical properties of phenylenedithiols will affect their properties as monolayers. Reports have shown that these molecules can self-assemble under the right conditions, with both *p*-nitrophenols and benzenethiols showing order in STM monolayers.^{28,29} However, others reports suggest that the order can be too low to be measured by STM, suggesting that order and self-assembly depend on preparation conditions.³⁰

Second, phenylenedithiols offer the possibility to move out of the purely non-resonant tunneling regime that is exhibited by alkane chains. Molecular length is ultimately what controls the dominance of tunneling versus charge injection in systems where the latter is possible. As shown by Dell et al., this change can be brought about by extending the number of repeat units in aromatic systems.³¹ This point typically occurs around 2-4 nm, depending on the system being studied. Even in short chains, the nature of the transport will depend on molecular properties. The β value discussed earlier– the tunneling decay parameter – varies depending on the molecular system used. Alkane-based molecular chains exhibit measured β values around 1 \AA^{-1} , whereas phenyl-based chains show lower β , typically in the range of $0.3 - 0.6 \text{ \AA}^{-1}$, showing evidence of potential resonant transport pathways. A basic explanation for this is that the HOMO for phenylenethiols lie much closer to E_F of gold (or most metals) compared to alkanethiols, lowering the barrier height that holes must transport through and increasing the probability for over-barrier transport, a transport mechanism which will have a lower length dependence on resistance.

It is important to see whether or not these effects are present, or to see what effects the nTP fabrication process might have on the properties of this basic molecular electronic system.

As will be expressed by the work in this chapter, the nTP fabrication process and architecture do bear a consequence on the molecular properties seen through the phenylenedithiols. Ultimately, while what was expected to be a basic aromatic system was studied in nTP junctions, the technique does have consequences on measured properties, which will lead to a discussion on effects of ME architectures on SAM-based systems in general.

3.1.5 Overview

In this chapter, we will present results from studying the ‘basic’ aromatic system of phenylenedithiols as SAMs on gold in nTP junctions. X-ray photoelectron spectroscopy (XPS) characterization will highlight the quality of phenylenedithiol monolayers and, in the case of deprotecting ethyltrimethylsilane (ETMS) protector groups on longer and less soluble phenylenedithiols, highlight that multiple factors can affect monolayer and electrical properties. ME junctions prepared with nTP were electrically characterized and compared to electrically identical junctions characterized by conductive atomic force microscopy (cAFM) tips directly on the monolayer. The different results from what were expected to be identical junctions prompt a discussion into the effects of nTP technique, which will lead to a commentary on the effects of bulk (greater than single molecule) junctions on observed molecular properties, and the validity of these junctions for future studies.

3.2 Experimental

3.2.1 Materials

1,4-benzenedithiol (mphDSH); 4,4'-biphenyldithiol (bphDSH); and *p*-terphenyl-4,4''-dithiol (tphDSH) were purchased from *Alfa Aesar*, *Tokyo Chemical Industry Co.*, and *Sigma Aldrich*, respectively, and used as received without further purification for monolayer growth. Ethyltrimethylsilane (ETMS) protected terphenyldithiol (tphDS-ETMS) and quaterphenyldithiol (qphDS-ETMS) molecules were synthesized (see Section 3.5). Unprotected phenylenedithiol solutions were prepared using 1 mM molecule in THF. ETMS-protected phenylenedithiol solutions were prepared using 1 mM molecule in THF and a 4:1 molar ratio of tetrabutylammonium fluoride (TBAF) solution in THF (*Sigma-Aldrich*) to phenylenedithiol as a deprotecting agent.

3.2.2 Gold Substrate and Self-Assembled Monolayer Preparation

Silicon wafers were cut into approx. 1 cm × 1 cm size for each device, then cleaned in RCA solution (2:1:1 water: ammonium hydroxide: hydrogen peroxide) for 15 minutes. Upon removal from RCA, the Si wafers were rinsed with water and ethanol, dried with N₂ gas, and cleaned in UV/ozone for 20 minutes. After cleaning, 5 nm Ti/ 40 nm Au were thermally evaporated on the wafers, the Ti layer at a rate of 1 Å/s, the Au layer starting at 1 Å/s for the first 5 nm then increased to 10 Å/s for the duration of the deposition. To prepare monolayers for all chemicals, freshly evaporated Au/Ti on Si substrates were immersed in the prepared phenylenedithiol THF solutions inside a N₂ glove box (O₂ < 5.0 ppm). After 24 hrs, substrates were removed from solution, sonicated in THF for 60 s to remove physisorbed molecules, then rinsed in ethanol and dried under N₂ gas.

3.2.3 Nanotransfer Printing

Perfluoropolyether (PFPE) stamps were prepared by ultraviolet (UV) curing liquid PFPE on PFPE-based molds with arrays of raised features. For curing, the UV cure chamber (ELC-500, *Electro-Lite Corporation*, 365 nm exposure) was purged for 15 mins with N₂, then UV light was illuminated for 30 s. Stamps were then removed from the PFPE-based molds and loaded into a thermal evaporator where 20 nm Au were deposited at 1 Å/s for the first 5 nm, then 10 Å/s for the duration. PFPE stamps with gold were then placed gold side down onto a monolayer on Au, tapped lightly to encourage contact with the unbound thiol of the dithiol monolayer, and placed in a vacuum for 30 min to remove air between stamp and monolayer. After removal from vacuum, the PFPE stamps are peeled off, exposing the patterned printed gold contacts on the monolayer device.

3.2.4 Atomic Force Microscopy

Nanotransfer printed electrodes were characterized and analyzed *via* atomic force microscopy (AFM), using an Asylum Atomic Force Microscope (Asylum MFP-3D, *Asylum Research*). Tapping-mode images were taken using silicon cantilevers (*BudgetSensors*, Tap300Al) with resonance frequencies of approximately 300 kHz and a force constant of approximately 40 N/m. For both “direct cAFM” and “nTP characterization”, conductive measurements of individual features were taken using the same AFM system. Cantilevers for these measurements were purchased from *Olympus* (AC240TS, force constant ~2 N/m), then modified by sputtering chromium and gold using the recipe: 2.5 nm Cr, 5.0 nm Au, 2.5 nm Cr, 10.0 nm Au, 2.5 nm Cr, 35.0 nm Au, 2.5 nm Cr, 50.0 nm Au. The resulting conductive tips had large tip radii (~30 nm) in order to sustain the currents measured in our junctions. Conductive measurements were made by applying 20 nN force to either the monolayer (in the case of “direct cAFM”) or individual nTP features (in the case of “nTP characterization”), then sweeping a bias

on the Si substrate/Au film. Each feature was measured 4 times to test for reproducibility of measurements.

3.2.5 X-Ray Photoelectron Spectroscopy

Monolayer quality was evaluated using x-ray photoelectron spectroscopy (XPS) characterization using a monochromatic Al K α source (source and detector from *Kratos*) with power output of 150 W. All signals were optimized to maximize the Au 4f_{7/2} signal. Au 4f spectra were obtained by averaging 2 sweeps at 500 ms per point, and S 2p spectra were obtained by averaging 6 sweeps at 800 ms per point, both with resolution of 50 mV. Spectra were analyzed by subtracting a Shirley background and then assigning a combination of Lorentzian and Gaussian (Voigt) functions. Spin-orbit separation between S 2p_{3/2} and S 2p_{1/2} signals was set to 1.18 eV, and separation between Au 4f_{7/2} and Au 4f_{5/2} signals was set to 3.67 eV.

3.3 Results and Discussion

3.3.1 ETMS Deprotection Effects on Monolayers

In order to establish the validity of our molecular junctions, we first examined the quality of the monolayers used to create these junctions. ETMS protected monolayers were examined to judge the deprotection conditions necessary to prepare good quality monolayers. It was originally assumed that deprotection would yield free thiol (-SH) bonds that would bind and self-assemble in a manner analogous to monolayers without ETMS groups. However, a dependence on monolayer quality was found as a function of TBAF used. This monolayer quality was examined in two ways in XPS – by looking at the S 2p core shell spectra, and by estimating monolayer height using the Au 4f intensity.

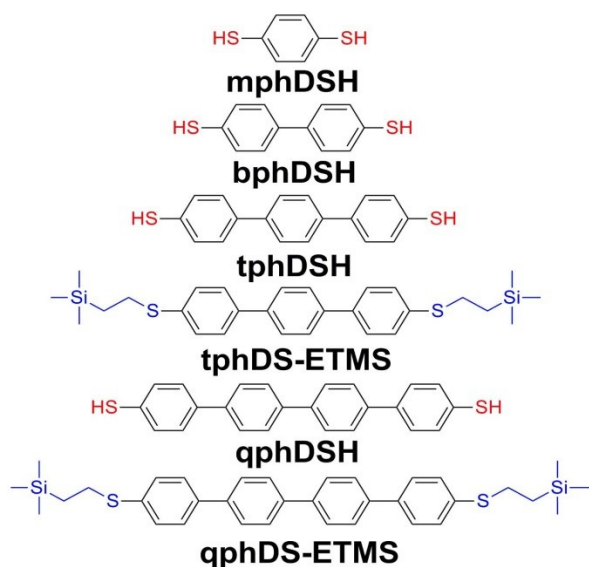


Figure 3.5 – Oligo-*para*-phenylenedithiols

Structures of the oligo-*para*-phenylenedithiol molecules ($n = 1-4$), both ETMS protected (DS-ETMS) and unprotected (DSH).

Figure 3.6 shows the S 2p core shell spectra for qphDSH monolayers, deprotected from qphDS-ETMS with corresponding molar ratios of TBAF. In the case of these oligo-*para*-phenylenedithiols, we expect two S 2p signals: a doublet corresponding to the thiol bound to gold, and a doublet corresponding to the unbound thiol. Previous studies of dithiol based monolayers have established the bound thiol on gold to have $\text{S } 2p_{3/2} = 161.9 \text{ eV}$, and the unbound thiol to have $\text{S } 2p_{3/2} = 163.4 \text{ eV}$.³² Both of these peaks dominate the S 2p spectra, but appear in different ratios for different TBAF conditions. Low TBAF conditions (1:2 qphDS-ETMS: TBAF) yield a 1:1 bound/unbound thiol peak ratio from raw data – though as will be expressed in a moment, this is actually a negative outcome due to bound thiol attenuation; we expect more unbound thiol signal than bound, so this actually represents a case either where the monolayer is low height off of the surface, hence low attenuation, and/or where more bound thiol is present. Either way, this indicates low TBAF monolayers are poor quality.

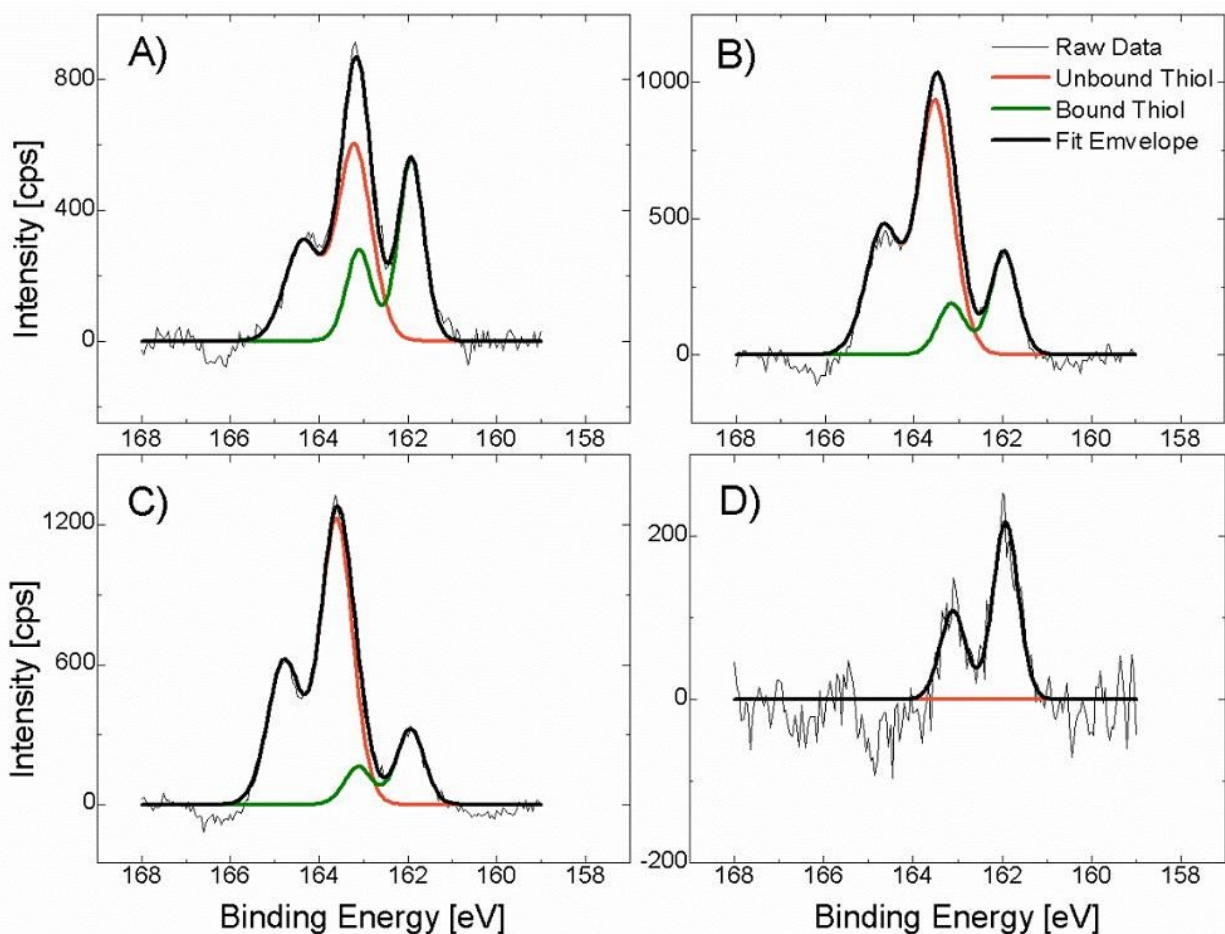


Figure 3.6 – qphDSH Monolayer Quality Based on TBAF Conditions

XPS S 2p spectra for qphDSH monolayers, prepared under the molar ratios qphDS-ETMS:TBAF **A)** 1:2, **B)** 1:4, **C)** 1:8, **D)** Excess TBAF. Thin black lines are raw data, thick black lines are the fit envelope, green lines represent bound thiol components ($S\ 2p_{3/2} \sim 161.9\text{ eV}$), orange lines represent unbound thiol components ($S\ 2p_{3/2} \sim 163.4\text{ eV}$). For **D**, the fit envelope and bound thiol peaks overlap, indicating only bound thiol was present. The best monolayer quality was yielded from the 1:4 qphDS-ETMS:TBAF molar ratio.

As more TBAF is added, the ratio of unbound to bound thiol increases with increasing TBAF – indicating a more standing up monolayer – but reaches a maximum, beyond which bound thiol begins to dominate again. When excess TBAF is added, only bound thiol is present, indicating the monolayer is lying almost exclusively flat on the gold surface and that this condition yields extremely poor SAM quality.

Extracted monolayer height corroborates the assessment from studying the S 2p signal. Monolayer height is estimated through the Au 4f_{7/2} peak intensity. Equation (3-2) is utilized to make this estimation:

$$Au_d = Au_{d=0} * \exp[d/(\cos[\theta] * \lambda_{AL})] \quad (3-2)$$

where Au_d represents the Au 4f_{7/2} peak intensity measured through a certain monolayer depth (d), θ is the angle between XPS x-ray source and detector (in this case, $\theta = 0^\circ$), and λ_{AL} is the attenuation length of our gold signal through the monolayer. We use 32.8 Å as the attenuation length in this study as calculated by Cumpson and Seah for attenuation of an electron traveling through a carbon based layer with kinetic energy corresponding to the Au 4f orbital.³³ A monolayer of hexadecanethiol with a measured height $d = 16$ Å is used as a reference comparison to measure the heights of the phenylenedithiol monolayers.

Table 3-1 – XPS Measured Monolayer Height for qphDSH Monolayers

| Molecule | Monolayer Length | | Tilt Angle |
|----------------------|---------------------|--------------------------|------------|
| | Measured Height (Å) | DFT Molecular Length (Å) | |
| qphDSH (TBAF 1:2) | 11.5 | 21.8 | 58.1 |
| qphDSH (TBAF 1:4) | 25.5 | 21.8 | [0.0] |
| qphDSH (TBAF 1:8) | 12.1 | 21.8 | 56.3 |
| qphDSH (TBAF Excess) | 5.7 | 21.8 | 74.7 |

Table 3-1 shows the monolayer height as a function of TBAF added estimated through this Au 4f intensity method. Monolayer height reaches a maximum for the TBAF 1:4 molar ratio condition, then drops off to a minimum with excess TBAF. This corroborates the assessment

made with the S 2p XPS spectra – that the best monolayer condition is obtained through an intermediate amount of TBAF. Our findings are similar to those of Valkenier *et. al.*³⁴ who show similarly that deprotection condition plays a large role in subsequent monolayer quality.

Based on this finding, a basic model to explain the results is given in Figure 3.7. In the case of dithiols, some molecules with the capability to have both ends bind to the surface (have both thiols deprotected) will do so. There is no steric hindrance inherent to the molecule to prevent this, and the chemical bond represents a favourable state given the fact that the thiol-gold bond naturally forms. The simplest way to prevent the double binding to gold is to provide steric hindrance to do so. Since no sterics come from intramolecular effects, the steric effect is supplied from other molecules. As more molecules bind to the surface, other molecules will be unable to lie flat on the gold surface, forcing them to maintain a standing and packed position alongside other standing molecules.

What we propose is the effect of TBAF concentration is that, under ideal conditions, a large number of molecules will be singly deprotected, i.e. have one ETMS group deprotected, and singly bind to the gold substrate in a manner that will encourage a more vertical monolayer as opposed to molecules that doubly bind their end groups to gold and lie flat. As more molecules attach in some vertical position, they will act as a seed that prevents other molecules from lying flat, encouraging a self-assembly in the vertical standing position. In this ideal condition, this will lead to a well-packed monolayer that can have their second ETMS group removed once the vertical position has been assumed and binding flat to the gold surface is sterically hindered. The closest to this ideal condition, based on experimental evidence presented above, appears to be the qphD-SETMS: TBAF 1:4 molar ratio (Figure 3.7b).

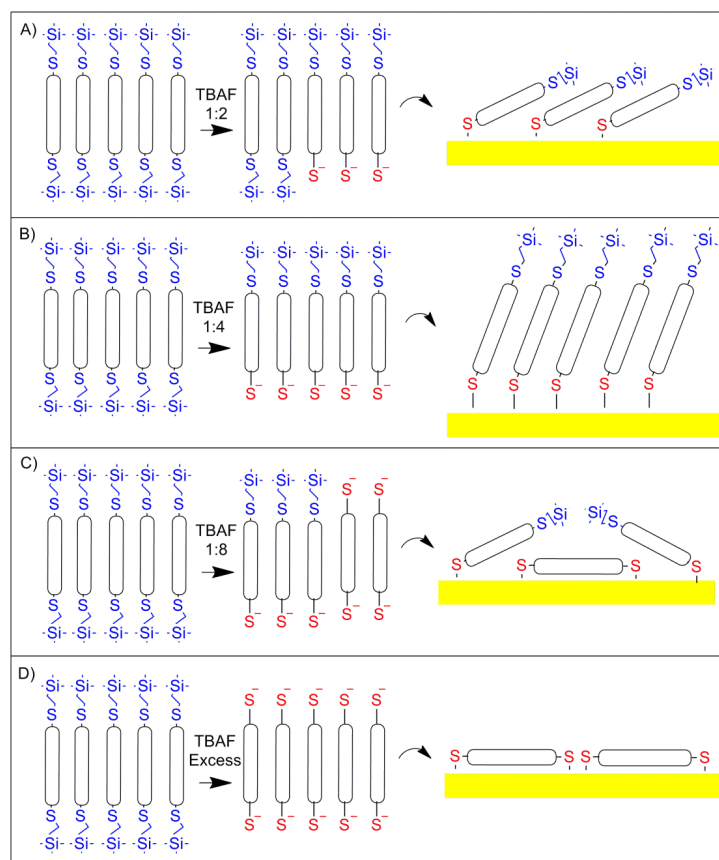


Figure 3.7 – Proposed Kinetics of ETMS Protection and Effects of Deprotectant Concentration

Visualizations are matched to conditions used in the experimental trials and represent conditions where **A)** too little deprotectant is used and not enough molecules are deprotected, **B)** an ‘ideal’ amount of deprotectant is added to deprotect enough molecules that can interact with each other and pack well on the surface, **C)** an excess of deprotectant starts to form doubly deprotected groups that inhibit packing on the surface, and **D)** and extreme excess of deprotectant leads to virtually all species lying down on the surface, giving very poor monolayer quality.

Below this condition, we expect only low coverage of molecules on the surface due to few numbers of molecules being deprotected and assuming a lower angle relative to the surface (Figure 3.7a). While few molecules should be doubly bound in this state, the seed of single bound molecules is sparse, and molecules binding to the surface will lie flatter to the gold, preventing access of other molecules to the gold around and leading to a low density, low angle monolayer. On the other hand, above the ideal condition, more molecules will begin to be doubly deprotected before the seed monolayer has taken full effect, yielding more flat molecules that

will inhibit ideal packing (Figure 3.7c). Proceeding further beyond the idea condition in this manner, i.e. in the excess deprotectant condition, nearly all molecules will be doubly deprotected before attaching to a surface (Figure 3.7d), leading to a flat surface with nearly no vertical attachment.

3.3.2 Phenylenedithiol Monolayer Characterization

With knowledge of deprotection conditions that lead to high quality monolayers (D-SETMS:TBAF 1:4), prepared monolayers of mono-*para*-phenylenedithiol, (mphDSH), bis-*para*-phenylenedithiol (bphDSH), ter-*para*-phenylenedithiol (tphDSH), and ETMS-protected quater-*para*-phenylenedithiol (qphDS-ETMS) (Figure 3.5) were prepared and characterized *via* XPS. As with the analysis above, the monolayer quality was measured by comparing bound and unbound thiol signals in the S 2p core spectra, and by estimating monolayer height by analyzing 4f_{7/2} signals from the gold thin films housing the monolayer and analyzing the attenuation of the gold signal through the carbon-based monolayer.

Table 3-2 – Estimated Heights of Oligo-*para*-phenylenedithiol Monolayers by XPS

| Molecule | Monolayer Length | | Tilt Angle |
|--------------------------------|---------------------|--------------------------|------------|
| | Measured Length (Å) | DFT Molecular Length (Å) | |
| mphDSH | 5.7 | 8.9 | 50.2° |
| bphDSH | 10.0 | 13.3 | 41.2° |
| tphDSH | 17.7 | 17.6 | [0.0°] |
| qphDSH (TBAF 1:4) ^a | 25.5 | 21.8 | [0.0°] |

^a The qphDSH based SAM was prepared by deprotecting the qphDS-ETMS molecule with a 4× molar excess of TBAF.

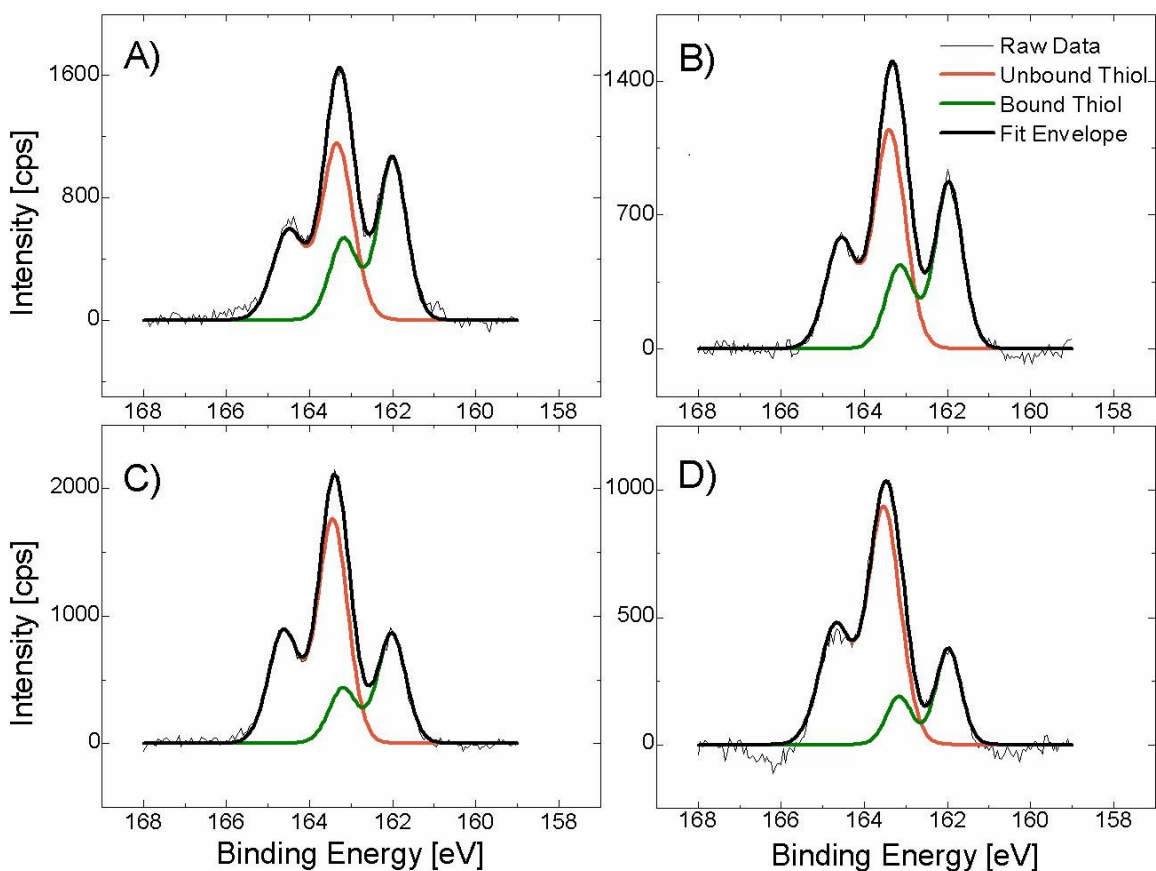


Figure 3.8 – XPS Spectra for Phenylenedithiol Monolayers

XPS S 2p spectra for **A)** mphDSH, **B)** bphDSH, **C)** tphDSH, **D)** qphDSH, prepared from qphDS-ETMS:TBAF 1:4 condition. Thin black lines are raw data, thick black lines are the fit envelope, green lines represent bound thiol components ($S\ 2p_{3/2} \sim 161.9\text{ eV}$), purple lines represent unbound thiol components ($S\ 2p_{3/2} \sim 163.4\text{ eV}$).

Table 3-2 expresses that, as expected, the measured monolayer heights increase with increasing number of phenylene rings, and the monolayer tilt angle relative to the normal decreases with increasing phenylene rings, both of which are in good agreement with previous studies.³⁵ Also, as seen in Figure 3.8, our S 2p spectra for the various phenylenedithiol monolayers match the expected signals for bound and unbound thiols. It is again worth noting that the ratios of the bound thiol to unbound thiol signals are not 1:1 despite the fact that a well-ordered monolayer should have one bound thiol for every unbound thiol. This occurs because,

similar to the case when we considered the Au 4f signals, the bound thiol signal is exponentially attenuated as it travels through the monolayer while the signal for the unbound thiol at the top of the monolayer is not. Thus, the ratio of the signals of bound thiol to unbound thiol would favor the latter with increasing molecular length, as we observed in our spectra.

Table 3-3 highlights the numerical ratio of these two signals as determined experimentally and compares it to an estimate of the expected ratio based on Equation (3-2) and the measured monolayer height. Such a comparison shows that the measured ratio drops below the expected ratio for longer monolayers. However, we note that the exponential decay equation assumes that an ejected electron travels through a layer of carbon, whereas in our monolayers, the carbon layers have grain boundaries and defects inherent in SAMs that will keep it from behaving as a full sheet of carbon.³⁶ Thus, this slight variance in observed and expected ratios is not unexpected. Nevertheless, we still obtain decent agreement between the two values.

Table 3-3 – XPS S 2p Fit Peak Parameters for Oligo-*para*-phenylenedithiol Monolayers

| Molecule | S 2p Spectra | | | Peak Ratio | | | |
|-----------------------|--------------|-----------|--------|-------------|---------------|----------------------|----------------|
| | Peaks (eV) | FWHM (eV) | Area % | Bound Thiol | Unbound Thiol | Ratio: Bound/Unbound | Expected Ratio |
| mphDSH | 162.0 | 0.790 | 30.2 | 45.3% | 54.7% | 0.828 | 0.774 |
| | 163.2 | 0.790 | 15.1 | | | | |
| | 163.3 | 0.878 | 36.4 | | | | |
| | 164.5 | 0.878 | 18.2 | | | | |
| bphDSH | 162.0 | 0.771 | 27.3 | 40.9% | 59.1% | 0.692 | 0.696 |
| | 163.2 | 0.771 | 13.6 | | | | |
| | 163.4 | 0.851 | 39.4 | | | | |
| | 164.6 | 0.851 | 19.7 | | | | |
| tphDSH | 162.0 | 0.791 | 21.1 | 31.6% | 68.4% | 0.462 | 0.569 |
| | 163.2 | 0.791 | 10.5 | | | | |
| | 163.4 | 0.841 | 45.6 | | | | |
| | 164.6 | 0.841 | 22.8 | | | | |
| qphDSH (TBAF 1:4)* | 162.0 | 0.699 | 16.1 | 24.2% | 75.8% | 0.319 | 0.443 |
| | 163.2 | 0.699 | 8.1 | | | | |
| | 163.5 | 0.901 | 50.5 | | | | |
| | 164.7 | 0.901 | 25.3 | | | | |

* The qphDSH based SAM was prepared by deprotecting the qphDS-ETMS molecule with a 4× molar excess of TBAF.

3.3.3 nTP Characterization of Phenylenedithiol Monolayers

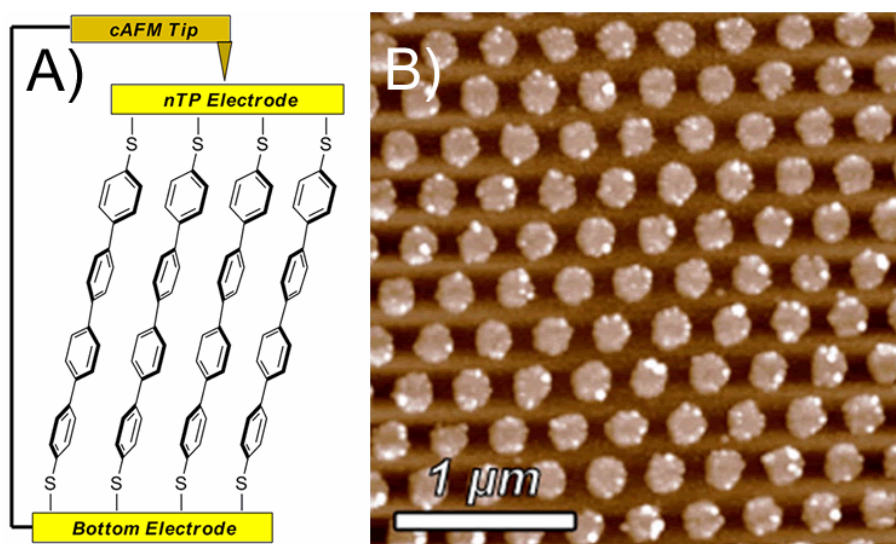


Figure 3.9 – Nanotransfer Printed Junctions with Phenylenedithiols

A) Diagram of “nTP characterization”, accomplished by bringing a cAFM tip in contact with an nTP printed electrode and applying a bias. **B)** Representative 200 nm diameter gold contacts, printed *via* nTP onto a tphDSH monolayer.

With monolayer quality validated, we can move to electrical measurements of these monolayers. In this study, we used two methods to fabricate and analyze electrical junctions. In the first, which will be referred to as “direct cAFM”, a silicon cantilever coated with alternating layers of chromium and gold to be made conductive is brought in direct contact with the monolayer. A small force (~ 20 nN) is applied from the tip onto the monolayer to encourage contact to a small number of molecules (expected to be on order of 10-100), and then an electrical measurement is made. The second method, which will be referred to as “nTP characterization” (Figure 3.9), involves using a patterned perfluoropolyether (PFPE) stamp to transfer 20 nm of evaporated gold onto a phenylenedithiol monolayer in an array of 200 nm diameter features. Once the top gold electrode has been transferred, the same cAFM tip as described above is placed on top of the nTP transferred electrode, a small force (~ 20 nN) is

applied to generate good contact, and an electrical measurement is made. Note that while both techniques utilize cAFM, the direct cAFM technique brings the conductive tip directly in contact with the monolayer and only forms a temporary junction, whereas the nTP characterization involves a processing step to attach a permanent top electrode, and the metal-molecule-metal junction with its chemically attached electrodes is measured. Also, nTP characterization creates and measures junctions with a much larger number of molecules (at least one order of magnitude larger) than direct cAFM.

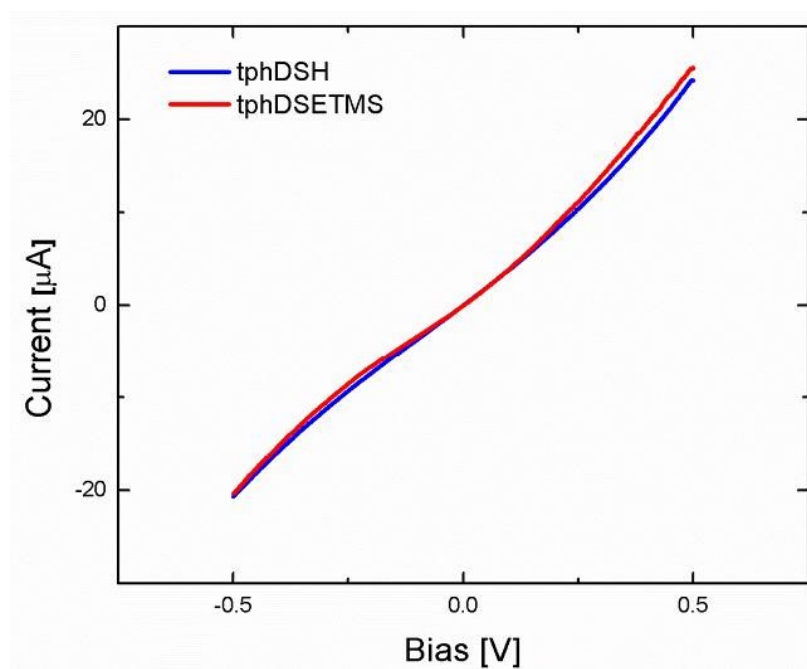


Figure 3.10 – Deprotected DS-ETMS Electrical Properties

Comparison of electrical measurements from nTP characterized devices prepared with tphDSH and ETMS-protected tphDS-ETMS. The latter was deprotected by TBAF under the condition tphDS-ETMS:TBAF 1:4 mole ratio. Each curve represents the average of measurements made on over 100 devices.

First, we need to validate that deprotection of D-SETMS molecules, which is necessary for the qphDSH molecule in this study due to its insolubility in its native dithiol form, does not influence the measured electrical properties. To do this, we also synthesized tphD-SETMS and

compared deprotected forms of this molecule to non-protected tphDSH in nTP junctions. Figure 3.10 shows average electrical outputs for over 100 devices of each monolayer (tphD-SETMS deprotected in the ideal 1:4 D-SETMS:TBAF ratio as established above). The electrical output for these monolayers is nearly identical, establishing the deprotection mechanism does not influence the electrical properties of monolayers prepared from ETMS protected species.

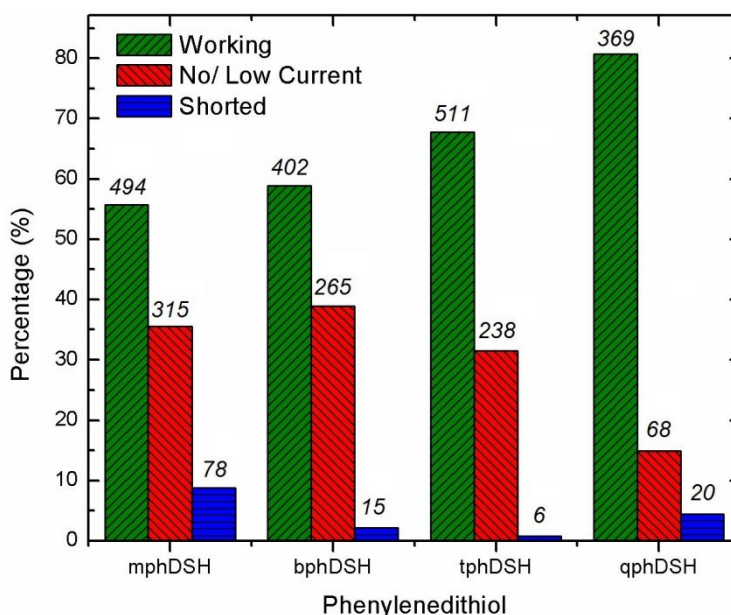


Figure 3.11 – Phenylenedithiol nTP Characterization

Percentage of working, low/no current, and shorted devices for phenylenedithiol devices prepared by nTP characterization. Bars represent percentages, and numbers above bars represent actual number of tested devices in the category.

Figure 3.11 shows the percentage of working devices prepared by nTP characterizations for each phenylenedithiol molecule. More than 50 percent of devices for each molecule gave high quality measurements, with the longest molecule (qphDSH) giving upwards of 80 percent working devices. Using our nTP characterization method, the largest hindrance for non-working devices was low current devices (where currents were several orders of magnitude below the working devices). Several factors could be attributed to this. First, thermal drift of tip location is

inherent in AFM, and unlike the direct cAFM measurements where monolayer exists in all locations and device function was subsequently greater than 75% for all monolayers, there is a possibility of missing a top contact in nTP characterization and instead probing the monolayer. Because each nTP electrode is in contact with many more molecules than the tip alone would be, missing an nTP electrode and instead probing the monolayer would yield a much lower current. Also, over time our gold-coated cAFM tips lost conductivity, and although the tip would be changed when a large number of devices yielded no current, it is difficult to identify if any given poor measurement was inherent to the device or the tip used at the time. Finally, we note the trend where longer molecules appear to give a larger number of working devices. This may be due to the fact that longer SAM molecules tend to stand up better and have better packing, and though Scotch tape tests and sonication have shown that the nTP transferred contacts are chemically bound to all phenylenedithiol molecules, better monolayer quality could enable more consistent transfer and contact of a gold electrode on the monolayer.

Direct cAFM measurements were not as dependent on molecule type as nTP characterization. All monolayers yielded greater than 75% working devices with less than 5% shorts and the remaining devices yielding low currents. Low currents were likely a result of poor contact from the cAFM tip to the monolayers.

Results for electrical characterization of both methods are seen in Figure 3.12. Charge transport relationships are compared against Equation (3-1) to evaluate β for the phenylenedithiols in the different junctions. We use β quantity to assess the differences in measured charge transport properties between the two systems. After measuring a large number of junctions for each molecule across multiple substrates, the measured β for the direct cAFM characterization of the phenylenedithiols (Figure 3.12c) was determined to be $\beta_{\text{cAFM}} = 0.407 \pm$

0.110 Å⁻¹ (Figure 3.12d). This value matches previously reported values for direct cAFM of phenylenethiol derivatives, indicating good behavior for the direct cAFM technique.^{37,38}

However, nTP characterization of identical monolayers (Figure 3.12a) leads to a distinct drop in β , yielding $\beta_{\text{nTP}} = 0.087 \pm 0.006$ Å⁻¹ (Figure 3.12b).

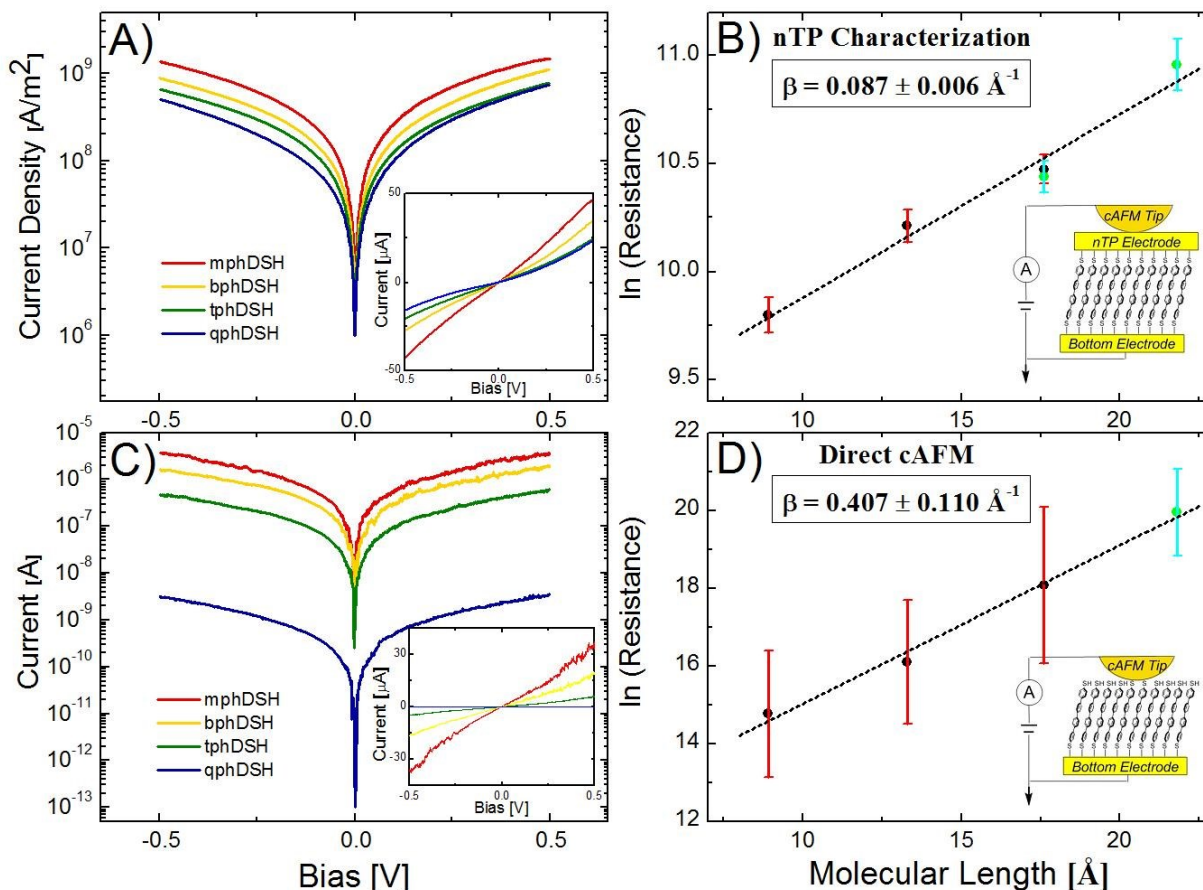


Figure 3.12 – Electrical Measurements for Oligo-*para*-phenylenedithiol Devices

A) Main image: average current densities for nTP characterization working devices. Inset: Average I-V data for same devices. **B)** Determining beta value for nTP characterization devices. Error bars represent one standard deviation on working devices. Black data points with red error bars represent devices prepared from unprotected phenylenedithiols, green data points with blue error bars represent devices prepared from ETMS-protected phenylenedithiols. **C)** Main image: average current densities for direct cAFM measurements. Inset: Average I-V data for same devices. **D)** Determining beta value for direct cAFM measurements. Error bars represent one standard deviation on working devices. Black points/ red bars and green points/ blue bars represent same as B.

3.3.4 Influence of Device Architecture on Measured ME Properties

Many factors can influence measured transport properties in ME devices, and using different fabrication or measurement techniques on similar systems has been shown to yield different β values.^{35,37} However to our knowledge, this is the first case of identical monolayers being measured in parallel with different techniques and yielding different transport properties. Equally striking is how low β is when measured via nTP characterization. $\beta < 0.1 \text{ \AA}^{-1}$ is often assigned to charge hopping and is seen in systems with high conjugation.³⁹ This property is not expected to be seen due to the native rotation of the phenylenedithiol phenyl rings, which one might expect to inhibit strong transport between phenyl units or intermolecularly. It should be stressed here that these measured values are reproducible across a large number of junctions and consistent across multiple substrates, indicating that our fabrication techniques are robust. Also, the high quality of our monolayers has been verified using XPS. In conjunction with the similarity of our direct cAFM measurements to literature studies, these factors lead to the conclusion that nTP characterization alters our monolayers and leads to a significantly lower measured β value.

We assign this drop in β during nTP characterization as an effect of the nTP fabrication process, specifically as an effect of the force induced on the sample during the nTP top contact attachment. To attach the 200 nm diameter electrode via nTP, we found that when the patterned gold on PFPE is brought in contact to the monolayer, a light tapping (measured to be approx. 0.01 - 0.03 N) with the flat side of a pair of tweezers was necessary to generate large area transfer onto the monolayer. The tapping created initial points of contact between the stamp and the monolayer, and placing the stamp/ substrate under vacuum after this encouraged growth of these contact points to form large areas of transfer. Without this tapping, we observed either no transfer or small amounts of transfer of significantly cracked and deformed features, even after

being placed under vacuum. While the tapping force is dispersed across the flat surface of the tweezers (approx. 0.6 cm x 0.6 cm), the monolayer on the substrate surface will still be subjected to a significantly higher force than administered during measurement techniques. More importantly, this force is administered before any electrical analysis is done, so while a controlled force of 20 nN is applied during electrical analysis, the system has already been subjected to much higher forces that can influence the state of the monolayer being measured. The net result is that while we have shown our monolayer is well behaved prior to adding the top electric contact *via* nTP, the nTP fabrication technique may influence the monolayer before the characterization.

Other studies have observed similar impacts of junction preparation on measured β value. Kronemeijer *et al.* report $\beta = 0.26 \text{ \AA}^{-1}$ for phenylenedithiol junctions prepared using PEDOT:PSS as an electrical contact to the monolayer,³⁵ suggesting that their large area junctions may have enabled torsion in the phenylenedithiol rings, thereby generating stronger π - π interactions that can either lower the HOMO-LUMO gap or lead to cooperative charge transport pathways, both of which can lower the measured β . Given our even greater drop in β from nTP characterization, our results appear to corroborate the idea of altered molecular orientation. While unmeasured to our knowledge, one can assume that the physical force on the monolayer induced by spin coating PEDOT:PSS as done by Kronemeijer *et al.* would be smaller than the tapping force applied during nTP top contact fabrication. This means that the force from our nTP process would provide a greater avenue for monolayer alteration, either in the form of monolayer reorganization *via* rotation, bending, or the like, or in the appearance of π - π interactions. As the changes in molecular orientation become more prevalent, their effects would be greater as well.

In this regard, it is no surprise that our measured β in nTP junctions is lower than any

previously reported for phenylenedithiol junctions because our nTP fabrication technique may be the most physically forceful and thereby most conducive to these effects occurring. The exact nature of the change in charge transport properties reflected by the change in observed β value is still under investigation, but it is apparent from this study together with other related studies that the fabrication technique is highly capable of influencing monolayer properties and thereby the monolayer charge transport properties. It is interesting to note that a large drop in β was not seen in our previous study of alkanedithiols studies using nTP characterization.²⁶ We can explain this in two ways. First, as stated previously, alkane monolayers are very well-ordered and well behaved, which is why they are used as model monolayers for virtually every ME technique. Such a high monolayer order relative to phenylenedithiols may inhibit some of the deformation effects we attribute to the phenylenedithiol nTP junctions here. In addition, unlike phenylenedithiols, alkanedithiols are not expected to have the possibility of any π - π or other cooperative effects that could change charge transport properties. While interactions between phenyl rings in the phenylenedithiols, either intra- or intermolecularly, could open up possibilities for new properties, it is unlikely that any deformation or molecular reorientation of alkanedithiols would promote any additional charge transport channels. Based on these factors, we can see why lower β values may not have been prevalent in alkanedithiol junctions but could have appeared in phenylenedithiol devices.

We stress again that the established monolayer quality prior to device fabrication coupled with the reproducibility of our measurements shows that nTP characterization is a valid method to generate and characterize permanent metal-molecule-metal junctions with these phenylenedithiol molecules. Though we measure low β values for the phenylenedithiols, there is no evidence to suggest that these junctions are shorted or damaged. What this study does

highlight, however, is that there are consequences to the choice of molecular electronic architecture and fabrication processes. nTP is a powerful technique for creating large area junctions that may utilize the unique effects ME has to offer. However, careful considerations and precautions must be taken in fabricating and analyzing molecular junctions as the field of molecular electronics moves toward studying more ‘exotic’ molecules that could exhibit similar alterations to those seen in our phenylenedithiol junctions.

3.4 Conclusions

The study in this chapter shows the design and study of the charge transport properties of phenylenedithiol self-assembled monolayers incorporated into ME devices using nTP.

Phenylenedithiols synthesized with ETMS protecting groups were studied in relation to deprotection conditions, highlighting the deprotection of molecules for SAM applications is non-trivial. XPS characterization of sulfur signals and gold attenuation through the film were utilized to identify ideal deprotection conditions, and a model to explain the dependence of deprotection SAM quality on deprotection conditions is proposed. The same techniques were utilized to verify the high quality of other phenylenedithiol monolayers.

Nanotransfer printing was utilized to incorporate the high quality SAMs of phenylenedithiols into ME junctions and electrically characterized using a cAFM tip. SAMs from ETMS-protected and unprotected terphenyldithiols showed nearly identical electrical properties, indicated the deprotection condition did not impact measured electrical output. nTP characterization was then done on SAMs from all phenylenedithiols, yielding a high percentage (between 54% and 80%) working devices for each molecule. Many devices were characterized to compare electrical output, and comparing the molecular trend versus a tunneling model, $\beta_{\text{nTP}} = 0.087 \pm 0.006 \text{ \AA}^{-1}$ was extracted. This value was much lower than the β obtained through

measuring the monolayers directly with a cAFM tip ($\beta_{\text{cAFM}} = 0.407 \pm 0.110 \text{ \AA}^{-1}$), indicating the nTP characterization method altered the properties of the phenylenedithiols.

A hypothesis is drawn that the nTP fabrication process and the force from the technique enables alternate electrical pathways to occur in electrical measurements. The phenylenedithiols, while natively having their phenyl rings rotated to one another, could either have the rotation between their rings lessened, which would increase conjugation and lower β , and/or the physical distance between phenylenedithiols could be reduced, introducing the possibility for intermolecular charge transport pathways that would also lessen measured length dependence. Future work needs to be done to further study this. Specifically, temperature dependent measurements will help elucidate this change in charge transport property. However, this is unable to be done with the present setup. 200 nm diameter pads as used in this chapter are too small to adapt to vacuum and cryostat setups where temperature dependent measurements would need to be done. Further, nTP was seen to work only up to a few microns in size before features began to have cracks electrically isolating regions of the pad.²² The investigation of alternative device architectures to be able to study nTP printed pads on phenylenedithiols in a setting for temperature dependent measurement is the motivation for Chapter 5 and will be discussed later. In the meantime, as this study shows, molecular architecture can have measurable impacts on the measured properties of organic monolayers.

3.5 Appendix

3.5.1 Synthetic Procedures

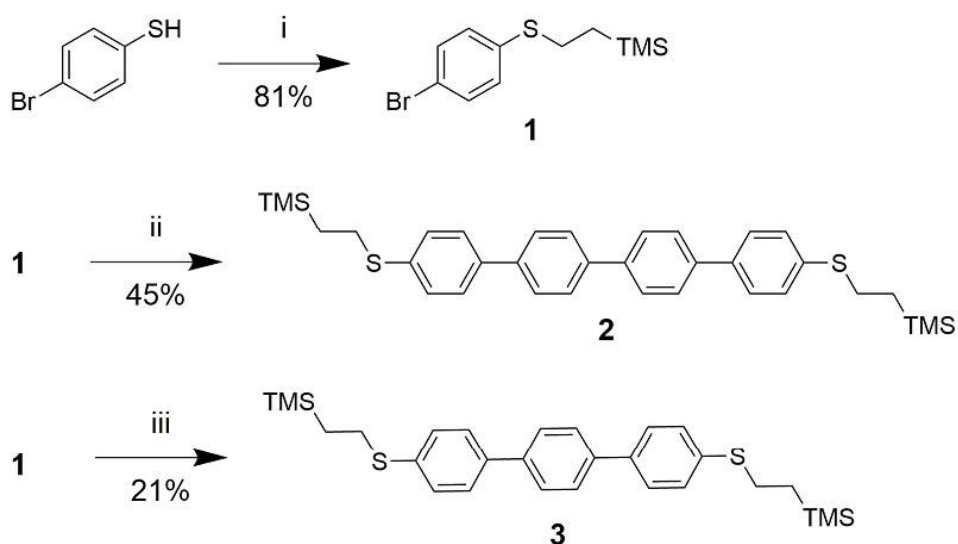


Figure 3.13 – Synthetic Route for ETMS-protected Phenylenedithiols

- (i) vinyltrimethylsilane, AIBN.
- (ii) 1) nBuLi, butyldiisopropoxyborane, THF. 2) Na₂CO₃·H₂O, 4,4'-dibromobiphenyl, Pd₂(dba)₃.
- (iii) Same as (ii) except replace 4,4' dibromobiphenyl with 1,4-dibromobenzene

General Methods. All reagents and chemicals were purchased from commercial sources (Aldrich, Acros, Alfa Aesar, Macros) and used without further purification unless stated otherwise. Reagent grade THF was dried over sodium and benzophenone and purified by distillation. ¹H nuclear magnetic resonance (NMR) spectra were obtained at 400 MHz as solutions in CDCl₃. ¹³C NMR proton-decoupled spectra were obtained at 100 MHz as solutions in CDCl₃. Chemical shifts are reported in parts per million (ppm, δ) and referenced from tetramethyl-silane. Elemental analysis was performed by Atlantic Microlab, Inc.

(2-((4-bromophenyl)thio)ethyl)trimethylsilane (1).⁴⁰ 4-bromothiophenol (5.00 g, 26.5 mmol), vinyltrimethylsilane (4.5 mL, 31.5 mmol), and AIBN (50 mg, 0.25 mmol) were added to

a bomb flask, which was sealed and stirred at 100 °C for 20 hours. The crude product was distilled at 160 °C under 0.55 torr vacuum to produce a clear oil. If present, unreacted 4-bromothiophenol sublimes first as a white solid, necessitating a fractional distillation with a heat gun to progress the solid through the distillation glassware. Yield: 6.2 g (81%). ¹H-NMR (CDCl₃, 400 MHz, δ): 7.39 (d, J = 8.4 Hz, 2H), 7.16 (d, J = 8.4 Hz, 2H), 2.93(t, J = 8.4 Hz, 2H), 0.92 (t, J = 8.8 Hz, 2H), 0.04 (s, 9H).

4,4'''-bis((2-(trimethylsilyl)ethyl)thio)-1,1':4',1'':4'',1'''-quaterphenyl (2). A solution of 1 (4.40 g, 15.2 mmol) in dry THF (20 ml) was added to a flame-dried flask (w/ condenser) under argon. The solution was cooled to -78 °C in a dry ice/acetone bath and sparged with Ar for 15 minutes. 2.5 M nBuLi in hexanes (9.5 mL, 24 mmol) was added and stirred for 2 hours. Butyldiisopropoxyborane (3.6 mL, 15.2 mmol) was added and stirred for 1 hour, after which the reaction was warmed to room temperature and stirred for 30 minutes. Na₂CO₃•H₂O (3.6 g, 29 mmol) was dissolved in distilled H₂O (9 mL), sparged with Ar for 30 minutes, and added to the reaction. 4,4'-dibromobiphenyl (1.87 g, 6.0 mmol) and THF (24 mL) were added, and the reaction was sparged with Ar for 15 minutes. PdCl₂(PPh₃)₂ (940 mg, 1.34 mmol, 9 mol %) was added in one portion and the reaction was stirred under reflux for 16 hours. The reaction mixture was poured into water and extracted into DCM. The organic layer was washed twice with brine, dried over MgSO₄, filtered, concentrated in vacuo, and purified by column chromatography on silica gel, using 4:1 hexanes:dichloromethane as the eluent. Yield: 1.96 g white solid (45%). ¹H-NMR (CDCl₃, 400 MHz, δ): 7.70 (q, J=8.4 Hz, 8H), 7.58 (d, J = 8.0 Hz, 4H), 7.39 (d, J = 8.0 Hz, 4H), 3.02 (m, J = 8.8 Hz, 4H), 0.98 (m, 4H), 0.07 (s, 18H). ¹³C-NMR (CDCl₃, 100 MHz, δ):

139.54, 138.03, 136.65, 129.25, 127.37, 127.33, 127.24, 29.70, 29.62, 16.98, -1.73. Anal. Calc'd for $C_{34}H_{42}S_2Si_2$: C, 71.52; H, 7.41; S, 11.23. Found: C, 71.13; H, 7.18; S 10.94.

4,4''-bis((2-(trimethylsilyl)ethyl)thio)-1,1':4',1''-terphenyl (3). 3 was prepared using the same method used for 2, substituting in dibromobenzene for dibromobiphenyl. Yield (not optimized): white solid (20%). 1H -NMR ($CDCl_3$, 400 MHz, δ): 7.66 (s, 4H), 7.58 (d, 8.4 Hz), 7.40 (d, $J = 8.0$ Hz, 4H), 3.03 (t, $J = 8.8$ Hz, 4H), 1.00 (t, $J = 8.8$ Hz, 4H), 0.08 (s, 18H). ^{13}C -NMR ($CDCl_3$, 100 MHz, δ): 139.41, 138.01, 136.65, 129.26, 127.32, 127.23, 29.62, 16.99, -1.69. Anal. Calc'd for $C_{28}H_{38}S_2Si_2$: C, 67.95; H, 7.74; S, 12.96. Found: C, 68.01; H, 7.46; S, 12.90.

3.5.2 NMR Spectra for Synthesized Compounds

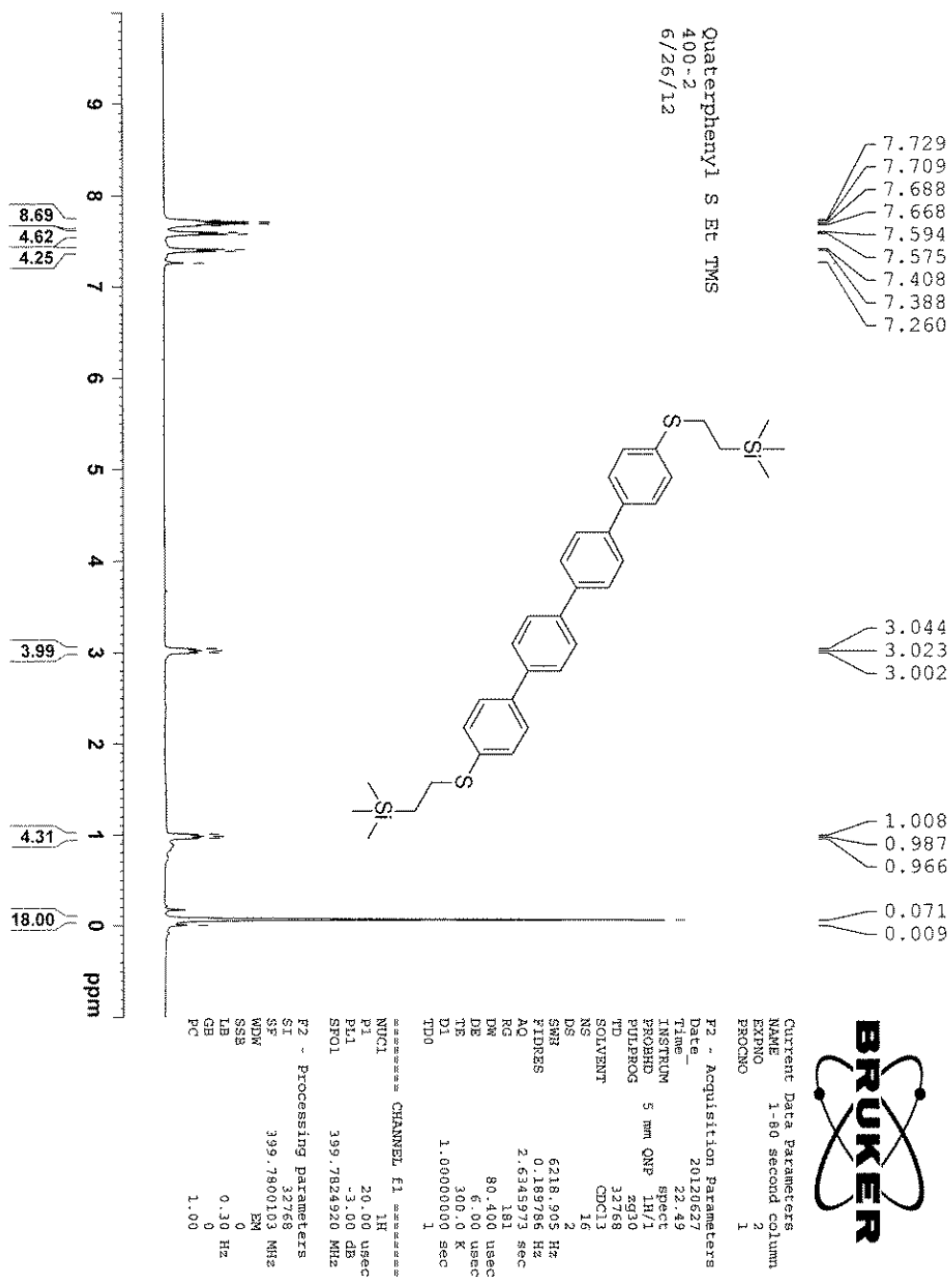


Figure 3.14 – ¹H-NMR for Synthesized qphD-SETMS

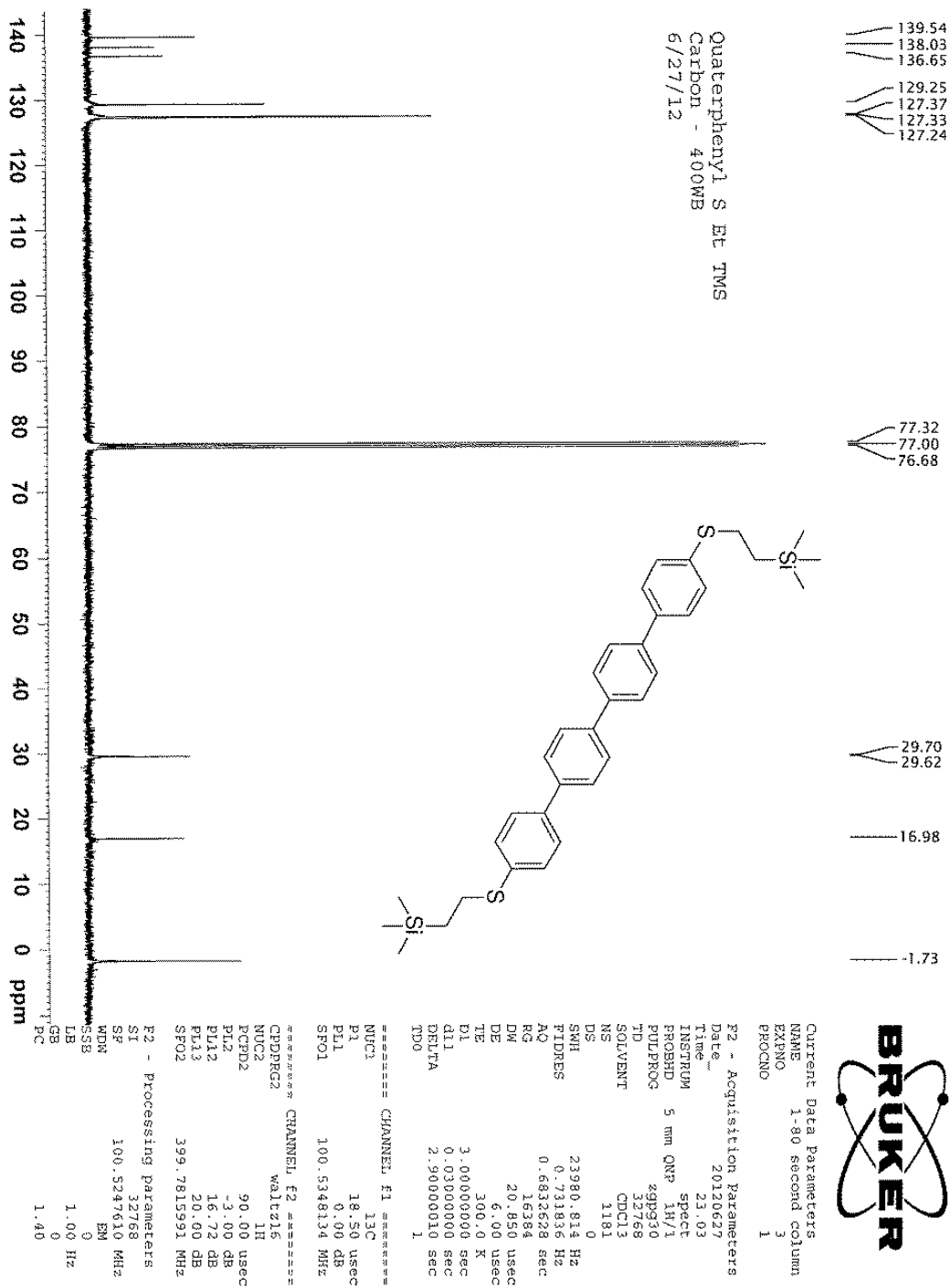


Figure 3.15 – ¹³C-NMR for Synthesized qphD-SETMS

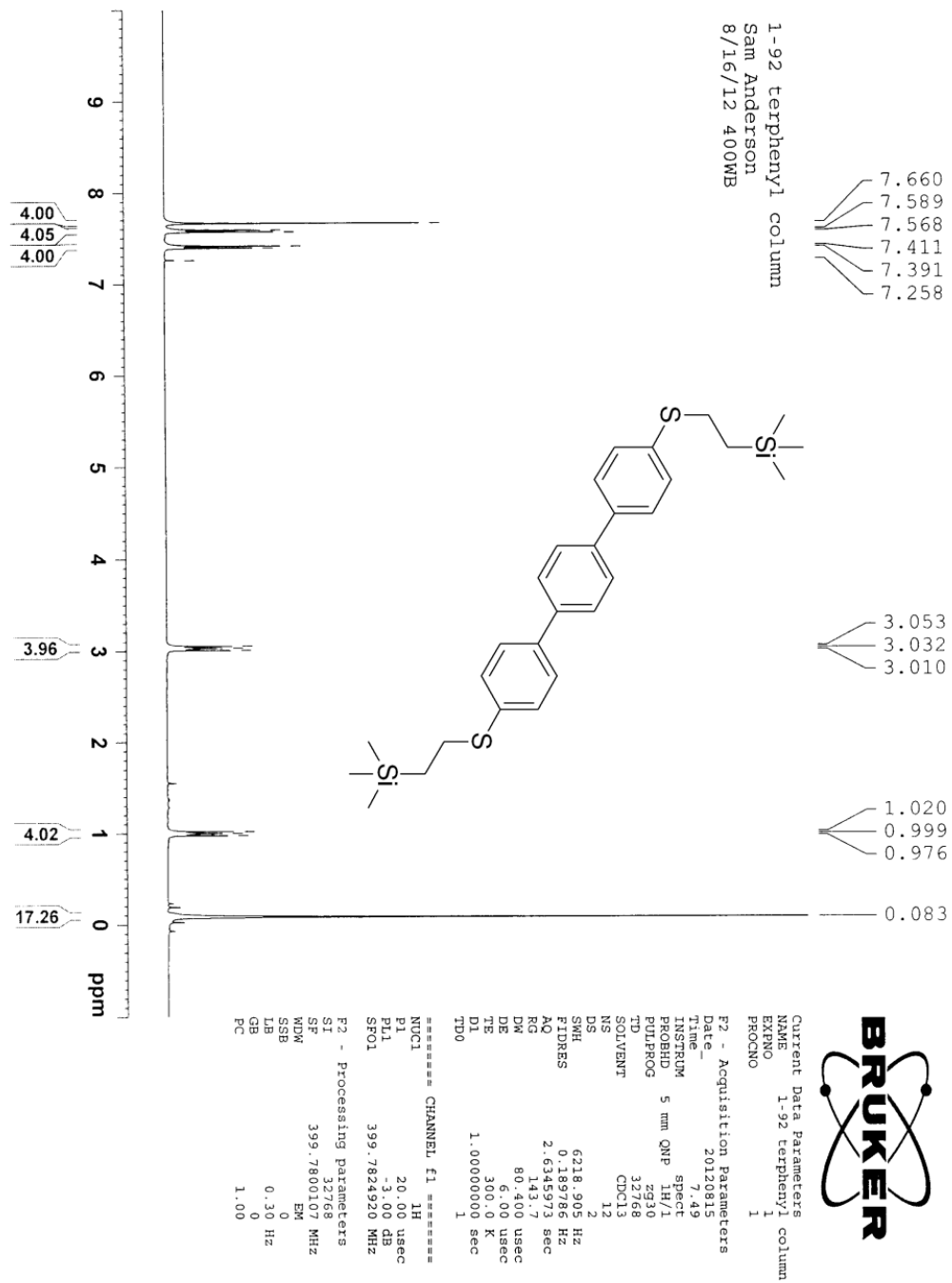


Figure 3.16 – H-NMR for Synthesized tphD-SETMS

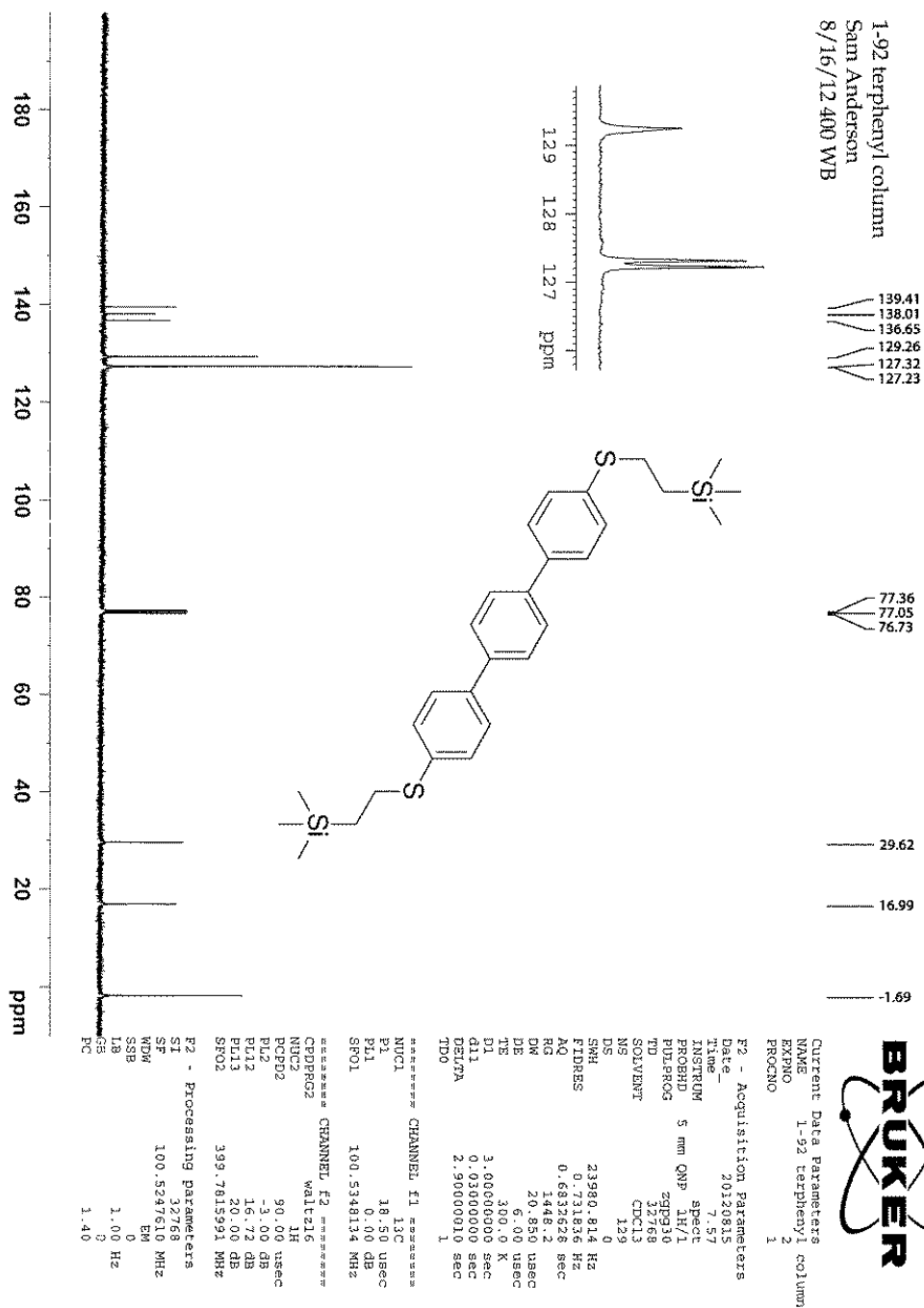


Figure 3.17 – ^{13}C -NMR for Synthesized tphD-SETMS

3.6 References

- (1) Lu, Q.; Liu, K.; Zhang, H.; Du, Z.; Wang, X.; Wang, F. *ACS Nano* **2009**, *3*, 3861–3868.
- (2) Vazquez, H.; Skouta, R.; Schneebeli, S.; Kamenetska, M.; Breslow, R.; Venkataraman, L.; Hybertsen, M. S. *Nat. Nanotechnol.* **2012**, *7*, 663–667.
- (3) Chen, Y.; Hsu, S.; Kaun, C.; Lin, M. *J. Phys. Chem. C* **2014**, *118*, 21199–21203.
- (4) Vericat, C.; Vela, M. E.; Salvarezza, R. C. *Phys. Chem. Chem. Phys.* **2005**, *7*, 3258–3268.
- (5) Srisombat, L.; Jamison, A. C.; Lee, T. R. *Colloids Surfaces A* **2011**, *390*, 1–19.
- (6) Wang, G.; Yoo, H.; Na, S.-I.; Kim, T.-W.; Cho, B.; Kim, D.-Y.; Lee, T. *Thin Solid Films* **2009**, *518*, 824–828.
- (7) Kurta, R. P.; Grodd, L.; Mikayelyan, E.; Gorobtsov, O. Y.; Zaluzhnyy, I. A.; Fratoddi, I.; Venditti, I.; Russo, V.; Sprung, M.; Vartanyants, I. A.; Grigorian, S. *Phys. Chem. Chem. Phys.* **2015**, *17*, 7404–7410.
- (8) Petta, J.; Slater, S.; Ralph, D. *Phys. Rev. Lett.* **2004**, *93*, 136601.
- (9) Xiong, Z. H.; Wu, D.; Vardeny, Z. V.; Shi, J. *Nature* **2004**, *427*, 821–824.
- (10) Jiang, J. S.; Pearson, J. E.; Bader, S. D. *Phys. Rev. B* **2008**, *77*, 035303.
- (11) Seferos, D. S.; Blum, A. S.; Kushmerick, J. G.; Bazan, G. C. *J. Am. Chem. Soc.* **2006**, *128*, 11260–11267.
- (12) Yoon, H. J.; Shapiro, N. D.; Park, K. M.; Thuo, M. M.; Soh, S.; Whitesides, G. M. *Angew. Chem. Int. Ed.* **2012**, *51*, 4658–4661.
- (13) Akkerman, H. B.; Blom, P. W. M.; de Leeuw, D. M.; de Boer, B. *Nature* **2006**, *441*, 69–72.
- (14) Xia, Y.; Whitesides, G. M. *Annu. Rev. Mater. Sci.* **1998**, *28*, 153–184.
- (15) Lee, S. H.; Cho, B.; Yoon, S.; Jeong, H.; Jon, S.; Jung, G. Y.; Cho, B. K.; Lee, T.; Kim, W. B. *ACS Nano* **2011**, *5*, 5543–5551.
- (16) Liang, X.; Sperling, B. A.; Calizo, I.; Cheng, G.; Hacker, C. A.; Zhang, Q.; Obeng, Y.; Yan, K.; Peng, H.; Li, Q.; Zhu, X.; Yuan, H.; Walker, A. R. H.; Liu, Z.; Peng, L.-M.; Richter, C. A. *ACS Nano* **2011**, *5*, 9144–9153.
- (17) Yang, R.; Zheng, X.; Wang, Z.; Miller, C. J.; Feng, P. X. *J. Vac. Sci. Technol. B* **2014**, *32*, 051203.

- (18) Jie, Y.; Niskala, J. R.; Johnston-Peck, A. C.; Krommenhoek, P. J.; Tracy, J. B. *J. Mater. Chem.* **2012**, *22*, 1962–1968.
- (19) Meitl, M. A.; Zhu, Z.-T.; Kumar, V.; Lee, K. J.; Feng, X.; Huang, Y. Y.; Adesida, I.; Nuzzo, R. G.; Rogers, J. A. *Nat. Mater.* **2006**, *5*, 33–38.
- (20) Jeong, H.; Kim, D.; Kim, P.; Rae Cho, M.; Hwang, W.-T.; Jang, Y.; Cho, K.; Min, M.; Xiang, D.; Daniel Park, Y.; Jeong, H.; Lee, T. *Nanotechnology* **2015**, *26*, 025601.
- (21) Burroughs, S.; Conner, R.; Furman, B.; Menard, E.; Gray, A.; Meitl, M.; Bonafede, S.; Kneeburg, D.; Ghosal, K.; Wagner, W.; Seel, S.; Sullivan, M. *6th Int. Conf. Conc. Photovolt. Syst.* **2010**, 163–166.
- (22) Niskala, J. R.; You, W. *J. Am. Chem. Soc.* **2009**, *131*, 13202–13203.
- (23) Menard, E.; Bilhaut, L.; Zaumseil, J.; Rogers, J. A. *Langmuir* **2004**, *20*, 6871–6878.
- (24) Hoertz, P. G.; Niskala, J. R.; Dai, P.; Black, H. T.; You, W. *J. Am. Chem. Soc.* **2008**, *130*, 9763–9772.
- (25) Raigoza, A. F.; Kolettis, G.; Brandt, T. E. S.; Caponigri-Guerra, G.; Agostino, C.; Kandel, S. A. *J. Phys. Chem. C* **2012**, *116*, 1930–1934.
- (26) Niskala, J. R.; Rice, W. C.; Bruce, R. C.; Merkel, T. J.; Tsui, F.; You, W. *J. Am. Chem. Soc.* **2012**, *134*, 12072–12082.
- (27) Wold, D. J.; Frisbie, C. D. *J. Am. Chem. Soc.* **2000**, *122*, 2970–2971.
- (28) Houmam, A.; Muhammad, H.; Koczkur, K. M. *Langmuir* **2011**, *27*, 13544–13553.
- (29) Sawaguchi, T.; Mizutani, F.; Yoshimoto, S.; Taniguchi, I. *Electrochim. Acta* **2000**, *45*, 2861–2867.
- (30) Kang, H.; Park, T.; Choi, I.; Lee, Y.; Ito, E.; Hara, M.; Noh, J. *Ultramicroscopy* **2009**, *109*, 1011–1014.
- (31) Dell, E. J.; Capozzi, B.; Xia, J.; Venkataraman, L.; Campos, L. M. *Nat. Chem.* **2015**, *7*, 209–214.
- (32) Castner, D. G.; Hinds, K.; Grainger, D. W. *Langmuir* **1996**, *12*, 5083–5086.
- (33) Cumpson, P. J.; Seah, M. P. *Surf. Interface Anal.* **1997**, *25*, 430–446.
- (34) Valkenier, H.; Huisman, E. H.; van Hal, P. A.; de Leeuw, D. M.; Chiechi, R. C.; Hummelen, J. C. *J. Am. Chem. Soc.* **2011**, *133*, 4930–4939.

- (35) Kronemeijer, A. J.; Huisman, E. H.; Akkerman, H. B.; Goossens, A. M.; Katsouras, I.; van Hal, P. A.; Geuns, T. C. T.; van der Molen, S. J.; Blom, P. W. M.; de Leeuw, D. M. *Appl. Phys. Lett.* **2010**, *97*, 173302.
- (36) Love, J. C.; Estroff, L. A.; Kriebel, J. K.; Nuzzo, R. G.; Whitesides, G. M. *Chem. Rev.* **2005**, *105*, 1103–1169.
- (37) Ishida, T.; Mizutani, W.; Aya, Y.; Ogiso, H.; Sasaki, S.; Tokumoto, H. *J. Phys. Chem. B* **2002**, *106*, 5886–5892.
- (38) Wold, D. J.; Haag, R.; Rampi, M. A.; Frisbie, C. D. *J. Phys. Chem. B* **2002**, *106*, 10–13.
- (39) Li, Z.; Park, T.-H.; Rawson, J.; Therien, M. J.; Borguet, E. *Nano Lett.* **2012**, *12*, 2722–2727.
- (40) Foucoin, F.; Caupène, C.; Lohier, J.-F.; Sopkova de Oliveira Santos, J.; Perrio, S.; Metzner, P. *Synthesis* **2007**, *9*, 1315–1324.

CHAPTER 4:

STUDIES OF MULTI[(PORPHINATO)METAL] OLIGOMER WIRES IN MOLECULAR ELECTRONIC DEVICES

Robert C. Bruce^{}, Ruobing Wang[†], Wentao Li^{*}, Michael J. Therien[†], Wei You^{*}*

^{*} Dept. of Chemistry, University of North Carolina- Chapel Hill, Chapel Hill, NC

[†] Dept. of Chemistry, Duke University, Durham, NC

4.1 Background

4.1.1 Organic Heterocycles for Spintronic Effects

As discussed in previous sections, there are strong advantages to adapting organic and organic-based materials for spintronic effects. Compared to inorganics, organic-based materials have long spin diffusion lengths, experimentally being seen to transport hundreds of nanometers through organic films.¹ The ability to maintain spin for these lengths allows for the possibility of injecting charge into an organic film instead of using inert tunnel barriers, allowing for spin manipulation from the active layer to become a realistic proposition and a wide range of interactions to come into play. Organic magnetoresistance (OMAR) has been observed as one effect of this injection, and these effects are still being investigated due to the apparent tunability of MR that can appear from various organic films.² Despite the fact that this effect is not completely understood, we can utilize one of the principles derived from OMAR studies to generate large MR effects in devices, that principle being restriction of current to a 1-dimensional plane.³ In this plane, with only one direction for charge to travel, the effects of

Coulomb blockades and other spin interactions will be most influential on transport of spin and therefore charge. Such principles have already been shown to lead to very large MR effects.⁴

Heterocycle-based organic units represent an interesting unit to study in regard to the principle discussed above. The heterocyclic center in compounds such as phthalocyanines and porphyrins provides a large breadth of synthetic control, yielding the ability to insert different metal centers or generate many different nanoarchitectures. For example, both 1-dimensional and 2-dimensional architectures have been presented by manipulating different ends of the molecule.^{5,6} This synthetic control provides opportunities to manipulate the charge transport properties of similar heterocycles. Manipulating bridgings on the heterocycle can alter the current realized through the porphyrin, and forcing current to pass through *para* or *ortho* ends of the porphyrin is shown to dramatically affect measured current in STM break junctions settings.⁷ Designing porphyrins such that they orient differently on a surface leads to electrodes bridging to different chemical groups and different measured currents.⁸ Connecting porphyrin heterocycles through different functional groups can also influence charge transport properties. Fusing heterocycles leads to higher conductivity over orthogonal rings,⁹ and even among orthogonal bridging groups, ethynylene ligands are shown to promote lower tunneling attenuation than single bonds.^{10,11}

As we focus on porphyrin heterocycles in particular, we see that even when not manipulating the transport properties synthetically, the transport properties of porphyrins are extremely interesting. Several studies have shown the ability to utilize porphyrins in single molecule junctions by attaching a metal binding group. Doing so highlights a temperature dependence of charge transport through the porphyrin wires.¹¹ The highly conjugated heterocycles in ethynylene-bridged porphyrin wires lead to extremely long polaron

delocalization lengths on the case of zinc metal center wires.¹² Quasi-Ohmic charge transport is also seen in these ethynylene-bridged porphyrins,¹³ one of the rare instances this is seen in organic-based molecular junctions. Such strong intramolecular coupling and charge transport makes porphyrins unique in a field where organic materials are expected to be dominated by resistive effects and tunneling transport. When combined with the large spin delocalization length and opportunity for spin injection and manipulation, porphyrins present a strong candidate to explore spintronic effects.

4.1.2 Spintronic Effects from Porphyrin Metal Centers

As stated previously, organic-based materials should lead to low instances of spin relaxation due to low spin orbit coupling. On top of this, a method to potentially manipulate spin current can come from the metal centers that can be incorporated into porphyrin heterocycles. Metal centers in porphyrins are known to be chemically active components, as shown through the classic example of hemoglobin where the iron metal center binds to oxygen.¹⁴ The spin state of these metal centers can also be manipulated under certain conditions. Iron metal centers in octaethylporphyrin chlorides are able to align spin state on a nickel substrate,¹⁵ and cobalt metal centers in similar octaethylporphyrins can magnetically couple to a nickel substrate.¹⁶ Ability to manipulate the spin state of the metal centers could lead to switchable spintronic properties through the porphyrin wires to be studied.

In the case of the previous examples, magnetic effects came from porphyrin molecules lying flat on a metal substrate and interacting with the magnetic field from the substrate. However, interesting effects can come from other switches and properties generated without magnetic fields. Reacting nickel metal center porphyrins with ammonia gas can change the magnetic properties from paramagnetic to diamagnetic.¹⁷ Also, light can induce magnetic switching in azopyridine functionalized nickel porphyrin monomers.¹⁸ Further, despite being

chemically active with outside species, the metal centers are coupled within the porphyrin unit enough to bear an influence on the overall properties of the molecule. Changing the metal center from hydrogen to zinc is shown to affect the energy levels of the porphyrin unit.¹⁹ Kondo effects – conductance changes due to magnetic fields, becoming most pronounced at extremely low temperature – can also be influenced in copper porphyrins through exposure to nitrous oxide gas.²⁰ Finally, theoretical computations predict that chromium metal porphyrins can exhibit inherent spin polarization.²¹

Overall, previous studies have expressed the ability for charge and spin transport in porphyrin heterocycles to be potentially manipulated by metal center, and for the charge and spin transport of the same systems to be switched externally. Coupled with the strong transport properties of porphyrin wires, the inherent ability to maintain spin through organic-based materials, and possible inherent impact of metal center on spin transport, we have strong motivation for use of porphyrins wires to be incorporated into settings for molecular electronic and spintronic studies.

4.1.3 Molecular Electronic Studies of Porphyrin Wires

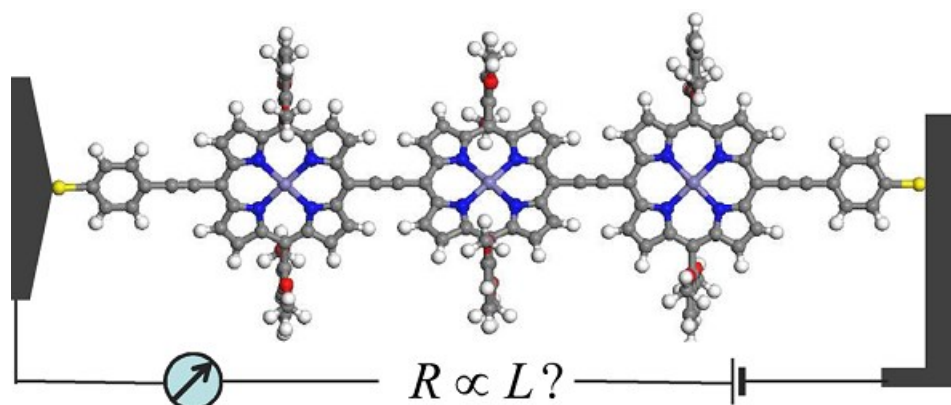


Figure 4.1 – Zinc Porphyrin Wires in STM-Break Junction

Representative image of zinc metal center porphyrin wires in STM break junctions. Reprinted with permission from Ref. 13. Copyright 2012 American Chemical Society.

Ethyne-bridged porphyrin wires have previously been adapted to STM studies.¹³ These wires were described above as possessing quasi-Ohmic charge transport in break junctions. The *para* ethyne bridge links together the porphyrin heterocycles, while the *ortho* attachments of large benzenealkoxy groups allow for solution processibility of the wires. The wires have been grown as oligomers up to 8-mers,¹² allowing for possible metal-metal coupling interactions from the porphyrin metal centers as with the cobalt valence tautomer in Chapter 2. All of the interesting effects already seen in these oligomers are with diamagnetic zinc metal centers; inserting other metals into these already interesting molecules could lead to more dynamic effects in these wires.

The goal then, given the promise exhibited by these porphyrin wires, is to adapt them to molecular electronic architectures that enable spintronic studies. Cryostat setups would allow for temperature dependent measurements and magnetic effects under inert atmosphere but require macroscopically accessible electrodes to be adapted to the in house setups. The first step toward

this adaptation is to prove that these porphyrin wires can be used in the more bulk-like junctions that will be adapted to the aforementioned large-area architectures and measurements.

4.1.4 Overview

To this end, we have adapted porphyrin oligomer wires to ‘bulk’ nTP devices to study their unique transport properties in this device architecture. A detailed study on establishing the most optimal monolayer quality for adaptation into more bulk-like devices is undertaken. Then, 200 nm nTP devices, studied under cAFM in ambient conditions, highlight the same transport properties as seen in single molecule measurements, an exciting and non-trivial finding given the results seen in Chapter 3 with phenylenedithiols in nTP devices. In addition, changing metal center is shown to have effects on the charge transport properties measured in these devices, highlighting the potential to manipulate charge and spin properties in these devices. Chapter 5 will detail work toward incorporating these molecules into macroscopically accessible devices, the second necessity for spintronic studies.

4.2 Methods

4.2.1 Materials

Ethyne-bridged porphyrins of various formulations were synthesized by Ruobing Wang (Duke University; see Section 4.5 for synthetic routes). Ethyltrimethylsilane (ETMS)-protected carbodithioate capped porphyrins were prepared in solutions of THF and deprotected with various amounts of tetrabutylammonium fluoride (TBAF), typically in a 1:4 porphyrin: TBAF molar ratio. Thioacetate capped porphyrins were prepared in solutions of either THF or dichloromethane (DCM) and deprotected with ammonium hydroxide (NH_4OH), typically in a 1:4 porphyrin: NH_4OH molar ratio.

4.2.2 Gold Substrate and Self-Assembled Monolayer Preparation

Silicon wafers were cut into approx. 1 cm × 1 cm size for each device, then cleaned in RCA solution (2:1:1 water: ammonium hydroxide: hydrogen peroxide) for 15 minutes. Upon removal from RCA, the Si wafers were rinsed with water and ethanol, dried with N₂ gas, and cleaned in UV/ozone for 20 minutes. After cleaning, 5 nm Ti/ 40 nm Au were thermally evaporated on the wafers, the Ti layer at a rate of 1 Å/s, the Au layer starting at 1 Å/s for the first 5 nm then increased to 10 Å/s for the duration of the deposition. To prepare monolayers for all chemicals, freshly evaporated Au/Ti on Si substrates were immersed in the prepared solutions inside a N₂ glove box (O₂ < 5.0 ppm). After 24 hrs, substrates were removed from solution, sonicated in a fresh solvent solution for 60 s to remove physisorbed molecules, then rinsed in ethanol and dried under N₂ gas.

4.2.3 Nanotransfer Printing

Perfluoropolyether (PFPE) stamps were prepared by UV curing liquid PFPE on PFPE-based molds with arrays of raised features. For curing, the UV cure chamber (ELC-500, *Electro-Lite Corporation*, 365 nm exposure) was purged for 15 mins with N₂, then UV light was illuminated for 30 s. Stamps were then removed from the PFPE-based molds and loaded into a thermal evaporator where 20 nm Au were deposited at 1 Å/s for the first 5 nm, then 10 Å/s for the duration. PFPE stamps with gold were then placed gold side down onto a monolayer on Au, tapped lightly to encourage contact with the unbound thiol of the dithiol monolayer, and placed in a vacuum for 30 min to remove air between stamp and monolayer. After removal from vacuum, the PFPE stamps are peeled off, exposing the patterned printed gold contacts on the monolayer device. Characterization of these features was done shortly after stamp removal.

4.2.4 Atomic Force Microscopy

Nanotransfer printed electrodes were characterized and analyzed *via* atomic force microscopy (AFM), using an Asylum Atomic Force Microscope (Asylum MFP-3D, *Asylum Research*). Tapping-mode images were taken using silicon cantilevers (*BudgetSensors*, Tap300Al) with resonance frequencies of approximately 300 kHz and a force constant of approximately 40 N/m. Conductive measurements (in this section, exclusively “nTP characterization”) of individual features were taken using the same AFM system. Cantilevers are prepared and conductive measurements are made as described in Chapter 3. Magnetic fields were applied by a Variable Field Module attachment (Oxford Instruments) to the Asylum AFM setup, attached directly beneath the sample, applying fields up to around 2700 Gauss with 1 Gauss resolution.

4.2.5 Photoelectron Spectroscopy

Monolayer properties on gold were evaluated using x-ray photoelectron spectroscopy (XPS) characterization and ultraviolet photoelectron spectroscopy (UPS). XPS was done using a monochromatic Al K α source (source and detector from *Kratos*) with power output of 150 W. All signals were optimized to maximize the Au 4f_{7/2} signal. Au 4f, Ni 2p, Cu 2p, and Zn 2p spectra were obtained by averaging 2 sweeps at 500 ms per point; and S 2p spectra were obtained by averaging 6 sweeps at 800 ms per point, all with resolution of 50 mV. XPS spectra were analyzed by subtracting a Shirley background and then assigning a combination of Lorentzian and Gaussian (Voigt) functions. Spin-orbit separation between S 2p_{3/2} and S 2p_{1/2} signals was set to 1.18 eV; between Au 4f_{7/2} and Au 4f_{5/2} signals, 3.67 eV; between Ni 2p_{3/2} and 2p_{1/2}, 17.27 eV; between Cu 2p_{3/2} and 2p_{1/2}, 19.80 eV; and between Zn 2p_{3/2} and 2p_{1/2}, 22.97 eV.

UPS was done using a helium source (He I, KE = 21.2 eV). UPS measurements were taken with 100 ms dwell times and 25 mV resolution for full scans, or 1200 ms dwell times and

10 mV resolution, averaging 3 sweeps. UPS spectra utilized linear backgrounds to identify onsets of the low energy and cutoff regions of the spectra.

4.2.6 Cyclic Voltammetry

Cyclic voltammetry was taken on a BASi EC Epsilon cyclic voltammeter, using a Ag/AgNO₃ reference electrode, Pt wire as counter electrode, and glassy carbon as working electrode. 0.1 M tetrabutylammonium-hexafluorophosphate (TBA-PF₆) was added to all solutions, along with active component, in DCM. Solutions were prepared with anhydrous solvent and purged with argon. All observed peaks were normalized to observed ferrocene (Fc/Fc⁺) oxidation in same solutions.

4.3 Results and Discussion

4.3.1 Carbodithioate Linkers in Porphyrin Monolayers

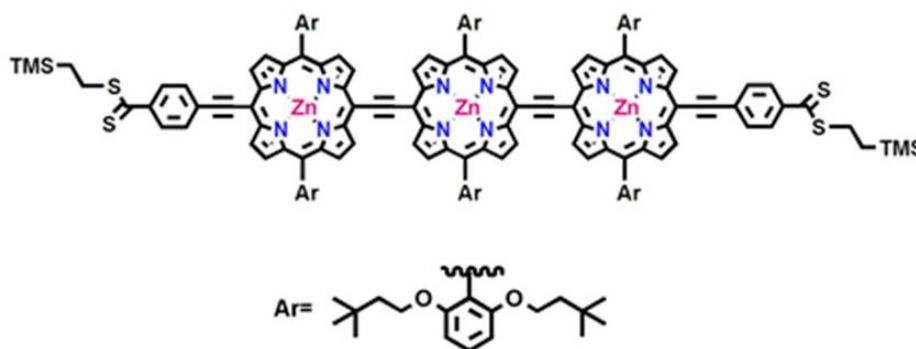


Figure 4.2 – PZn-CS₂ Structure

Representative image of PZn-CS₂, protected with ETMS groups on both ends and benzenealkoxy ligand (“Ar”). In particular, this represents PZn₃-CS₂ for the three Zn metal center heterocycles.

To this point, monolayers with thiol (-SH) linkers have been discussed almost exclusively. However, many other metal binding groups exist throughout the literature. In STM break junctions, different binding geometries are shown to influence conductances through

molecules,²² and different anchor groups are shown to yield different conductances and interact stronger or weaker with metallic surfaces.^{23,24} However, there is a lack of consensus in the literature about whether or not linker groups influence conductances and other measured charge transport properties of ME junctions. Devices with liquid metal eutectic Ga-In electrodes (EGaIn) have shown no dependence on output on linker group.²⁵ Perhaps this argument relates back to device architecture, as EGaIn junctions utilize a physical barrier from the Ga-In metal, whereas metal binding can occur from an STM tip.

If we assume that the chemical attachment plays a role on linker effects, or simply that the setup we are designing will be more closely aligned with the STM on gold studies mentioned above, then the linker group is expected to be important for our nTP junctions. To this end, we consider the carbodithioate ($-\text{CS}_2$) linker for use with the porphyrins. Carbodithioates are expected to form a bidentate ligand to a gold substrate, with the distance between the sulfurs in the CS_2 group (2.87 Å) nearly identical to the spacing between gold molecules on a (111) surface (2.9 Å).²⁶ XPS studies show that the native binding mode of carbodithioates to gold appears to be identical to thiols.²⁷ Despite this fact, carbodithioates show superior electrical contact and thermal stability in monolayers on metal surfaces.²⁸ UPS studies have shown that carbodithioate linkers can lower metal work function, enabling stronger electronic coupling to the molecule and potentially enabling ambipolar transport in a well-tuned ME device.²⁹ Altogether, these effects can lead to a reported order of magnitude increase in conductance of molecular wires with carbodithioates over thiols.³⁰

With these potential advantages in mind, porphyrin monomers with zinc metal centers and carbodithioate linkers ($\text{PZn}_1\text{-CS}_2$, where $n = 1$ represents the monomer form of the porphyrin wire) were tried first in monolayer formations. Figure 4.2 represents the general PZn-CS_2

structure, where $\text{PZn}_1\text{-CS}_2$ represents the molecule with just one heterocycle in the wire. The advantage to testing this system first is the zinc metal center is diamagnetic and should not have oxygen reactivity. While thiols are oxygen sensitive and can form disulfides, carbodithioates are known to be even more oxygen sensitive, desorbing from surfaces and showing measurable changes on a surface in under 24 hrs.³¹ With this in mind, carbodithioates were protected with ETMS groups before surface attachment, significantly increasing their air stability prior to surface attachment. Deprotection was done *in situ* on a gold substrate with TBAF. As expressed in Chapter 3, deprotection conditions can significantly affect monolayer quality, so initial samples tested different deprotection conditions.

Figure 4.3 shows S 2p signals from XPS for $\text{PZn}_1\text{-CS}_2$ monolayers prepared from 0.1 mM solution in THF with different deprotection amounts. Two observations are of note in these spectra. First, there is a distinct dependence of monolayer quality on deprotection condition, as seen previously with the phenylenedithiols. The peak at 163.4 eV, representing unbound thiols,³² appears to reach a maximum around 1:4 PZn_1 : TBAF, otherwise the peak is of lower intensity if present at all. At excess TBAF condition, no unbound thiol is present, indicating a monolayer lying flat on the surface with both ends bound to gold. As with other ETMS protected monolayers, an intermediate amount of TBAF is necessary for good monolayer formation.

Comparing Au 4f spectra and obtaining monolayer heights using Equation (3-2) yields the monolayer heights in Table 4-1. As expected, monolayer height drops significantly for excess TBAF samples. The other feature of note is the peak at 161.0 eV in all spectra. The peak at 161.9 eV matches a bound thiol, which is expected, as is the 163.4 eV peak which matches unbound thiol. The peak at lower binding energy, however, is unexpected for these monolayers given that the bound and unbound thiol are expected to be the dominant and, in principal, only observed

Table 4-1 – XPS Measured Heights for PZn₁-CS₂ Monolayers

| Molecule | Monolayer Length | | |
|--|---------------------|--------------------------|------------|
| | Measured Length (Å) | DFT Molecular Length (Å) | Tilt Angle |
| PZn ₁ -CS ₂ (TBAF 1:1) | 13.1 | 27.2 | 61.2° |
| PZn ₁ -CS ₂ (TBAF 1:2) | 13.3 | 27.2 | 60.7° |
| PZn ₁ -CS ₂ (TBAF 1:4) | 13.7 | 27.2 | 59.8° |
| PZn ₁ -CS ₂ (Excess TBAF) | 9.7 | 27.2 | 69.1° |

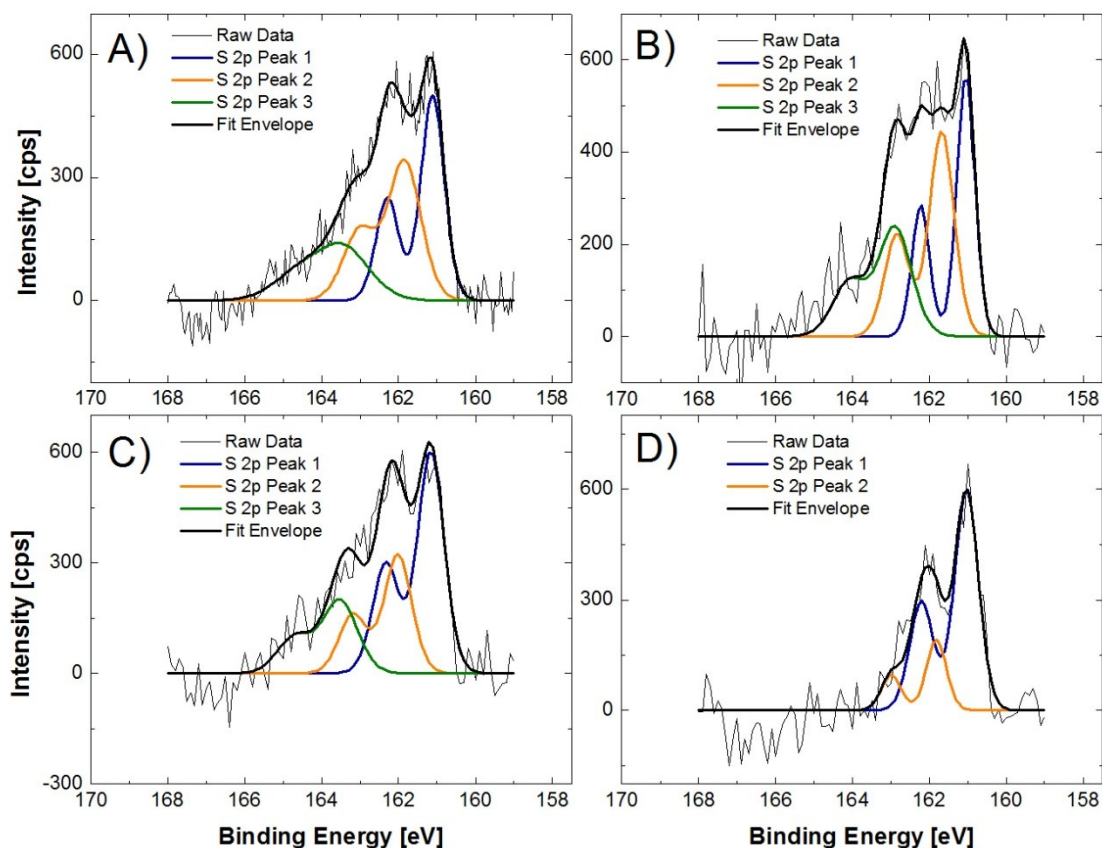


Figure 4.3 – PZn₁-CS₂ Monolayers on Gold Substrates

XPS S 2p spectra for Zn-porphyrin monomer wires on gold with carbodithioate linkers, 0.1 mM from THF, prepared with different TBAF concentrations- PZn₁:TBAF **A)** 1:1, **B)** 1:2, **C)** 1:4, **D)** TBAF excess.

peaks. Moreover, this peak is the highest intensity in samples with any amount of TBAF, and larger amounts of TBAF appear to increase the peak intensity. Looking through literature yields studies that suggest poorly packed monolayers of alkanethiols, either due to insufficient soaking time or damage to the monolayer, can exhibit this peak at 161.0 eV.³³ Damage to the monolayer is not likely in this instance – this monolayer is prepared under inert environment without heating and allowed sufficient time (24 hrs or longer) to allow for as much surface coverage as possible – and TBAF has been utilized for high quality monolayers with gold on phenylenedithiols. To attempt to assist the potential packing issue, monolayers were prepared from PZn₁-CS₂ solutions of 1 mM and 10 mM concentration. As shown in Figure 4.4, increasing concentration slightly decreases the 161.0 eV peak but never fully removes it. At this point, it is impractical to increase concentration of solution due to the amount of material required, and even at the 10 mM concentration there is no indication that the peak is close to being fully removed.

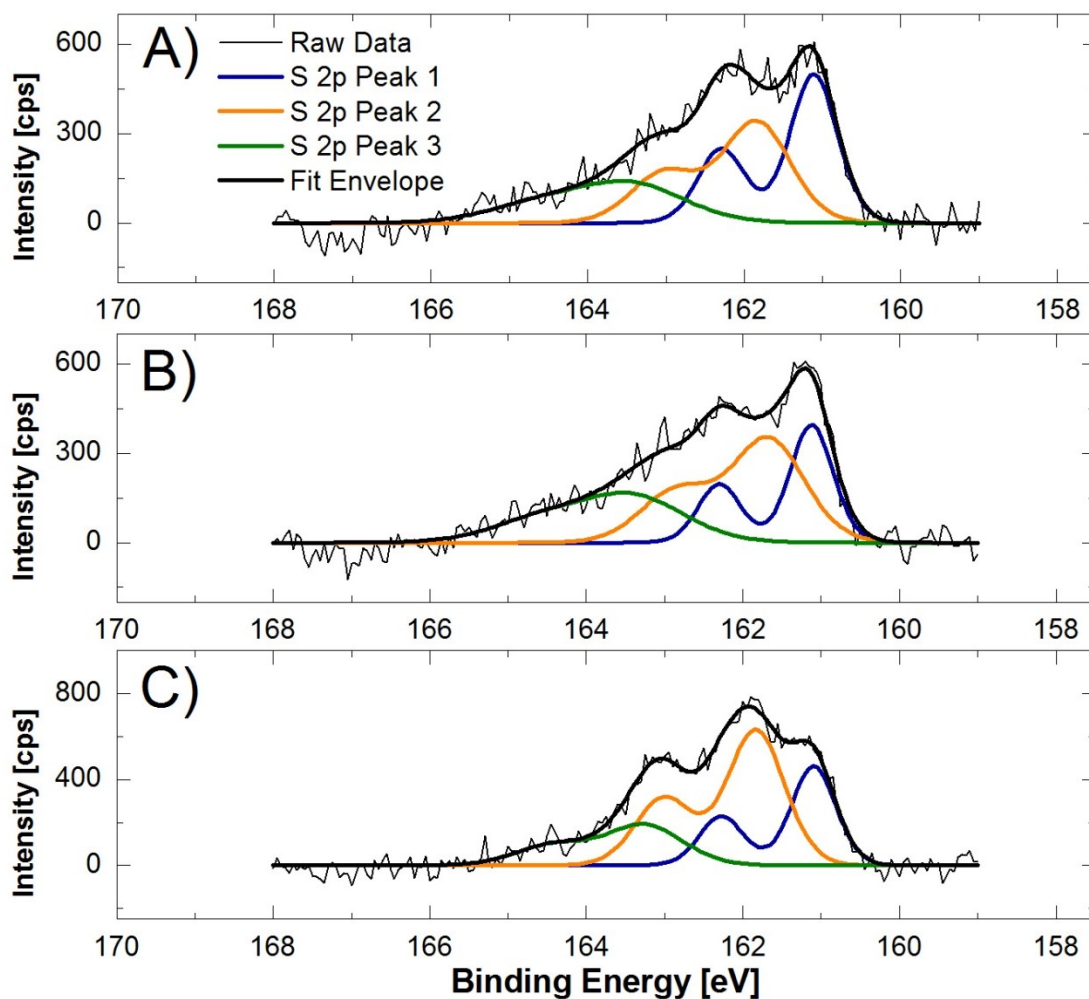


Figure 4.4 – PZn₁-CS₂ Concentration Dependence

Zinc-porphyrin monomers with carbodithioate linkers, prepared at **A)** 0.1 mM, **B)** 1 mM and **C)** 10 mM concentration. All were prepared from intermediate amounts of TBAF deprotectant (1:4 PZn₁: TBAF).

4.3.2 Deprotection Effects on Metal Binding Groups

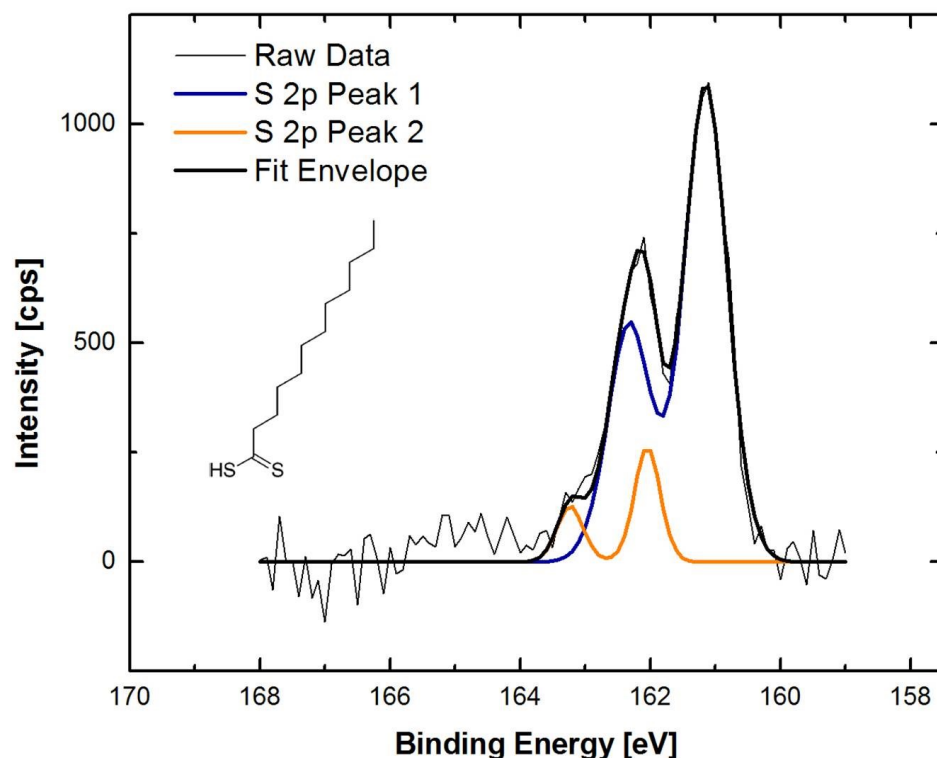


Figure 4.5 – XPS of Alkanecarbodithioate Monolayer

ETMS-protected alkanecarbodithioate monolayer, prepared with monolayer: TBAF 1:4.

To test the results a bit further, several test monolayers with the carbodithioate linker were prepared. First, synthesized alkanecarbodithioates that should have more ideal packing due to the nature of the alkane chain were utilized. These molecules were ETMS protected and deprotected with 1:4 molecule:TBAF condition. Analyzing these ‘ideal’ monolayers still yielded evidence of this 161.0 eV peak (Figure 4.5). This indicated the 161.0 eV peak from these ETMS protected CS₂ monolayers may not be from the inability of the porphyrin molecular structure to pack well, but may be more inherent to the linker group itself. Most interesting about the protected alkanecarbodithioate XPS result is that it did not match literature spectra for similar molecules.

Unprotected alkanecarbodithioates on gold by Lee *et al.* showed only the 161.9 eV bound thiol peak, indicating that the CS₂ linker is capable of binding to gold similarly to thiols.³¹

The only difference of this test system was the ETMS protector and deprotection process, which may point to this as the culprit. While the 161.0 eV peak is sometimes associated with poor monolayer quality in thiols, ultimately the peak simply represents a different binding mode to the gold substrate. Theoretical predictions have shown that changing the hybridization with which sulfur binds to gold can shift the observed binding energy in XPS by almost 1 eV.³⁴ Furthermore, while ETMS deprotection is expected to restore the native carbodithioate, the impact of the hydrogen on the thiol is unknown,³⁵ and further unknown is whether the deprotected CS₂ group is restored to possessing its hydrogen or whether this bears any consequence. Clearly deprotection condition affects monolayer quality, and regardless of the hydrogen question, the kinetics of this deprotection in the case of the carbodithioates appear to make it possible to bind to a gold surface in this normally unseen binding mode.

In light of this, the deprotection of the ETMS group was explored further. To test this, carbodithioates with and without the ETMS deprotection monolayers were prepared on gold surfaces. To come closer to mimicking the phenyls previously studied, benzenecarbodithioates were synthesized, one with ETMS protection (PhCS₂-ETMS) and one without (PhCS₂-H). Due to difference in solubility, PhCS₂-ETMS monolayers were prepared from organic solvent (ethanol), whereas PhCS₂ was prepared from aqueous solution.

Figure 4.6 shows XPS spectra for PhCS₂-ETMS monolayers. All spectra from these ETMS protected molecules, even from monolayers prepared without TBAF, contain the 161.0 eV peak. Further, utilizing different TBAF concentrations highlights that the 161.0 eV peak prevalence depends on TBAF added, the same trend seen with PZn₁-CS₂ films. On the other

hand, Figure 4.7 shows XPS for PhCS₂-H monolayers, where only 161.9 eV peaks are present. Adding excess TBAF as a check shows that TBAF alone is not responsible for the presence of the 161.0 eV peak. This unprotected monolayer result matches what was seen in literature,³¹ indicating the CS₂ linker can form high quality monolayers. However, these results were not reproducible with ETMS protected CS₂ groups. At this point, it is evident that the deprotection of the ETMS group in carbodithioate linkers is responsible for the 161.0 eV peak, with the most likely explanation being that the protected carbodithioates result in bindings to gold surface with different orientation or hybridization than unprotected carbodithioates.

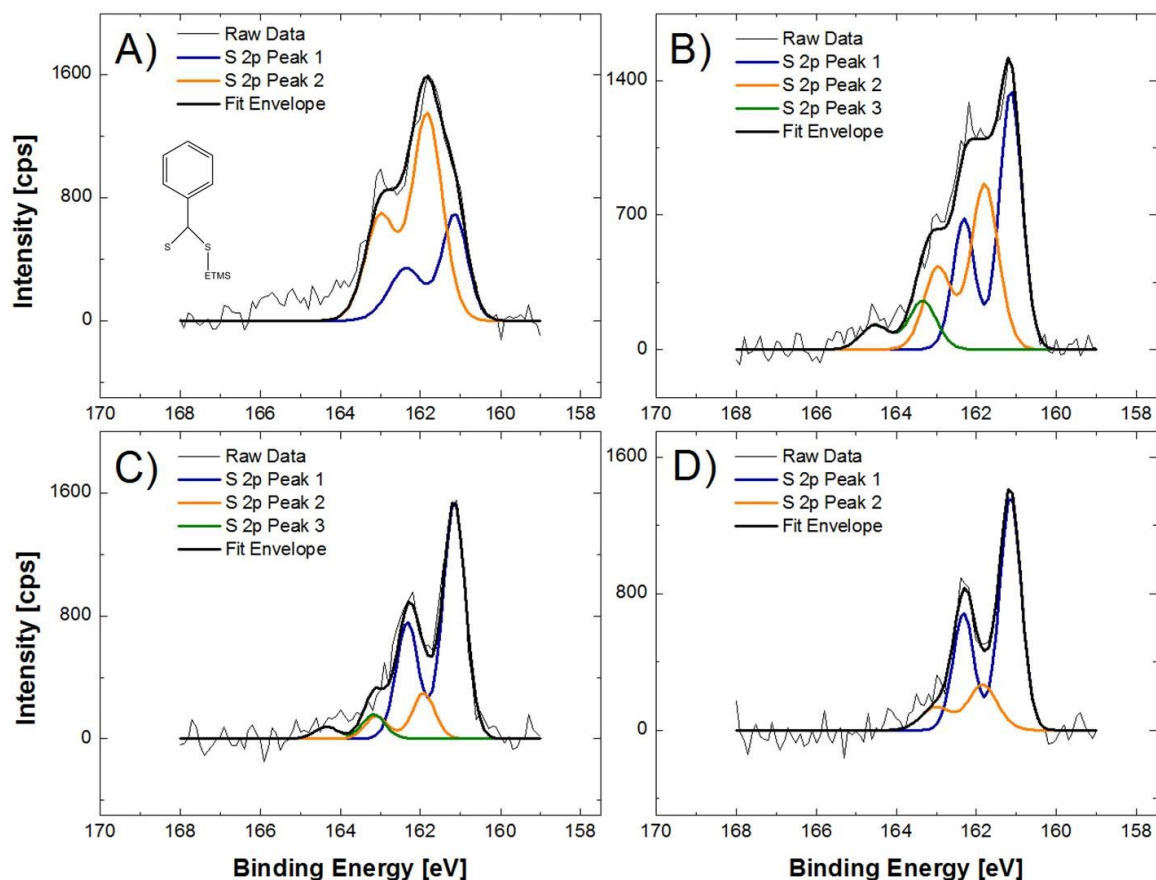


Figure 4.6 – XPS of Benzenecarbodithioate with ETMS Protection

S 2p spectra of PhCS₂-ETMS monolayer with ETMS protection, prepared on gold substrates with **A)** No TBAF, **B)** PhCS₂:TBAF 1:2, **C)** PhCS₂:TBAF 1:8, and **D)** Excess TBAF. All surfaces show evidence of the 161.0 eV peak.

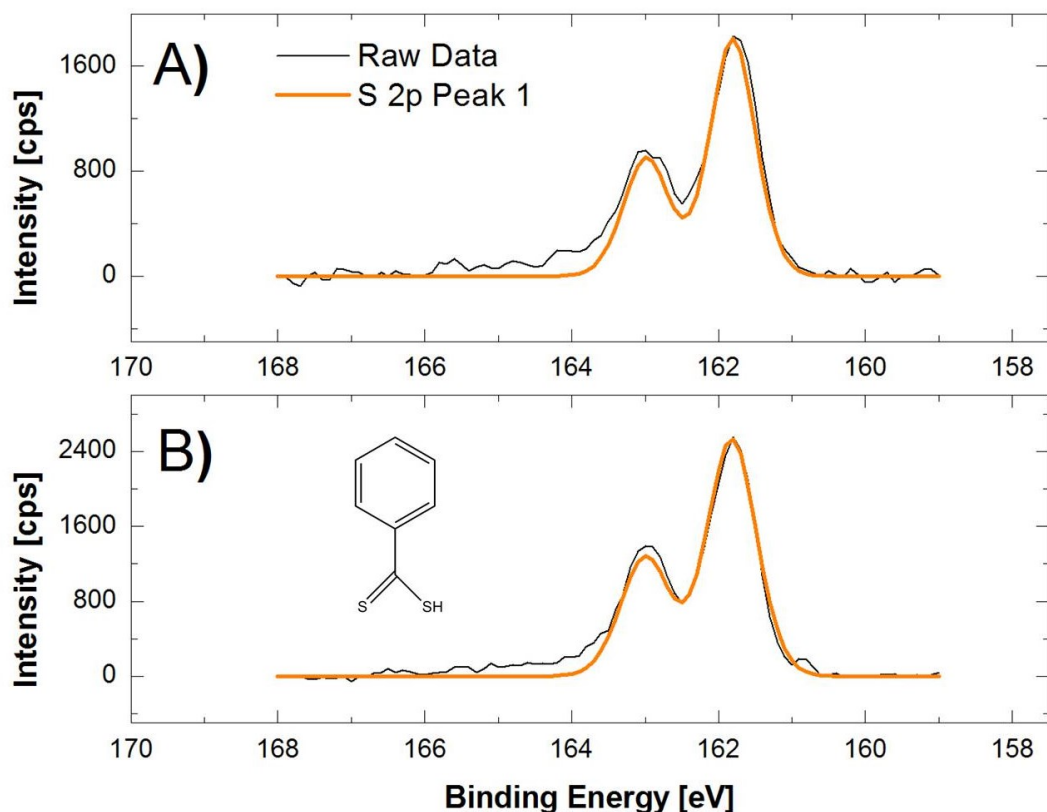


Figure 4.7 – XPS of Benzenecarbodithioate Without Protection Group

S 2p spectra for PhCS_2 monolayers without ETMS protection, prepared **A)** without TBAF and **B)** with excess TBAF.

Due to the oxygen sensitivity of CS_2 linkers, working with molecules without the ETMS protection is not a viable option. Production of porphyrin molecules is too costly and time consuming to rely on a new batch of material for every monolayer and experiment. Relying on monolayers that have complex hybridizations and/or binding modes could also be a costly expenditure, as any interaction with the substrate will be equally complex. To alleviate both problems, the CS_2 linker was abandoned in lieu of a more straightforward thiol linker group.

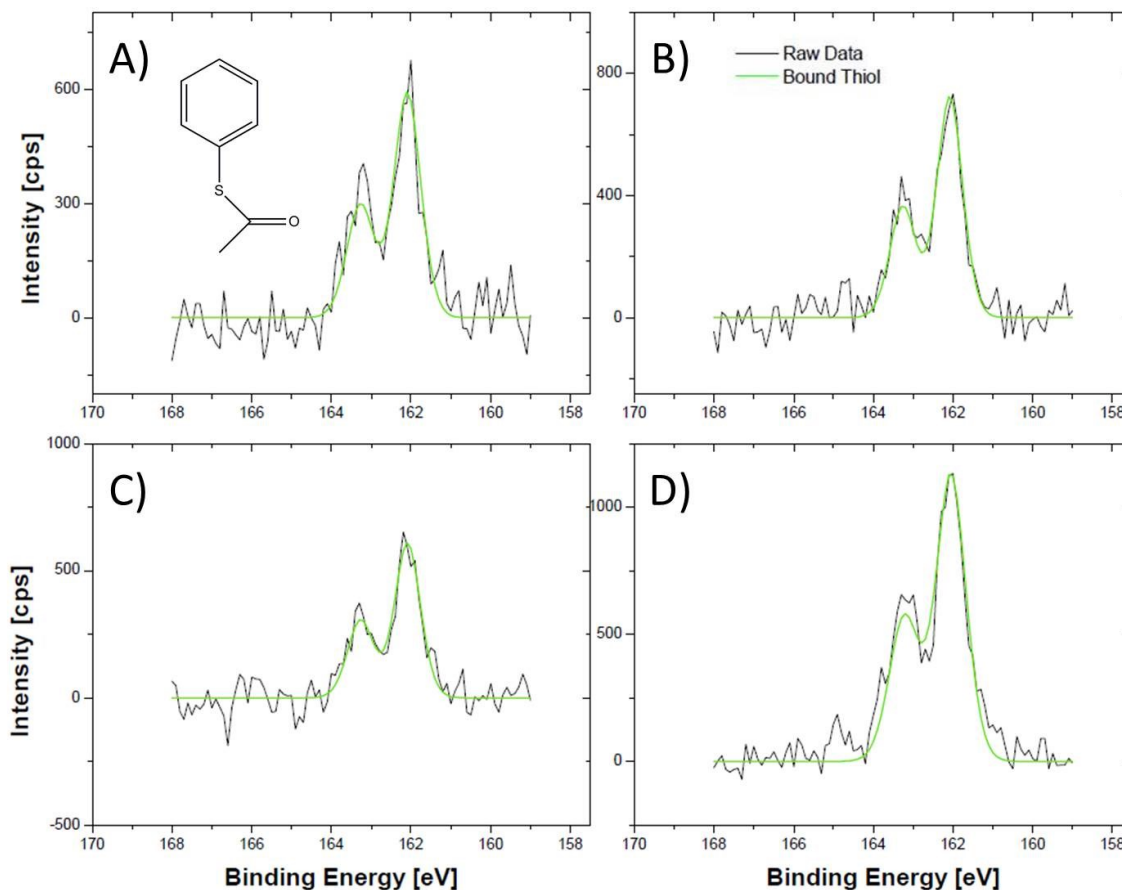


Figure 4.8 – Phenylthioacetate Monolayers on Gold

PhSAc monolayers prepared on gold surfaces under different deprotectant conditions: **A)** No NH_4OH , **B)** PhSAc: NH_4OH 1:1, **C)** PhSAc: NH_4OH 1:4, and **D)** Excess NH_4OH .

Thioacetyl (-SAc) linkers represent a protected metal binding group that can be deprotected to yield the thiol group used with monolayers like the phenylenedithiol. While losing the large metal coupling advantages offered by carbodithioates, monolayers produced from thioacetyl linkers are quickly seen to remove the issues seen with the deprotection of the CS_2 group while still maintaining the potential for metal-molecule coupling effects. Test monolayers of phenylthioacetate (PhSAc) are prepared on gold substrates (Figure 4.8). In cases of all deprotection conditions (where NH_4OH is used for deprotection), only the bound thiol signal is obtained, indicating more uniform attachment modes of the molecules onto the substrate.

Interestingly, very little effect of deprotectant concentration is observed in the XPS spectra, and what appear to be high quality monolayers can be formed from solutions without any deprotectant added, indicating that the acetyl group does not fully inhibit sulfur interaction with the metal surface. Either way, high quality monolayers can be prepared from this test system.

4.3.3 Thioacetyl Linkers in Porphyrin Monolayers

With the ability to form high quality monolayers with acetyl protected thiols, thioacetate end capped porphyrins were synthesized and tested. PZn_1 -SAC molecules were attached to a gold surface using different deprotectant conditions. As seen in Figure 4.9, monomers (PZn_1 -SAC) form high quality monolayers, possessing only bound and unbound thiol signals and lack the ‘disordered’ 161.0 eV peak seen throughout PZn_1 -CS₂. Intermediate amount of deprotectant appeared to lead to highest film quality, replicating the findings on the matter from earlier. As expected, thioacetyl capped porphyrins lead to better quality attachment of the porphyrins to the surface.

However, several further observations of these data need to be made. First, even in the best monolayers (PZn_1 :NH₄OH 1:4 condition), the raw bound thiol signal is higher in intensity than the raw unbound thiol, which indicates a monolayer with significant number of molecules lying flat with more doubly bound thiol groups. Dimers and trimers of the PZn -SAC series (Figure 4.9B, C; synthesis in Section 4.5) showed similar properties in comparing the bound to unbound thiol ratio, indicating these molecules also have a finite number of molecules lying flat and doubly bound to the gold surface. Furthermore, these longer molecules showed evidence of the 161.0 eV peak, smaller than in the carbodithioate molecules, but possibly indicating disorder in these monolayers. The peak can be optimized to the minima shown in Figure 4.9, but it is clear the binding of these longer oligomers is not as well-packed as the monomer and that this

Table 4-2 – XPS Measured Heights for PZn-SAc Series

| Molecule | Monolayer Length | | |
|-----------------------|---------------------|--------------------------|------------|
| | Measured Length (Å) | DFT Molecular Length (Å) | Tilt Angle |
| PZn ₁ -SAc | 18.1 | 28.9 | 51.2° |
| PZn ₂ -SAc | 19.8 | 39.8 | 60.2° |
| PZn ₃ -SAc | 29.2 | 50.7 | 54.8° |

* All monolayers prepared with 1:4 PZn: NH₄OH deprotectant

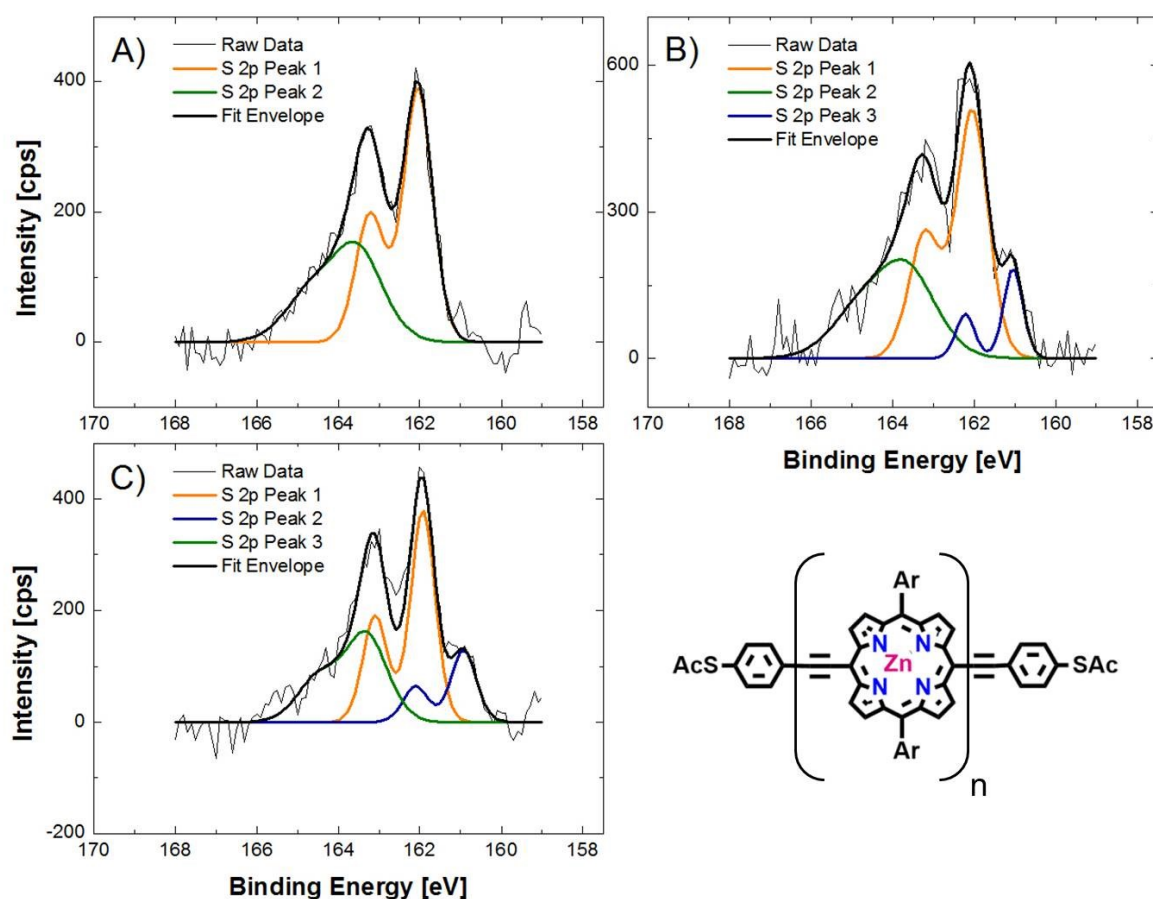


Figure 4.9 – PZn-SAc Monolayers Prepared on Gold

XPS S 2p spectra of zinc porphyrin monomers with thioacetyl linkers, for **A)** PZn₁-SAc, **B)** PZn₂-SAc, and **C)** PZn₃-SAc. All monolayers prepared under the deprotection condition of PZn: NH₄OH 1:4.

effect depends on the length of the molecule. Despite this, molecular length from the monomer to the trimer still increases (Table 4-2). Large tilt angles exist throughout the molecules, but a trend of increasing length with increasing units still exists. Increased concentration would be expected to reduce and perhaps remove the presence of the 161.0 eV peak, but to the limitations of the materials available, this represented the best films attainable. Overall, this still represents a marked improvement over CS₂ linked porphyrins.

4.3.4 *Picturing Porphyrin Wires on a Surface*

Given the data obtained where bound thiol signals are much larger than unbound thiol, we attempt to describe and explain the surface, starting with a look to the molecular interactions and size effects in the porphyrin molecule. The porphyrin molecules used in this study represent a unique system to use as a monolayer. Typically, monolayers are expected to self-assemble due to preferential intermolecular interactions and steric effects that prevent molecules from lying flat on a surface. Good packing across possibly large areas on a surface is not uncommon in systems such as alkanethiols.³⁶ However, while it is expected that the porphyrins can form monolayers, an expectation verified by the bound thiol signals shown above, the idea that these porphyrins self-assemble may be somewhat erroneous. Figure 4.10 shows the DFT calculated orientation for the PZn₁-CS₂ molecule (the CS₂ linker version of the molecule is expected to be analogous to the SAc version) and gives some evidence of why this may be the case.

Unlike most monolayers that have a much larger vertical component than horizontal, the porphyrin molecules possess bulky alkylether groups on the benzene ligands. These ligands, as shown by the calculation, stick out from the plane of the porphyrin backbone in the lowest energy configuration, measuring 13.5 Å end to end. The consequence of these ligands is that there is steric hindrance to the packing of porphyrin molecules in a monolayer. Any good packing would need to result in rotating these ligands, an effect that does not appear to happen as

seen by the bound/unbound thiol ratios. Also, because they are rotated to the plane of the porphyrin heterocycle, these solubilizing ligands provide steric hindrance to the intermolecular π - π interactions that would lead to strong packing. Though there may be a gain in the intermolecular interactions if these ligands were to rotate, the experimental evidence suggests it does not occur, and the molecules instead exhibit a large tilt toward the surface.

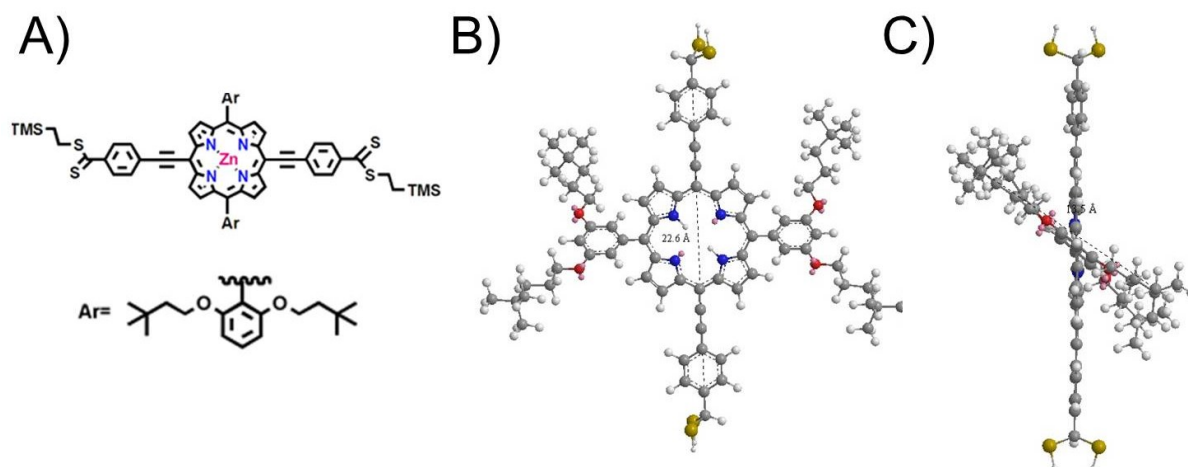


Figure 4.10 – DFT Calculated Orientation for PZn₁-CS₂

DFT calculation for orientation of PZn₁-CS₂. **A)** Molecular structure of PZn₁-CS₂. **B)** DFT calculated orientation, where gray represents carbon atoms, blue represents nitrogen atoms, red represents oxygen atoms, and yellow represents sulfur atoms. Zinc is not represented in the calculation. Length between CS₂ linkers measured to be 22.9 Å. **C)** Side view of same calculated orientation. End to end length of benzenealkylether ligands calculated to be 13.5 Å.

In lieu of this observation, it is slightly surprising that this system can have both thiol groups interact with a gold substrate. For the same reason that π - π interactions between porphyrin heterocycles appear unlikely, porphyrin heterocycles lying flat on the surface – as seen in other heterocycle systems from the literature^{16,37} – is expected to be just as unlikely. The bulky alkylether chains might have been expected to prevent heterocycles from their typical interaction on the metal surface and the lying down of the molecule. However, this clearly is happening given the bound/unbound thiol ratio. The 161.0 eV S 2p peak appearing for PZn₂- and PZn₃-SAC

may ultimately be an indication of molecules lying flat, as lack of packing/ monolayer disorder (which the peak tends to correlate with) would be further generated by longer molecules lying flat on a substrate.

In light of the information obtained about monolayer quality, Table 4-3 and Figure 4.11 attempt to provide a pictorial description of this effect on a surface. If we account for expected attenuation of the bound thiol signal based on measured monolayer height from S 2p, and calculate the actual percentage of bound thiol to unbound thiol (i.e. accounting for signal expected to be removed by attenuation of the bound thiol) using Equation (3-2), we observe that there is between 70-84% bound thiol on our substrates relative to 16-30% unbound, depending on the particular length studied (Table 4-3). Synthesizing porphyrins with different metal centers will be discussed more momentarily, but if we include information about porphyrin monomers with iron (PFe₁-SAc) and copper (PCu₁-SAc) metal centers, we see that these numbers fall close to what is observed in the PZn series.

Table 4-3 – S 2p Peak Ratios for Various PM_n-SAc Monolayers

| Molecule | Monolayer Height (Å) | Raw S 2p Ratios | | Attenuated S 2p Ratios | |
|-----------------------|----------------------|-----------------|---------------|------------------------|---------------|
| | | Bound Thiol | Unbound Thiol | Bound Thiol | Unbound Thiol |
| PZn ₁ -SAc | 18.1 | 57.5 % | 42.5 % | 70.0 % | 30.0 % |
| PZn ₂ -SAc | 19.8 | 74.2 % | 25.8 % | 84.0 % | 16.0 % |
| PZn ₃ -SAc | 29.8 | 60.9 % | 39.1 % | 79.1 % | 20.9 % |
| PFe ₁ -SAc | 25.8 | 69.1 % | 30.9 % | 83.1 % | 16.9 % |
| PCu ₁ -SAc | 17.0 | 52.2 % | 47.8 % | 64.7 % | 35.3 % |

* Attenuations calculated using Equation (3-2). All monolayers prepared from 1:4 PM_n: NH₄OH.

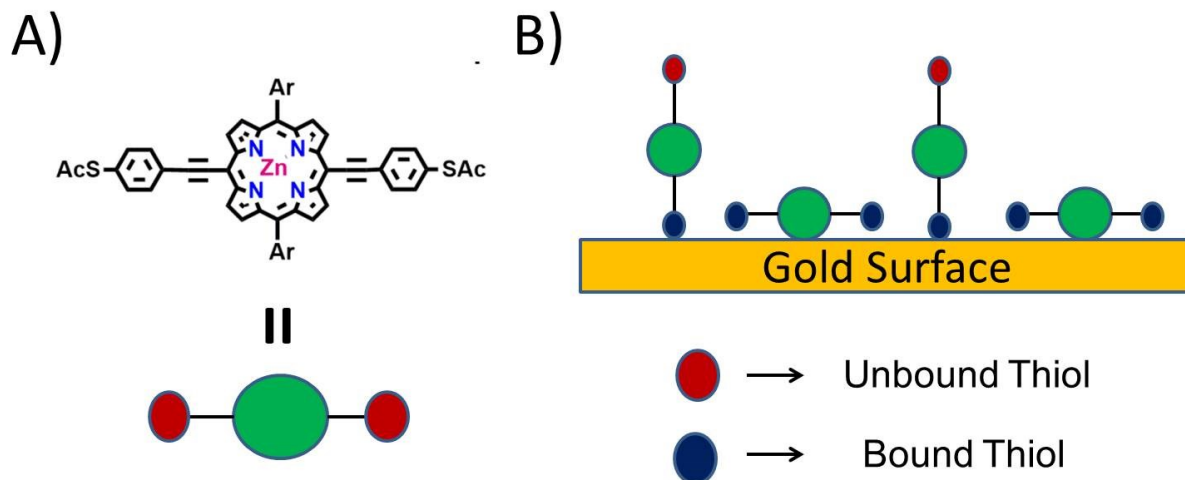


Figure 4.11 – Model of Porphyrin Wires on a Surface

Visualizing porphyrin wire attachment to a surface. **A)** Modeling the wires, separating the core (green ball) from the metal binding groups (red balls, modeled as blue if bound to surface). PZn1-SAc is used here, but the model is intended to be general for different metal centers and lengths. **B)** Proposed attachment to a surface, highlighting one molecule lying flat (both thiols bound to surface) for every molecule standing up (one bound thiol and one unbound thiol) to represent 25% unbound thiol and 75% bound thiol.

To explain the data, we take a round number and assume approximately 75% bound thiol and 25% unbound thiol are observed by S 2p, a number about in the middle of the percentages observed. Assuming these numbers to be about true, it would indicate the presence of three bound thiols for every unbound thiol on the surface. Such a scenario would indicate a monolayer where one molecule is standing up (one bound thiol, one unbound thiol) for every molecule lying flat (two bound thiols). This would likely lead to what was previously discussed, that there is not a significant amount of packing of molecules and very little intermolecular interaction.

What is interesting in this case is that we can postulate that the molecules that are standing up are not as significantly bent as expressed by the previously calculated bend angle numbers. Equation (3-2) assumes that electrons are being attenuated through a layer of non-vacuum material, and the end calculated molecular length represents essentially a sheet

thickness. However, based on the description just given from the S 2p signal, we know this is not the case. If we have sites where molecules are both standing up and lying flat, the attenuation will be different due to sites of different thicknesses of carbon-based material, and ultimately, the value we calculate from Equation (3-2) will be a weighted average of those two scenarios. What this means is that the molecules that are standing up, as indicated by the presence of unbound thiols in all porphyrin monolayers, will be a decent amount taller than the values given in Table 4-3. Calculating the exact bend to these molecules that are standing would involve a more thorough analysis with many assumptions, but what is important to us here is that these molecules are standing straighter than the monolayer thickness implies and therefore with lower bend, a factor which will be important when we begin to discuss attaching top contacts.

This picture ultimately shows that the idea of these porphyrin wires self-assembling is likely erroneous. However, we have observed an increasing thickness to the monolayers with molecular length and expressed that there are likely molecules still standing up in these monolayers. Ultimately, this gives evidence that this system may still be suited for the electrical devices intended to be produced and utilizing nanotransfer printing (nTP). As shown in Figure 4.12, nTP of 200 nm diameter gold features can be reliably and reproducibly transferred onto PZn₁-SAC monolayers on gold. Note that the nTP process as developed in this study has only shown quality transferred features on substrates with metal binding groups at the surface. The fact that pads can be transferred indicates that the unbound thiols present are sufficient to create transfer of features onto these monolayers. Nearly identical quality transfer was seen through all PZn-SAC monolayer lengths, validating our evaluation of some molecules standing up and for taking these monolayers to be used for electrical measurements.

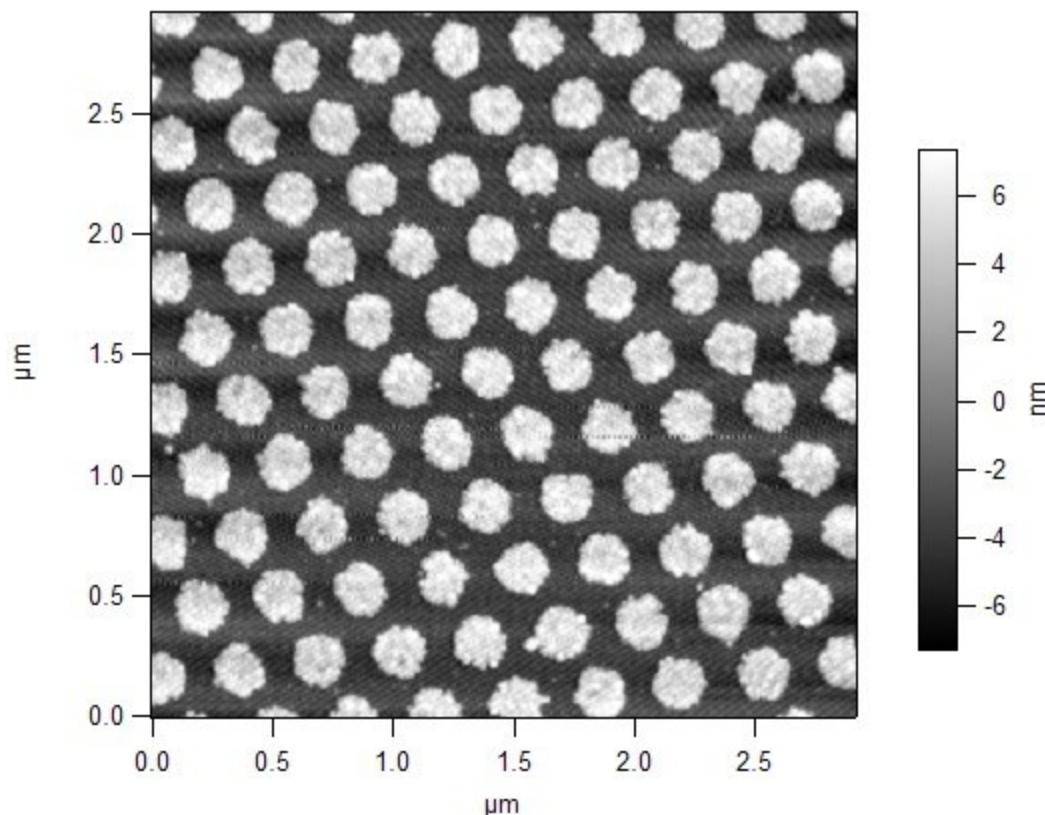


Figure 4.12 – PZn₁-SAc Nanotransfer Printed Electrodes

200 nm diameter gold pads, printed onto a monolayer of PZn₁-SAc by nTP.

4.3.5 Changing Porphyrin Metal Centers

While zinc metal centers were the standard for the studies above, in part because of the ease of inserting and maintaining constant properties in the diamagnetic metal, different metal centers are shown to be inserted into the porphyrins that are subsequently placed on a surface. Specifically, copper, nickel, and iron metals were utilized in porphyrin metal centers. These paramagnetic metals, if successfully inserted into the porphyrin wires, should provide the basis for interesting spintronic effects and spin manipulation through the molecular chains.

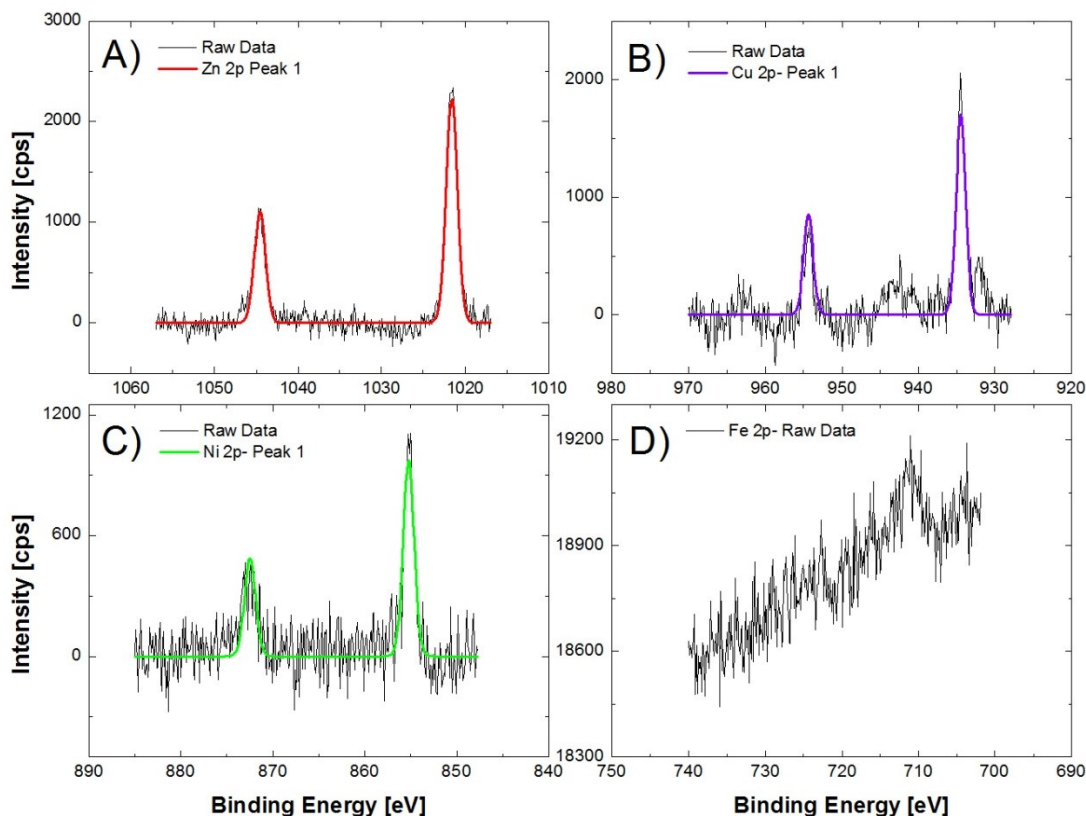


Figure 4.13 – XPS of Metal Centers for Different PM₁-SAC Species

Main metal spectra from XPS for paramagnetic metal centers in porphyrin monomer wires. **A)** Zn 2p, for PZn₁-SAC, **B)** Cu 2p, for PCu₁-SAC, **C)** Ni 2p, for PNi₁-SAC, and **D)** Fe 2p, for PFe₁-SAC.

Figure 4.13 shows XPS spectra to identify the metal center used in monomers of the zinc (PZn₁-SAC), copper (PCu₁-SAC), nickel (PNi₁-SAC), and iron (PFe₁-SAC) porphyrin wires. Zinc, copper and nickel can easily be identified in their respective monolayers. Possible oxidation effects can be seen from the presence of satellite peaks in the case of PCu₁-SAC, though these are clearly not the dominant peaks in the spectra. All monolayers were prepared under inert (nitrogen) environment, and XPS characterization was done under ultra-high vacuum. The source of the oxygen binding could have come from when the molecules were loaded into XPS; samples were exposed to air for a short period of time (< 5 mins), which could explain the results seen. The Fe 2p spectra for PFe₁-SAC monolayers, on the other hand, possess little indication of

iron above background noise. It is likely the iron was removed sometime during the monolayer formation. While unexpected, it is possible for the porphyrin heterocycles to be produced without a metal center, and it seems the solution conditions used were enough to remove the iron metal center. Length dependent studies with PFe-SAc were not done based on this finding.

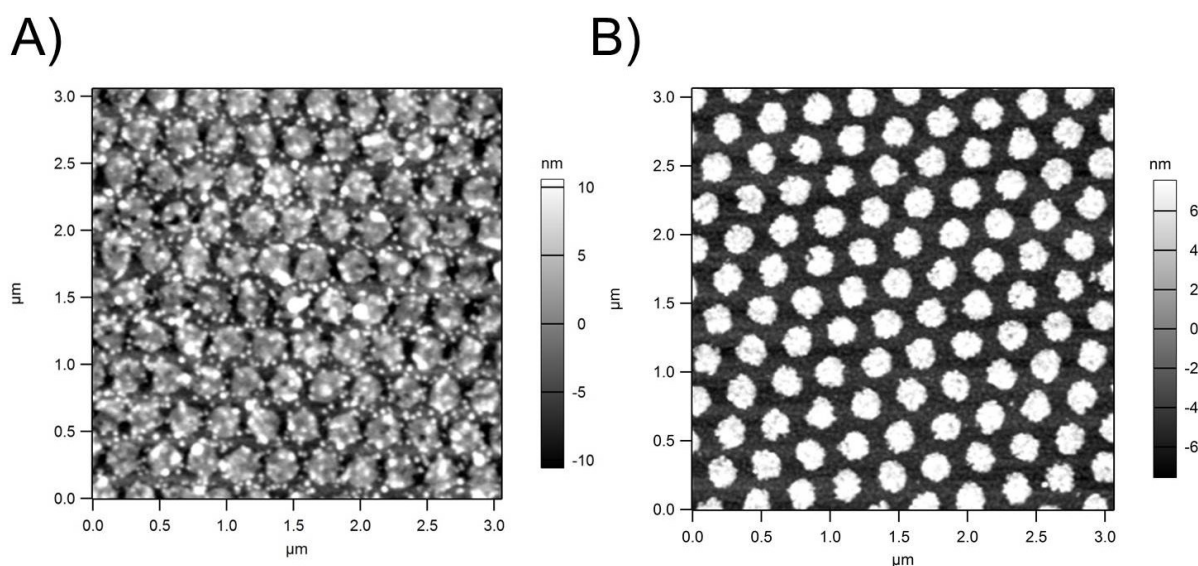


Figure 4.14 – AFM of nTP Pads on PCu₃-SAc from Different Solvents

Tapping mode AFM image of 200 nm diameter nTP pads on PCu₃-SAc monolayers, prepared from **A)** THF and **B)** DCM solution, both with 1:4 PCu₃:NH₄OH deprotectant. Significant agglomeration of PCu₃-SAc is seen from THF, and resulting electrical measurements yielded no current, whereas DCM produced monolayers on gold with no agglomeration that were used for subsequent electrical measurements.

Unlike the PZn-SAc series, PCu-SAc series appeared to have solvent dependent effects on monolayer formation. Figure 4.14A shows a substrate from PCu₃-SAc prepared from THF that has nTP pads for electrical characterization transferred. No current was seen through this device, and an explanation is apparent – there is agglomeration of the molecule on the surface. As highlighted in Table 4-4, the measured thickness of the molecule prepared from THF was longer than the DFT calculated length in the case of the dimer and trimer. A simple explanation could be that disulfides formed; however, the disulfide formation is typically oxygen catalyzed,

and preparation under inert environment should mitigate this. The likely explanation is that coordination effects from the solvent and metal center led to agglomeration, leading to a surface thicker than a monolayer. Utilizing a non-coordinating solvent, in this case dichloromethane (DCM), quickly removed these effects (Figure 4.14B). No physical agglomeration was seen in DCM substrates, and molecular lengths on the surface were more consistent with monolayer lengths seen in PZn-SAc series. PNi-SAc showed no agglomeration for either solvent.

Table 4-4 – PCu-SAc Thicknesses on Gold From Different Solvents

| Molecule | DFT Calculated Height (Å) | THF Prepared Monolayer | | DCM Prepared Monolayer | |
|-----------------------|---------------------------------|-------------------------|------------|-------------------------|------------|
| | | Monolayer Height (Å) | Tilt Angle | Monolayer Height (Å) | Tilt Angle |
| PCu ₁ -SAc | 28.9 | 18.7 | 49.7° | 15.9 | 56.6° |
| PCu ₂ -SAc | 39.8 | 80.4 | [0.0°] | 20.7 | 58.7° |
| PCu ₃ -SAc | 50.7 | 127.3 | [0.0°] | 26.4 | 58.6° |

* All monolayers prepared from 1:4 PCu_n: NH₄OH.

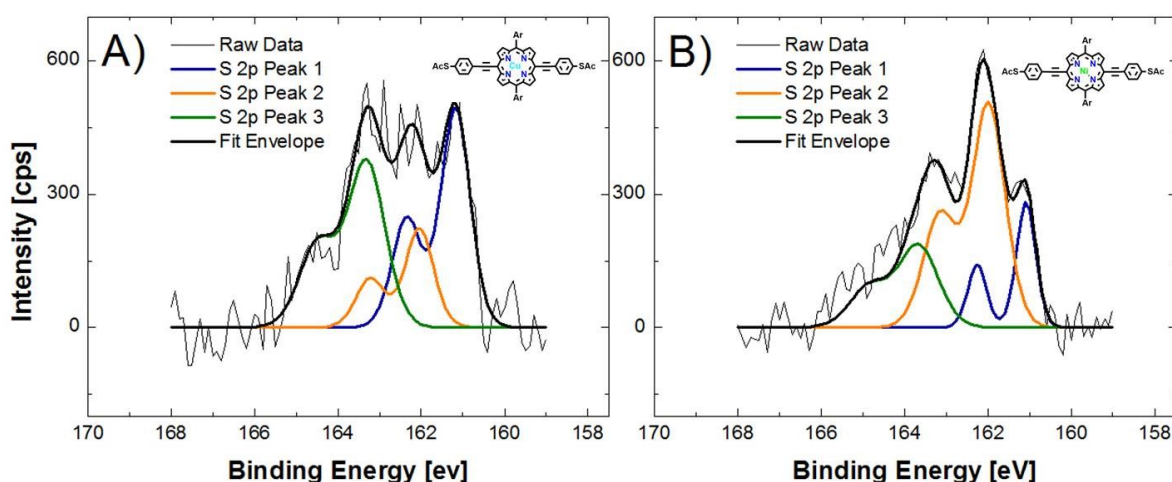


Figure 4.15 – Copper and Nickel Porphyrin Monomer Monolayers

XPS S2p spectra for monolayers of **A)** PCu₁-SAc and **B)** PNi₁-SAc.

Figure 4.15 highlights XPS S 2p spectra for PCu₁-SAc and PNi₁-SAc molecules. While optimized conditions for the PZn-SAc series removed the 161 eV peak in the monomer, some evidence of this peak could be seen in the PNi₁ and PCu₁ molecules. The explanation for this is unclear. It is possible metal effects from different molecules in solution prevented the molecules from orienting in the ideal metal binding configuration, perhaps similar to the influences that lead to PCu agglomeration from THF. However, good length for the monomers is determined via Au 4f attenuation, so we proceed forward with these monomers.

4.3.6 Nanotransfer Printed Porphyrin Oligomer Wire Devices

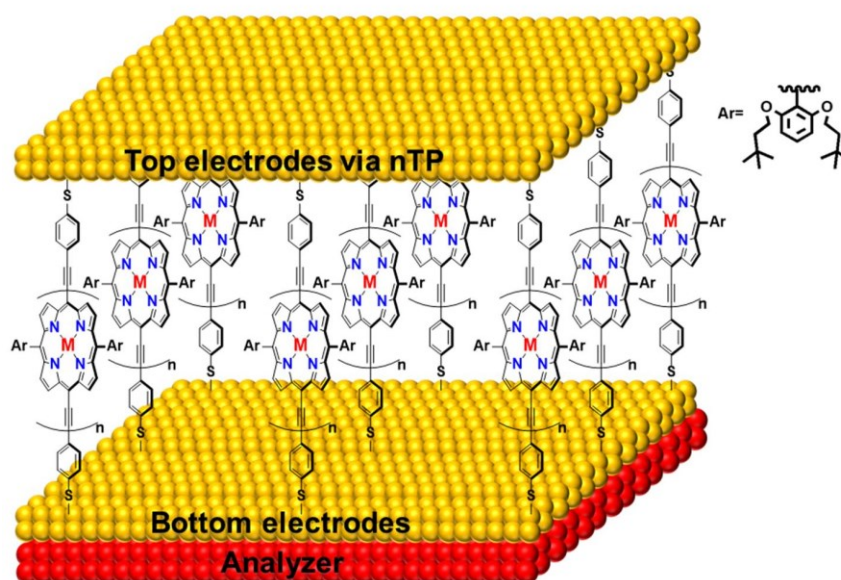


Figure 4.16 – nTP Junction with PM_n-SAc Monolayer

Diagram of nTP junction incorporating porphyrin monolayers. “Ar” represents the benzenealkylether solubilizing group off the porphyrin heterocycle.

With the ability to nanotransfer print gold features onto monolayers of porphyrins, we now turn to electrical measurements. Figure 4.17 shows length dependent transport measurements for PZn-SAc series (monomer through trimer) in nTP junctions, measured by the

nTP characterization method (cAFM tip on 200 nm nTP pad). Resistance of the electrical measurements was taken from the slope of the linear portion of the IV measurements (-0.1 V to 0.1 V). For each data point, over 100 devices from three or more samples were obtained and analyzed. Plotting the resistance values against natural log of resistance allows us to apply Equation (3-1) and extrapolate the β for the PZn series, yielding $\beta_{\text{PZn-SAc}} = 0.048 \text{ \AA}^{-1}$ for PZn in the nTP junctions. We should note that this is an extremely low β for organic monolayers, an occurrence which is seen in a few organic systems³⁸ but is, overall, rather rare. In this case, such a low value is expected due to the near-Ohmic properties measured in STM junctions of the same molecule.¹³ In fact, when we directly compare this result to that obtained by single molecule STM break junctions (blue curve in Figure 4.17), which yielded $\beta = 0.034 \text{ \AA}^{-1}$, we see that the values obtained in are ‘bulk’ nTP junctions are nearly identical to the single molecule measurements. This is an exciting finding, and one of the rare instances in literature that bulk electrical measurements of organic monolayers are directly correlated to measured single molecule properties. This validates the use of nTP characterization for the porphyrins and provides promise that changes to the electrical properties of the wires via changing metal center should be measurable with this device architecture.

An interesting comment to be made regarding the analogous single molecule and bulk junction measurements is that the poor packing of the monolayers may contribute to the similarities of the results obtained from these two architectures. With so many molecules lying flat and the large solubilizing groups providing steric hindrance, intermolecular interactions are unlikely to be present in the bulk film. This will allow the same factors that determine the single molecule measurements to be prevalent in the bulk nTP measurements. This is different from the β drop in phenylenedithiol junctions in Chapter 3 where we have identified the potential for

intermolecular interactions to become prevalent in nTP junctions. Because of the factors preventing intermolecular interactions in porphyrins, it is possible that these effects will not become prevalent. Or perhaps, intermolecular interactions in porphyrin devices are present in both the single molecule and bulk devices, leading to β being extremely low for both. Temperature dependent measurements, a goal of future work, will help elucidate this further. Either way, nTP junctions appear to exhibit the same molecular interactions as the single molecule level, and as such they are able to reproduce the electrical properties of PZn-SAc break junction measurements, providing verification that the nTP technique can generate reliable junctions for specialized and non-ideal molecules such as the porphyrins.

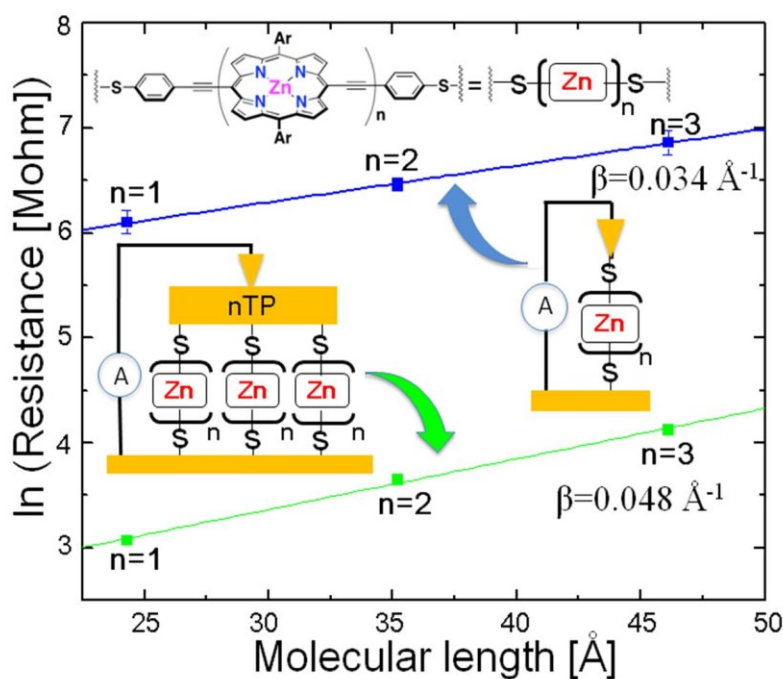


Figure 4.17 – Measured Electrical Devices for PZn-SAc Series

Resistances of electrical junctions incorporating PZn_n-SAc molecules for ($n = 1-3$), measured using STM-break junction (blue line)¹³ and nTP characterization (green line).

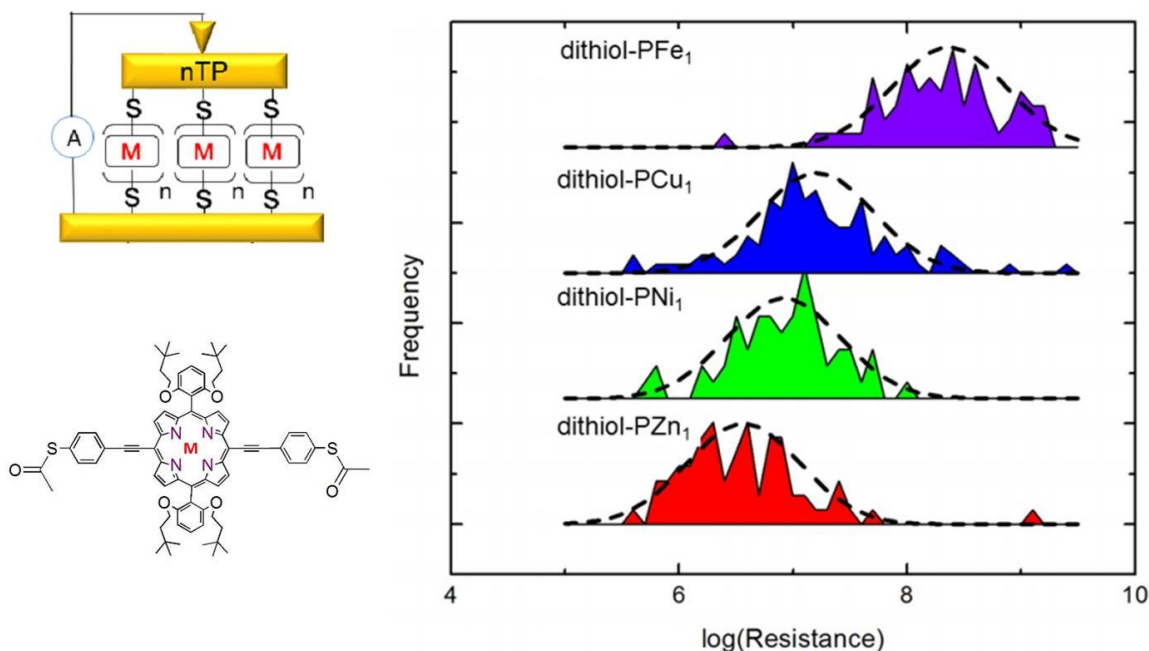


Figure 4.18 – Histograms for PM₁-SAC nTP Junctions

Electrical outputs for PM₁-SAC monolayers, prepared and characterized by nTP characterization. Left: diagram of nTP junction, and representative molecular image of molecule, with M = Zn, Ni, Cu, or Fe. Right: Normalized histograms of conductance output for different metal centers.

The next test is to see if different metal centers affect the charge transport properties of the resulting devices. Figure 4.18 shows normalized histograms of resistance for porphyrin monomers with different metal centers (PM₁-SAC, where M = Zn, Cu, Ni, Fe). Strikingly, different average conductance values are obtained for each different metal, showing that inserting different metal centers into porphyrins leads to different electrical properties in the wires. Again, this is exciting because it means impacting the properties of the metal center will affect the electrical and, potentially, spin properties of the porphyrin molecular wires.

As a note, PFe₁-SAC molecules may not actually possess any iron when put onto a surface, so the wires attributed to the iron metal center may actually represent the metal-less porphyrin molecule. The fact that this molecule yields the most resistive results may provide

evidence that charge transport goes through and is dependent upon the metal center, though this may be redundant given that the other metal centers also yield measurable impacts on charge transport. Altogether, this provides evidence that altering the metal center changes charge transport properties through the wire.

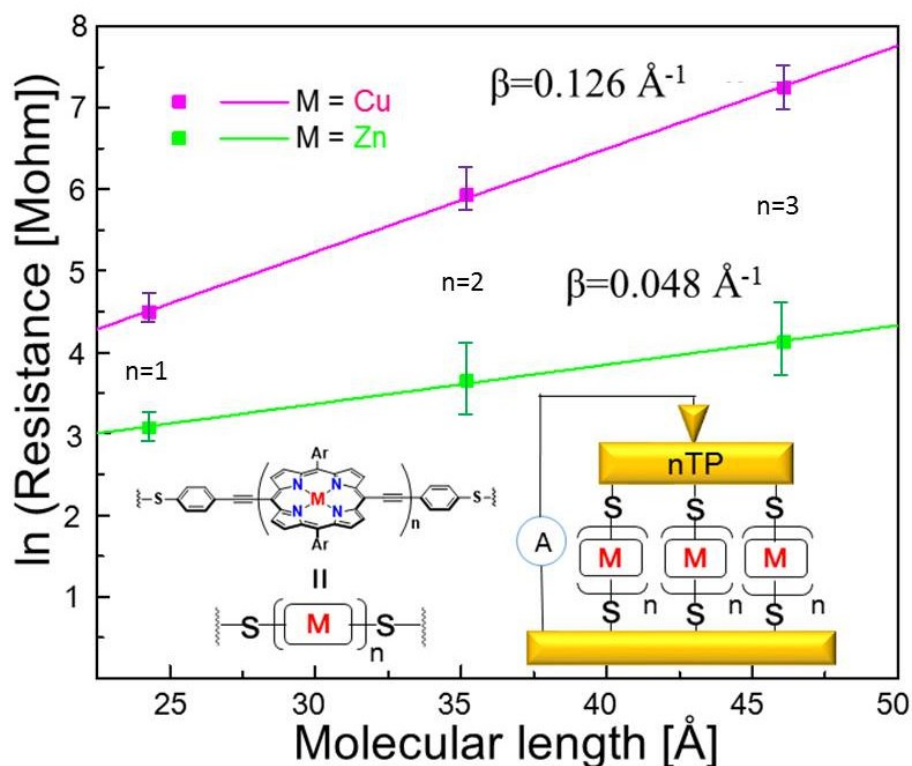


Figure 4.19 – Length Dependent Resistance for PM_n-SAc Junctions

PZn_n-SAc (green) and PCu_n-SAc (purple) electrical properties based on molecular trend ($n = 1-3$). Analyzing these curves using Equation (3-1) yields $\beta_{\text{PZn}} = 0.048 \text{ Å}^{-1}$ and $\beta_{\text{PCu}} = 0.126 \text{ Å}^{-1}$.

Beyond monomer measurements, the length dependent measurements of different metal centers also support the analysis that metal center changes charge transport properties. Figure 4.19 compares the output from PCu-SAc monomers through trimers to analogous PZn-SAc molecules. Comparing the length dependence of each series and comparing β values shows that different β values are obtained. For PCu-SAc, β_{PCu} is measured to be 0.126 Å^{-1} , a value more

than double that obtained for the PZn-SAc series ($\beta_{\text{PZn}} = 0.048 \text{ \AA}^{-1}$). This corroborates the trends seen in the porphyrin monomers, where resistance of PCu₁-SAc was greater than that from PZn₁-SAc. A point of note is that extrapolating the length trends of resistance to zero length to obtain the contact resistance of the wires (R_0) yields similar values for both the PZn and PCu wires ($R_{0,\text{PZn}} = 6.7 \text{ M}\Omega$; $R_{0,\text{PCu}} = 4.5 \text{ M}\Omega$). This indicates these β changes are predominantly from the properties of the wires. More exciting than this, the altered β implies that the nature of the charge transport through these different metal center wires may be changed. Higher β is correlated with a more tunneling-like transport property, and could simply reflect the fact that the copper has changed the energy levels of the porphyrin wire, or that the copper molecule couples to the porphyrin backbone differently and changes the transport from less Ohmic to perhaps more charge hopping. It is worth noting that in the realm of organic electronics, the β_{PCu} is still quite low and still likely reflects the large conjugation and possibly long polaron delocalization length seen in the PZn series. From a zeroth order standpoint, no matter what the effect, this experiment has definitively shown that changing the metal center can directly affect the transport properties of the porphyrin wires.

4.3.7 UPS Measurements of Porphyrin Monolayers

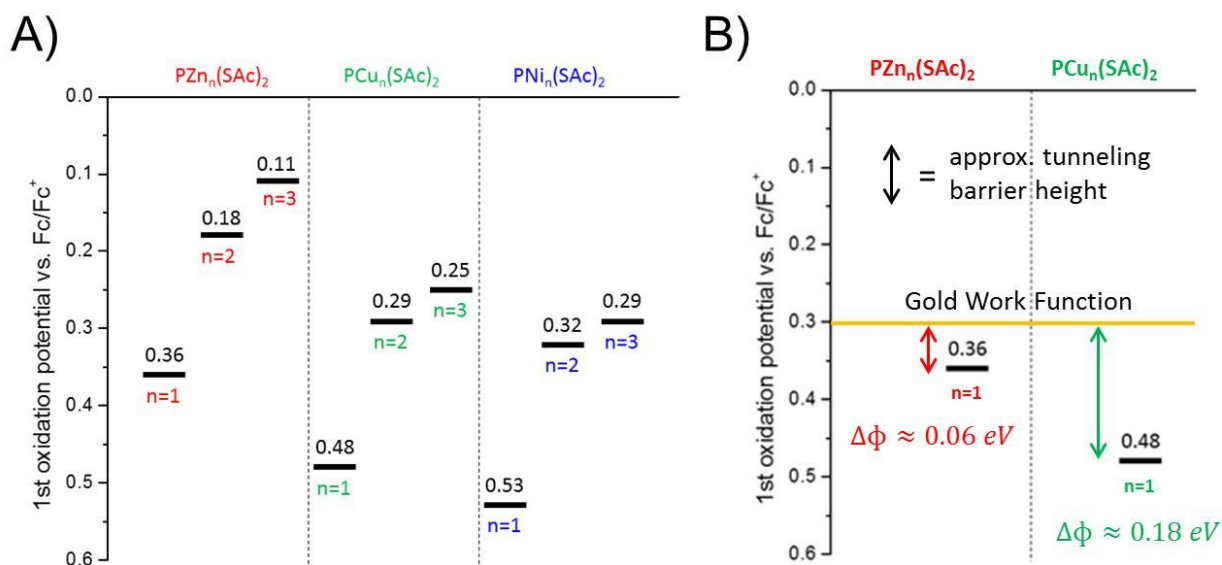


Figure 4.20 – Cyclic Voltammetry Data for Porphyrin Wires

Cyclic voltammetry data for PM_n -SAc solid ($M = Zn, Cu, Ni$; $n = 1 - 3$) taken in DCM. **A)** Identification of HOMO level (1st oxidation potential) relative to oxidation of ferrocene (Fc/Fc^+). **B)** Comparison of PZn_1 -SAc and PCu_1 -SAc HOMO relative to literature work function of gold (5.1 eV).

To provide a possible justification for the results seen thus far, we take a look at the energy levels for the porphyrin wires and look for shifts in the measured highest occupied molecular orbital (HOMO) levels where transport is expected to be mediated. First, these energy levels are measured in solution. Figure 4.20A shows the cyclic voltammetry (CV) measured first oxidation potential (HOMO) for the porphyrin solids in solution. Also referenced on the plot is the gold work function energy from literature, a value that was confirmed by subsequent UPS measurements (Table 4-5). Insofar as these individual values allow us to compare, it appears the copper metal center porphyrin as compared through the monomer HOMO energy level is further from the work function of gold than the zinc metal center porphyrin. Such a consequence would mean, in a basic tunneling model, that copper would have a larger β in charge transport

measurements due to the larger barrier height. This matches the experimental trend seen, where again $\beta_{\text{PCu}} > \beta_{\text{PZn}}$.

Despite the picture given in the previous section, a true evaluation of energy levels needs to come from the monolayer in a device configuration, i.e. on the gold substrate. It is known that dipole and other metal-molecule interactions will affect energy levels on a surface, sometimes leading to emergence of new energy levels due to hybridization and other interactions.³⁹ In order to understand these effects if they are occurring in these porphyrin monolayers, we must experimentally measure the samples of porphyrins on gold and measure their valence energy levels. Such an evaluation can be done through UPS. Though we are somewhat limited because we cannot characterize the molecule with two electrodes due to a physical shielding of the molecule to incident beams, we can still evaluate the monolayer on a gold surface and obtain some evidence of the molecule nature in device configuration.

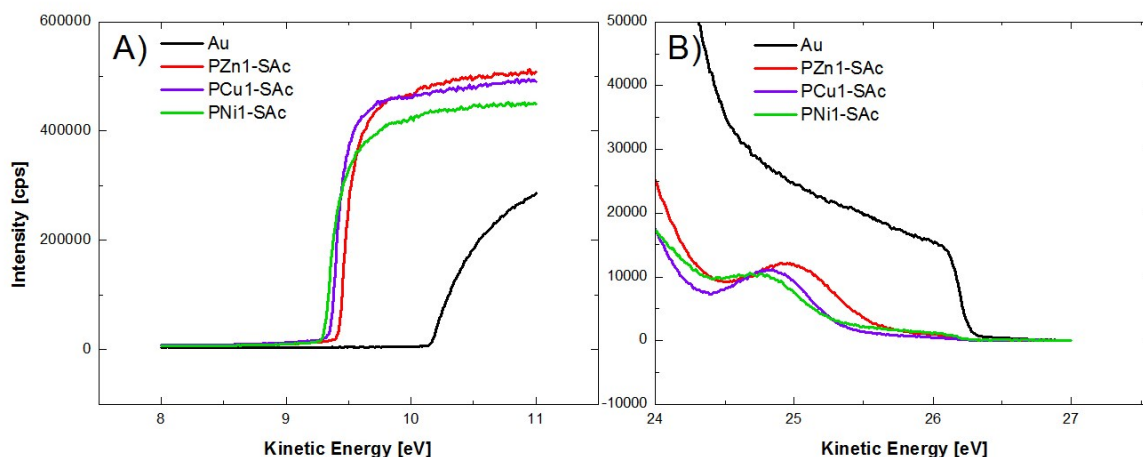


Figure 4.21 – UPS of Porphyrin Monomers

UPS of porphyrin monomers on gold, with bare Au sample for reference. **A)** Cutoff region (low kinetic energy), used to determine work function. **B)** High kinetic energy region, used to determine $E_F - E_{\text{HOMO}}$.

Monolayers of porphyrin monomers with Zn, Ni, and Cu metal centers are prepared on gold substrates, and their UPS results for these monolayers alongside a gold layer for reference

are shown in Figure 4.21. All monomers are short enough that the Fermi level from gold, identified at a kinetic energy of 26.2 eV, can be seen in the spectra, allowing for a reference point for all energy levels. There are two regions of interest in these UPS spectra. First, we look at the low kinetic energy (KE) side of the spectra, also known as the cutoff region. The cutoff region will indicate the work function of the monolayers on gold. By extrapolating a linear baseline, we can estimate the onset energy and thereby the work function (ϕ_{SAM}) by taking into account the energies of the source and the measured Fermi level:

$$\phi_{SAM} = E_{source} - E_F + E_{cutoff} \quad (4-1)$$

where E_F is the aforementioned Fermi energy of 26.2, E_{source} is the energy of the electron from the He (I) source (21.2 eV), and E_{cutoff} is the measured high KE cutoff on the spectra. Each metal appears to yield a different ϕ_{SAM} , with the values compiled in Table 4-5, though the measured work functions are all within 0.1 eV of one another.

Table 4-5 – Statistics Derived from UPS Spectra

| Molecule | Fermi Energy (eV) | Cutoff Energy (eV) | ϕ_{SAM} (eV) | $\Delta\phi_{SAM}$ (eV) | HOMO Peak Onset (eV) | $E_F - E_{HOMO}$ (eV) |
|-----------------------|-------------------|--------------------|-------------------|-------------------------|----------------------|-----------------------|
| Au | 26.2 | 10.14 | 5.14 | - | - | - |
| PZn ₁ -SAC | - | 9.26 | 4.26 | 0.88 | 25.78 | 0.42 |
| PCu ₁ -SAC | - | 9.19 | 4.19 | 0.95 | 25.62 | 0.58 |
| PNi ₁ -SAC | - | 9.18 | 4.18 | 0.96 | 25.55 | 0.65 |

The other region of interest lies on the high KE side, close to the Fermi level. Distinct peaks for all porphyrin monomers can be seen with an onset of around 25.2 to 25.5 eV that are not in the background gold films. These appear to correspond to the HOMO levels for the

porphyrin monomers. Interestingly enough, the relative energy shifts of these peaks seem to correspond to the shifts seen in the CV results. Evaluating their shifts relative to the Fermi level ($E_F - E_{HOMO}$) should give the critical value that comments on the barrier height and therefore the β for each junction. As expressed in Table 4-5, the barrier heights in fact do increase from PZn to PCu. The barrier heights estimated from the CV results seems to be larger than what we expect given the ultralow attenuation and low β values measured in the junctions. However the trend still verifies the experimental results where $\beta_{Cu} > \beta_{Zn}$.

These two results – the ultralow β from cAFM studies and the finite barrier height from UPS – need to be rationalized, as the attenuation values seen from cAFM studies would very likely be too small to be explained by a tunneling device with $\phi \cong 0.4 - 0.6$ eV as observed by UPS. To do this, we can examine the porphyrin molecule in a multibarrier model. β ultimately comments on the length dependence in the entire molecular junctions, and we know from the large conjugation and polaron delocalization lengths from previous PZn-SAc studies¹² that there is strong electron transport along the porphyrin backbone. Therefore, while the electron exists along the porphyrin ring, very little attenuation occurs. It would appear then that the barrier height comes predominantly from injection into the molecule at the molecular interface, accounting for the $E_F - E_{HOMO}$ values. This effect could be caused, in part, by the thiol linker group. Different reports cite the β_{thiol} to be either around 1.00 \AA^{-1} using cAFM⁴⁰⁻⁴² or around 0.05 \AA^{-1} in large area junctions.⁴³ These values are drastically different from one another, and perhaps comment on different effects of architecture and interfaces in molecular electronic devices. Either way, the extremely low β measured through the porphyrin wires would lead to the idea that the interface barrier and attenuation are very likely larger than through the molecule. While relevant, this alone would not explain our findings of lower and alterable β values.

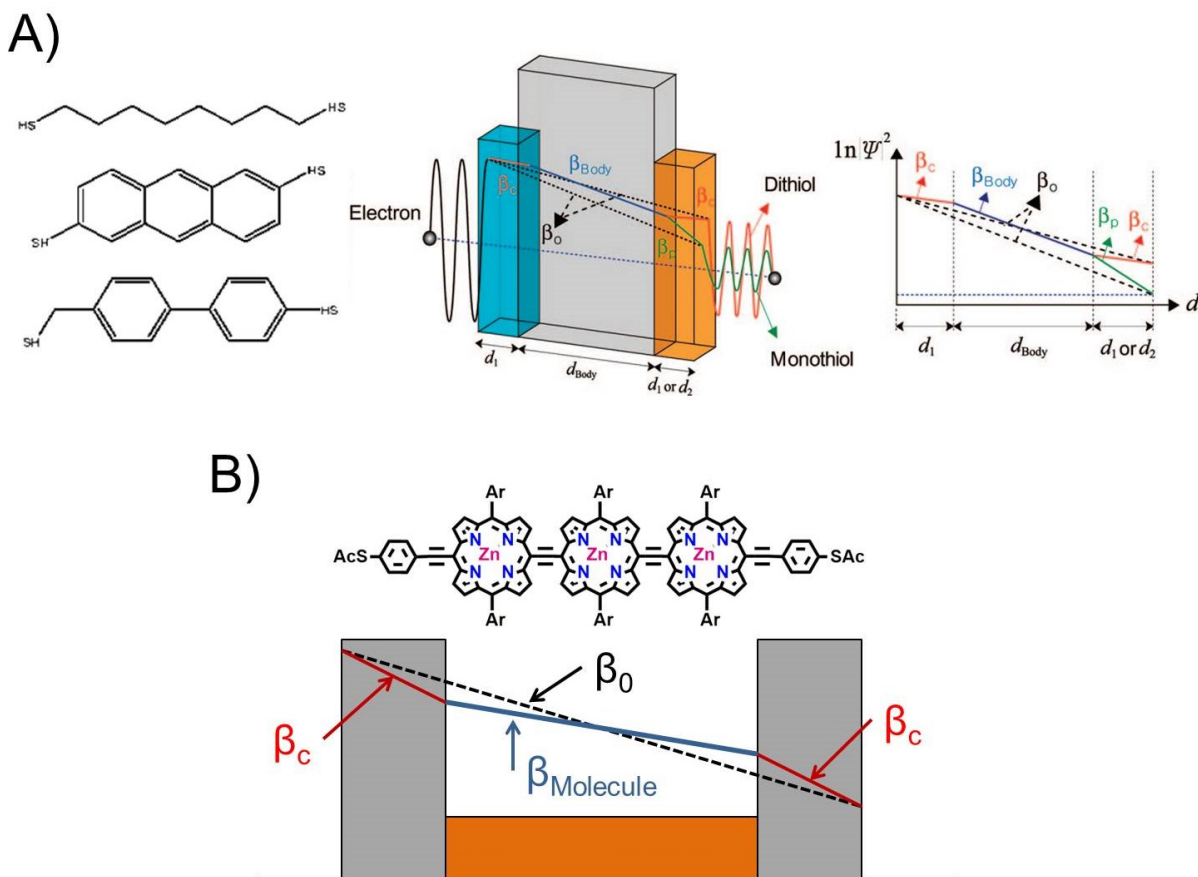


Figure 4.22 – Multibarrier Model for Molecules with Metal Binding Groups

Multibarrier model, depicting tunneling effects that differ through molecule and metal binding group. **A)** Model for most tunneling molecules, including alkane-, acene-, and phenyldithiols, where the average measured β_0 is determined by two factors, the tunneling through each linker (β_c for chemically bounded contacts, and β_p for physically bound contacts), and tunneling through the molecule (β_{Body}), where $\beta_{\text{Body}} > \beta_c$, reflecting the barrier height inside the molecule (ϕ_{Body}) being greater than in the linker (ϕ_{Linker}). Adapted with permission from Ref. 43, Copyright 2008 American Chemical Society. **B)** Model for the porphyrin oligomer wires, where the effective β_{Molecule} is lower than β_c , pictorially represents where $\phi_{\text{Linker}} > \phi_{\text{Molecule}}$.

A more general description to explain our results would highlight the difference in energy levels of the gold and molecule as a whole and the tunneling-like behavior caused by the need to overcome this barrier (even if it is small) in conjunction with the excellent transport properties along the molecule. This description would again focus on the ability of the molecule to enable charge transport, so perhaps the initial difference in energy levels (the $\phi \cong 0.4 - 0.6$ eV) would

come into play, but the effective length of this difference in barrier height would be much shorter than the length of the wire due to more resonant and cooperative transport along the chain. Little attenuation along the chain would occur but β would still be reflected by the injection of the hole (electron) into the wire and the barrier height needed to do so. This would explain the results seen here, where β for the whole junction can be different for different porphyrin series due to changes in the energy level and therefore the initial injection barrier of holes into the wires.

Figure 4.22 shows a visualization of this effect, pictorially highlighting the unique nature of this organic-based system where the decay effects from transport do not appear to predominantly occur along the molecule backbone. This is an exciting finding because the small backbone attenuation seen thus far will presumably allow even small changes to the transport properties along the backbone to have a dramatic effect on the overall transport. For example, even if the effects from the paramagnetic metal centers are small, any effects or preference for different spins could lead to small changes in barrier heights for the transport and therefore large changes in observed resistance for the two different pathways, an effect augmented by the long length in the porphyrin wires and the multiple metal centers to be incorporated into them. Temperature dependent measurements will ultimately shed more light on the charge transport properties of the system and comment on this proposed diagram. Regardless, what is clear from this work is that, despite the lower attenuation along the backbone relative to the interface/charge injection effects, we still clearly see different results in these devices as evidenced by different β values for different metal centers that is controlled by the different metal center species and corresponds to the changing HOMO levels of the metals. For now, the picture that this molecule is both highly conductive and tunable appears to be verified, providing an exciting future for studies with this system.

4.4 Conclusions

In conclusion, porphyrin wires with different metal centers, both diamagnetic and paramagnetic, were prepared on gold surfaces. Carbodithioate (CS₂) porphyrins were first tested, though these molecules appeared to have more complex binding modes than seen in other monolayers, exhibiting a 161.0 eV peak in the S 2p spectra that is assigned to a low density sulfur-gold binding mode. Test studies on basic CS₂ monolayers showed that this peak was associated with deprotection of an ETMS group, necessary due to the large oxygen sensitivity of the metal linker group, with non-protected carbodithioates showing only the bound thiol signal and matching literature spectra. In light of this, thioacetyl capped porphyrins were instead studied, yielding much more reliable sulfur signals that indicate better monolayer quality. A larger portion of the thiols in these monolayers appeared to be bound to a gold surface. Analyzing the DFT calculated configuration of the molecule indicates that this likely comes from steric hindrances from the benzenealkylether ligands, hindering possible intermolecular interactions and reducing the ability of the molecule to pack. However, understanding the interplay between increased bound thiol signal versus molecular thickness leads to a model where a finite number of molecules are standing in a much more vertical position off of the surface, a model verified by the ability to transfer gold pads onto the standing metal binding groups.

With ability to transfer nTP pads verified, electrical transport was studied in porphyrin molecules of different length and metal center. PZn-SAc molecules yielded extremely low attenuation values ($\beta_{\text{PZn}} = 0.048 \text{ \AA}^{-1}$), which is nearly identical to the single molecule measurements in literature, indicating the ability of ‘bulk’ nTP junctions to exhibit the single molecule properties of the porphyrin wires. That these junctions are able to exhibit porphyrin molecular properties was further shown by altering metal center, yielding different conductances

with different metal center. Length dependence of PZn-SAc and PCu-SAc junctions was also studied, yielding different β for the different molecular wires. The measured β were related to the difference in the HOMOs of the molecules, shown both via CV and by UPS, verifying the trend of $\beta_{\text{PCu}} > \beta_{\text{PZn}}$. Finally, we extend the multitunneling barrier to fuse the observations of finite barrier height from $E_{\text{F}} - E_{\text{HOMO}}$ in the UPS experiment and the low β from length dependent cAFM results, postulating that tunneling properties come from injection into the molecule, but that the low β highlights the low attenuation along the molecular wire, showing a rare case in molecular electronics where attenuation along an organic molecule can be smaller than attenuation from an interface and/or charge injection.

Future work will focus upon incorporating different metal centers into these studies. While initial studies with PFe molecules yielded porphyrins with no metal center, modifications to synthetic procedures and attaching different groups, such as oxygen or chlorine, to the metal center may prevent it from being removed. Also to be accomplished are temperature dependent and spin measurements of these systems. The capabilities necessary for these measurements went beyond what we were able to do with the in-house cAFM and 200 nm nTP pads. Chapter 5 focuses on adapting nTP and other soft lithography techniques to macroscopically accessible junctions that can be inserted into cryostat setups for temperature dependent measurements and spin injection studies.

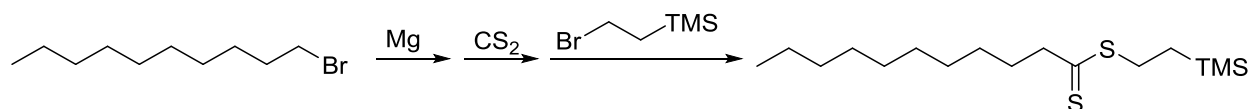
4.5 Appendix

4.5.1 Synthetic Schemes

General methods.

1-Bromodecane, bromobenzene, magnesium filing, and (2-bromoethyl)trimethylsilane were received from commercial suppliers (Acros Organics, Sigma-Aldrich and TCI) and used without further purification. Anhydrous THF was obtained by distillation from sodium/benzophenone prior to use. Carbon disulfide was dried over magnesium sulfate prior to use. ^1H nuclear magnetic resonance (NMR) spectra were obtained at Bruker 400 MHz DRX spectrometer as solutions in CDCl_3 . Chemical shifts are reported in parts per million (ppm, δ) and referenced from tetramethylsilane.

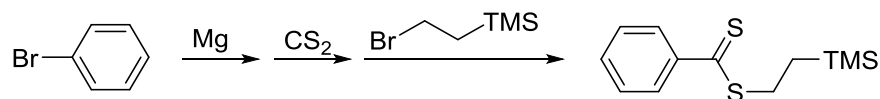
2-(Trimethylsilyl)ethyl undecanedithioate.



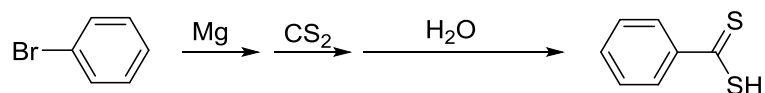
Under argon atmosphere, a solution of 1-bromodecane (0.664 g, 3.0 mmol) in anhydrous THF (~50 mL) was added dropwise onto stirring magnesium filings (0.087 g, 3.6 mmol) in a flame-dried 100 mL flask equipped with condenser. In the case where no bubbling was observed on the surface of magnesium filings, one drop of 1,2-dibromoethane was added to initiate Grignard reagent. After complete addition, the reaction mixture was refluxed for four hours. The reaction mixture was then cooled to room temperature. Dried carbon disulfide (0.571 g, 7.5 mmol) was added in one portion, and the reaction mixture turned orange (or red if the concentration was high). After one hour of stirring, (2-bromoethyl)trimethylsilane (0.725 g, 4.0 mmol) was added in one portion, and the reaction was further stirred for two hours. The reaction mixture was then washed with brine for three times, dried over sodium sulfate, filtered, concentrated, and purified

over silica column with hexane as eluent, yielding the title compound as a yellow oil (0.300 g, 0.9 mmol, 31% yield). **¹H NMR** (400 MHz, CDCl₃), δ : 3.23-3.18 (m, 2H), 2.99 (t, J = 7.6 Hz, 2H), 1.81 (quin, J = 7.6 Hz, 2H), 1.35-1.26 (m, 16H), 0.96-0.92 (m, 2H), 0.88 (t, J = 6.4 Hz, 3H), 0.07 (s, 9H).

2-(Trimethylsilyl)ethyl benzodithioate.

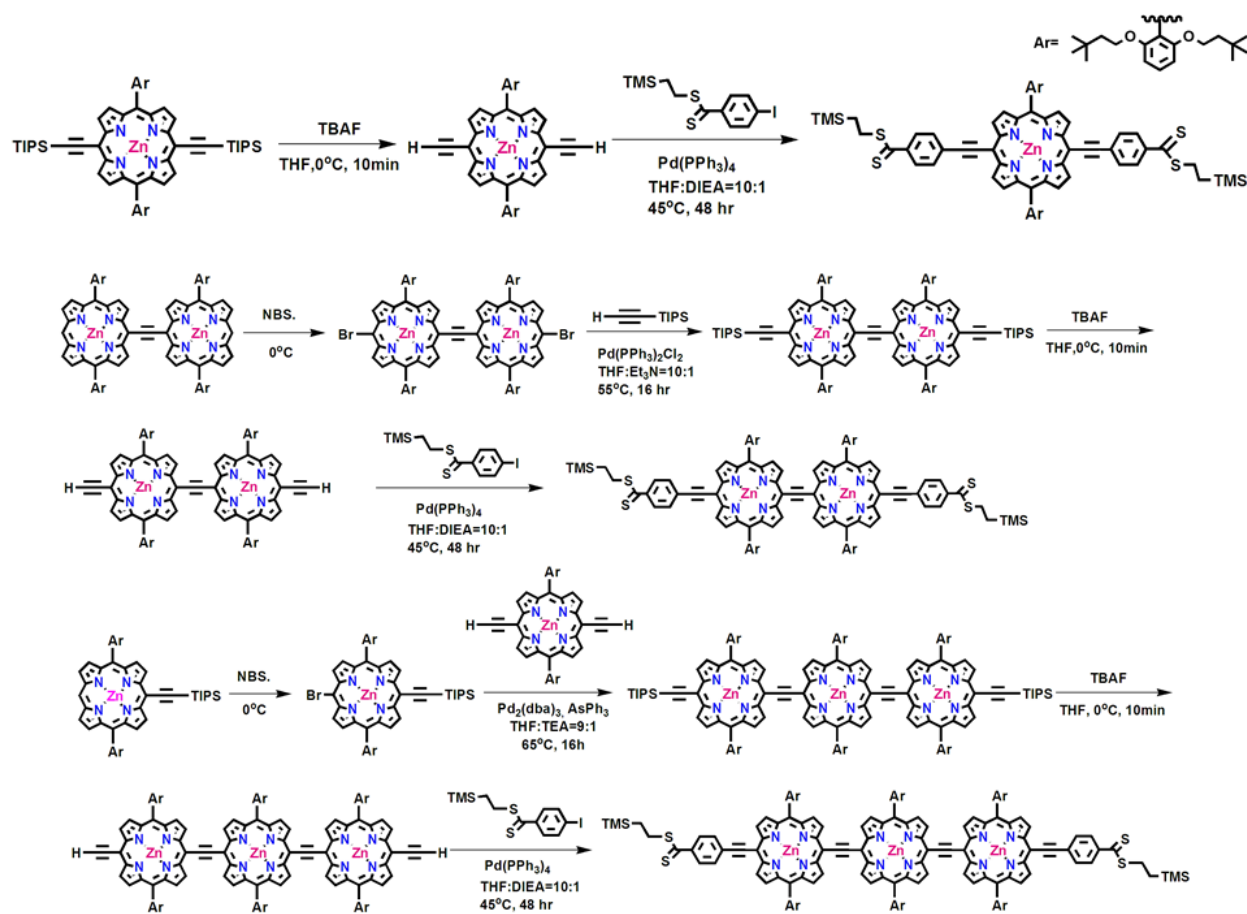


In a two-neck flask equipped with condenser was charged magnesium filings (0.145 g, 5.97 mmol) and filled with argon. Anhydrous THF (~ 100 mL) and bromobenzene (0.853 g, 5.43 mmol) were added in one portion. The mixture was refluxed for two hours before cooling to -78 °C. Dried carbon disulfide (0.486 g, 6.52 mmol) was added in one portion under -78 °C. After stirring for one hour, (2-bromoethyl)trimethylsilane was added in one portion and slowly warmed to room temperature. After stirring for one hour, the reaction was quenched by saturated ammonium chloride aqueous solution, and extracted with ethyl acetate. After drying and concentration, the crude product was then dissolved in a small amount of hexane and passed through a silica plug with hexane as eluent to yield the title compound (0.422 g, 1.66 mmol, 31% yield). **¹H NMR** (400 MHz, MeOD), δ : 7.91-7.88 (m, 2H), 7.50-7.42 (m, 1H), 7.46-7.31 (m, 2H), 3.34 (m, 2H), 1.00 (m, 2H), 0.04 (s, 9H).

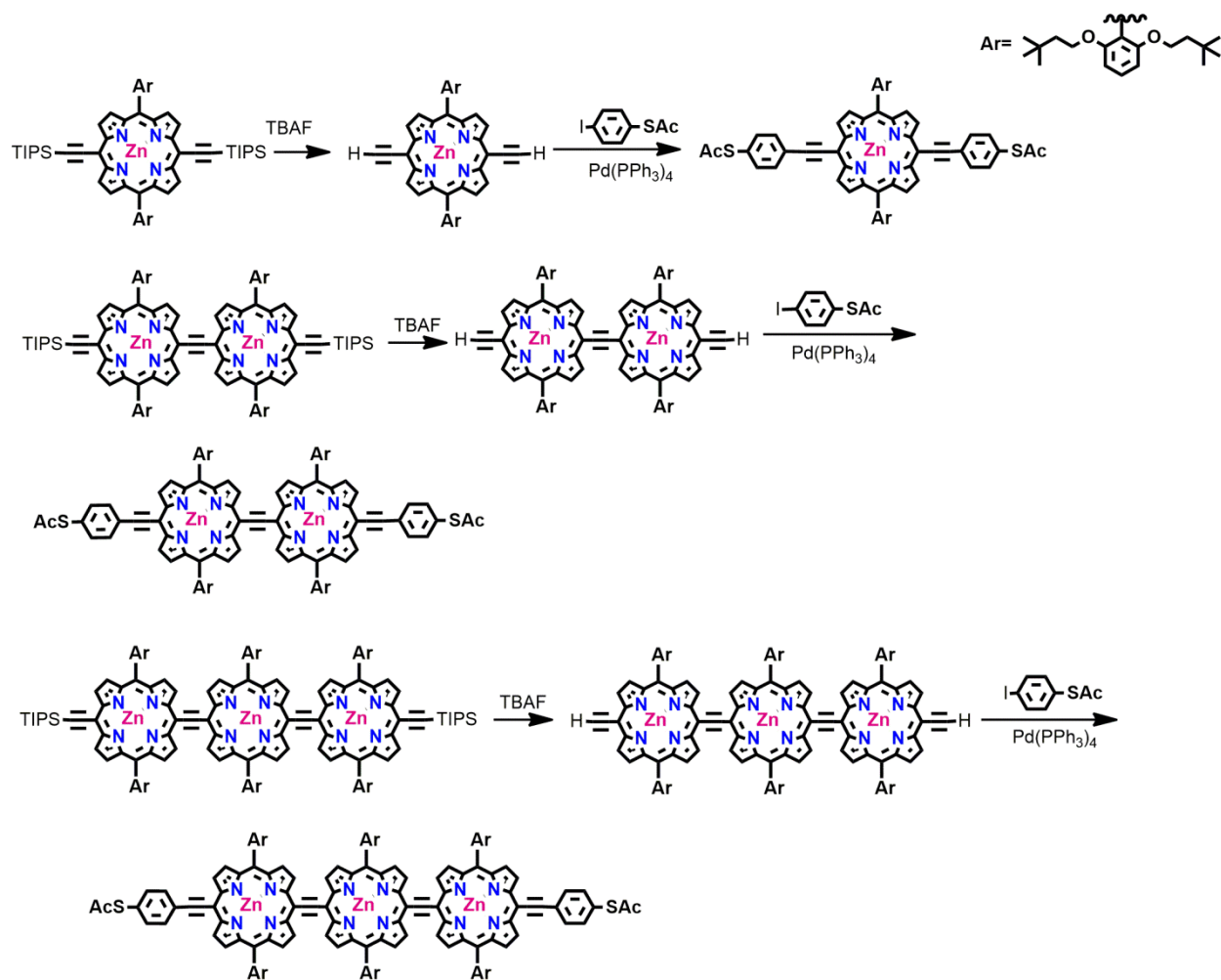
Benzodithioic acid.

In a two-neck flask equipped with condenser was charged magnesium filings (0.267 g, 11.0 mmol) and filled with argon. Anhydrous THF (~ 100 mL) and bromobenzene (1.570 g, 10.0 mmol) were added in one portion. The mixture was refluxed for two hours before cooling to -78 °C. Dried carbon disulfide (0.914 g, 12.0 mmol) was added in one portion under -78 °C. After stirring for one hour the reaction was warmed to room temperature, and saturated ammonium chloride aqueous solution was added. After another hour of stirring, the reaction mixture was extracted with ethyl acetate, dried, filtered, and concentrated to yield the title compound of sufficient purity (0.400 g, 2.59 mmol, 26% yield). ¹H NMR (400 MHz, MeOD), δ: 8.04-8.02 (m, 2H), 7.22-7.19 (m, 1H), 7.19-7.10 (m, 2H).

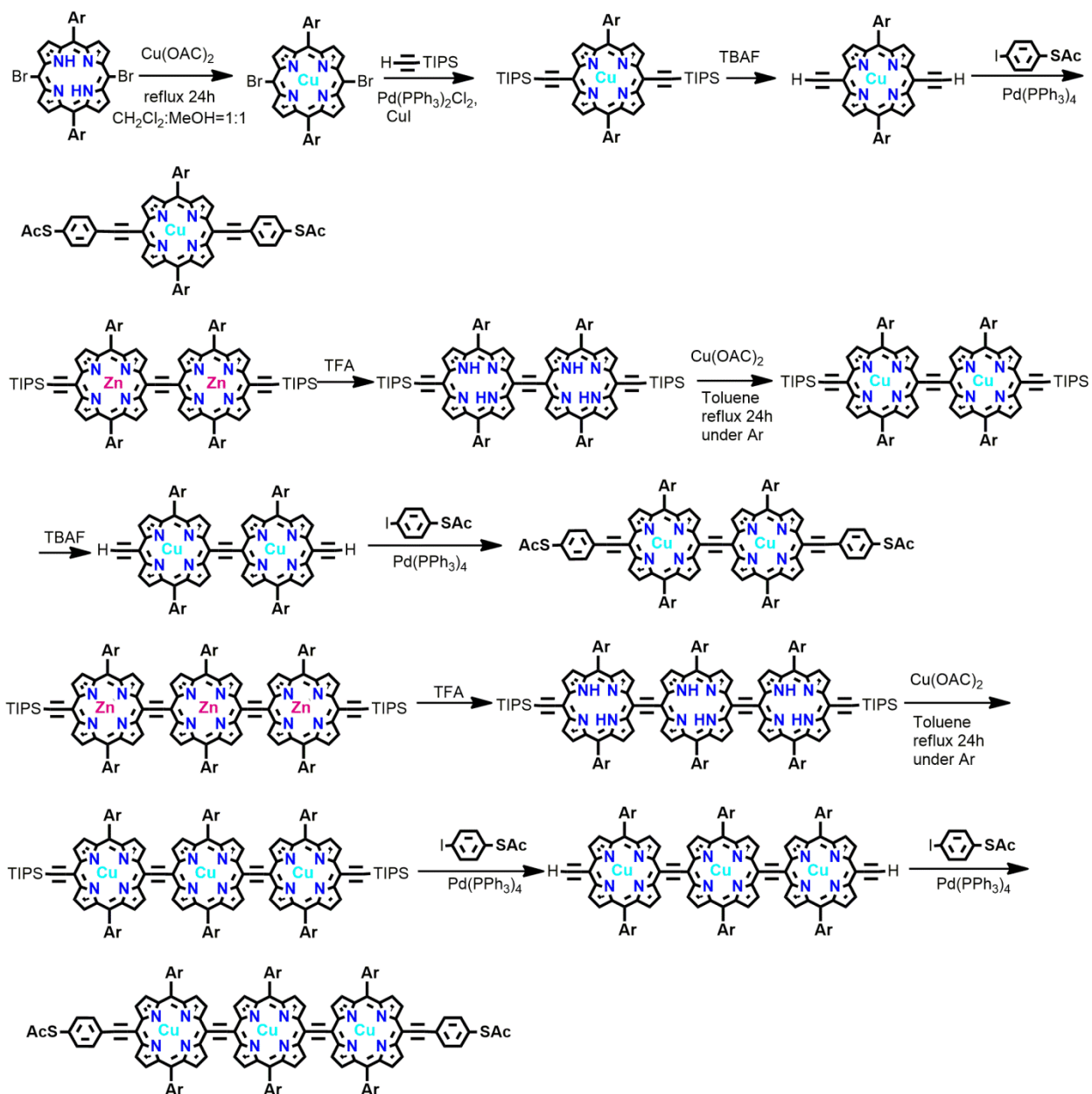
Porphyrin Synthesis – PZn_nCS₂ Series.



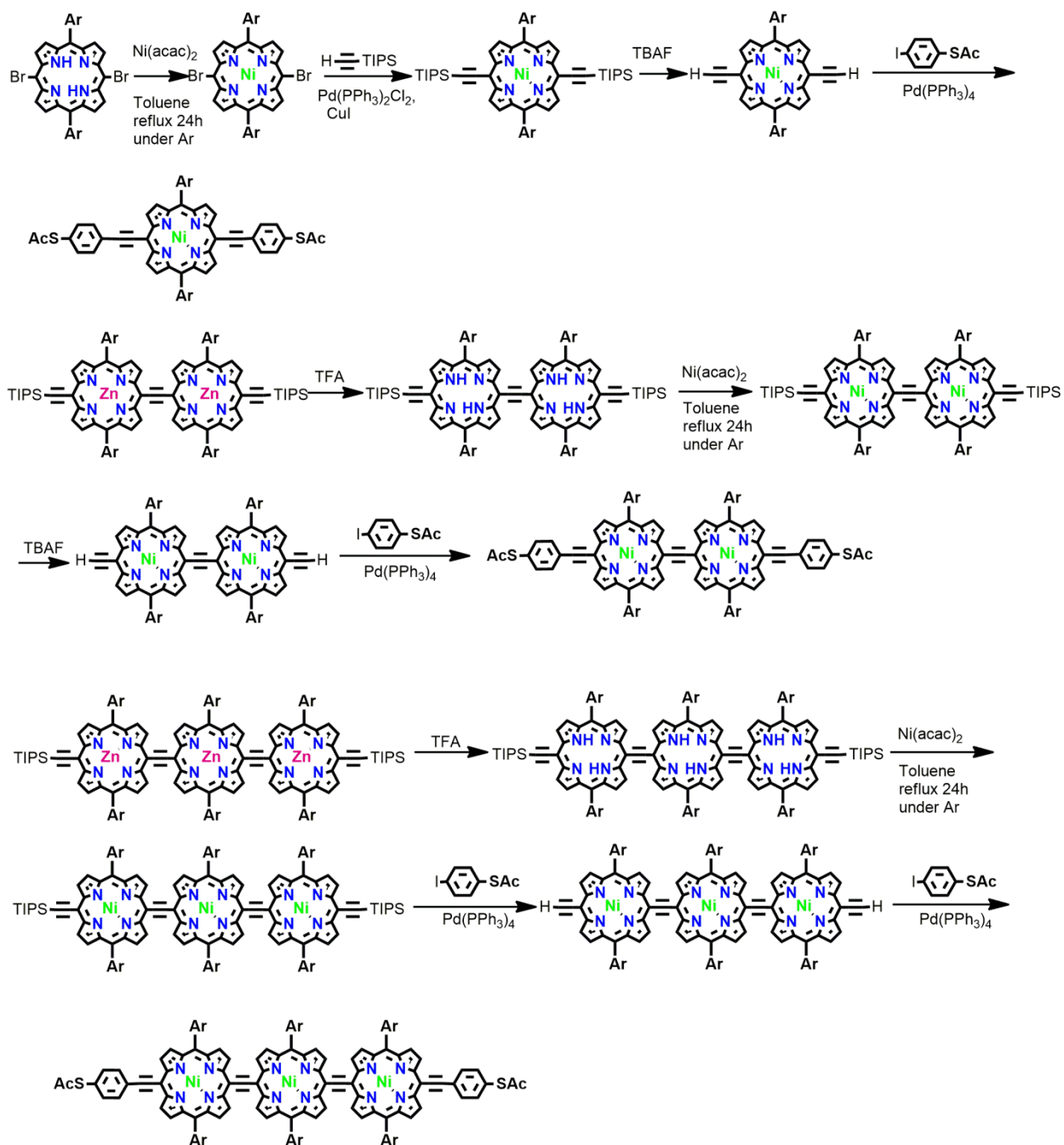
Porphyrin Synthesis – PZn_nSAc Series.



Porphyrin Synthesis – PCu_nSAC Series.



Porphyrin Synthesis – PNi_nSac Series.



4.5.2 XPS Spectra

General Methods.

All measured peaks for high resolution scans are fit by Gaussian-Lorentzian functions. For high resolution scans taken, fit envelopes are given as sums of fit peaks when more than one peak is given to evaluate the overall fit compared to raw data. See methods above (Section 4.2.5) for full experimental details.

XPS Spectra.

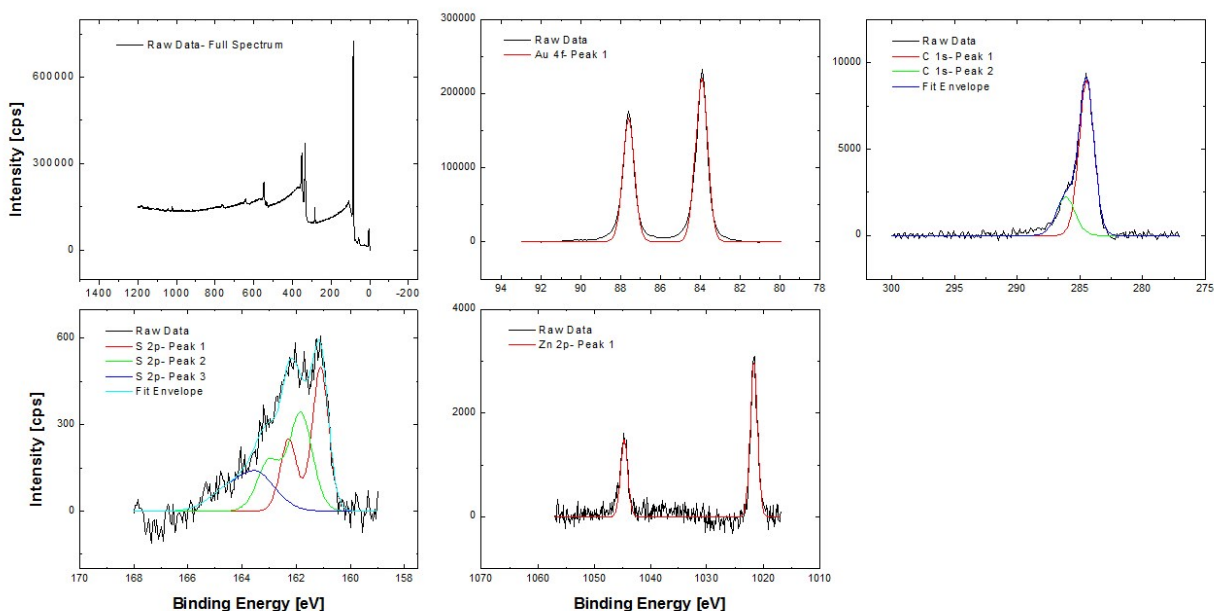


Figure 4.23 – XPS- PZn₁CS₂- 0.1 mM, 1:4 PZn:TBAF

XPS spectra for PZn₁-CS₂ layers, prepared at 0.1 mM concentrations and with 1:4 molecule:TBAF deprotection condition, measured at RT. Full spectrum; Au 4f, with one doublet fitted; C 1s with two singlets fitted; S 2p, with three doublets fitted; Zn 2p, with one doublet fitted.

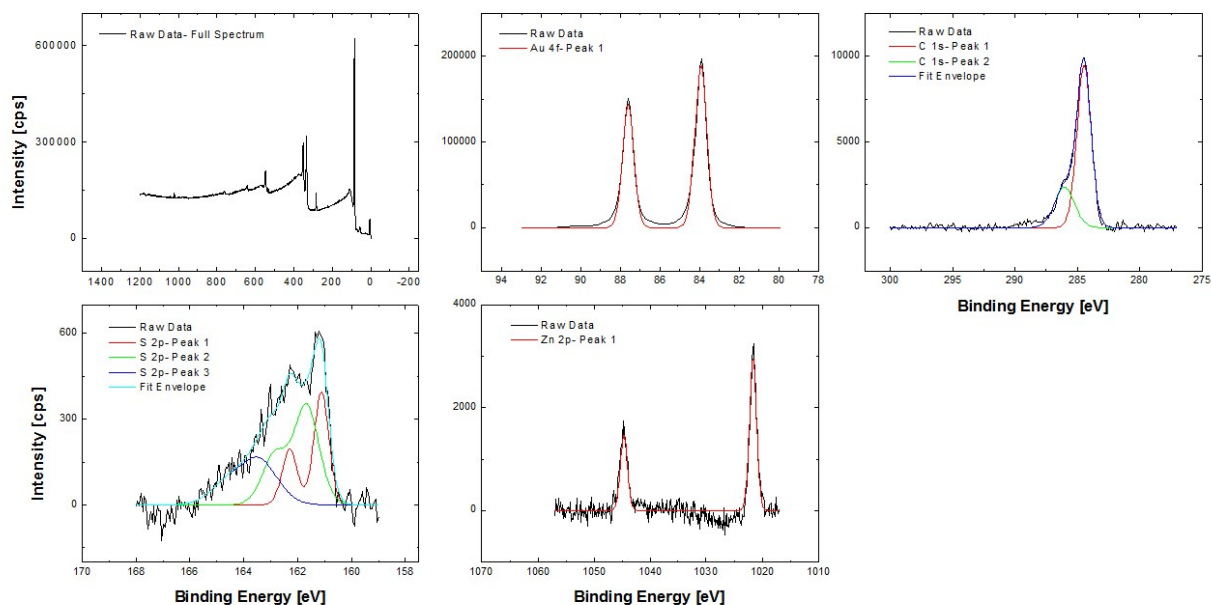


Figure 4.24 – XPS- PZn₁CS₂- 1 mM

XPS spectra for PZn₁-CS₂ layers, prepared at 1 mM concentrations and with 1:4 molecule:TBAF deprotection condition, measured at RT. Full spectrum; Au 4f, with one doublet fitted; C 1s with two singlets fitted; S 2p, with three doublets fitted; Zn 2p, with one doublet fitted.

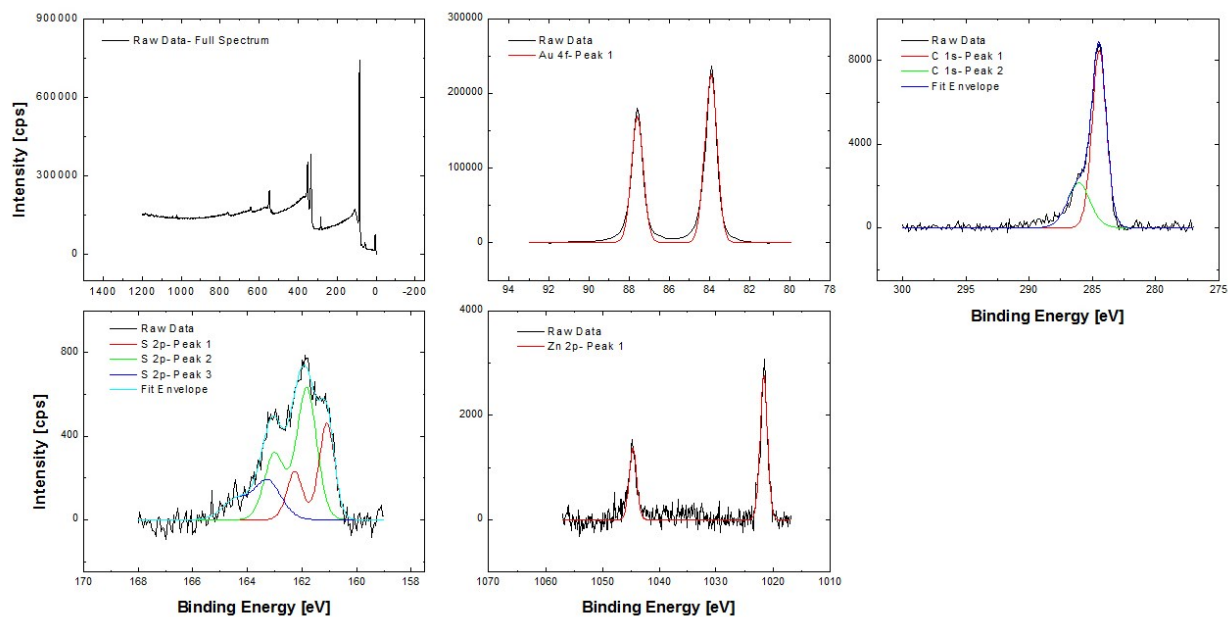


Figure 4.25 – XPS- PZn₁CS₂- 10 mM

XPS spectra for PZn₁-CS₂ layers, prepared at 10 mM concentrations and with 1:4 molecule:TBAF deprotection condition, measured at RT. Full spectrum; Au 4f, with one doublet fitted; C 1s with two singlets fitted; S 2p, with three doublets fitted; Zn 2p, with one doublet fitted.

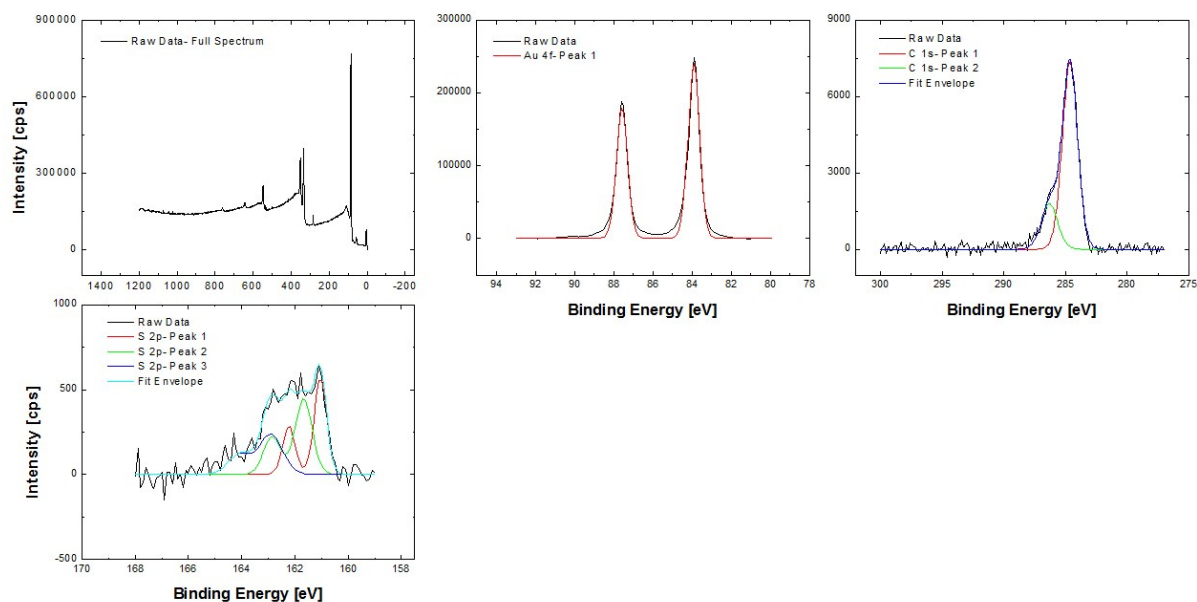


Figure 4.26 – XPS- PZn₁CS₂- 1:2 molecule: TBAF

XPS spectra for PZn₁-CS₂ layers, prepared at 0.1 mM concentrations and with 1:2 molecule: TBAF deprotection condition, measured at RT. Full spectrum; Au 4f, with one doublet fitted; C 1s with two singlets fitted; S 2p, with three doublets fitted.

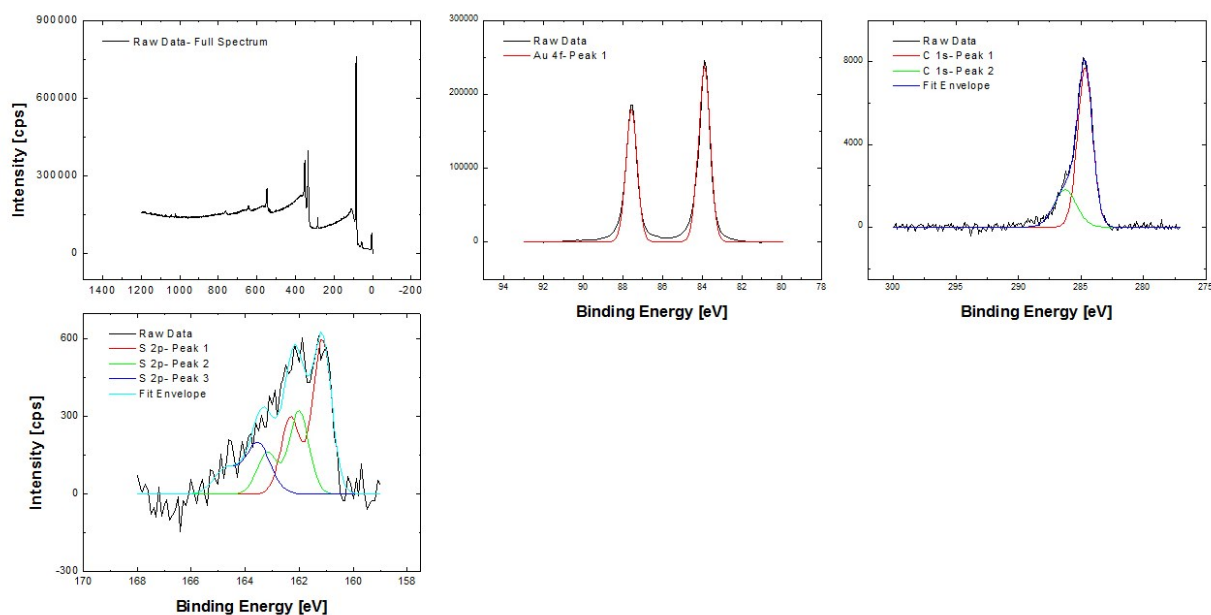


Figure 4.27 – XPS- PZn₁CS₂- 1:4 molecule: TBAF

XPS spectra for PZn₁-CS₂ layers, prepared at 0.1 mM concentrations and with 1:4 molecule: TBAF deprotection condition, measured at RT. Full spectrum; Au 4f, with one doublet fitted; C 1s with two singlets fitted; S 2p, with three doublets fitted.

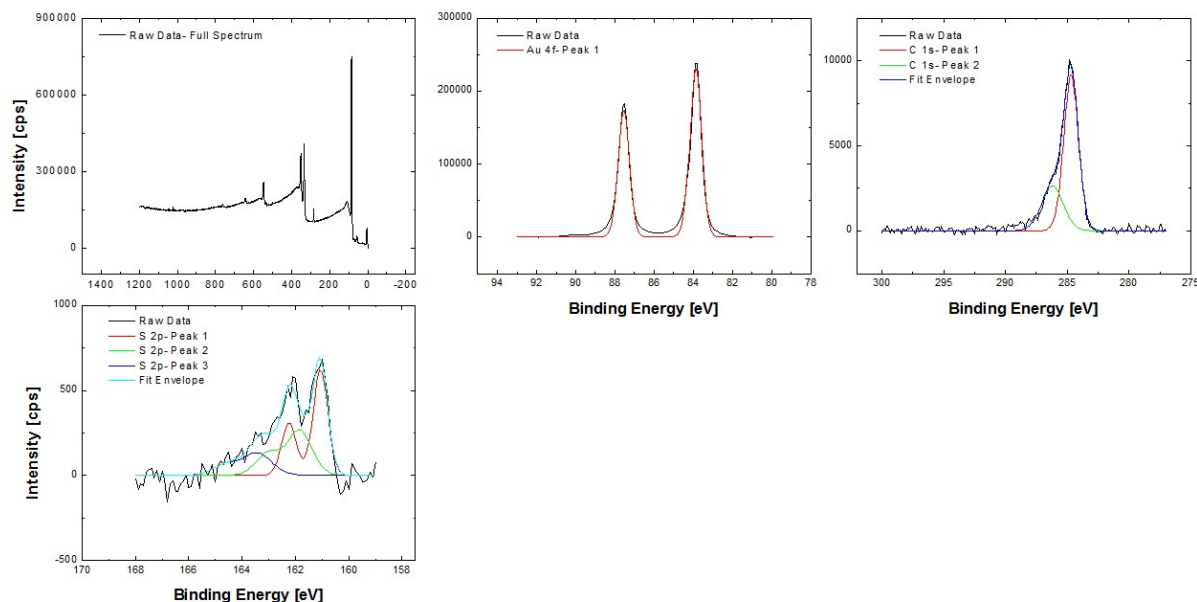


Figure 4.28 – XPS- PZn₁CS₂- 1:16 molecule: TBAF

XPS spectra for PZn₁-CS₂ layers, prepared at 0.1 mM concentrations and with 1:16 molecule: TBAF deprotection condition, measured at RT. Full spectrum; Au 4f, with one doublet fitted; C 1s with two singlets fitted; S 2p, with three doublets fitted.

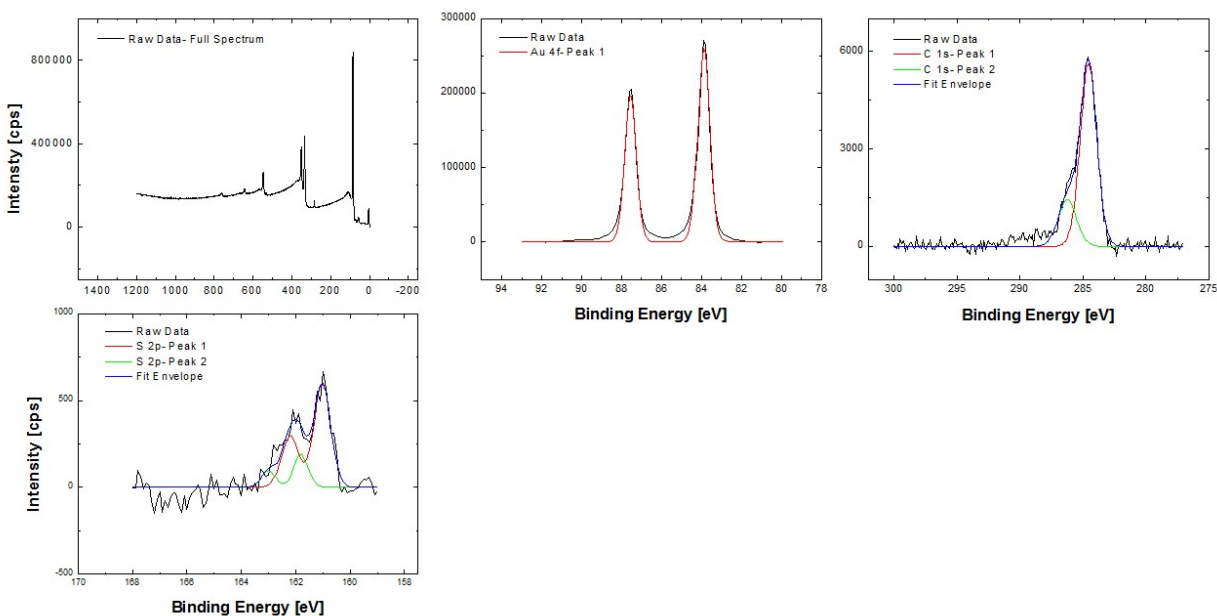


Figure 4.29 – XPS- PZn₁CS₂- Excess TBAF

XPS spectra for PZn₁-CS₂ layers, prepared at 0.1 mM concentrations and with excess TBAF (~1 mL) deprotection condition, measured at RT. Full spectrum; Au 4f, with one doublet fitted; C 1s with two singlets fitted; S 2p, with two doublets fitted.

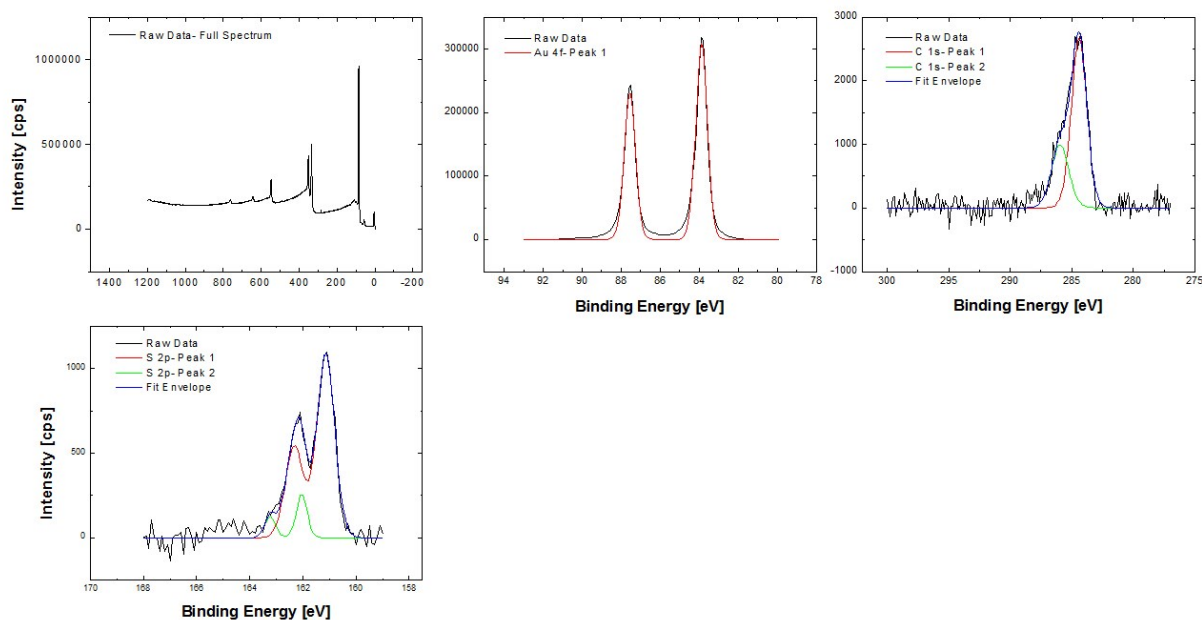


Figure 4.30 – XPS- $C_{10}CS_2$

XPS spectra for decanecarbodithioate layers, prepared at 0.1 mM concentrations and with 1:4 molecule: TBAF deprotection condition, measured at RT. Full spectrum; Au 4f, with one doublet fitted; C 1s, with two singlets fitted; S 2p, with two doublets fitted.

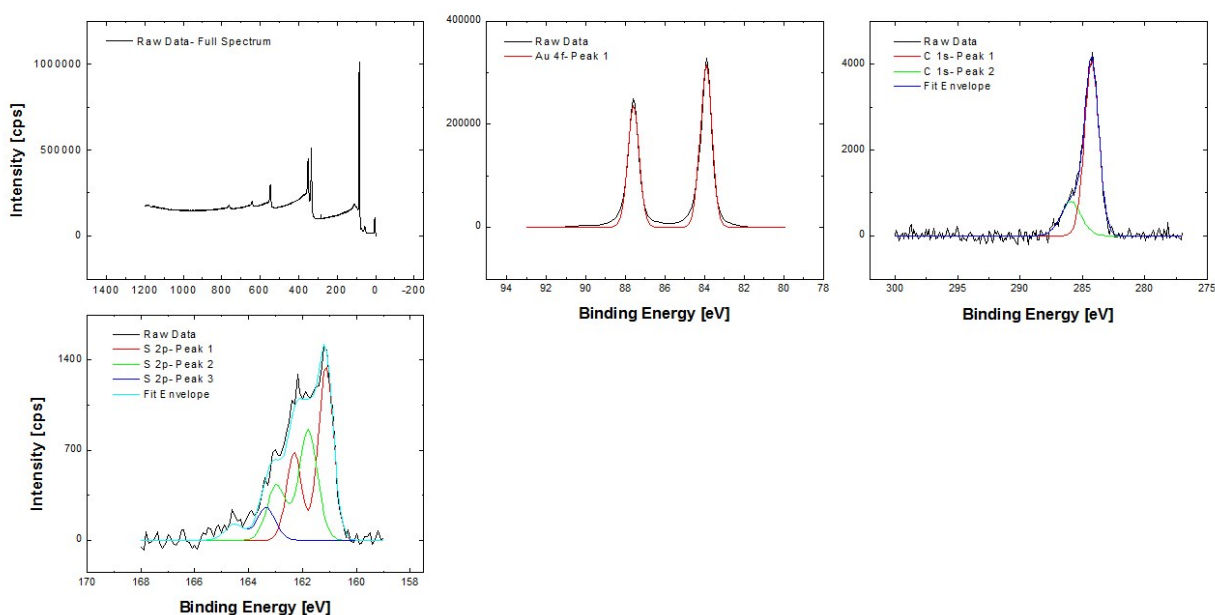


Figure 4.31 – XPS- $PhCS_2$ -ETMS- 1:2 molecule: TBAF

XPS spectra for ETMS protected benzenecarbodithioate layers, prepared at 0.1 mM concentrations and with 1:2 molecule: TBAF deprotection condition, measured at RT. Full spectrum; Au 4f, with one doublet fitted; C 1s, with two singlets fitted; S 2p, with three doublets fitted.

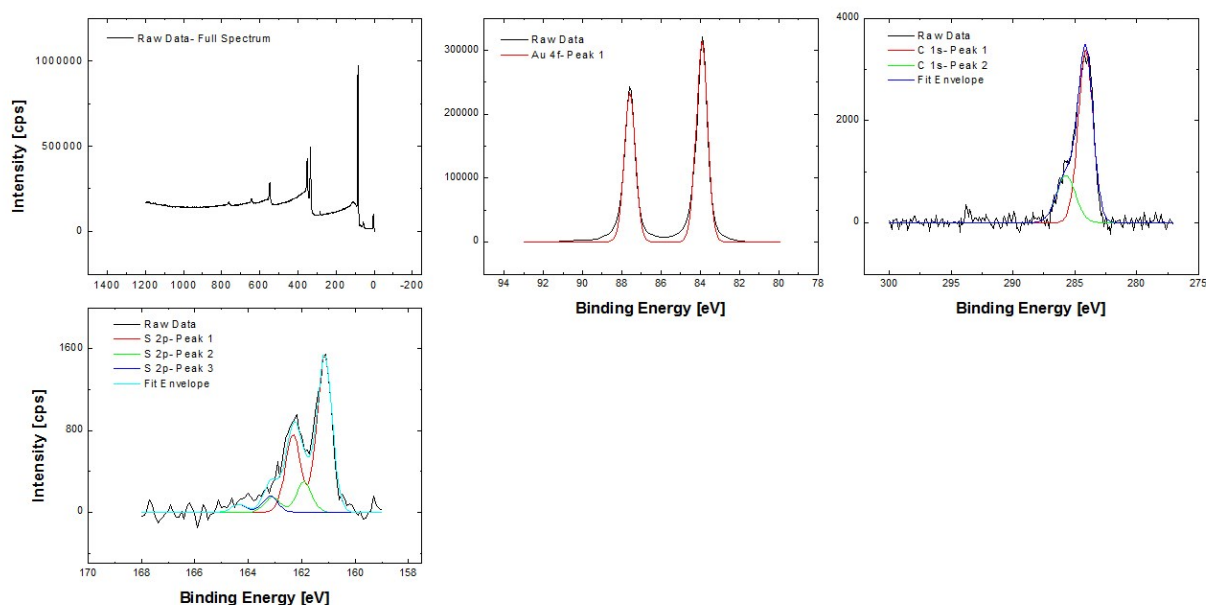


Figure 4.32 – XPS- PhCS₂-ETMS- 1:8 molecule: TBAF

XPS spectra for ETMS protected benzenecarbodithioate layers, prepared at 0.1 mM concentrations and with 1:8 molecule: TBAF deprotection condition, measured at RT. Full spectrum; Au 4f, with one doublet fitted; C 1s, with two singlets fitted; S 2p, with three doublets fitted.

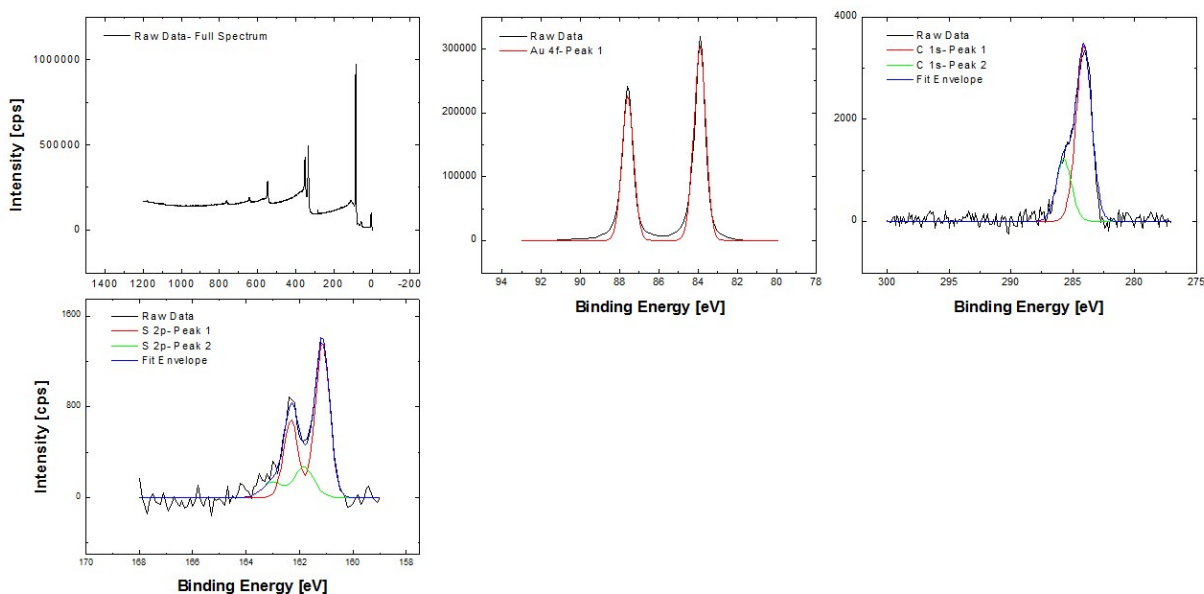


Figure 4.33 – XPS- PhCS₂-ETMS- Excess TBAF

XPS spectra for ETMS protected benzenecarbodithioate layers, prepared at 0.1 mM concentrations and with excess TBAF deprotection condition, measured at RT. Full spectrum; Au 4f, with one doublet fitted; C 1s, with two singlets fitted; S 2p, with three doublets fitted.

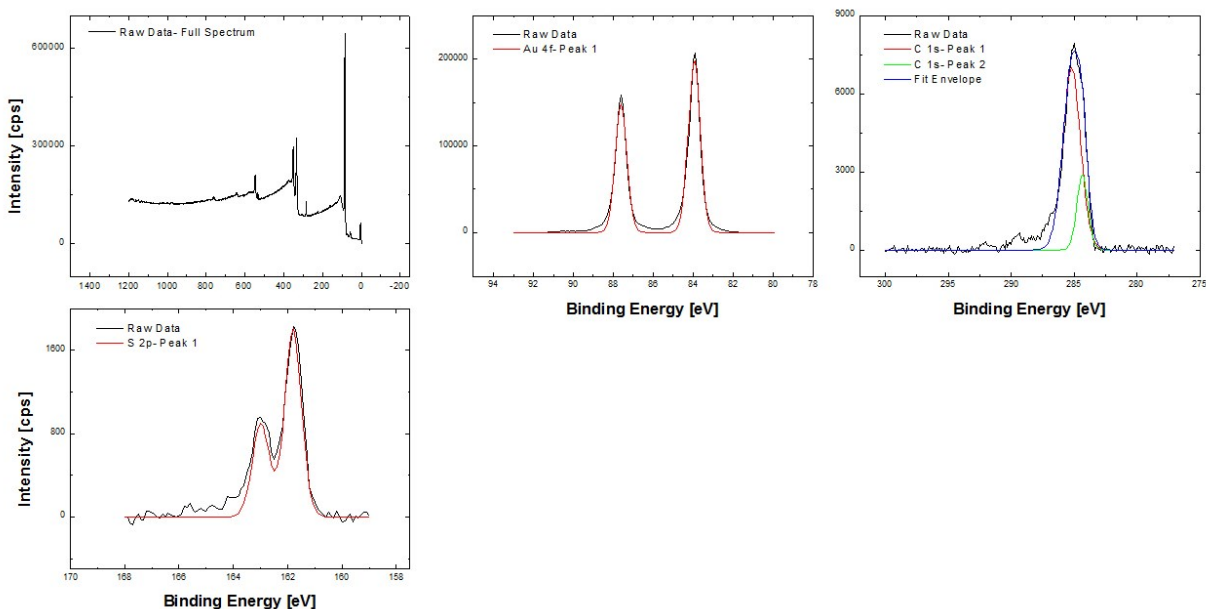


Figure 4.34 – XPS- PhCS₂-H- Without TBAF

XPS spectra for non-protected benzenecarbodithioate layers, prepared at 0.1 mM concentrations and with no TBAF deprotectant added, measured at RT. Full spectrum; Au 4f, with one doublet fitted; C 1s, with two singlets fitted; S 2p, with one doublet fitted.

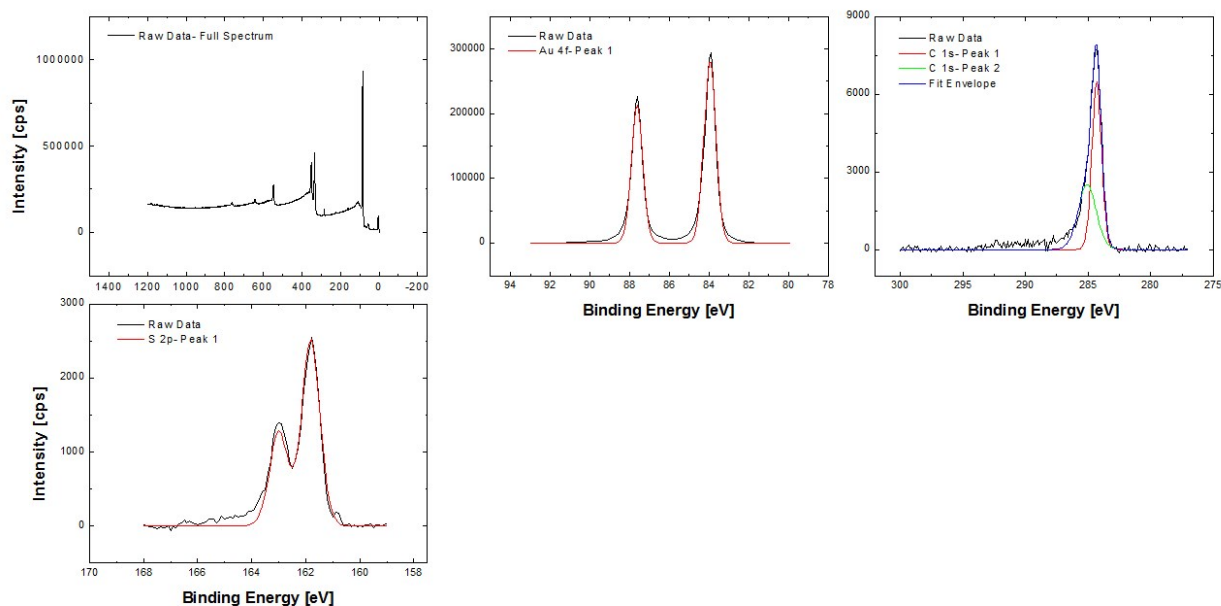


Figure 4.35 – XPS- PhCS₂-H- With TBAF

XPS spectra for non-protected benzenecarbodithioate layers, prepared at 0.1 mM concentrations and with excess TBAF deprotectant added, measured at RT. Full spectrum; Au 4f, with one doublet fitted; C 1s, with two singlets fitted; S 2p, with one doublet fitted.

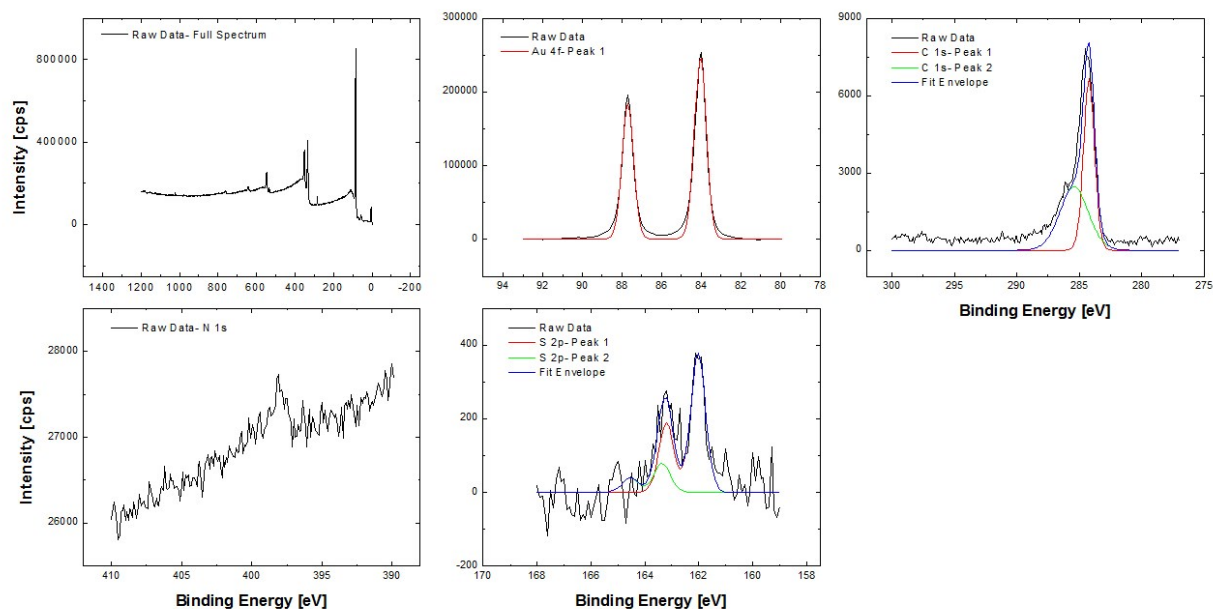


Figure 4.36 – XPS- PhSAc- 1 mM

XPS spectra for phenylthioacetyl layers, prepared at 1 mM concentrations and with 1:4 molecule: NH_4OH deprotectant added, measured at RT. Full spectrum; Au 4f, with one doublet fitted; C 1s, with two singlets fitted; N 1s, with no fits but perhaps small indication of signal from remnant NH_4OH ; S 2p, with one doublet fitted. Results here differ from sample above, and may indicate effect of deprotectant affecting monolayer under rare circumstances, as seen in Ref. ⁴⁴.

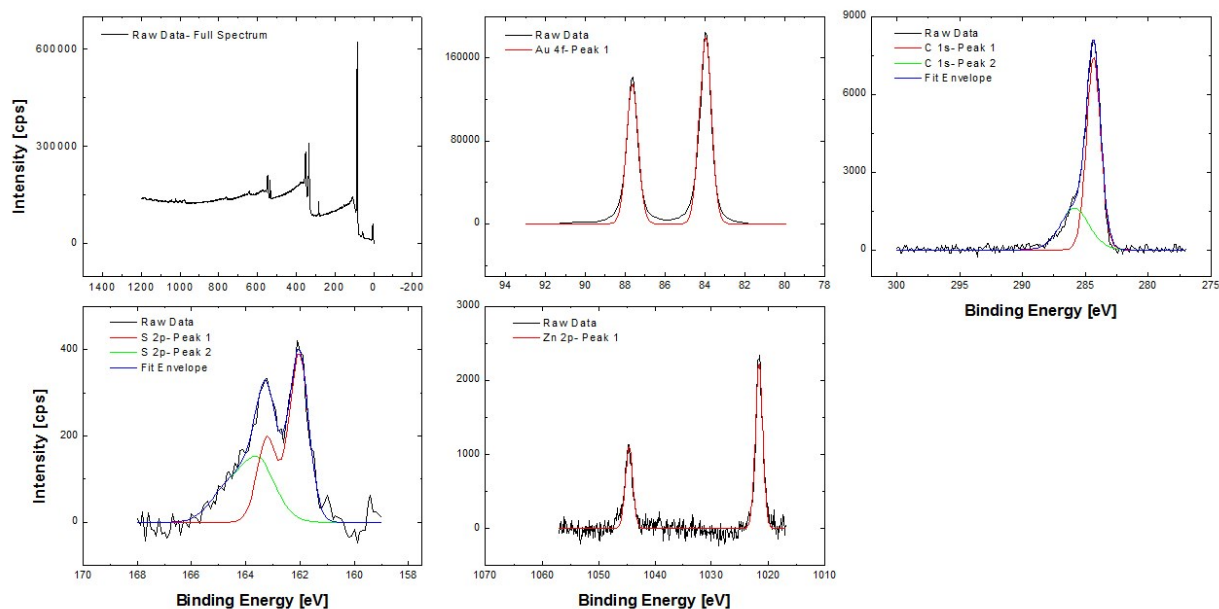


Figure 4.37 – XPS- PZn₁-SAc

XPS spectra for PZn₁-SAc layers, prepared at 0.1 mM concentrations and with 1:4 molecule: NH₄OH deprotectant added, measured at RT. Full spectrum; Au 4f, with one doublet fitted; C 1s, with two singlets fitted; S 2p, with two doublets fitted; Zn 2p, with one doublet fitted.

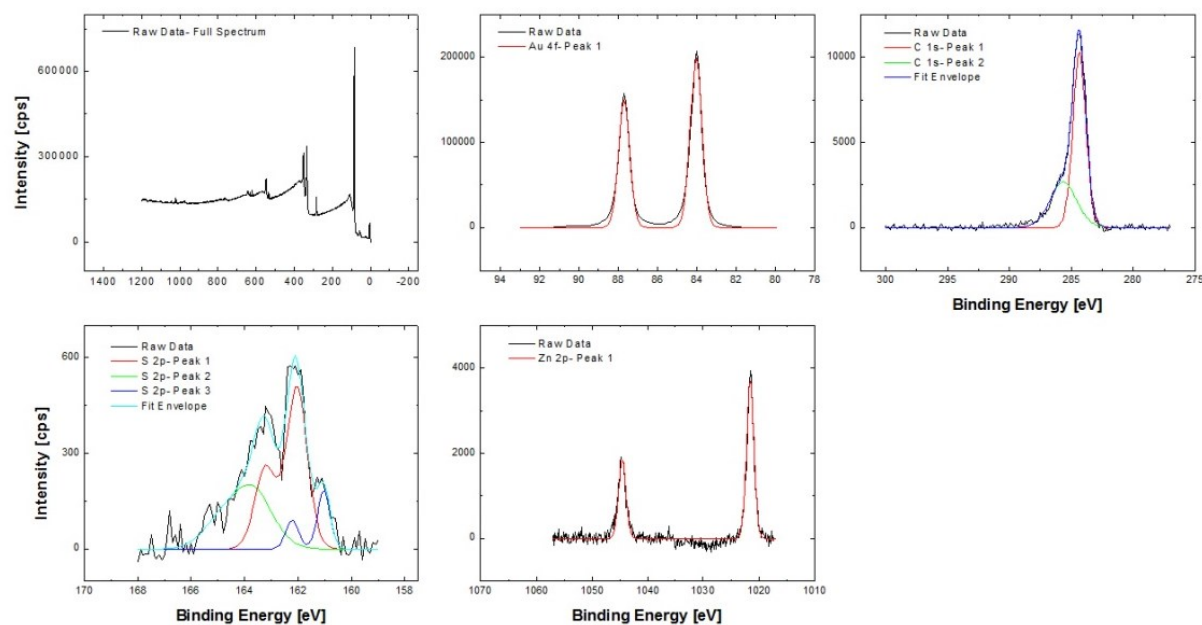


Figure 4.38 – XPS- PZn₂-SAc

XPS spectra for PZn₂-SAc layers, prepared at 0.1 mM concentrations and with 1:4 molecule: NH₄OH deprotectant added, measured at RT. Full spectrum; Au 4f, with one doublet fitted; C 1s, with two singlets fitted; S 2p, with three doublets fitted; Zn 2p, with one doublet fitted.

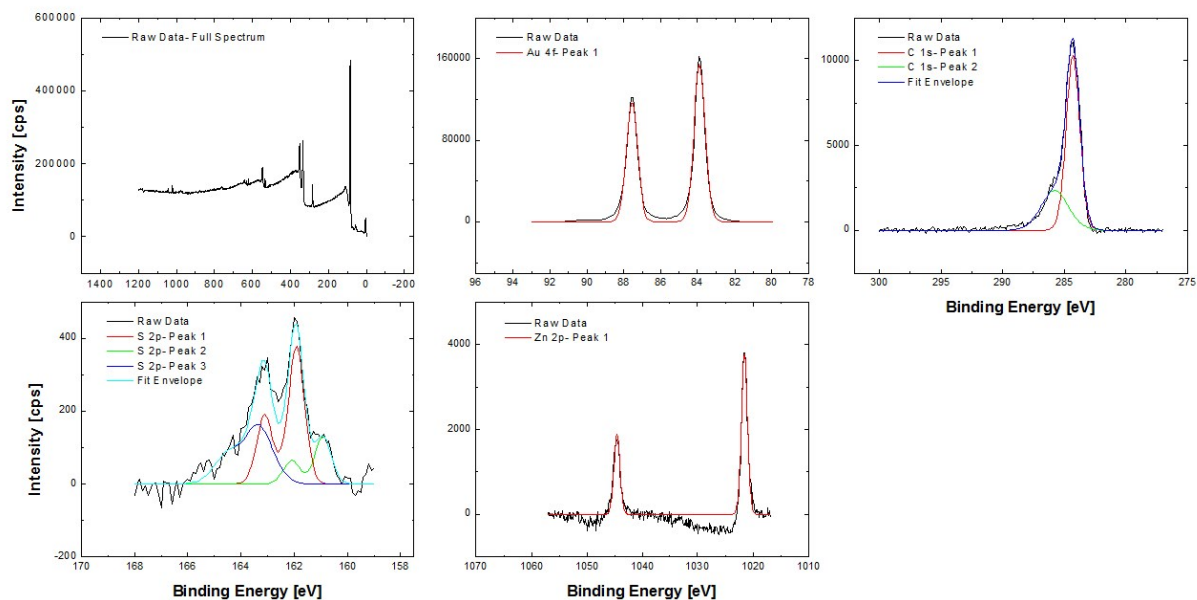


Figure 4.39 – XPS- PZn₂-SAc

XPS spectra for PZn₂-SAc layers, prepared at 0.1 mM concentrations and with 1:4 molecule: NH₄OH deprotectant added, measured at RT. Full spectrum; Au 4f, with one doublet fitted; C 1s, with two singlets fitted; S 2p, with three doublets fitted; Zn 2p, with one doublet fitted.

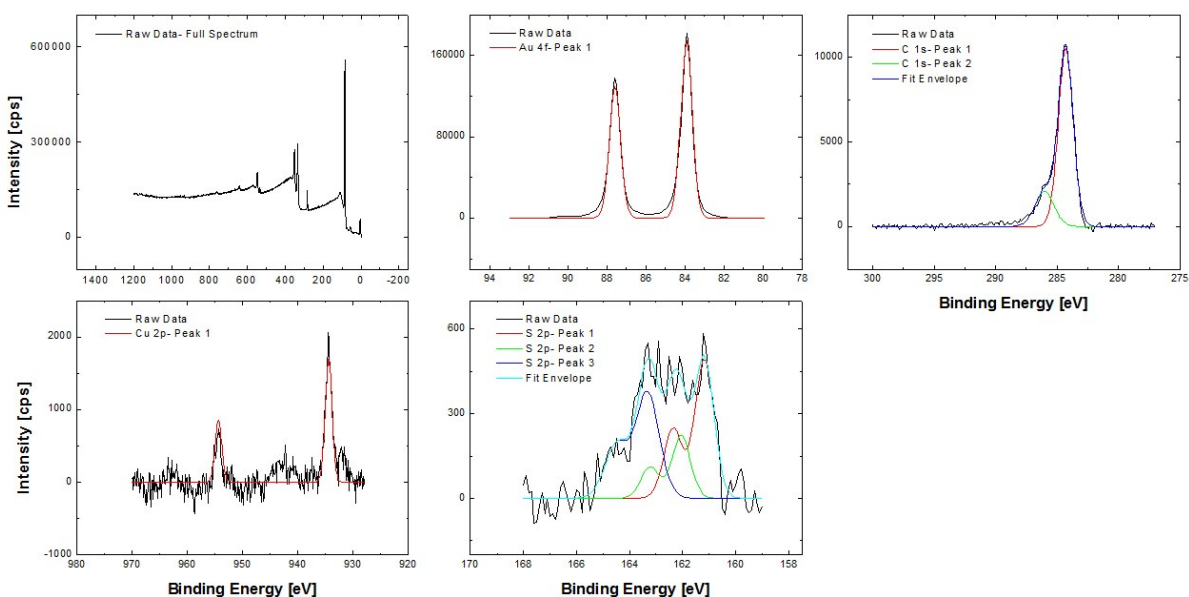


Figure 4.40 – XPS- PCu₁-SAc DCM

XPS spectra for PCu₁-SAc layers, prepared at 0.1 mM concentrations in DCM and with 1:4 molecule: NH₄OH deprotectant added, measured at RT. Full spectrum; Au 4f, with one doublet fitted; C 1s, with two singlets fitted; Cu 2p, with one doublet fit, and perhaps satellite peaks to indicate small amount of oxide; S 2p, with three doublets fitted.

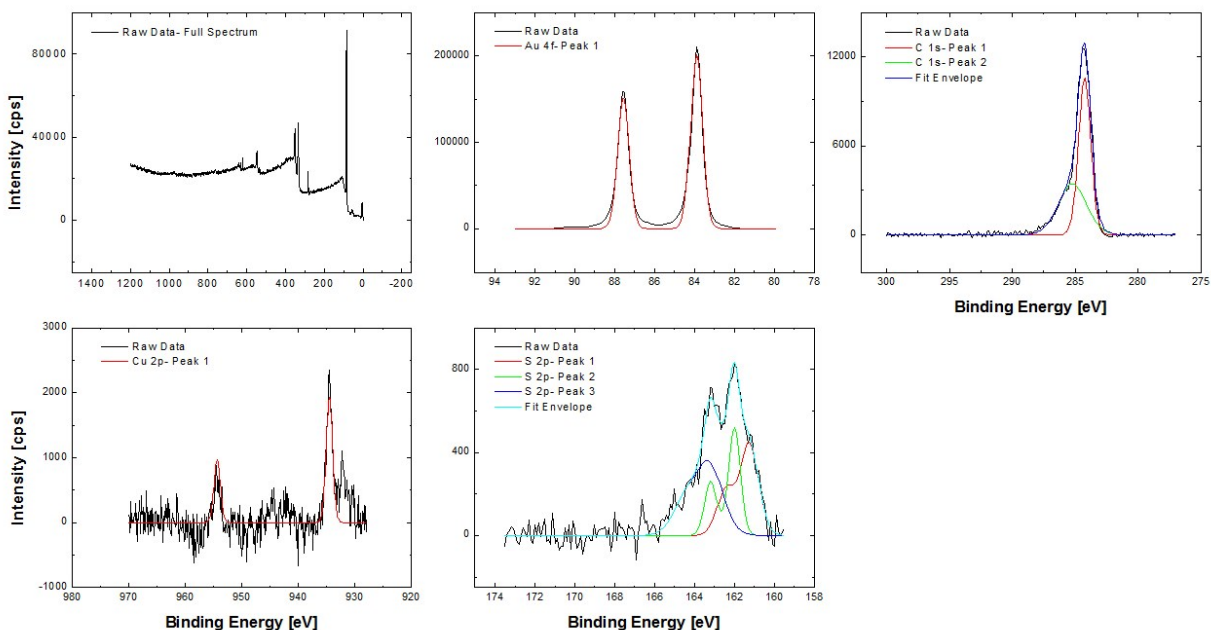


Figure 4.41 – XPS- PCu₂-SAc DCM

XPS spectra for PCu₂-SAc layers, prepared at 0.1 mM concentrations in DCM and with 1:4 molecule: NH₄OH deprotectant added, measured at RT. Full spectrum; Au 4f, with one doublet fitted; C 1s, with two singlets fitted; Cu 2p, with one doublet fit, and perhaps satellite peaks to indicate small amount of oxide; S 2p, with three doublets fitted.

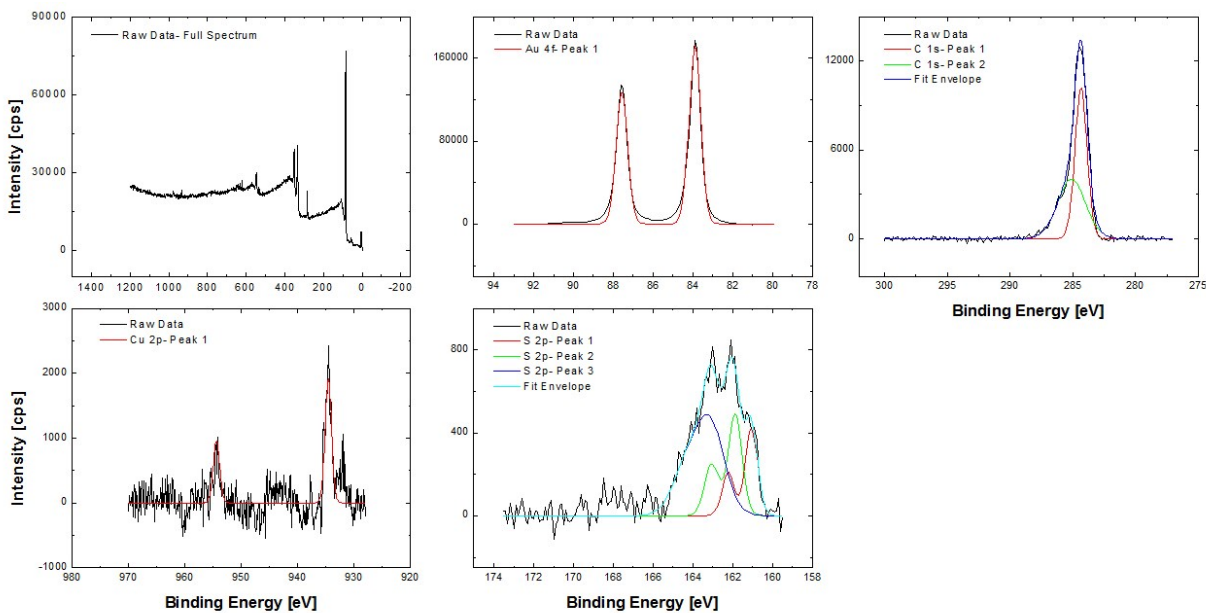


Figure 4.42 – XPS- PCu₃-SAC DCM

XPS spectra for PCu₃-SAC layers, prepared at 0.1 mM concentrations in DCM and with 1:4 molecule: NH₄OH deprotectant added, measured at RT. Full spectrum; Au 4f, with one doublet fitted; C 1s, with two singlets fitted; Cu 2p, with one doublet fit, and perhaps satellite peaks to indicate small amount of oxide; S 2p, with three doublets fitted.

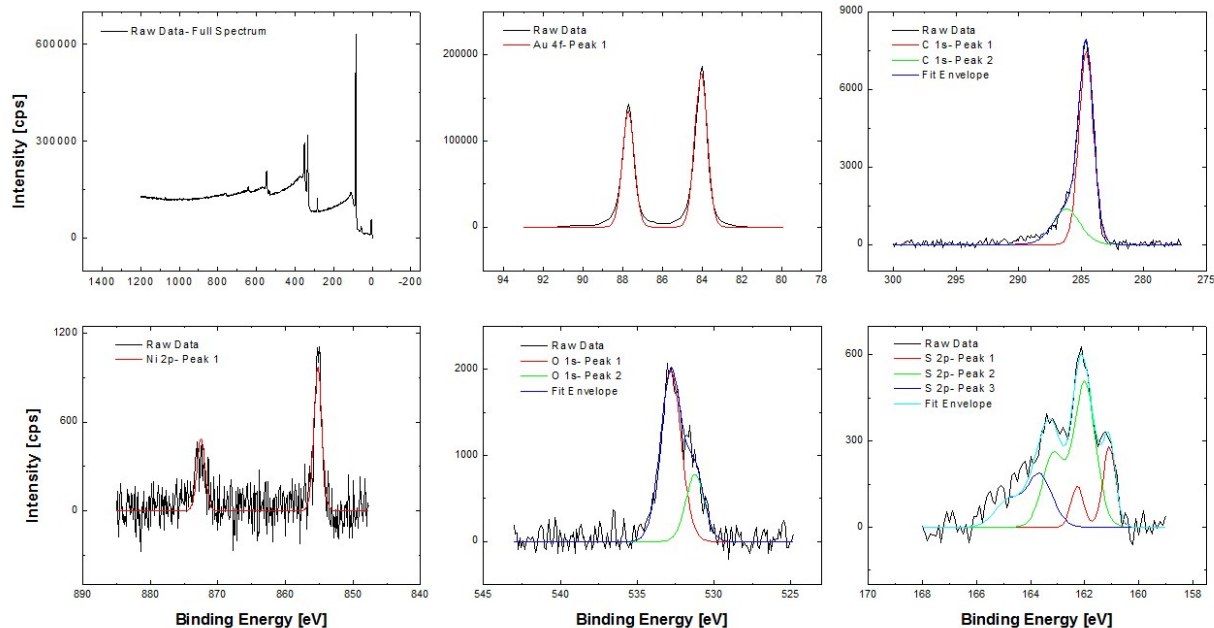


Figure 4.43 – XPS- PNi₁-SAc

XPS spectra for PNi₁-SAc layers, prepared at 0.1 mM concentrations and with 1:4 molecule: NH₄OH deprotectant added, measured at RT. Full spectrum; Au 4f, with one doublet fitted; C 1s, with two singlets fitted; Ni 2p, with one doublet fit; O 1s, with two singlets fit; S 2p, with three doublets fitted.

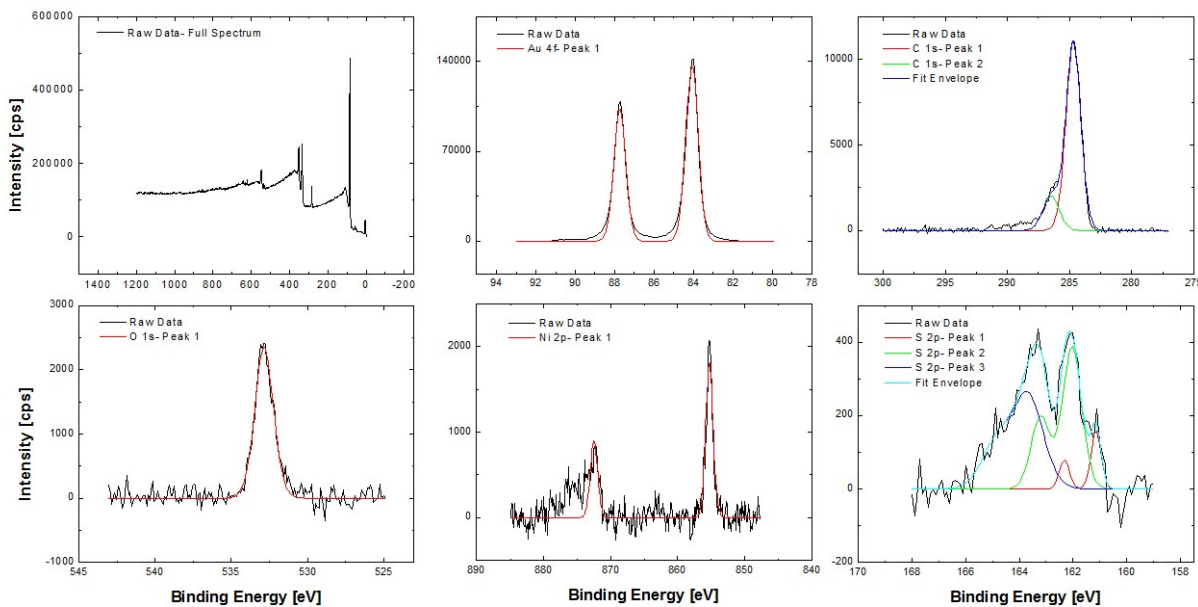


Figure 4.44 – XPS- PNi₂-SAc

XPS spectra for PNi₂-SAc layers, prepared at 0.1 mM concentrations and with 1:4 molecule: NH₄OH deprotectant added, measured at RT. Full spectrum; Au 4f, with one doublet fitted; C 1s, with two singlets fitted; Ni 2p, with one doublet fit; O 1s, with one singlet fit; S 2p, with three doublets fitted.

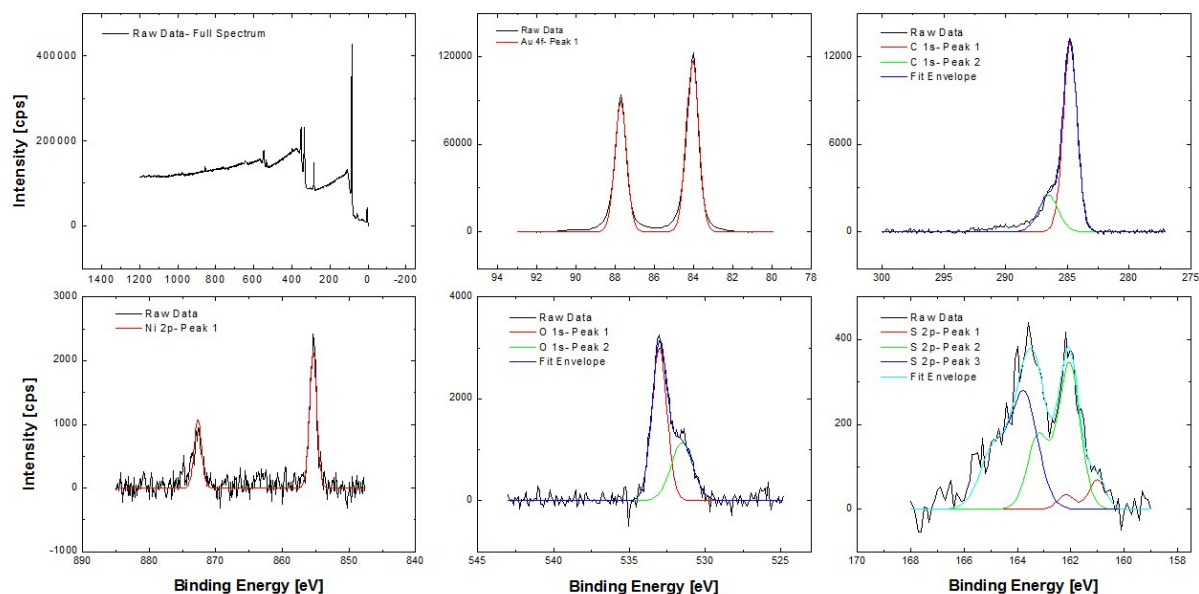


Figure 4.45 – XPS- PNi₃-SAc

XPS spectra for PNi₃-SAc layers, prepared at 0.1 mM concentrations and with 1:4 molecule: NH₄OH deprotectant added, measured at RT. Full spectrum; Au 4f, with one doublet fitted; C 1s, with two singlets fitted; Ni 2p, with one doublet fit; O 1s, with two singlets fit; S 2p, with three doublets fitted.

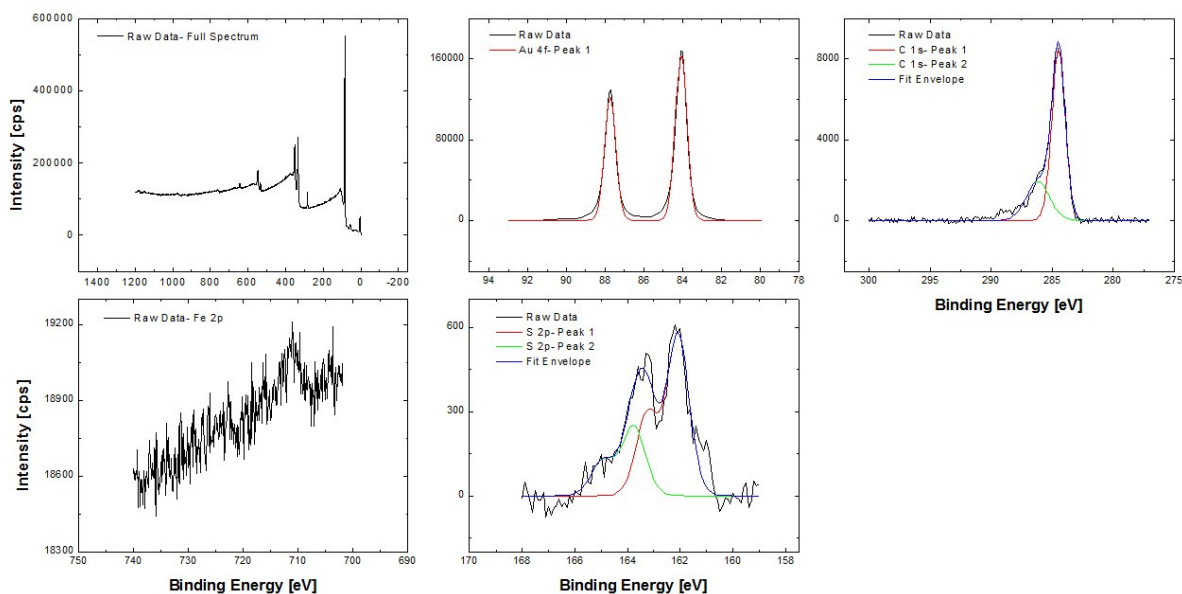


Figure 4.46 – XPS- PFe₁-SAc

XPS spectra for PFe₁-SAc layers, prepared at 0.1 mM concentrations and with 1:4 molecule: NH₄OH deprotectant added, measured at RT. Full spectrum; Au 4f, with one doublet fitted; C 1s, with two singlets fitted; Fe 2p, with no peaks identified but perhaps a small amount of iron present; S 2p, with two doublets fitted.

4.5.3 UPS Spectra

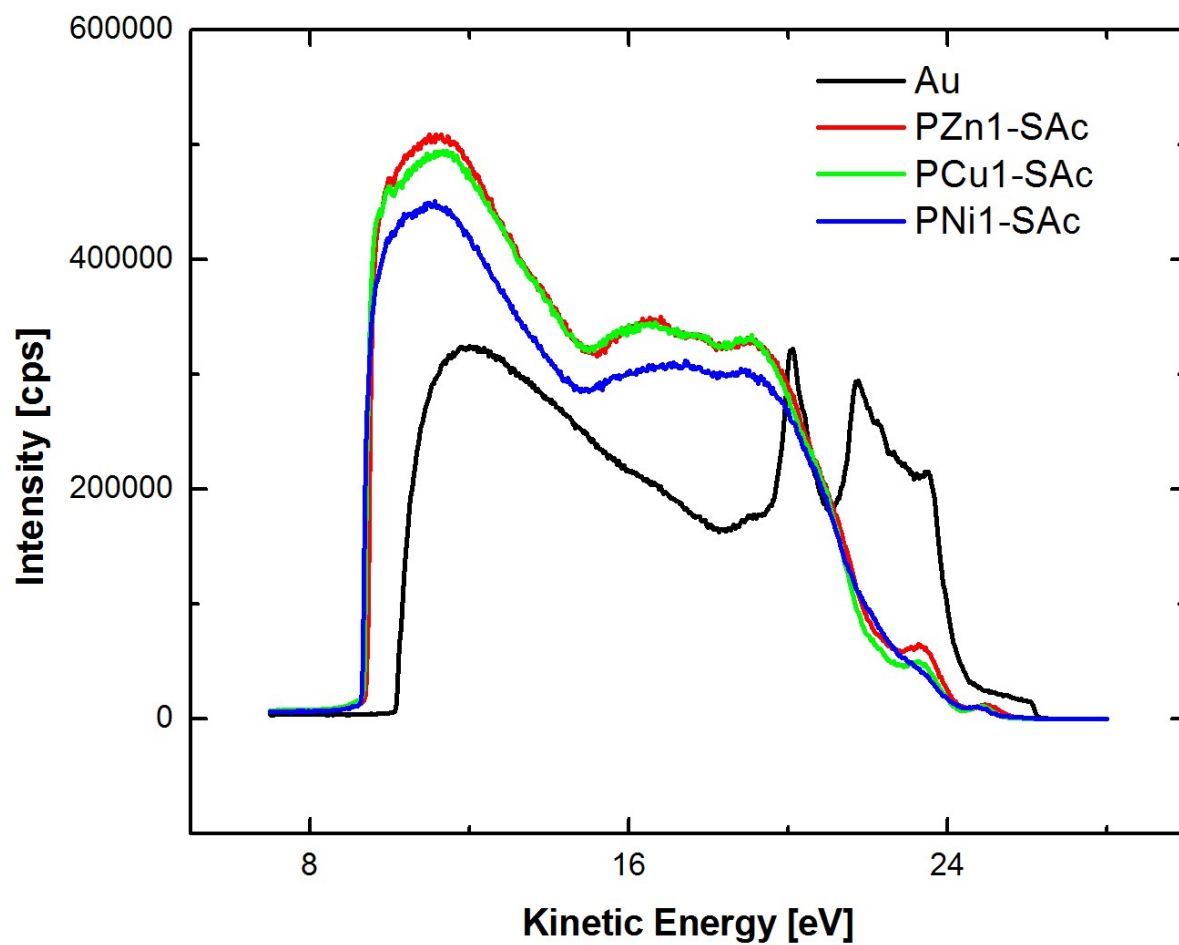


Figure 4.47 – UPS of Porphyrin Monomers

UPS full spectra for porphyrin monomers (indicated by respective colors) and gold substrate for comparison.

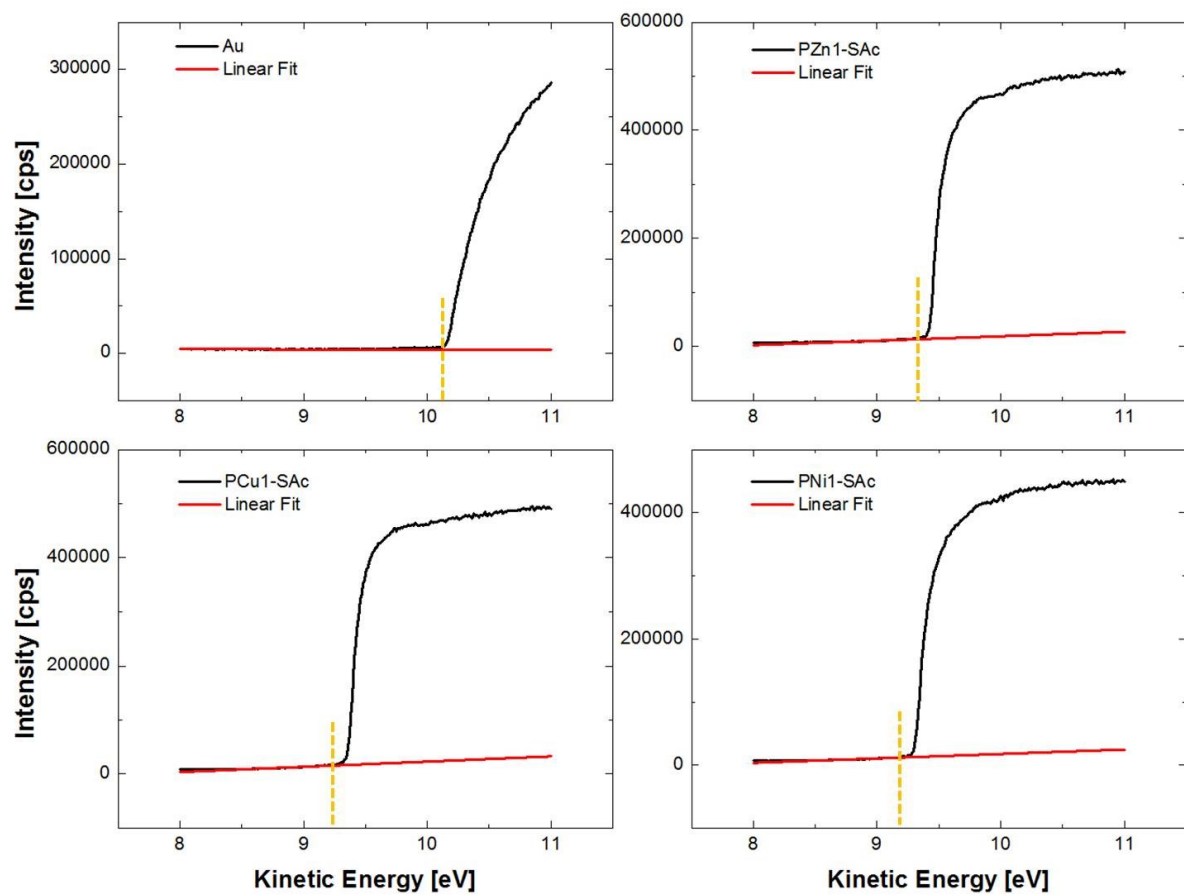


Figure 4.48 – UPS- Cutoff Region

UPS in the high kinetic energy region for gold films, PZn₁-SAc, PCu₁-SAc, and PNi₁-SAc surfaces. Black lines indicate raw data, red lines indicate linear fits from background region, orange dashed line indicates onset energy.

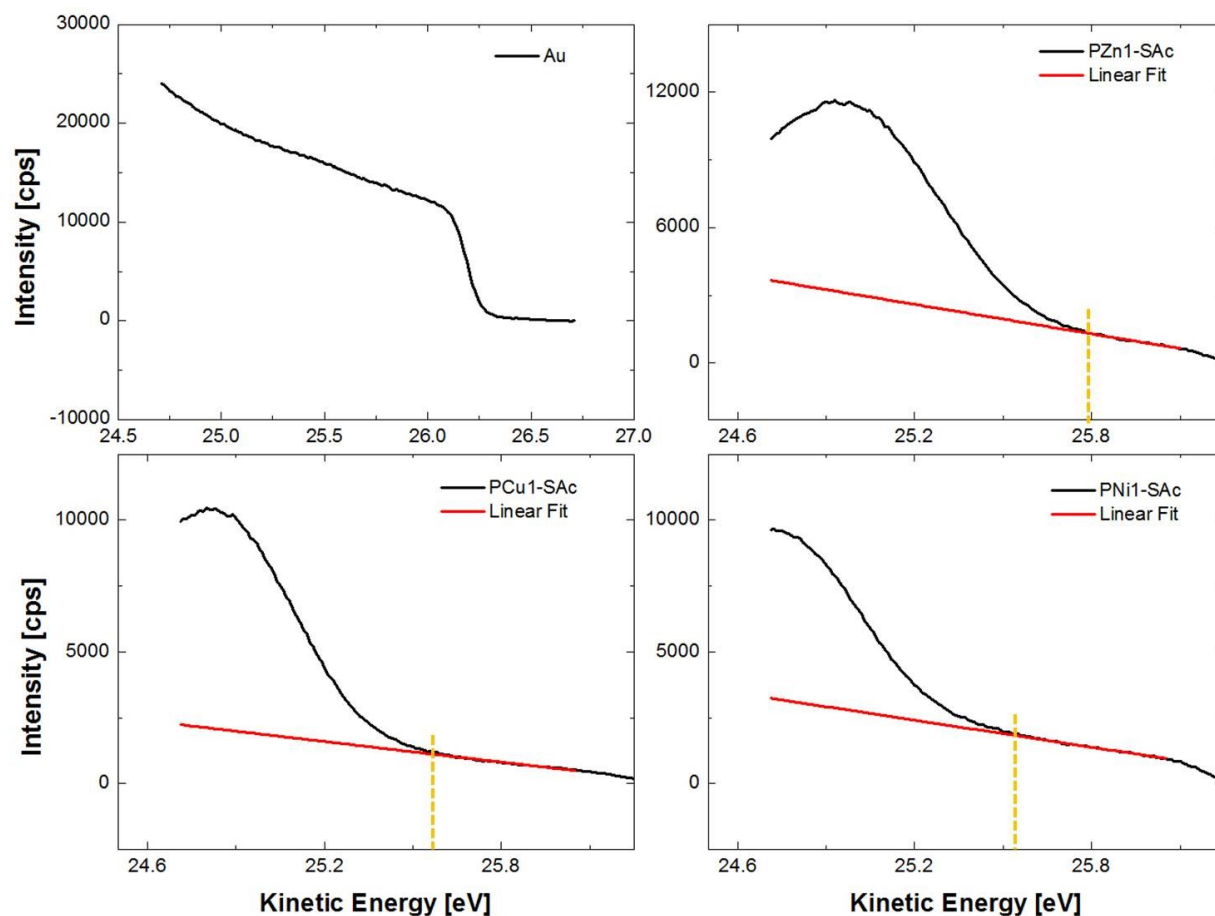


Figure 4.49 – UPS- High Kinetic Energy Region

UPS in the high kinetic energy region for gold films, PZn₁-SAc, PCu₁-SAc, and PNi₁-SAc surfaces. Black lines indicate raw data, red lines indicate linear fits from background region, orange dashed line indicates onset energy for porphyrin monomers. Au spectra shows Fermi energy at 26.2 eV and no discernable signals in the range of the HOMOs for the porphyrin monomers.

4.6 References

- (1) Gobbi, M.; Golmar, F.; Llopis, R.; Casanova, F.; Hueso, L. E. *Adv. Mater.* **2011**, *23*, 1609–1613.
- (2) Wohlgenannt, M. *Phys. status solidi RRL* **2012**, *6*, 229–242.
- (3) Kersten, S. P.; Meskers, S. C. J.; Bobbert, P. A. *Phys. Rev. B* **2012**, *86*, 045210.
- (4) Mahato, R. N.; Lülfi, H.; Siekman, M. H.; Kersten, S. P.; Bobbert, P. A.; de Jong, M. P.; De Cola, L.; van der Wiel, W. G. *Science* **2013**, *341*, 257–260.
- (5) Otte, F. L.; Lemke, S.; Schu, C.; Krekieh, N. R.; Jung, U.; Magnussen, O. M.; Herges, R. *J. Am. Chem. Soc.* **2014**, *136*, 11248–11251.
- (6) Grill, L.; Dyer, M.; Lafferentz, L.; Persson, M.; Peters, M. V.; Hecht, S. *Nat. Nanotechnol.* **2007**, *2*, 687–691.
- (7) Li, Z.; Borguet, E. *J. Am. Chem. Soc.* **2012**, *134*, 63–66.
- (8) Perrin, M. L.; Prins, F.; Martin, C. A.; Shaikh, A. J.; Eelkema, R.; van Esch, J. H.; Briza, T.; Kaplanek, R.; Kral, V.; van Ruitenbeek, J. M.; van der Zant, H. S. J.; Dulić, D. *Angew. Chem. Int. Ed.* **2011**, *50*, 11223–11226.
- (9) Kang, B. K.; Aratani, N.; Lim, J. K.; Kim, D.; Osuka, A.; Yoo, K.-H. *Chem. Phys. Lett.* **2005**, *412*, 303–306.
- (10) Sedghi, G.; Esdaile, L. J.; Anderson, H. L.; Martin, S.; Bethell, D.; Higgins, S. J.; Nichols, R. J. *Adv. Mater.* **2012**, *24*, 653–657.
- (11) Sedghi, G.; García-Suárez, V. M.; Esdaile, L. J.; Anderson, H. L.; Lambert, C. J.; Martín, S.; Bethell, D.; Higgins, S. J.; Elliott, M.; Bennett, N.; Macdonald, J. E.; Nichols, R. J. *Nat. Nanotechnol.* **2011**, *6*, 517–523.
- (12) Susumu, K.; Frail, P. R.; Angiolillo, P. J.; Therien, M. J. *J. Am. Chem. Soc.* **2006**, *128*, 8380–8381.
- (13) Li, Z.; Park, T.-H.; Rawson, J.; Therien, M. J.; Borguet, E. *Nano Lett.* **2012**, *12*, 2722–2727.
- (14) Couture, M.; Yeh, S.-R.; Wittenberg, B. A.; Wittenberg, J. B.; Ouellet, Y.; Rousseau, D. L.; Guertin, M. *Proc. Natl. Acad. Sci.* **1999**, *96*, 11223–11228.
- (15) Wende, H.; Bernien, M.; Luo, J.; Sorg, C.; Ponpandian, N.; Kurde, J.; Miguel, J.; Piantek, M.; Xu, X.; Eckhold, P.; Kuch, W.; Baberschke, K.; Panchmatia, P. M.; Sanyal, B.; Oppeneer, P. M.; Eriksson, O. *Nat. Mater.* **2007**, *6*, 516–520.

- (16) Hermanns, C. F.; Tarafder, K.; Bernien, M.; Krüger, A.; Chang, Y.-M.; Oppeneer, P. M.; Kuch, W. *Adv. Mater.* **2013**, *25*, 3473–3477.
- (17) Wäckerlin, C.; Tarafder, K.; Girovsky, J.; Nowakowski, J.; Hählen, T.; Shchyrba, A.; Siewert, D.; Kleibert, A.; Nolting, F.; Oppeneer, P. M.; Jung, T. A.; Ballav, N. *Angew. Chem. Int. Ed.* **2013**, *52*, 4568–4571.
- (18) Venkataramani, S.; Jana, U.; Dommaschk, M.; Sönnichsen, F. D.; Tucek, F.; Herges, R. *Science* **2011**, *331*, 445–448.
- (19) Lembo, A.; Tagliatesta, P.; Guldi, D. M.; Wielopolski, M.; Nuccetelli, M. *J. Phys. Chem. A* **2009**, *113*, 1779–1793.
- (20) Kim, H.; Chang, Y. H.; Lee, S.-H.; Kim, Y.-H.; Kahng, S.-J. *ACS Nano* **2013**, *7*, 9312–9317.
- (21) Cho, W. J.; Cho, Y.; Min, S. K.; Kim, W. Y.; Kim, K. S. *J. Am. Chem. Soc.* **2011**, *133*, 9364–9369.
- (22) Wang, C.; Batsanov, A. S.; Bryce, M. R.; Martín, S.; Nichols, R. J.; Higgins, S. J.; García-Suárez, V. M.; Lambert, C. J. *J. Am. Chem. Soc.* **2009**, *131*, 15647–15654.
- (23) Leary, E.; La Rosa, A.; González, M. T.; Rubio-Bollinger, G.; Agraït, N.; Martín, N. *Chem. Soc. Rev.* **2015**, *44*, 920–942.
- (24) Arroyo, C. R.; Leary, E.; Castellanos-Gómez, A.; Rubio-Bollinger, G.; González, M. T.; Agraït, N. *J. Am. Chem. Soc.* **2011**, *133*, 14313–14319.
- (25) Yoon, H. J.; Bowers, C. M.; Baghbanzadeh, M.; Whitesides, G. M. *J. Am. Chem. Soc.* **2014**, *136*, 16–19.
- (26) Colorado, R.; Villazana, R. J.; Lee, T. R. *Langmuir* **1998**, *14*, 6337–6340.
- (27) Morf, P.; Raimondi, F.; Nothofer, H.-G.; Schnyder, B.; Yasuda, A.; Wessels, J. M.; Jung, T. A. *Langmuir* **2006**, *22*, 658–663.
- (28) Von Wrochem, F.; Gao, D.; Scholz, F.; Nothofer, H.-G.; Nelles, G.; Wessels, J. M. *Nat. Nanotechnol.* **2010**, *5*, 618–624.
- (29) Schmidt, R. D.; Shultz, D. A.; Martin, J. D.; Boyle, P. D. *J. Am. Chem. Soc.* **2010**, *132*, 6261–6273.
- (30) Li, Z.; Smeu, M.; Park, T.; Rawson, J.; Xing, Y.; Therien, M. J.; Ratner, M. A.; Borguet, E. *Nano Lett.* **2014**, *14*, 5493–5499.

- (31) Lee, T.-C.; Hounihan, D. J.; Colorado, R.; Park, J.-S.; Lee, T. R. *J. Phys. Chem. B* **2004**, *108*, 2648–2653.
- (32) Castner, D. G.; Hinds, K.; Grainger, D. W. *Langmuir* **1996**, *12*, 5083–5086.
- (33) Ishida, T.; Choi, N.; Mizutani, W.; Tokumoto, H.; Kojima, I.; Azebara, H.; Hokari, H.; Akiba, U.; Fujihira, M. *Langmuir* **1999**, *15*, 6799–6806.
- (34) Leavitt, A. J.; Beebe, T. P. *Surf. Sci.* **1994**, *314*, 23–33.
- (35) Matthiesen, J. E.; Jose, D.; Sorensen, C. M.; Klabunde, K. J. *J. Am. Chem. Soc.* **2012**, *134*, 9376–9379.
- (36) Vericat, C.; Vela, M. E.; Salvarezza, R. C. *Phys. Chem. Chem. Phys.* **2005**, *7*, 3258–3268.
- (37) Eguchi, K.; Takagi, Y.; Nakagawa, T.; Yokoyama, T. *J. Phys. Chem. C* **2014**, *118*, 17633–17637.
- (38) Giacalone, F.; Segura, J. L.; Martín, N.; Guldi, D. M. *J. Am. Chem. Soc.* **2004**, *126*, 5340–5341.
- (39) Lee, Y.; Carsten, B.; Yu, L. *Langmuir* **2009**, *25*, 1495–1499.
- (40) Niskala, J. R.; Rice, W. C.; Bruce, R. C.; Merkel, T. J.; Tsui, F.; You, W. *J. Am. Chem. Soc.* **2012**, *134*, 12072–12082.
- (41) Wold, D. J.; Frisbie, C. D. *J. Am. Chem. Soc.* **2001**, *404*, 5549–5556.
- (42) Cui, X. D.; Zarate, X.; Tomfohr, J.; Sankey, O. F.; Primak, A.; Moore, A. L.; Moore, T. A.; Gust, D.; Harris, G.; Lindsay, S. M. *Nanotechnology* **2002**, *13*, 5–14.
- (43) Wang, G.; Kim, T.-W.; Jang, Y. H.; Lee, T. *J. Phys. Chem. C* **2008**, *112*, 13010–13016.
- (44) Valkenier, H.; Huisman, E. H.; van Hal, P. A.; de Leeuw, D. M.; Chiechi, R. C.; Hummelen, J. C. *J. Am. Chem. Soc.* **2011**, *133*, 4930–4939.

CHAPTER 5:

LARGE AREA JUNCTIONS FROM SOFT LITHOGRAPHY FOR MACROSCOPICALLY ACCESSIBLE MOLECULAR ELECTRONIC DEVICES

Robert C. Bruce, Joshua D. Yablonski, Wei You

5.1 Background

5.1.1 *Limitations of Fabrication Techniques in Molecular Electronic*

Arguably the largest stumbling block toward implementing molecular electronics and their unique properties into mass-producible, modern electronics is the ability to actually produce these devices in a non-destructive manner while enabling them to be easily accessed. Organic and organic-based materials, especially at the single molecule level, are unable to withstand many processing techniques typically utilized for inorganic electronics, with techniques such as metal evaporation leading to large numbers of damaged and shorted devices¹ or inconsistent molecular junctions.² Previous chapters have detailed processes for formation of junctions with analytic techniques,^{3–5} though again these are not extendable to practical settings and applications. As interesting as the effects and advantages that exist with molecular electronics, inability to design consistent devices will continue to be a holdup to the applicability of the field.

In particular, heat can be an issue with particular systems. Though the ease of forming monolayers from the gold-thiol system have been shown, both in this work and elsewhere,⁶ the thiol bonds are only thermally stable until around 80 °C,⁷ which is strongly limiting when macroscopic device fabrication processes are introduced. This represents at least one issue that

can occur with direct metal evaporation. Also, many photoresists require baking steps either to activate cross-linking groups that enable the patterning or pre-exposure to remove solvent and prevent defects from forming during or after exposure.^{8,9} Other non-metal deposition processes, such as PECVD, which is often used to deposit insulating layers such as silicon nitride or silicon oxide, impact molecules with hot molecules and ions or require heating for operation. Even cleaning and patterning steps can indirectly impact these bonds and impact the integrity of the monolayer.

Given the possibility of damaging the thiol bond, if not the organic monolayer as a whole, the challenge is to design a molecular electronic architecture extendable to temperature dependent and spin measurements of arbitrary molecular system – which practically means possessing macroscopically accessible electrodes – and do so without any steps that require heating or otherwise damage the substrate. The work in this chapter represents several attempts at this goal, and discusses the effects of literature and novel processes and their effects on macroscopically accessible organic monolayer junctions.

5.1.2 Overview

Several different techniques and architectures are reported here toward macroscopically accessible junctions for organic monolayers, including nanoindentation of 200 nm nTP features, several soft lithographic processes for patterning metal contacts directly onto a monolayer on a macroscopic scale, and graphene as a spin retentive buffer layer in ME devices. Each technique possesses its own advantages and disadvantages, as will be discussed in the appropriate sections. As a whole, this section will comment on the needs and requirements for unique molecular systems, such as the porphyrin wires, to be utilized in electrical device architectures that, ideally, could be utilized in modern electrical applications.

5.2 Methods

5.2.1 General

1,10-decanedithiol was purchased from Alfa Aesar and used without further purification. Electrical devices were prepared on RCA (2:1:1 H₂O:H₂O₂:NH₄) cleaned silicon oxide wafers. Bottom electrodes were patterned through standard lithographic processes, leading to patterned bottom contacts of 40 nm gold (evaporated at 1 Å/s for first 5 nm, 10 Å/s for duration) with 5 nm titanium (evaporated at 1 Å/s) as an adhesion layer that was adapted to the various techniques described below.

5.2.2 Atomic Force Microscopy

Atomic force microscopy (AFM) imaging and other techniques were done using an Asylum Atomic Force Microscope (Asylum MFP-3D, *Asylum Research*). Tapping-mode images were taken using silicon cantilevers (*BudgetSensors*, Tap300Al) with resonance frequencies of approximately 300 kHz and a force constant of approximately 40 N/m. Conductive measurements of individual features were taken using the same AFM system, using cantilevers purchased from *Olympus* (AC240TS, force constant ~2 N/m) and prepared with a conductive layer as described in previous Chapters.

Indentations for the nanoindentation method were done by increasing the force from the tip on the sample while measuring deflection of the tip, measured in the IGOR software as “Deflection Voltage”. Resist layers of different thicknesses were prepared; in particular, PMMA, 4% w/w in anisole, was spun-cast at 4000 rpm and led to films ~ 150 nm thick, while S1813 films spun cast at 7000 rpm led to films ~ 1 µm thick. For the former, 9.5 V of deflection voltage (22.5 µN of force) were used to produce holes in the polymer film, whereas the latter utilized 25 µN, the maximum that could be applied in the setup.

5.2.3 Kinetic Controlled Transfer Printing (KTP)

Features for KTP were defined on SiO_x. Hexamethyldisilazane (HMDS) was drop cast onto wafers to allow for good adhesion of photoresist. JSR NFR-016 negative photoresist was spun-cast onto cleaned SiO_x wafers at 3000 rpm for 1 min, with a pre-bake anneal of 90 s at 90 °C. Films were exposed using a Karl Suss mask aligner for 10 s at 10 mW power, then post-exposure baked for 90 s at 90 °C and developed for 1 min in MF-319. Features were deposited by sputtering 200 nm gold at 2 Å/s through the patterned photoresist. Finally, photoresist was lifted off in acetone, leaving the patterned features on SiO_x.

To transfer patterned features, a small amount of SiO_x was etched to facilitate picking up of KTP features from the donor. The donor with features was dipped in 5% HF for 30 s, then rinsed with DI water. Features were picked up on a polydimethylsiloxane (PDMS) stamp following the etch, prepared from 3.5:1 prepolymer to crosslinker (~1 cm thick), with a quick peel. PDMS stamp with features were then brought in contact with the receiving substrate, and a slow peel of the stamp enabled transfer to the receiving substrate.

5.2.4 Electron Beam Lithography

Poly(methyl methacrylate) (PMMA) films for patterning were spun-cast from 4% w/w solutions in anisole at 500 rpm for 30 sec, three times consecutively for each sample. Films were not completely dry after this step and needed approximately 10 mins air drying, forming ~1.5 µm thick films. Electron beam lithography (e-beam lithography) was done using a Hitachi S-4700 field emission scanning electron microscope on prepared PMMA films. Programmed featured were written at 510 µC/cm², then exposed samples were developed in methyl isobutyl ketone (MIBK):IPA 1:3 solution for 60 s, and rinsed in IPA and blown dry in N₂ gas stream.

5.2.5 Oxygen Plasma Cleaning

Oxygen (O_2) plasma cleaning was done in an Alcatel AMS 100 Deep Reactive Ion Etcher. O_2 gas was flown at 9 sccm. A power of 250 W was applied to the gas, the minimum required for operation in the setup, with no bias on the substrate holder. To mitigate heating issues, the substrate holder was cooled to as low as $-20\text{ }^\circ\text{C}$ during operation. Seasoning of the chamber for 15 mins before first sample runs was necessary for operation. For PEDOT:PSS, 5 min runs under these conditions removed conductivity in blank regions on the substrate as measured by voltmeter. For graphene devices, 1 min removed conductivity in blank regions.

5.2.6 Graphene Transfer and Device Fabrication

PECVD prepared graphene was received as grown on copper foil. Elastomeric polymer was spun-cast onto the graphene layer of the copper; either PMMA or poly(vinyl acetate) (PVAc) was spun cast from 10% w/w chlorobenzene solution at 4200 rpm for 45 s and annealed at 180°C for 1 min. Copper was then etched from the copper/ graphene/ polymer stacks in 0.1 M $(\text{NH}_4)_2\text{S}_2\text{O}_8$ aqueous solutions overnight, leading to the graphene/ polymer stacks floating on the water solution. Before transferring to final substrate, the graphene was cleaned in a dilute RCA solution (50:1:1 H_2O : H_2O_2 : NH_4OH) for 15 mins to remove residual copper from the stack.¹⁰ After final rinsing in water bath, graphene/ polymer stacks were scooped from water onto the transfer substrate (SiOx wafer, possibly with monolayer) and allowed to dry overnight. Depending on conditions tested, samples were annealed, $150\text{ }^\circ\text{C}$ for 15 mins for PMMA films, or $50\text{ }^\circ\text{C}$ for 15 mins for PVAc films. Polymer films were then removed with gentle stream of acetone. Patterning of transferred graphene was done with e-beam lithography and O_2 -plasma with a freshly spun-cast PMMA film. Top electrodes were sputtered through a shadow mask, 200 nm gold at $2\text{ }\text{\AA}/\text{s}$.

5.2.7 Raman Spectroscopy

Raman spectroscopy was done on a Renishaw InVia Raman microscope using a 514 nm laser and 1800 grooves/mm grating. Exposure time was 1 s, with 25 accumulations.

5.2.8 PEDOT:PSS Devices

Clevios pH500 poly(3,4-ethylenedioxythiophene) polystyrene sulfonate (PEDOT:PSS) was used with 5% by weight DMSO and a fluoroadditive, ZONYL (*Sigma Aldrich*), added 2 drops to a 5 mL aliquot of PEDOT:PSS. Aqueous solutions of PEDOT:PSS, DMSO, and ZONYL were spun cast onto substrates at 4000 rpm for 1 min, then fully dried in air. Top electrodes were attached *via* metal sputtering, 200 nm at 2 Å/s through a shadow mask. Top electrodes acted as a mask for the oxygen plasma cleaning process to remove PEDOT:PSS between samples.

5.3 Results and Discussion

5.3.1 Nanoindentation of 200 nm nTP Features

In previous chapters, nanotransfer printing (nTP) has been used to regularly create large numbers of reproducible metal-molecule-metal junctions on organic monolayers. One of the disadvantages of the technique as used is the inability to infinitely scale the printed features. Previous work has shown that cracks and significant defects in printed features begin to form on the tens of microns scale, creating electrically isolated regions.¹¹ Lacking the ability to directly print totally connected large contacts, the primary option becomes finding a way to make contact to these small scale features and scale the contact to the macroscopic scale. cAFM was used as an analytic method in previous chapters, but as already mentioned, this is not adaptable to permanent devices. Therefore, we turn to methods that expose these features for macroscopic electrode deposition.

Nanoindentation has been expressed as a method to physically pattern photoresists at a smaller scale than can be typically done in a mask aligner.¹² The technique utilized an AFM tip to physically dig a hole in a photoresist film, exposing a region as small as on the order of tens of nanometers in the resist layer. The process can be monitored in real time and, if any height difference in the film is present, aligned to any features or objects that can be measured by the imaging mode of the AFM. Even if not possible, if only a general (optically visible) region is desired for patterning, the technique is very suitable. For 200 nm diameter pads, it was necessary to check whether alignment could be had through a resist film.

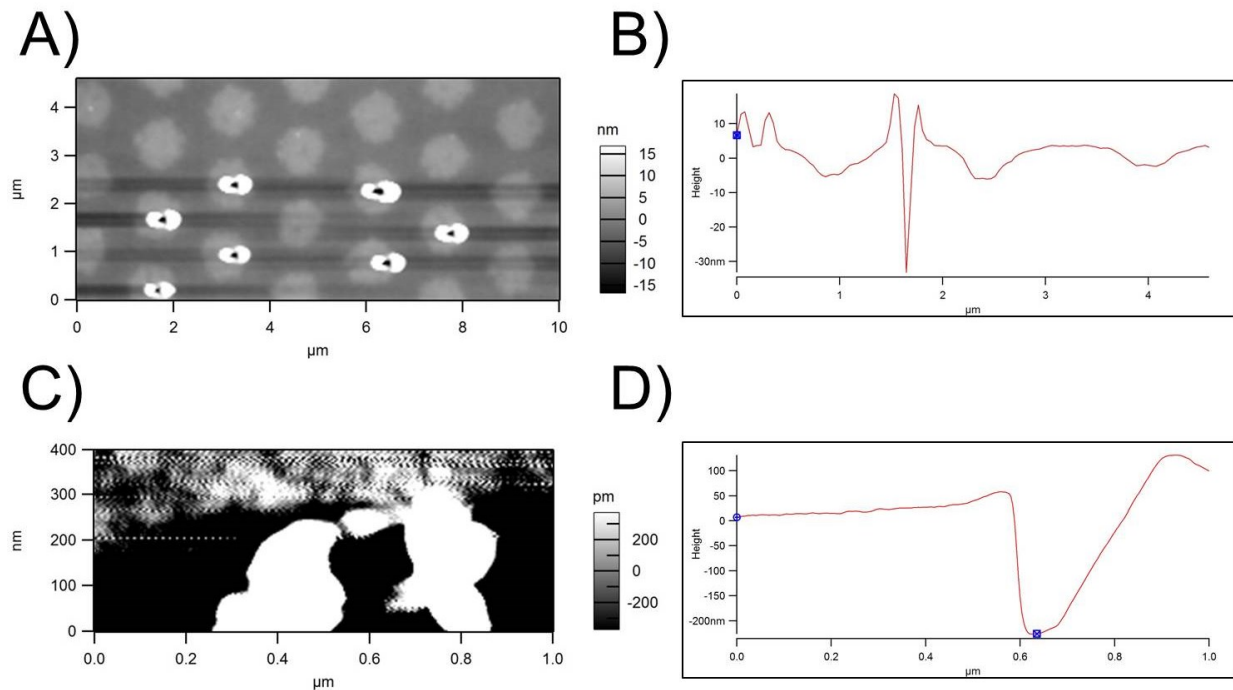


Figure 5.1 – Nanoindentation on Different Photoresist Formulations

Nanoindentation done *via* AFM on Shipley S1813 positive photoresists (PR). **A)** 4000 rpm spun-cast PMMA, indented with moderate force to make electrical contact with 200 nm nTP pads (visible in AFM through PR). **B)** Cross sectional AFM of hole made in A. **C)** 7000 rpm spun-cast S1813. Force needed to make contact through the film exceeded the AFM capability (PR thickness $\sim 1.5 \mu\text{m}$), and affected area $> 200 \text{ nm}$ size of pad aimed at. **D)** Cross sectional AFM of hole made in C.

As shown in Figure 5.1 A and B, the technique can be very well suited for exposing holes on 200 nm features. Even with a PMMA resist layer on top, the regions where features are printed produce a height different through the resist, indicating the locations where the nTP pads are and where nanoindentation should occur. For a thin enough film, reliable indentations can occur through the resist layer as well. The figures show that the impacted regions from the AFM can be restricted to the nTP features, in theory preventing any further processing – such as attachment of a macroscopically accessible electrode attachment – from affecting the monolayer directly and potentially shorting the device. When this technique is done using a conductive tip, a feedback loop can be programmed to indicate when the conductive nTP pad has been contacted. In the case of all nanoindented features shown in Figure 5.1 A, current between the tip and the nTP pad could be measured, indicating contact was in fact being made through the resist to the feature beneath. It should be noted that the film is thicker than the height profile in Figure 5.1 B fully indicates, though the conductive properties through the hole indicate it is deep enough to penetrate the film.

The problem with this technique, however, falls to the inability to extend these nanoindentations to macroscopic contacts. The thin resist films used in initial trials are too thin to withstand the metal sputtering of macroscopic leads, shorting in pinholes and defects at any number of locations throughout the film. A simple solution to prevent metal shorting is to increase the thickness of the photoresist film. However, this leads to a different issue. Whereas thin films can have very reliable and small holes generated to make contact to nTP pads, due to the increasing diameter dimensions of the AFM tip above the top, thicker films require larger holes to be made in order for the tip to dig deeper and contact the nTP feature. The result is what is shown in Figure 5.1 C and D, where a hole larger than the feature beneath it is generated, and

potential damage of a larger area of film may be occurring due to the physical pushing of resist to form the hole. Subsequent devices from thicker films were also shorted, likely due to these reasons.

Several other formulations of resists were used; unfortunately, they all experienced similar results. Thinner tips could presumably be used, however there would be a stronger potential for tips breaking as greater force on a smaller area are utilized. Given the limitations experienced, and with few methods to accurately align and develop resists smaller than the 200 nm scale apart from this, we focus on working on efforts with other techniques on larger features.

5.3.2 *Kinetic Controlled Transfer Printing*

The nTP technique as developed in our lab has limitations for the size with which it can reliably generate features. However, variations on the soft lithography process have been generated to transfer features of various sizes. While printing larger features than the 200 nm features discussed here would reduce the density of electrical devices on a substrate, for the purposes of research and device fabrication, it would open up many more possibilities. Exposing micron sized printed features on monolayers would not rely on nanoindentation and similar techniques; standard processes like photolithography could be adapted, allowing for much more uniform and reproducible processes for fabricating macroscopically accessible electrodes.

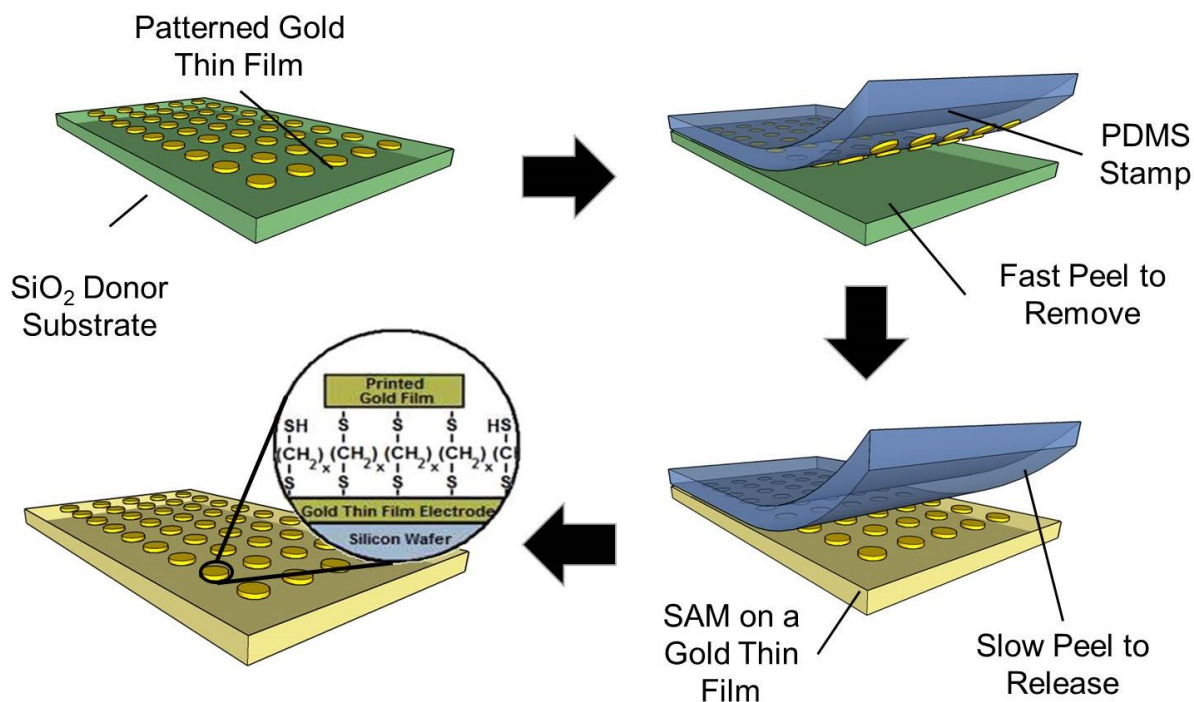


Figure 5.2 – Kinetic Controlled Transfer Printing (KTP) Process

Diagram of KTP transfer process. See section 5.2.3 for full experimental details.

To this end, a different soft lithographic process, which is referred to here as kinetically-controlled transfer printing (KTP), is explored. This process is adapted from work by Meitl *et al.*¹³ As used in this work, the nTP process relies on metal binding groups to transfer patterned features onto monolayers, and molecules lacking these metal binding groups will not receive well-structured features. KTP, however, relies solely on the energy of interaction between feature and stamp/ substrate and utilizes different surface energies to receive or transfer substrates. Figure 5.2 details the KTP procedure, where features of arbitrary size and shape can be patterned on a donor substrate using standard lithographic procedures and transferred onto a device which, in our case, possesses our monolayer of interest. Briefly, an elastomeric stamp, here made of polydimethylsiloxane (PDMS), is brought in contact with the features on the donor substrate and quickly peeled off the donor. The fast stamp removal creates a strong interaction

between the patterned features on the donor and the stamp, preventing (weak) intermolecular interactions from holding the features on the donor and promoting their transfer to the PDMS stamp. To transfer the features, the opposite effect is used. Once the stamp and features are brought into contact with the receiving substrate, a slow peel back promotes good transfer of the features off of the stamp. In this manner, features can be transferred reliably and in large number onto an arbitrary substrate.

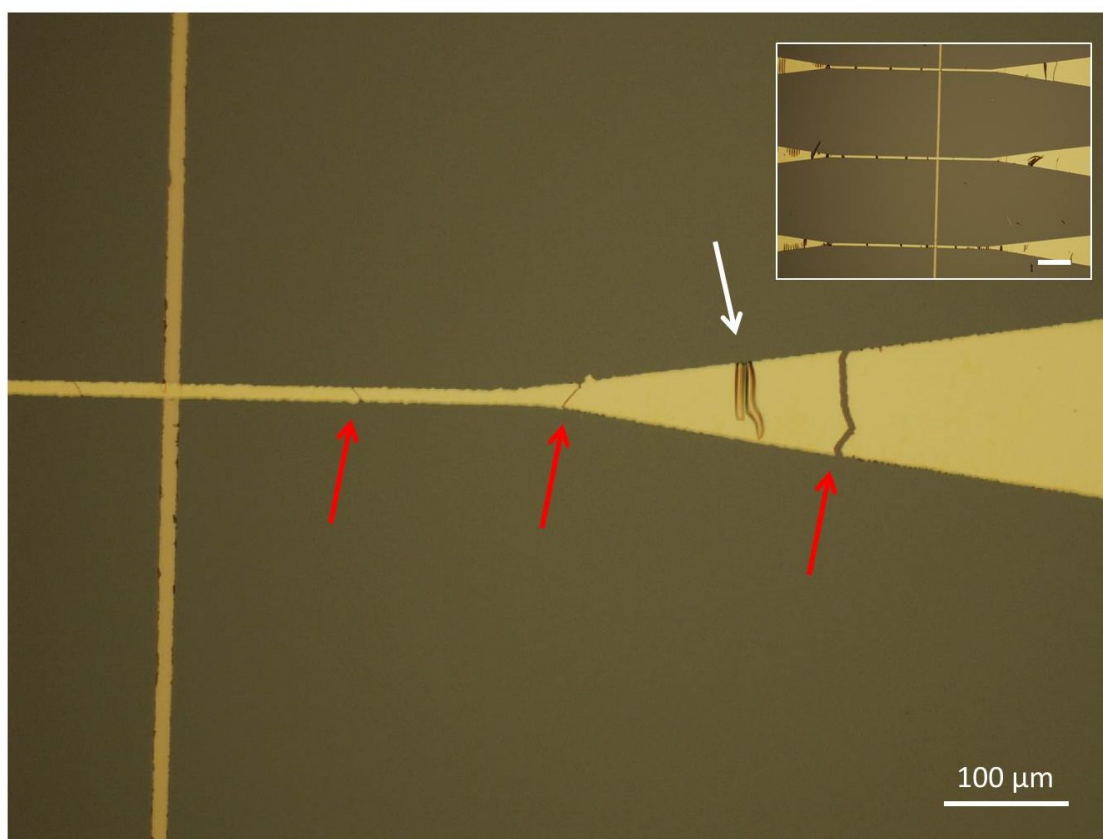


Figure 5.3 – KTP Crossbars on a Au/SiOx Substrate

KTP transferred crossbar features, 20 μm in size over active device area. Vertical bar is bottom substrate, prepared by metal evaporation (before KTP feature transferred, 20 μm in size). Horizontal feature is KTP transferred feature. Red arrows indicate cracks across the feature, electrically isolating regions of the feature. White arrow indicates folds that do not fully isolate features but are physical defects. Inset: More representative features, highlighting various folds and cracks. Scale bar for inset- 100 μm .

Though the process can in principle transfer features of any size and shape, the practical limitations of the process show that the bending of the stamp from peeling will lead to cracks on transferred features that are large. As shown in Figure 5.3, the attempt to print macroscopically accessible crossbars on top of the sample showed numerous cracks and folds, preventing conductivity across the bar. Perhaps this is an aspect ratio issue or requires different conditions (stiffer stamp, thicker gold, etc.) than what was tested. Either way, a one-step attachment of macroscopically accessible electrode to generate a ME junction was not attainable here.

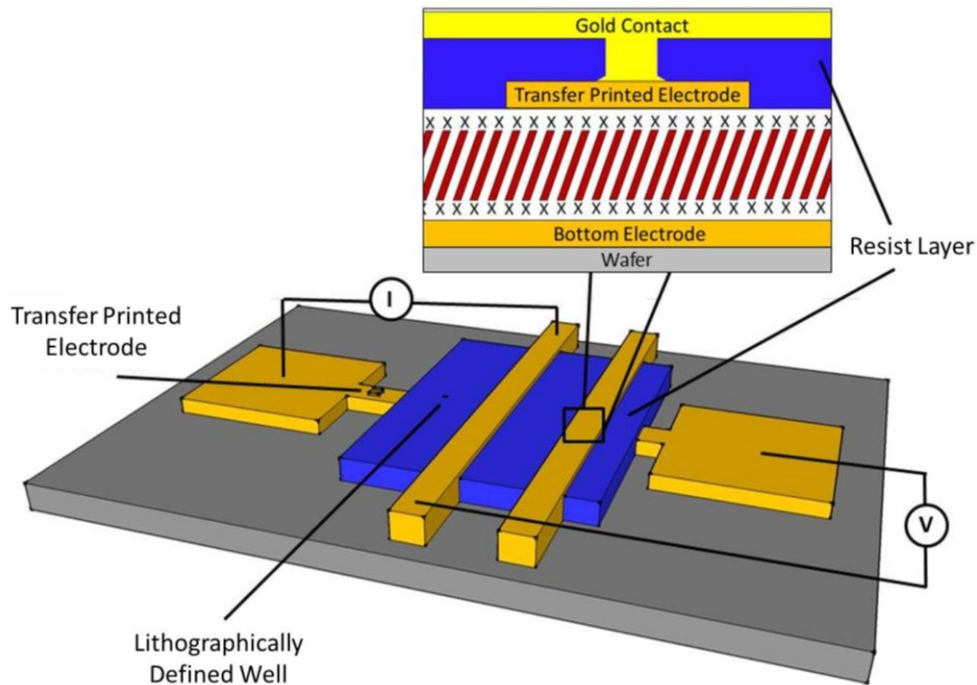


Figure 5.4 – KTP Device Architecture

Proposed device architecture to incorporate micron sized KTP features into four-terminal crossbar devices. Resist layer can be photoresist; throughout this work, PMMA for e-beam lithography is used.

In spite of the cracks evident in the larger crossbar transferred features, smaller (tens of micron scale), more symmetric gold features can be transferred very regularly through this technique. In light of this, an approach was taken to isolate these transferred features and create devices on the micron scale incorporating organic monolayers. Figure 5.4 shows a diagram of the

proposed device architecture. Because the features are on the micron scale, standard lithographic procedures can be done on the samples. In particular, electron beam lithography (e-beam lithography) is used here to open wells through a PMMA resist such that top contacts can be deposited only on transferred features and not on the bare monolayer.

The question needing to be addressed in this process is whether or not the lithographic process could withstand a sputtering process. As designed, the procedure for these features was to expose micron sized KTP pads and sputter onto the PMMA such that the only part of the substrate below the PMMA that would be characterized would be the KTP feature and the monolayer underneath it. However, there was expected to be a tradeoff between PMMA thickness needed to withstand shorts from sputtering and the ability to expose reliable features in the PMMA. Furthermore, heat annealing could not be done due to degradation that would occur in the monolayer, which likely prevented the PMMA from the optimal molecular orientation.

Various tests of PMMA thickness were done, where polymer was spun cast at low speed (as low as 500 rpm) on hexamethyldisilazane (HMDS) functionalized SiO_x and allowed to air dry for ~15 mins. To counteract the lack of strong morphology that would be generated by thermal annealing of the PMMA film, a UV-cross linking group, diethoxyacetophenone (DEAP) was added to the PMMA and cross-linked before e-beam exposure. It was determined that approximately 1 μm thick polymer was needed to withstand the metal sputtering process (i.e. not exhibit shorts or defects across a substrate), and with this 1% crosslinker recipe, nearly all films were insulating to metal sputtering processes. The film needed for top crossbar deposition is thus much thicker than the films typically used in e-beam lithography. Despite this, tuning of the e-beam conditions – in particular, turning up the exposure to account for the thicker film – allowed for reliable formation of micron sized features, as evidenced in dark-field imaging of a

developed PMMA exposure test (Figure 5.5), where the bright regions represent non-smooth portions of the sample (in this case, caused by the sides of the features). It is expected that this much thicker PMMA recipe will inhibit finer (smaller) features from being effectively patterned, as more scattering events would be likely to occur through the thicker polymer film. However, as shown, the conditions appear valid for good development of features on the micron scale. Greater than 85% wells on test samples were developed enough to show current after sputtering through the exposed bottom contact.

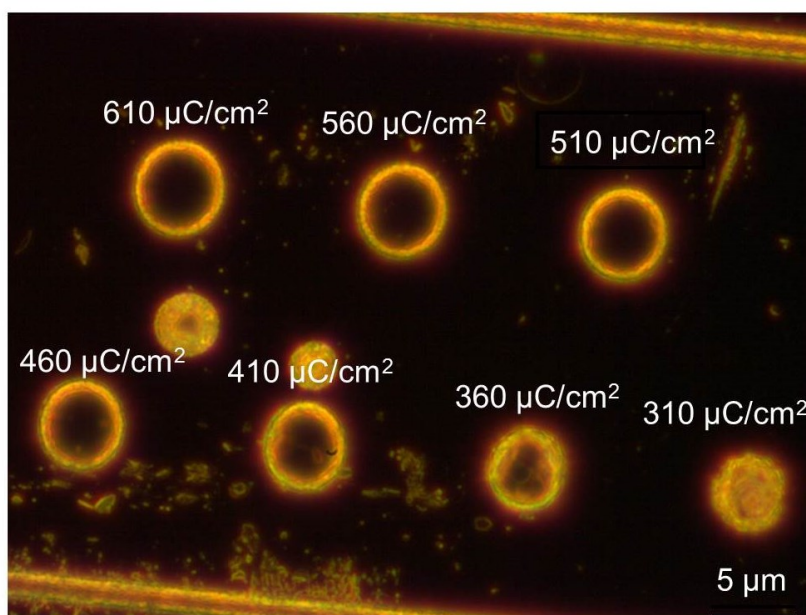


Figure 5.5 – E-beam Exposure Test on 1 μm thick PMMA

Exposing 5 μm circles using e-beam lithography on 1 μm thick PMMA with 1% w/w DEAP, images in an optical scope with dark field microscopy. Labels above the feature indicate exposure dosage used. Bright regions indicate scattered light, showing non-smooth areas in the PMMA. 310 $\mu\text{C}/\text{cm}^2$ was too low a dosage to fully develop a feature, leading to a rough PMMA that has not been fully developed. Above around 460 $\mu\text{C}/\text{cm}^2$, features appear fully developed. 510 $\mu\text{C}/\text{cm}^2$ was used on films throughout this work.

Even though PMMA is insulating and will typically not yield any reliable images in an electron microscope due to charging, an advantage of the KTP features is that they provide a conductive site that is visible through the PMMA, allowing for visualization of the features and

therefore alignment for development on top of the features (Figure 5.6 A). Even the bottom contact is slightly visible (running vertically on in the image, left edge near vertical white bar), allowing for identification of pads transferred on the conductive portion of the substrate.

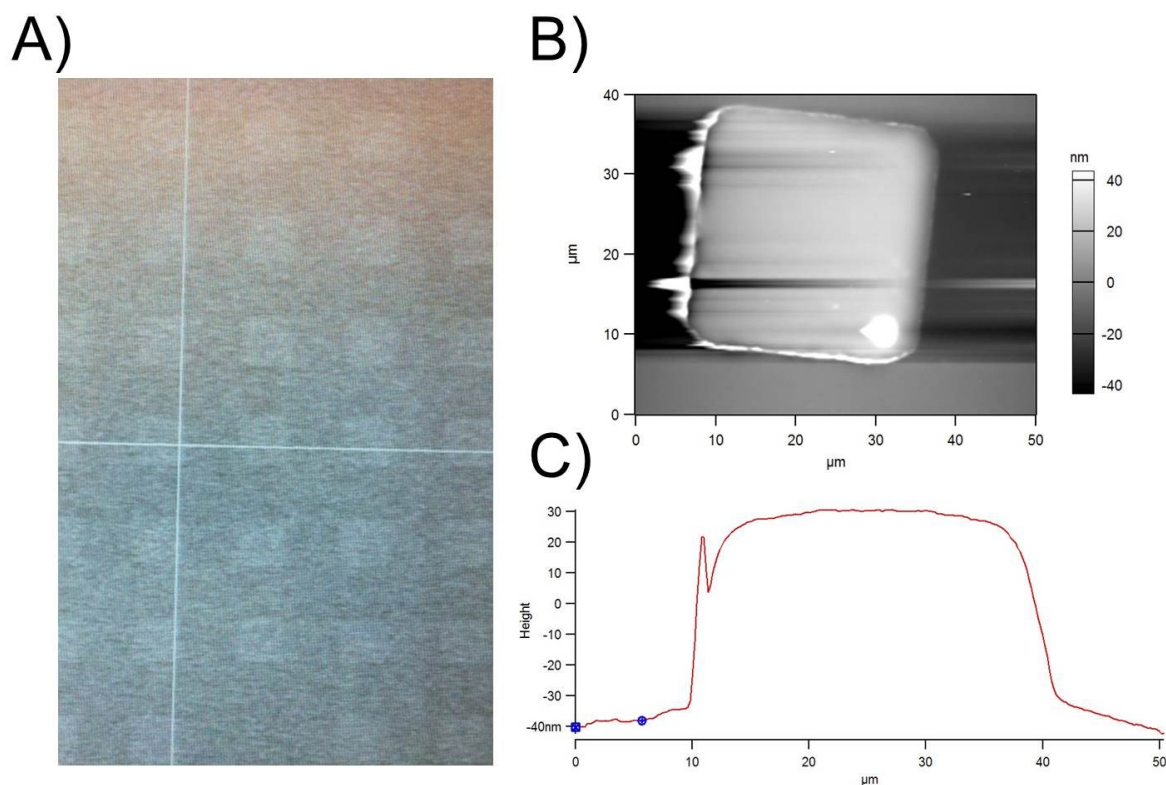


Figure 5.6 – KTP Features Imaged through PMMA

$30\ \mu\text{m} \times 30\ \mu\text{m}$ square features transferred onto a monolayer on gold substrate (see Figure 5.4 for device architecture). **A)** KTP features with $1\ \mu\text{m}$ PMMA as visualized in SEM, prior to e-beam lithography. **B)** Same features visualized through AFM. **C)** Cross-sectional image of KTP feature in AFM.

Despite this good control with thick PMMA, all devices both with monolayer and without exhibited subsequently shorted devices, evidenced through less than $1\ \Omega$ resistance and lack of tunneling nature in the electrical output. The alkanedithiols utilized should have shown strong tunneling behavior, and based on previous results, expected resistances for these junctions were 100s of Ω s.¹¹ To provide a possible explanation, we turn back to the fact that these features were very readily identifiable through the PMMA. As discussed in the nanoindentation study of 200

nm diameter nTP features, a slight protrusion of the features in the resist film was present, enabling identification of the location of these features. Likewise, with the KTP features, AFM readily showed a height difference between the resist layer on the printed feature versus off (Figure 5.6 B and C). Despite the $\sim 1.5\ \mu\text{m}$ thick PMMA on top of the feature, the 200 nm thick KTP feature showed a near 70 nm protrusion out of the PMMA film. It is clear from this that the PMMA film was not regularly distributed, highlighting the inability of spin casting to form smooth films on non-smooth surfaces despite being thicker than the features being deposited on top of.

The concern, and the possible explanation for the shorted devices, is that these raised features create thinner regions in the PMMA when it was seen that thinner films could be shorted through. It is difficult to measure exactly how much PMMA is on top of the features due to irregularities in the deposited PMMA – we only know for sure how far the feature has protruded off the surface – but the amount is undoubtedly less. Furthermore, film behavior at the edges of the feature is a cause for concern. Because the film is irregular and, as shown from Figure 5.6 C, slightly rounded around the edges, the thickness of the PMMA in these regions is likely even less than on top. This provides even more ample opportunity for deposited metal films to short through the film to the substrate beneath, thereby shorting the device.

Attempts to thicken the film further by drop casting PMMA led to films that were 5-10 μm thick. However, KTP features were not visible through SEM imaging with this thickness of PMMA. Ironically, the ability to visualize the KTP features in SEM as shown above may have only been because of the thinner PMMA on top of the feature. At this point, without the ability to thicken the PMMA while still maintaining our ability to align these features in the SEM, this approach is shown to be non-effective at generating large area devices.

One other possibility exists, which will in part motivate the next attempt to generate future works with these large area features. We know the organic monolayers used throughout these and other studies cannot withstand direct metal evaporation for a number of reasons, including penetration of metal, destruction of monolayer, and heating of the substrate. The idea of printing a metal contact and creating a macroscopically accessible top contact on it takes care of the previous two issues, as a good quality printed pad without cracks should be able to withstand evaporated material. However, we have implicitly assumed that heating effects from sputtering on the transferred gold pads would not occur or would not be relevant in these fabrication procedures. Being a strong conductor, the gold used as electrodes throughout these studies will transfer heat as well as electricity. It is possible that the evaporated or sputtered top metal contact transferred energy in the form of heat to the KTP pad, which then heated up the monolayer chemically bound to it. Given the low temperature needed to disrupt the gold-thiol bond (80 °C), it would not take much of a heating effect to damage the film. This damage could be a point of concern, if not the root cause, for shorting of devices in this procedure.

An attempt was made to help mitigate the heating issue of sputtering directly onto the conductive substrate by reintroducing PEDOT:PSS on top of KTP pads. As an aqueous soluble polymer, the PEDOT:PSS was not expected to interfere with the developed PMMA layers. As such, the device design would be the same as before, only with PEDOT:PSS inserted between KTP pad and top sputtered macroscopic contact. In this manner, the desirable metal-molecule-metal contact between bottom electrode- molecule- KTP pad could be preserved, with the PEDOT:PSS potentially mitigating heating issues in the substrate beneath it. The processing steps needed to be added then are spin-casting of PEDOT:PSS and patterning of the polymer once top contacts have been deposited. A ZONYL surfactant was added to enable the

PEDOT:PSS to adhere to the surface of the hydrophobic PMMA, a technique used with other hydrophobic resist layers.¹⁴

Table 5-1 – Exposures and Control Regions for PEDOT:PSS on PMMA Devices

| Molecule | 1% DEAP | | | 5% DEAP | |
|----------------------------|----------------------------------|-------------------------------|--------------------------------|----------------------------------|-------------------------------|
| | - 10 °C O ₂ Plasma | 0 °C O ₂ Plasma | 20 °C O ₂ Plasma | - 10° C O ₂ Plasma | 0 °C O ₂ Plasma |
| Exposure- Conductive | 0 | 1 | 0 | 2 | 0 |
| Exposure- No Current | 4 | 3 | 4 | 2 | 4 |
| No Exposure- Conductive | 0 | 1 | 0 | 0 | 0 |
| No Exposure- No Current | 4 | 3 | 4 | 4 | 4 |

* 'Exposure' signifies devices where PMMA was developed for a well; 'No exposure' signifies no development

**Temperature refers to temperature of substrate holder in O₂ plasma during process

The issue with this architecture was almost the opposite as seen with direct sputtering onto KTP features. Whereas previously too many shorts were occurring, the process incorporating PEDOT:PSS created issues without any current.

Table 5-1 presents results for several different formulations of PMMA and processing conditions. Regions without e-beam exposure and without well formation (control regions) typically measured no current, which is a positive result, but e-beam exposed samples where wells were developed and current should have been seen led to very few conductive samples. It is apparent then that either PEDOT:PSS could not access the open wells, a factor that is not likely given the ability to enter wells in similar studies using photolithography,¹⁴ or that the well is being somehow removed and blocking electrical contact. The point at which this may be occurring is during the O₂ patterning step of the PEDOT:PSS to create individual features. It has

been reported that heating the PMMA above its glass transition temperature (T_g) of 120°C will cause flow of the polymer and potentially remove any developed features. The best explanation is that the flow of the PMMA was large enough that it ultimately isolated the device. Different concentrations of DEAP were used, and cooling the substrate holder to as low as the base temperature of – 20 °C were used to attempt to mitigate this heating, but to the threshold of the equipment used and inhibiting the polymer film properties (which occurred above 5% w/w DEAP, where all films had defects that led to shorts in control samples), this could not be done. As far as using PEDOT:PSS as a heat buffer for KTP pads, we were unsuccessful at incorporating it.

It should be noted that if the interpretation is true that heating effects caused flow of the PMMA, then it is very likely that the monolayer beneath it would have been damaged by the same problem. While we have no direct means of measuring the temperature of the sample during the plasma process, the PMMA appears to indicate the conditions that the sample was subjected to, and appears to indicate that, even while attempting to cool the sample with substrate holder, the heating effects were too large for the sample.

Without the ability to remove the appearance of thin PMMA on top of KTP features, we ultimately cannot verify the heating problem from direct contact of a metal evaporated film as a root cause of device failure. However, this still motivates a movement to transfer large area pads without using metal evaporation techniques on the substrate, even those that are indirect to the monolayer (i.e. on printed nTP/KTP pad on a monolayer). As shown above (Figure 5.3), printing macroscopic and long pads with arbitrary dimension is not amenable to the KTP process. As will be discussed in future works (Chapter 6), other soft lithographic transfer processes exist that could mitigate these concerns.

5.3.3 *Graphene as a Molecular Electronic Buffer Layer*

Throughout this work, a chemically bound, metal-molecule-metal junction has been stressed as a desirable junction toward realizing unique electronic and spintronic properties in molecular junctions. While this is still true, the approach of using a buffer to facilitate device fabrication is still an intriguing alternative. The consideration that must be met for this to be a valid option for these studies is that it does not restrict the observation of the electronic and spintronic properties of molecules. The latter is especially important to this study and the reason why PEDOT:PSS and rGO were avoided for most of the work. Transporting spin can be done cleanly through certain materials, but thick, spun-cast buffer films will at best possess their own magnetoresistive effect from an OMAR type effect,¹⁵ or at worst, scatter spin altogether.

Graphene is a unique material to consider in this buffer approach. Made from a highly conjugated network of benzene rings, graphene is presently unparalleled in the realm of organic electronics in its transport and conductivity properties. Large electron densities, measured up to 10^{13} carrier/cm⁻² concentration, coupled with mobilities comparable to some conductive metals, makes graphene a realistic alternative for electronic applications.¹⁶ PECVD has been useful for generating large sheets of graphene on common metals such as copper and nickel,¹⁷ after which the graphene can be transferred to an arbitrary substrate using any number of techniques, most of which focusing on utilizing an elastomeric polymer as a transfer material.¹⁰ Though the PECVD process can be slow on individual substrates, equipment and processes have been generated to facilitate the PECVD growth of graphene into a roll-to-roll process, providing the possibility to large scale production¹⁸ and, as of this writing, the best chance for graphene to come into mainstream electronic use.

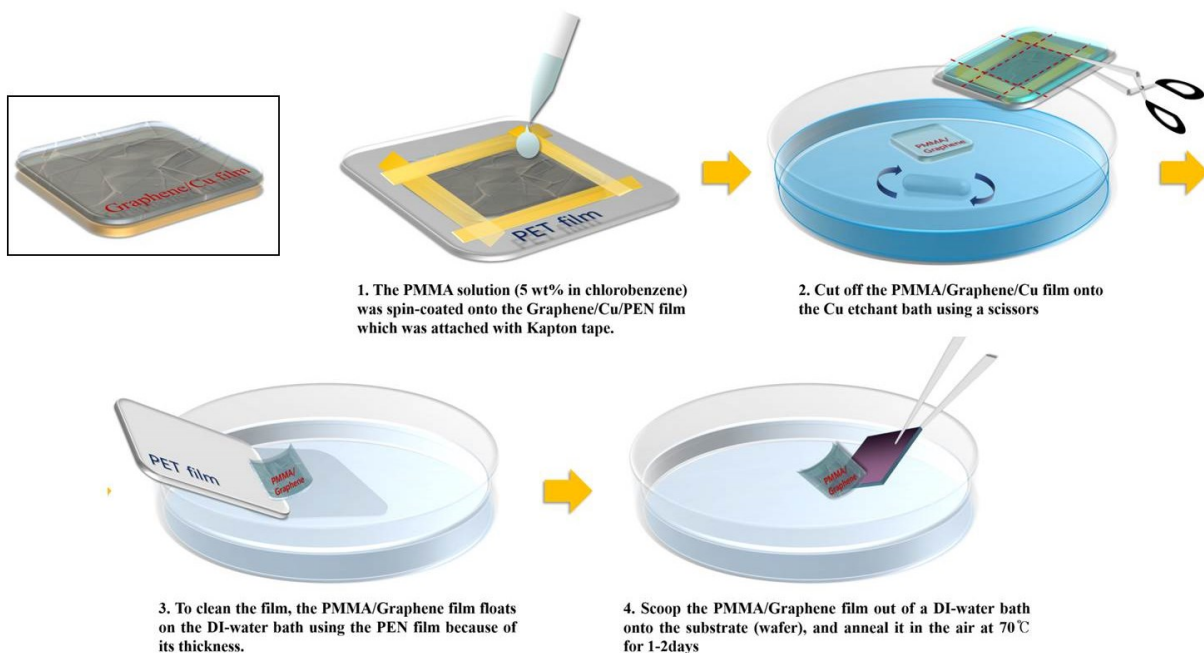


Figure 5.7 – Graphene Transfer Process

Representative images of transferring graphene from copper foil onto arbitrary substrate. Images courtesy of Prof. Youngu Lee at DGIST (South Korea).

What makes graphene a valid option as a buffer layer for these studies is its ability to serve as a spin tunnel barrier. Unlike PEDOT:PSS and the solution processable derivative of the graphene material (rGO), graphene is known to sustain spin over long distances, enabling its use in a number of spintronic studies. Spin lifetimes on the order of a micron have been reported,¹⁹ allowing spin transport along graphene to be utilized for magnetoresistive junctions between two ferromagnetic electrodes.²⁰ Furthermore, graphene has been utilized as a spin tunnel barrier, sustaining spin and potentially helping organic materials overcome the conductivity mismatch problem.²¹ This last point is most intriguing to our setup. If we can generate a monolayer and transfer graphene as a buffer layer directly on top of the monolayer, we should be able to measure the spin transport through the material. Any spin effects from chemical binding of the top metal contact to the molecule would be lost, but this would still provide an avenue for

examining spin effects of, for example, the porphyrin metal centers on spin transport along the backbone.

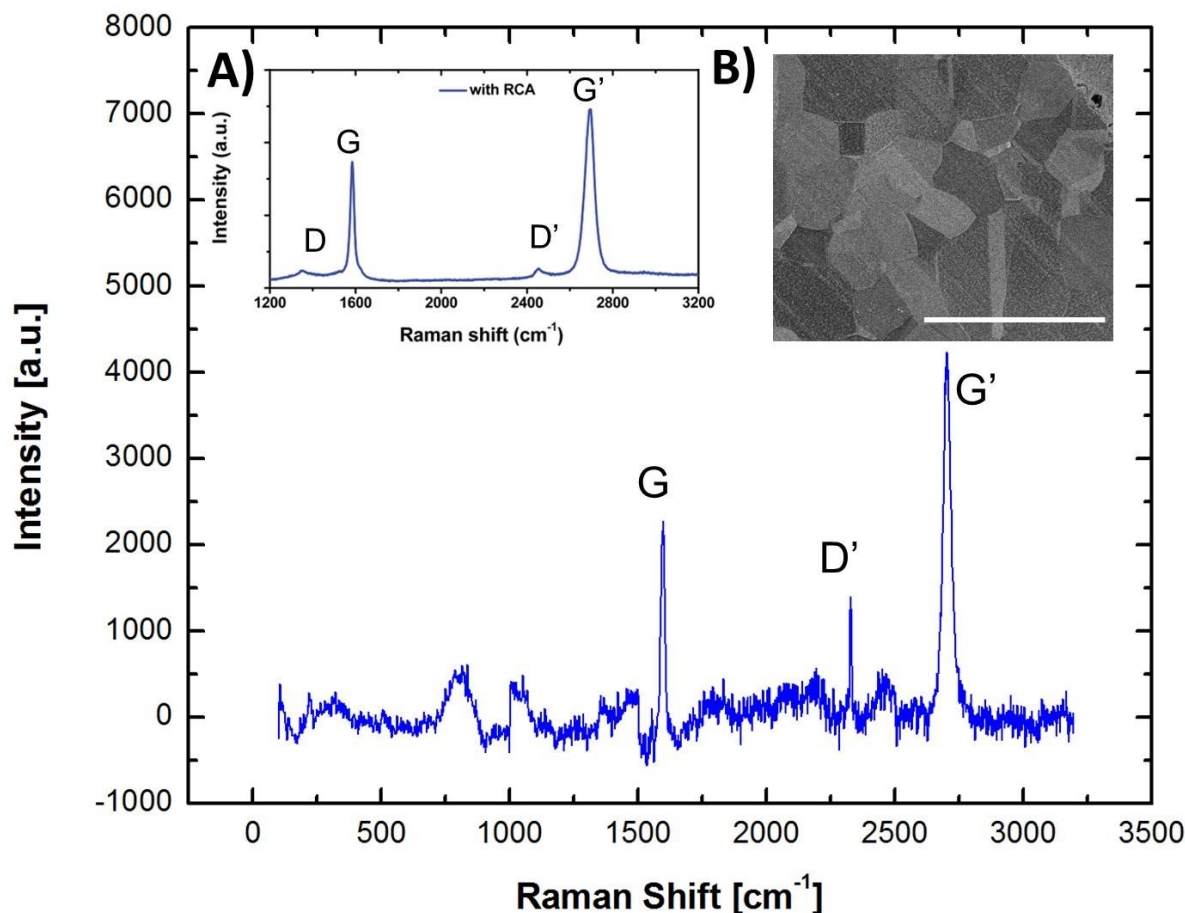


Figure 5.8 – Raman of Graphene Films

Raman spectroscopy of graphene films on copper foil, with G', D', and G peaks identified (D peak was not readily visible). Insets: **A)** Literature graphene Raman spectrum. Reprinted with permission from Ref. 10. Copyright 2011 American Chemical Society. **B)** Scanning electron microscopy (SEM) image of graphene, highlighting micron sized grains in graphene film. Scale bar: 200 μm.

With this in mind, we seek to transfer graphene on top of organic monolayers and then evaporate material on top of patterned graphene. PECVD graphene on copper foil is provided by Prof. Youngu Lee (Daegu Gyeongbuk Institute of Science and Technology, DGIST). Figure 5.8 shows Raman spectroscopy that was done on the graphene on copper film, highlighting peaks

characteristic of graphene from the literature.¹⁰ Initially, a procedure similar to Figure 5.7 was utilized, with PMMA as a transfer polymer. As discussed, heat is an issue with organic monolayers, so one of the first points to be addressed was annealing the PMMA film. Typical procedure involves annealing PMMA above its T_g to help the PMMA/graphene stack adhere to a substrate. However, doing so would damage the gold-thiol bond in monolayers, making it a requirement to change this step.

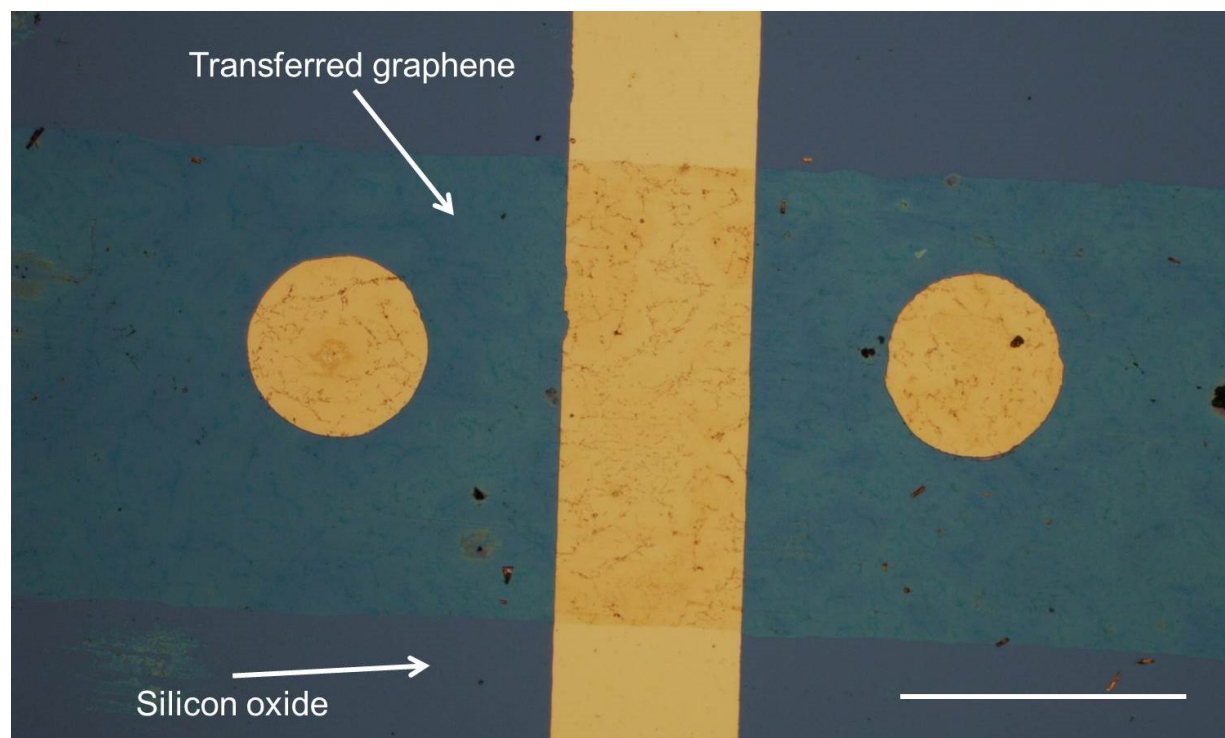


Figure 5.9 – Heatless Graphene Transfer

PE-CVD graphene, transferred from PMMA sacrificial polymer without heat annealing onto patterned silicon oxide wafer. Gold circles are used for alignment of strip transfer location, vertical gold bar used for electrical contact in finished device. Scale bar: 500 μm .

It was discovered with initial work that graphene could be transferred from PMMA stacks without any annealing. Figure 5.9 shows an example of a graphene strip that could be transferred to a patterned bottom substrate without any annealing before dissolving of the polymer layer (gold circles were used for alignment). However, two consequences to this heat-

less transfer process were discovered. First, testing the resistance of the junctions yielded unreliable resistances, sometimes in the GΩs, indicating poor contact with the substrate. Second, further lithographic steps were unable to be done to further pattern the graphene strips. Removal of resist layers damaged the graphene films, so devices had active areas too large to lead to any results other than shorted devices or resistances that made them indistinguishable from shorts. The 150 °C anneal removed this issue, appearing to give better contact that allowed for patterning *via* resist layers. Though the transfer could be done, the thermal anneal appeared necessary to establish good quality for device fabrication.

To remove this issue, PMMA was substituted with a lower T_g polymer to attempt to transfer graphene and make good contact without utilizing temperatures that damaged the monolayer. In particular, poly(vinyl acetate) (PVAc) has a reported T_g of around 28 °C. Films of PVAc were thus utilized in analogous manner to the PMMA, spin-casting the material onto PECVD graphene and using it to transfer onto a silicon oxide substrate. Subsequent patterning can be done on the transferred film (Figure 5.10). In particular, using a different PMMA film for e-beam lithography (utilizing the same recipe described above for KTP features, such that heat annealing of the PMMA film is not required) allows for isolation of graphene strips across a substrate. An O₂-plasma step cleans the exposed graphene from the developed resist away.

Figure 5.10 shows patterning of the PVAc transferred graphene *via* e-beam lithography. With e-beam lithography as used being a positive resist process, there is a tradeoff between the area of PMMA exposed and the time it takes for the process. Because of this, we cannot develop all non-essential PMMA on the substrate and leave just graphene for contact to the substrate. Instead, we can only remove a region of PMMA around the graphene for a top contact in order to leave a patterned feature on the bottom contact. Though a limitation to use PMMA in this way, it

was found that the plasma process to clean the exposed graphene removed a decent amount of PMMA in the non-exposed regions, not enough that the graphene under it was compromised, but enough that metal evaporation over the patterned graphene strips could be electrically accessed with low resistance. This provides an advantage over photoresist films where the liftoff needed after development was seen to damage the graphene films underneath.

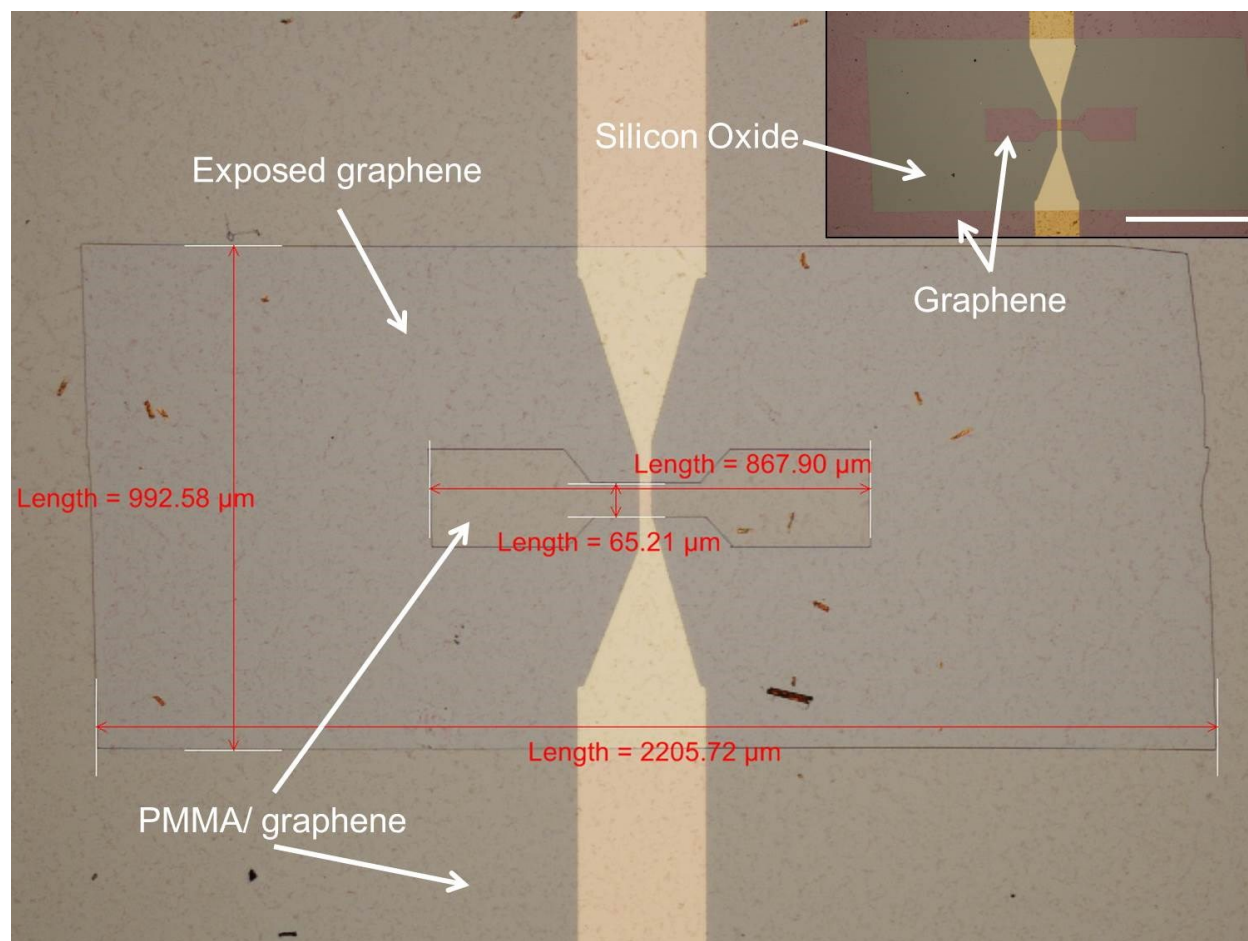


Figure 5.10 – E-beam Patterned Graphene

PE-CVD grown graphene, transferred *via* PVAc polymer layer, with PMMA layer patterned by e-beam lithography. Main image: exposed and developed PMMA, exposing graphene layer only in the inner portion of the image to pattern a $60 \times 20 \mu\text{m}$ active layer on the gold substrate. Sizes indicated by measurement lines. Inset: post-O₂ plasma and PMMA liftoff, exposing graphene (purple regions) and silicon oxide where graphene has been removed (green region). Scale bar: 50 μm .

While electrical contact could be made to the graphene and finished devices prepared, junctions incorporating alkanedithiol monolayers yielded Ohmic (non-tunneling) behavior with sub- 1 Ω resistance. Given the protection of the monolayer throughout the fabrication process, the most likely cause of the shorting is the heating/ damaging of the monolayer during the O₂-plasma step.

5.3.4 Evaluation of Macroscopic Fabrication Techniques

To the last point above, numerous steps in the fabrication process were introduced to attempt at removing heating issues, but it is still possible that other steps – namely the sputtering steps and the O₂ plasma process – could have still caused problems. Examining monolayer quality after a top contact has been sputtered is difficult to do, but for the latter point, we can turn to a control study with PEDOT:PSS as a buffer layer to comment on the effects of heating from the plasma.

Since PEDOT:PSS will not act as an effective spin transport layer, we use it here solely as a control study to compare to literature reports of devices using it as a buffer layer.¹⁴ In these devices, decanedithiol – a good test system due to its well-behaved monolayer properties⁶ – is deposited, and PEDOT:PSS is spun cast directly on the monolayer. The large sizes of the polymer units in the aqueous soluble polymer mixture enable the polymers to lie on top of monolayer instead of going through defects and grain boundaries. PEDOT:PSS is robust enough to withstand metal evaporation, so macroscopically accessible contacts can be directly evaporated on top of the film. Figure 5.11 shows the device architecture at this step. At this step is, the conductive PEDOT:PSS covers the substrate and electrically connects all devices. Patterning of the PEDOT:PSS is necessary, and as reported by Akkerman *et al.*, all that is needed is exposure to oxygen plasma to remove the PEDOT:PSS between devices due to the top gold contacts serve as a shadow mask for the process, removing the need for further resist layers.¹⁴

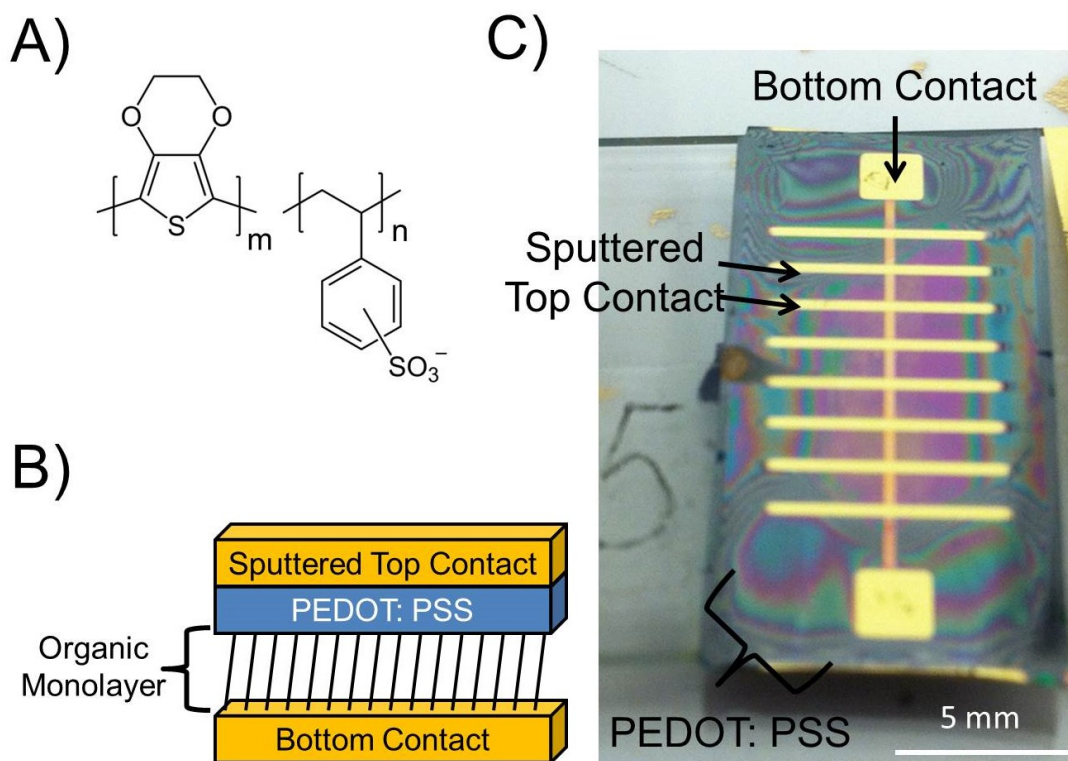


Figure 5.11 – Large Area Junctions Prepared with PEDOT:PSS Buffer Layer

Diagrams of electrical devices using PEDOT:PSS to incorporate monolayers into a device. **A)** Chemical structure of PEDOT:PSS. **B)** Cross-sectional view of PEDOT:PSS device junction. **C)** Optical (top down) view of PEDOT:PSS device, with alkanedithiol as a monolayer in the junction, before PEDOT:PSS is patterned *via* O₂ plasma.

Though Akkerman *et al.* report the ability to pattern under proper conditions, we find here that plasma conditions damage the molecules on the substrate even without direct access of the plasma to the monolayer. Nearly all devices prepared through this technique were shorted after oxygen plasma (250 W, 5 mins, 9 sccm). This represents the second instance in this work where plasma resulted in shorted devices, and while there are other differences between the graphene and PEDOT:PSS buffer layer architectures, there is still a possible explanation of why their common denominator would lead to device failure.

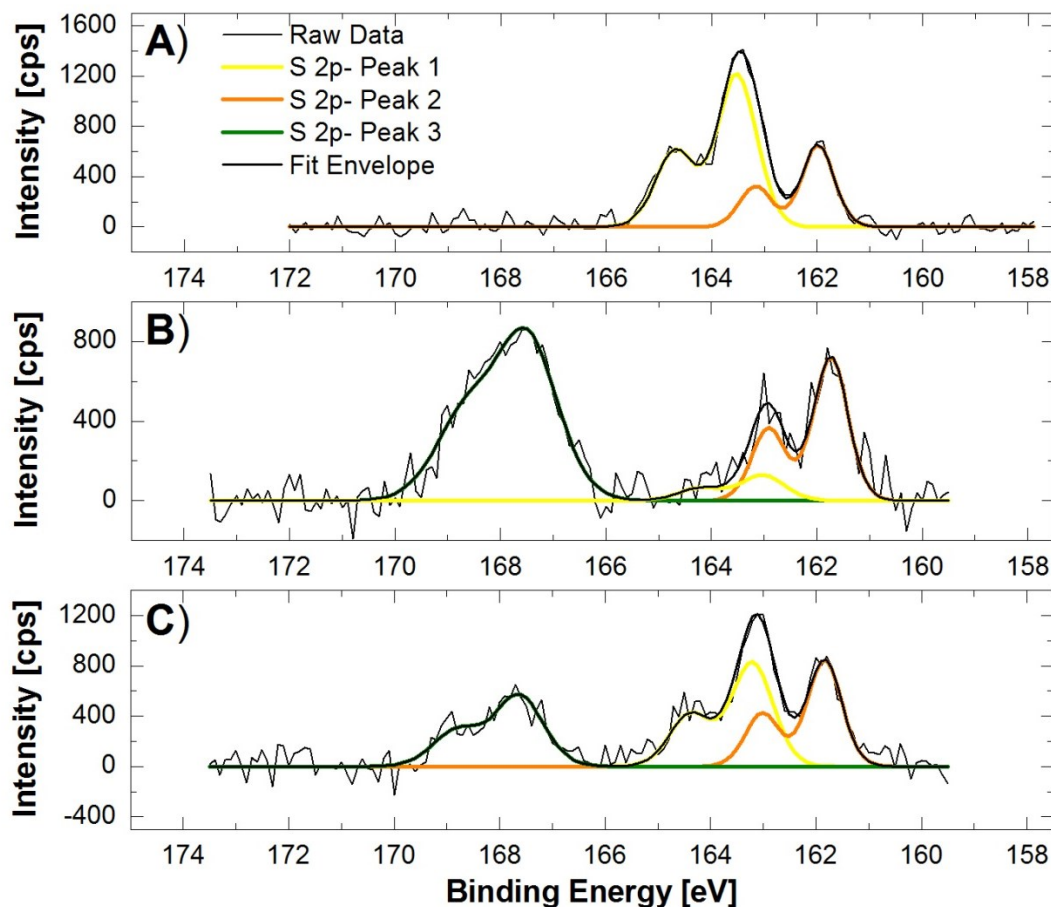


Figure 5.12 – XPS Evidence of Heat Effects in Decanedithiol

S 2p spectra for decanedithiol after certain conditions. **A)** Measurement on freshly prepared DDT. **B)** Measurement after heating substrate on hot plate. Sulfur-oxide peak (167.8 eV) strongly increases, and bound thiol (161.9 eV)/ unbound thiol (163.4 eV) peak strongly favors bound thiol, giving further evidence of monolayer degradation. **C)** Measurement after O₂-plasma process, with photoresist during process and lifted off after plasma. Shows intermediate amounts of sulfur-oxide and monolayer degradation.

To test that common denominator, we tested decanedithiol monolayer quality after subjecting samples to different conditions by XPS. Leaving the sample in air leads to the presence of an unbound thiol (163.4 eV) to bound thiol signal (161.9 eV), with larger unbound thiol due to bound thiol attenuation, implying the monolayer is still of good quality (Figure 5.12 A). Applying heat (Figure 5.12 B) causes severe degradation of the monolayer, potentially

catalyzing the sulfur-oxygen peak that appears ($S\ 2p_{3/2} = 167.8\text{ eV}$),²² and causing a near removal of the unbound thiol signal. When O_2 plasma is applied to a monolayer under a photoresist protecting layer (Figure 5.12 C), designed to prevent direct irradiation of the monolayer, a result inbetween the two cases above are seen. Given that the photoresist ($>1\ \mu\text{m}$) presumably should protect the monolayer from direct plasma and is still present at the end of the plasma process, the implication observed is that the heating effects from the plasma on the monolayer degrades it even with a physical protection barrier. Such a result is very likely indicative of the effects seen in the PEDOT:PSS and graphene junctions and a root cause of the shorted devices.

Though the oxygen plasma successfully removes the PEDOT:PSS and graphene, it appears the consequence of the technique is that the monolayer is damaged from heating effects. Such a conclusion shows that processing can damage monolayers even through resist layers. In the case of graphene, a much milder plasma was used, and it should be noted that the plasma effects according to the XPS study appear milder than directly placing the sample on a hot plate. However, a reality must be considered that large area junctions rely on near perfect attachment of an electrode to an enormous landscape of molecules. Even when using milder fabrication processes, only a small portion of the organic monolayer needs to be affected for shorted devices to be observed. As we scale up the size of the junctions, greater opportunity exists for these small probability occurrences to become relevant. Even the physical effects of the KTP process, which induces a finite force on the substrate, could prove relevant when discussing monolayers that inherently have defects and grain boundaries.⁶

The advantage to these types of junctions is that we can design junctions from single molecules, but this is also its biggest drawback due to the relatively fragile devices that these

molecules generate. Given the advantages discussed throughout this work that single molecules offer, the reward of accomplishing electronics on a single molecule scale is great, but equally great care must be taken with these devices if single molecule electronics are to be fully realized in a mass producible manner. Most importantly, non-damaging techniques and tolerant systems must be utilized, several suggestions of which are given in Chapter 6. Though only shorted devices were seen in the work above, these types of changes may be able to take the ideas and successes in patterning and sample damage mitigation shown here and generate large scale devices toward both unique characterization of interesting molecules and applicability toward practical use in electronic devices.

5.4 Conclusions

In conclusion, several large area junctions toward incorporating organic molecules, such as the phenylenedithiol and porphyrin monolayers studied in this work, into architectures to study their temperature dependent and spin properties, were attempted. Nanoindentation was utilized with 200 nm nTP pads and shown to form reliable holes with thin resist films through which a macroscopic top contact could be attached. However, the films necessary to make sufficiently small holes were too thin to withstand metal evaporation, and thicker films could not work with the AFM tips presently available due to long range damage in the AFM films.

Larger electrodes could be transferred utilizing a variation on the soft lithography technique, kinetically controlled transfer printing (KTP), which opened up the possibility for more standard lithographic techniques. In particular, e-beam lithography was utilized to open wells on top of the KTP features, enabling formation of macroscopically accessible features on micron scale devices. However, it was found that even micron thick resist layers were non-homogenous on top of KTP printed features, and the subsequent shorted devices were attributed

to this. Printing macroscopically accessible features would be an avenue to remove the need for lithography that led to the shorting here, though at present KTP appears to lead to cracks in these large features.

Finally, graphene was utilized as a buffer layer in molecular electronic devices, utilizing a soft lithographic process to transfer a large strip for a macroscopically accessible electrode. It was discovered that heat anneal of elastomeric polymer was not necessary to facilitate transfer of graphene off of a polymer and onto a substrate, but this led to graphene that did not appear to make good contact with a surface and could easily be removed with subsequent patterning step. Both problems were resolved, the first by utilizing a lower T_g polymer, poly(vinyl acetate), which, when subjected to a 50 °C anneal, enabled the same quality transfer of graphene as that from 150 °C annealed PMMA. Further processing with e-beam lithography and subsequent oxygen plasma patterning of transferred graphene enabled a process where resist did not need to be lifted off to make electrical contact to finished devices. This process ultimately also led to shorted devices, likely due to heating from the O₂ plasma despite a shorter exposure time. Though the whole film may not have been affected in the process, any small area of the film being affected could have led to a shorted device, and given the large area of the junctions tested, perhaps this probability was closer to unity at the length scales (tens of microns) being worked with.

This section highlights that while many techniques and patterning processes exist to design molecular electronic devices, the processing techniques can easily damage devices if care is not taken. Even though care was taken in this work to not directly subject monolayers to harsh conditions, O₂ plasma was shown to affect monolayers, likely through heating, through resist protective layers. Also, though evaporating macroscopic contacts was not done directly onto

monolayers, it is possible that the heat from these high energy processes could still transfer through electrodes to monolayers and damage them. This chapter shows that the processing steps for designing reproducible junctions with molecular electronic components must be carefully selected, and efforts toward using less destructive processes, creating more heat stable or robust systems, or ensuring the smallest junctions reasonably producible may be a necessity to generate mass reproducible devices from these materials.

5.5 Appendix

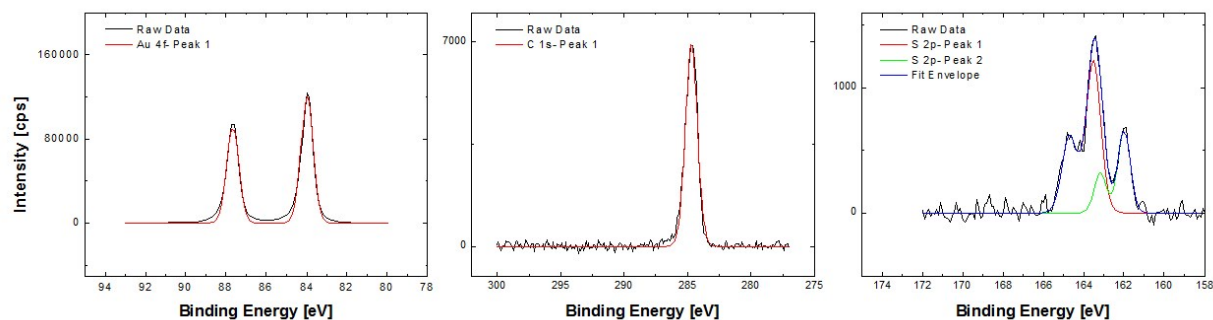


Figure 5.13 – XPS- DDT Monolayer

XPS spectra for freshly prepared DDT monolayers, prepared at 30 mM concentration. Au 4f, with one doublet fitted; C 1s with two singlets fitted; S 2p, with three doublets fitted.

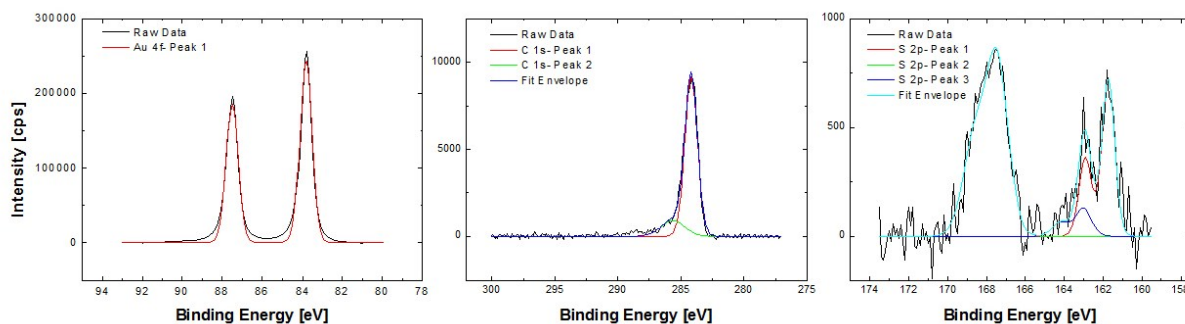


Figure 5.14 – XPS- DDT after Heat Exposure

XPS spectra for DDT monolayers, prepared at 30 mM concentration, after heat exposure. Au 4f, with one doublet fitted; C 1s with two singlets fitted; S 2p, with three doublets fitted.

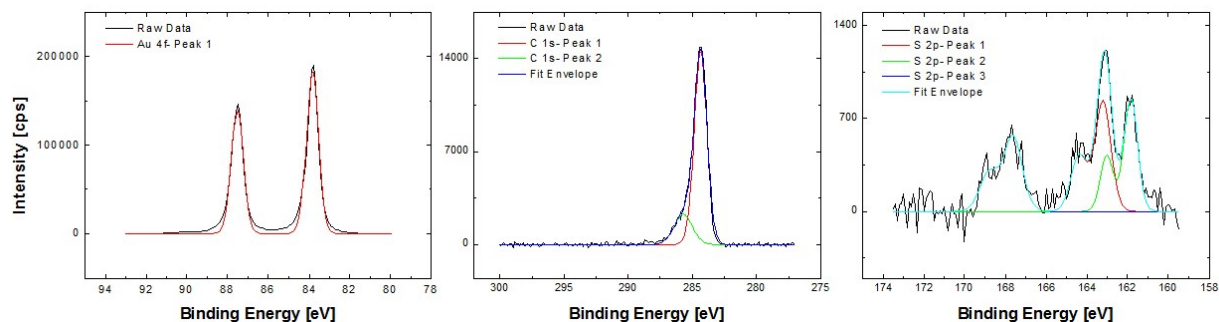


Figure 5.15 – XPS- DDT after O₂ Plasma Exposure

XPS spectra for DDT monolayers, prepared at 30 mM concentration, after oxygen plasma exposure while under photoresist layer (spectra taken after photoresist liftoff). Au 4f, with one doublet fitted; C 1s with two singlets fitted; S 2p, with three doublets fitted.

5.6 References

- (1) Wang, G.; Yoo, H.; Na, S.-I.; Kim, T.-W.; Cho, B.; Kim, D.-Y.; Lee, T. *Thin Solid Films* **2009**, *518*, 824–828.
- (2) Petta, J.; Slater, S.; Ralph, D. *Phys. Rev. Lett.* **2004**, *93*, 136601.
- (3) McCreery, R. L. *Chem. Mater.* **2004**, *16*, 4477–4496.
- (4) Kim, B.; Choi, S. H.; Zhu, X.-Y.; Frisbie, C. D. *J. Am. Chem. Soc.* **2011**, *133*, 19864–19877.
- (5) Baghbanzadeh, M.; Simeone, F. C.; Bowers, C. M.; Liao, K.; Thuo, M.; Baghbanzadeh, M.; Miller, M. S.; Carmichael, T. B.; Whitesides, G. M. *J. Am. Chem. Soc.* **2014**, *136*, 16919–16925.
- (6) Vericat, C.; Vela, M. E.; Salvarezza, R. C. *Phys. Chem. Chem. Phys.* **2005**, *7*, 3258–3268.
- (7) Srisombat, L.; Jamison, A. C.; Lee, T. R. *Colloids Surfaces A* **2011**, *390*, 1–19.
- (8) Walker, J. E. *IEEE Trans. Electron Devices* **1975**, *22*, 464–466.
- (9) Oh, H.-K.; Kim, D. W.; Lee, J.-E. *Jpn. J. Appl. Phys.* **2008**, *47*, 8349–8353.
- (10) Liang, X.; Sperling, B. A.; Calizo, I.; Cheng, G.; Hacker, C. A.; Zhang, Q.; Obeng, Y.; Yan, K.; Peng, H.; Li, Q.; Zhu, X.; Yuan, H.; Walker, A. R. H.; Liu, Z.; Peng, L.-M.; Richter, C. A. *ACS Nano* **2011**, *5*, 9144–9153.
- (11) Niskala, J. R.; Rice, W. C.; Bruce, R. C.; Merkel, T. J.; Tsui, F.; You, W. *J. Am. Chem. Soc.* **2012**, *134*, 12072–12082.
- (12) Bouzehouane, K.; Fusil, S.; Bibes, M.; Carrey, J.; Blon, T.; Du, M. Le; Seneor, P.; Cros, V.; Vila, L. *Nano Lett.* **2003**, *3*, 1599–1602.
- (13) Meitl, M. A.; Zhu, Z.-T.; Kumar, V.; Lee, K. J.; Feng, X.; Huang, Y. Y.; Adesida, I.; Nuzzo, R. G.; Rogers, J. A. *Nat. Mater.* **2006**, *5*, 33–38.
- (14) Akkerman, H. B.; Blom, P. W. M.; de Leeuw, D. M.; de Boer, B. *Nature* **2006**, *441*, 69–72.
- (15) Wohlgenannt, M.; Bobbert, P. A.; Koopmans, B.; Bloom, F. L. In *Organic Spintronics*; 2010; pp. 67–136.
- (16) Novoselov, K. S.; Geim, A. K.; Morozov, S. V.; Jiang, D.; Zhang, Y.; Dubonos, S. V.; Grigorieva, I. V.; Firsov, A. A. *Science* **2004**, *306*, 666–669.

- (17) Kim, H. H.; Chung, Y.; Lee, E.; Lee, S. K.; Cho, K. *Adv. Mater.* **2014**, *26*, 3213–3217.
- (18) Ryu, J.; Kim, Y.; Won, D.; Kim, N.; Park, J. S.; Lee, E.-K.; Cho, D.; Cho, S.-P.; Kim, S. J.; Ryu, G. H.; Shin, H.-A.-S.; Lee, Z.; Hong, B. H.; Cho, S. *ACS Nano* **2014**, *8*, 950–956.
- (19) Avsar, A.; Yang, T.-Y.; Bae, S.; Balakrishnan, J.; Volmer, F.; Jaiswal, M.; Yi, Z.; Ali, S. R.; Güntherodt, G.; Hong, B. H.; Beschoten, B.; Özyilmaz, B. *Nano Lett.* **2011**, *11*, 2363–2368.
- (20) Liu, Y. P.; Idzuchi, H.; Fukuma, Y.; Rousseau, O.; Otani, Y.; Lew, W. S. *Appl. Phys. Lett.* **2013**, *102*, 033105.
- (21) Cobas, E.; Friedman, A. L.; Erve, O. M. J. Van; Robinson, J. T.; Jonker, B. T. *Nano Lett.* **2012**, *12*, 3000–3004.
- (22) Willey, T. M.; Vance, A. L.; van Buuren, T.; Bostedt, C.; Terminello, L. J.; Fadley, C. S. *Surf. Sci.* **2005**, *576*, 188–196.

CHAPTER 6:

SUMMARY OF CONCLUSIONS AND RECOMMENDATIONS FOR FUTURE WORK

6.1 Summary of Conclusions

Incorporating organic molecules into molecular electronic applications stands to offer large benefits in practical electronic devices. Varieties of sometimes cheap, functionalizable, and tunable systems can be deposited using facile methods for large scale and reproducible processing of organic electronic devices^{1,2}, including creating surfaces of single molecule arrays in the form of self-assembled monolayers.³ With electronic devices from these materials capable of being designed with as small as a single molecule, the potential for extremely highly dense electronic devices can be realized from molecular electronics. Moreover, the organic and organic-based materials utilized for these substrates can possess a multitude of diverse properties that can add functionality to electronics, such as molecular switching,⁴ quantum interference,⁵ and current rectification.⁶ Both the scaling effects as well as added functionality offers enormous advances for electronic applications if they can be adapted for practical applications.

To this end, many organic systems with diverse properties have been studied analytically, utilizing temporary electrical junctions to probe the effects described above and effectively showing that specialized organic materials can possess dynamic resistance changes and magnetic properties that sometimes can be tuned by external stimuli.⁷ The problem, however, is these junctions all exist in a laboratory with equipment currently incompatible with mass-producible electronics. A number of techniques have been developed for studies of these molecules in more

practical settings,⁸⁻¹⁰ however a slightly different problem exists here – proof of concept has been shown for many architectures with alkane-based molecular junctions, which are very well behaving, while the effects of the more interesting molecules mentioned above in these architectures has not been studied. Efforts from both sides – generating interesting molecules, and studying their effects in accessible architectures – is required for furthering efforts in this field, and as such both interesting molecules and the architectures that are used with them are studied here.

6.1.1 Adapting Spintronic Molecules to Molecular Electronic Settings

We first attempted to adapt a cobalt metal center valence tautomer molecule (CoVT)¹¹ to a molecular electronic system by growing it off of a surface in a layer-by-layer (LbL) approach. A ligand exchange approach was utilized, attaching the CoVT to a surface by exchanging the pyridine-based ligand of the molecule with an alkane-pyridine-thiol monolayer attached to a gold surface. XPS showed evidence of the CoVT on the surface, and between control studies and the cleaning steps utilized with the surface, we conclude that the molecule had in fact attached to the surface by ligand exchanging with the pyridine-based monolayer. However, attempts to build a multilayer with a similar ligand exchange approach – utilizing a pyridine based linker group – appeared to remove the CoVT monomer from the surface. Oligomer length chains were attempted, and while evidence for regions of large thickness was seen across substrates, these regions were not regular across the surface, indicating a layer could not be formed.

To study the spin properties of the CoVT monomer, XPS was again used. First, an iron-crossover molecule (FeSCO) with similar metal center switching from paramagnetic to diamagnetic spin state was deposited on a gold surface and shown that its spin state could be determined *via* XPS by looking at the shake-up (satellite) peaks from the iron metal center. The same spectroscopic evidence was utilized in analyzing the tautomer effects of the CoVT.

However, the CoVT monomer did not show any crossover effects, showing that the molecule lost its VT properties when tethered to a surface. This is attributed to the changing of the CoVT ligand, which had been shown in previous studies to affect VT temperatures or appearance.¹¹ Despite this finding, the LbL ligand exchange approach was successful at attaching the molecule to the surface and could be used here could be utilized for attaching similar molecules with interesting spin (or other) properties to a surface.

6.1.2 Studying Phenylenedithiol Monolayers in nTP Molecular Junctions

Previous studies with ‘bulk’ nanotransfer printed (nTP) junctions incorporating ideal alkanedithiols showed good behavior,¹² so the capability of this architecture was analyzed with other molecules. In particular, a rather basic system of phenylenedithiols was incorporated into ME junctions utilizing nTP. First, we showed that incorporation of phenylenedithiols into bulk junctions is non-trivial, given the need to use ETMS protected molecules due to the low solubility of longer phenylenedithiol molecules. Different deprotection conditions led to drastically different monolayer properties as studied by XPS, specifically looking at the S 2p and Au 4f core shells for bound/unbound thiol ratios¹³ and molecular attenuation,¹⁴ respectively. Well-ordered monolayers could be prepared with an intermediate amount of deprotectant, leading us to propose a kinetics based model to describe the effects of different deprotection rates on monolayer packing and overall formation.

With high quality monolayers formed, nTP junctions were prepared and characterized through “nTP characterization”, which involved using cAFM to electrically characterize 200 nm diameter gold nTP pads. By looking at the tunneling attenuation value, β , we can comment on the transport properties of the molecular junctions. The β obtained, $\beta_{\text{nTP}} = 0.087 \pm 0.006 \text{ \AA}^{-1}$, is significantly smaller than literature reports,^{15,16} and as experimentally determined, lower than the same monolayers in electrically identical junctions created by directly contacting the SAM with

a cAFM tip ($\beta_{\text{cAFM}} = 0.407 \pm 0.110 \text{ \AA}^{-1}$). These effects are highlighted as a consequence of the nTP fabrication, most specifically the force from the fabrication that could bring molecules physically closer together and reduce the rotation between intramolecular phenyl rings, an effect which would reduce the measured β .¹⁶ More generally, evidence of intermolecular transport is seen through the β reduction, which overall indicates that the fabrication process has changed the monolayer properties and therefore the transport properties in this basic molecular system. Such a finding highlights the impacts ME architectures can have on molecular properties and output and the need to consider these effects when designing architectures for specialized molecular systems.

6.1.3 Studies of Porphyrin Oligomer Wires in Molecular Electronic Devices

While growing molecular wires with metal centers from the CoVT molecule via LbL was unsuccessful, systems incorporating multiple metal centers for dynamic spintronic effects can be synthesized and incorporated into ME junctions. Ethyne-bridged porphyrin oligomer wires had previously shown interesting charge transport properties,¹⁷ and with the ability to change metal center to paramagnetic metal centers alongside theoretical support that doing so could lead to inherent spin polarization through the wire,¹⁸ this proved to be an interesting study to incorporate for electrical study in bulk junctions and spin transport studies. We incorporated porphyrin oligomer wires ($n = 1-3$) as monolayers on gold surfaces. Our first attempt utilized carbodithioate (CS_2) linkers, expected to give better electronic coupling to a gold substrate,¹⁹ but disorder was evidenced on monolayer surfaces by analyzing the sulfur signals in XPS spectra. Test molecules showed that ETMS protected- CS_2 molecules inherently gave these disordered signals, which identical but non-protected (and therefore air sensitive) CS_2 groups did not. Again, the kinetics of the deprotection process appeared to affect monolayer quality, this time in a manner that could be mitigated using deprotectant concentration but never fully removed.

Because of the air sensitivity of non-protected molecules, we turned back to thiols, protecting them with thioacetyl (SAC) moieties and showing that they could be used to form high quality monolayers.

With this knowledge in hand, SAC-protected porphyrin monolayers were prepared. Zn, Cu, Ni, and Fe metal-center porphyrins could ultimately be used to form monolayers on gold surface with relatively good order. XPS highlights the lack of a fully packed surface, with large amounts of bound thiols indicating many molecules lying flat on the surface, likely due to possible intermolecular effects being blocked by bulky solubilizing chains. Nevertheless, evidence of unbound thiols and further analysis indicates some molecules are standing up, a fact verified by the ability to use nTP and attach top contacts. nTP junctions were then analyzed analogously to the phenylenedithiols, highlighting through β values electrical properties in the more ‘bulk’ junctions that matches previous studies of single molecule measurements.¹⁷ These electrical properties could be altered by changing metal center, highlighted by testing PZn, PCu, PNi, and PFe monomers. Further evidence for changing electrical properties was seen by comparing length dependent measurements through $PZn_{n=1-3}$ and $PCu_{n=1-3}$, yielding significantly different β values ($\beta_{PZn} = 0.048 \text{ \AA}^{-1}$; $\beta_{PCu} = 0.126 \text{ \AA}^{-1}$). These β values were correlated to energy level differences for the highest occupied molecular orbital (HOMO) relative to gold Fermi level, measured initially by cyclic voltammetry (CV) and confirmed on a surface by ultraviolet photoelectron spectroscopy (UPS). Such evidence confirms the porphyrin metal center has a direct impact on electrical properties of the system, an impact expected to be extended to the spin properties of the porphyrin wires as well.

6.1.4 Large Area Junctions from Soft Lithography for Macroscopic ME Junctions

To fully study the systems above, different molecular electronic architectures were necessary to incorporate these molecules into settings where temperature dependent

measurements and spin injection at low temperature could be done. Given the ease at which the molecular systems could be destroyed using direct evaporation of metals for electrode deposition,²⁰ several soft lithographic processes were attempted.

First, nanoindentation was utilized with the 200 nm nTP pads shown in previous studies. nTP pads could be identified in AFM setup, and in the case of thin resist layers, selective contact could be made through the resist to the nTP pads. However, deposition of top contacts resulted in shorted devices, likely due to resist layers that were too thin. Thicker resists could inhibit the penetration of metal contacts, but proved to be unusable for selective indentation as damage larger than the size of the nTP pads resulted upon attempting to penetrate the films. Unable to tune the process to the small features, this process was abandoned.

To print larger pads than possible by the nTP process used here, a variation of the transfer printing process – kinetically-controlled transfer printing (KTP)²¹ – was utilized. Unlike nTP, KTP relies solely on peeling rates and differences in surface interaction, allowing for larger features to be transferred. Attempts to print macroscopic crossbars with the process proved unsuccessful, as cracks and folds were readily apparent in larger features. However, smaller (tens of micron sized) and more symmetric features could easily be transferred without visible defect, with these features on a size scale such that more traditional lithographic processes could be done. In particular, electron beam lithography (e-beam lithography) was utilized in conjunction with KTP features. After identifying recipes for poly(methyl methacrylate) (PMMA) that could withstand metal sputtering, wells were opened on top of features identified by the scanning electron microscope (SEM), and finished devices made by evaporating macroscopically accessible contacts. Unfortunately, this process led to shorted devices, an outcome assigned to

thinness of PMMA on and around KTP features as evidenced by cross-sectional AFM and possibly due to the force of the KTP process on monolayers.

Finally, we utilized graphene in ME devices with the goal of utilizing it as a spin tunneling barrier.²² Literature processes,²³ along with modification of the soft lithographic processes to utilize lower glass transition polymers (poly(vinyl acetate) [PVAc]), enabled transfer of graphene from copper foil on which the graphene was grown to monolayer substrates. The importance of the annealing of polymer films above glass transition temperature (T_g) was observed to obtain good contact of graphene to substrate. A processes was designed to generate large area graphene devices, however the finished devices were subsequently shorted. Here, we assign shorting issues to the oxygen plasma process needed to pattern graphene for device fabrication. The heat from the O_2 plasma was shown to degrade the monolayer, even through protective resists, and while only a mild plasma process was needed for the atomically thin graphene, we believe it was still sufficient to short the large area device.

This chapter highlights the impacts and influences of device architecture and fabrication process, ultimately showing that any heat generating or high force process can damage monolayers, even the well-behaved alkanedithiols utilized here. We highlight that great care and non-destructive techniques are vital when less than ideal molecules (such as the studied porphyrin molecules) are incorporated into these junctions in order to realize their unique properties in practical applications.

6.2 Recommendations for Future Work

6.2.1 *Thermally Stable Metal Binding Groups*

The gold-thiol bonds utilized in this study are well-suited for forming well-ordered monolayers, but as expressed throughout the large area fabrication sections, thermal stability is a strong issue with these systems. Certain circumventions can be done to avoid this issue, but a large amount of patterning and lithographic processing is rendered unusable due to the low thermal stability. Even with the supposedly mild O₂ plasma used to remove sheets of graphene, the effects were enough to damage monolayers. In order to do thorough studies of systems under different conditions, such as those incorporating buffer layers, as well as increasing the applicability of the systems for practical application, greater stability is necessary in order to facilitate patterning or other lithographic processes and the fabrication of large numbers of devices on a substrate.

Different metal binding groups can offer the stability desired for future processing. For example, phosphonic acid linkers are known to be more stable than thiols and provide a strong alternative for molecular electronic applications. Regular self-assembled monolayers have been shown through basic alkane molecules with phosphonic acid linkers, and in the case of these monolayers, annealing is actually required to generate strong attachment to substrates like silicon, highlighting their thermal stability.²⁴ These molecules can be adapted to a variety of surfaces, including oxides on metals such as the conductive indium tin oxide (ITO)²⁵ and, most relevant to spintronic studies, the ferromagnetic substrate of LSMO. In fact, studies on the latter surface have shown that spin transport can be observed through phosphonic acid linker monolayers on LSMO,^{26,27} providing a strong candidate for the work proposed here. Metal binding groups represent the final step in the synthetic route of porphyrin wires, which may indicate that they should be easily incorporated into the synthetic routes already established.

While test studies would need to be done, this could represent a logical and facile step to take for patterning of these molecules into macroscopically accessible contacts.

6.2.2 Silicon Substrates for Analyzing Monolayer Properties

As exhibited in the phenylenedithiol work, molecular properties in ME junctions may strongly impact output in a device. While designing ME junctions with two chemically bound electrodes promotes strong electronic coupling between molecule and device and promotes the robustness of the device, one disadvantage is it prevents us from spectroscopically studying the monolayers incorporated in it. Evidence can be indirectly observed about monolayer properties – we used changes in β here to comment on charge transport pathways, a fact which would be further commented on by temperature dependent measurements – but no direct evidence of the surface is given due to the inability to access it through the electrodes. Desirable substrates would provide methods to comment on molecular properties in a device setting so they can be correlated with electronic output.

We have focused on monolayers designed on metals for these studies, but monolayers on silicon substrates have been studied previously. The thiol-silicon bond has been shown as a possible mechanism for substrate attachment.²⁸ Direct carbon to H-terminated silicon,^{29,30} as well as bonds to the oxides of silicon oxide, are also possible. The phosphonic acid linkers mentioned above can be used on silicon substrates, potentially providing advantages from both of the modifications proposed here.²⁴ There is a drawback in that these monolayers can lead to large Schottky barriers and less dense surfaces than have been seen in gold-thiol surfaces. Most studies show electrical behavior at a higher bias to overcome the Schottky barriers.

The relevance of the silicon substrate to these studies is that silicon is infrared transparent. This allows spectroscopic analysis of monolayers that are attached to the silicon, potentially commenting on molecular orientation and geometry. In particular, *p*-polarized

backside reflection absorption infrared spectroscopy (pb-RAIRS) has been shown as capable of characterizing monolayer properties in two electrode devices.³¹ As reported in Coll *et al.*, infrared (IR) beams are reflected off of back gold contacts, passing through silicon electrodes and observing properties of monolayers in these junctions.²⁸ In principle, silicon-molecule-silicon substrates could be generated, allowing for a totally IR transparent substrate and removing the need for backscattering. Such a study could be extended, studying molecules such as phenylenedithiols, formulated with different techniques and, ideally, prepared under different pressures. The latter would be able to comment on the observation in this and other studies¹⁶ of the potential rotation of phenyl rings to be in plane with one another. In general, evidence of sample crystallinity, effects on bond order and rotation, and so on would be accessible in these architectures.

6.2.3 Solvent Assisted Transfer Printing

As expressed throughout this work, the fabrication techniques used to incorporate organic molecules can have finite impacts on the organic materials used with them. Soft lithography was utilized throughout this work as a means to reduce these effects, predominantly metal penetration and damage of the substrates, but even the fabrication processes for the methods used here appeared to have finite impacts. Graphene patterning required O₂ plasma that damaged monolayers. Even with processes that used only physical pressure for transfer, such as nTP and KTP, the force effects can impact the measured properties of a monolayer, such as with the phenylenedithiols SAMs, or potentially damage the monolayers that possess inherent grain boundaries and defects. Even amongst soft lithographic processes, care must be taken that these techniques and required patterning steps do not damage monolayers, a problem that is paramount to consider as scaling increases possibilities for one or a few defect sites to lead to a shorted device.

This work is not the only place where such effects have been proposed. Large area junctions of phenylenedithiol monolayers, prepared with PEDOT:PSS buffer layers, have shown drops in β in literature and have been predicted to be caused by rotation of the phenyl rings.¹⁶ As we proceed forward toward molecules that are even less ordered, such as the porphyrin monolayers that we have shown to have low molecular packing on a surface, great care must be taken in generating large area devices such that the larger possibilities for defects do not translate into all devices shorting. Techniques which exert the lowest amount of force onto a molecule while still producing chemical bonds and reliable junctions should be sought after in light of this.

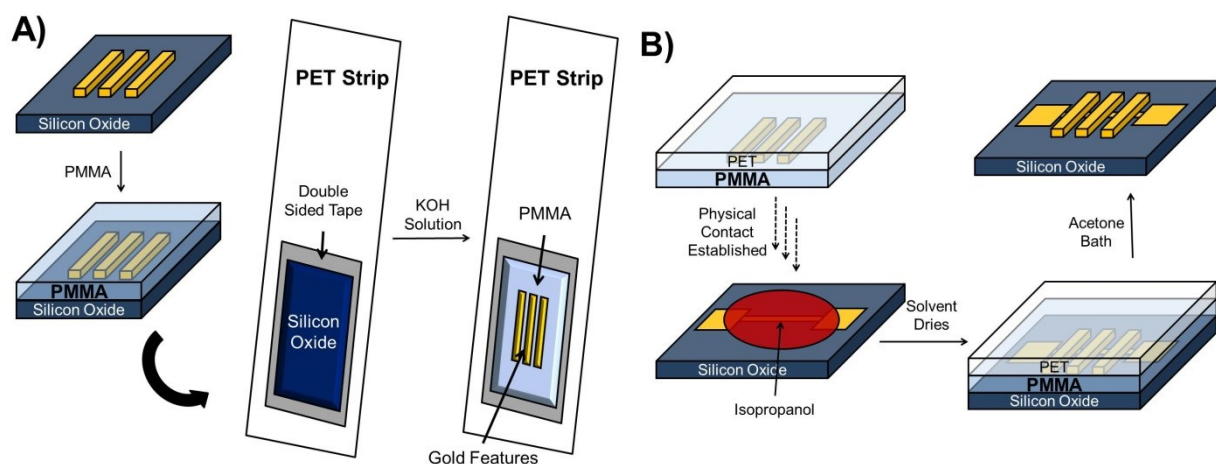


Figure 6.1 – Solvent Assisted Transfer Printing (SATP)

Procedure for SATP. **A)** Lithographically defined features on silicon oxide (SiOx) have PMMA spun cast on top. This stack is attached, PMMA side down, to double sided tape on a polyethylene terephthalate (PET) strip. Soaking in potassium hydroxide solution etches the SiOx enough to release it, exposing the gold features on PMMA underneath. **B)** The PET/PMMA/gold features stack is placed in physical contact onto a receiving substrate with predefined bottom electrodes. Several drops of solvent are placed before the contact is made. As the solvent dries, features are brought into contact with the substrate. Lastly, soaking in acetone dissolves the PMMA, allowing release of the PET stamp and finishing the feature transfer.

The least damaging process would obviously be one where no force or external stimulus is required to make contact between electrode and monolayer, and no patterning is required post transfer. A process that comes very close to this situation, and a proposed technique for large area molecular electronic devices, is what we call solvent assisted transfer printing (SATP). This is modified from literature reports by Jeong *et al.*³² The keys to this process are that all electrode patterning is done on sacrificial substrates and transferred to a monolayer on a surface without further modification, and that the driving force for contact between transferred pad and substrate is capillary action from solvent evaporation. Patterning with resists can be done to the surface to limit the area which the electrode makes contact to, and the transferred pad ultimately gives a macroscopic contact to the monolayer.

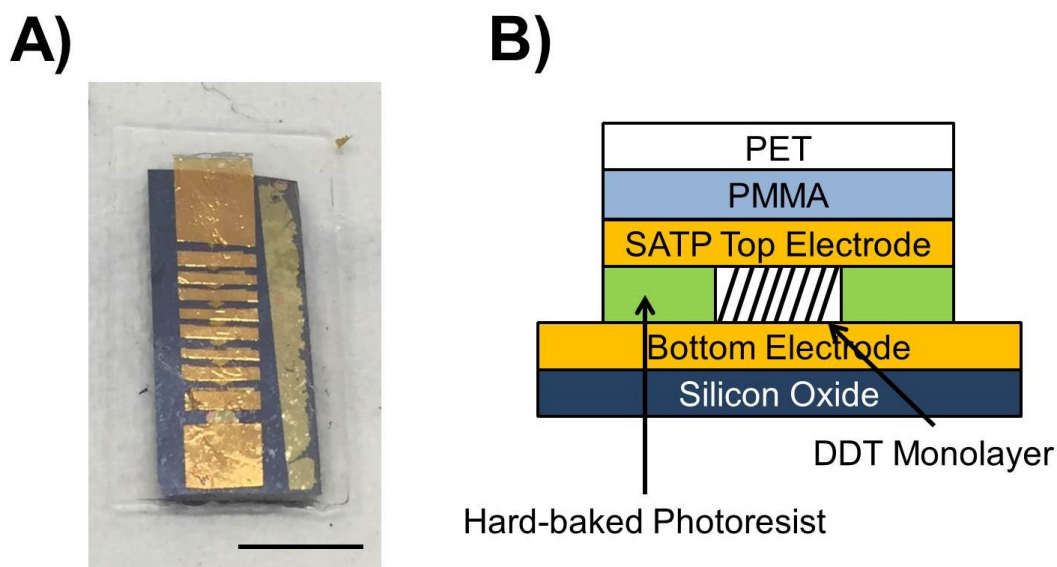


Figure 6.2 – Sample SATP Transfer Substrate

A) Sample substrate with SATP electrodes. Scale bar: 1 cm. **B)** Cross-section of device in A. PET/PMMA is still present in this particular image, as reflected by the cross-sectional image.

Figure 6.2 shows an example of electrodes transferred using this technique onto a patterned device with decanedithiol (DDT) as a monolayer. Initial trials have shown cracks in transferred features, mainly due to damage caused during the acetone soak in the final step to remove the stamp, but this step can be improved. As this and other minor improvements to transferred feature handling and cleaning are made, large area features should be able to be transferred without significant crack or defect, allowing for a low force and non-destructive technique to generate macroscopically accessible electrodes for substrates through which temperature dependent and, once ferromagnetic electrodes are adapted to the technique, spin dependent measurements can be made.

6.2.4 Metal Effects in Porphyrin Nanowires

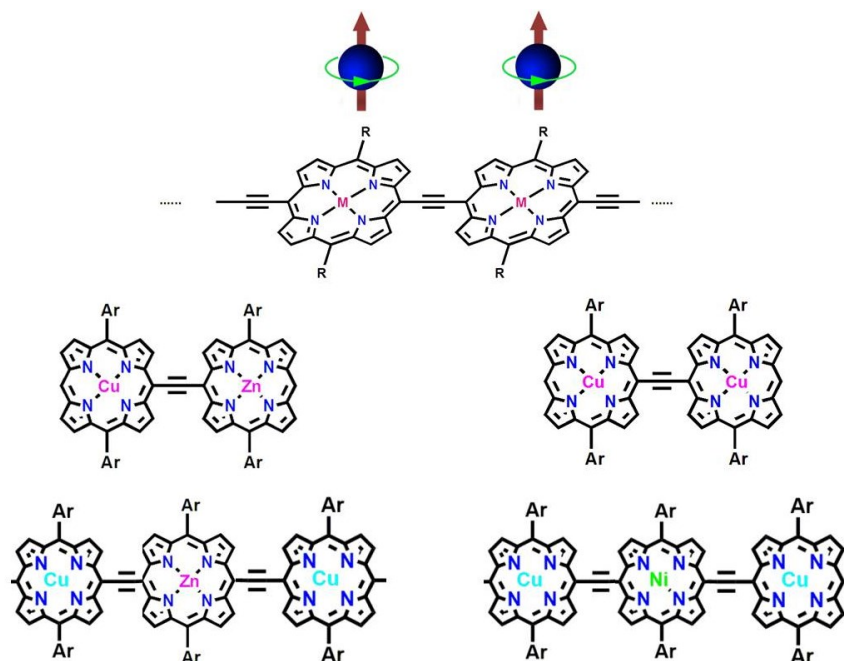


Figure 6.3 – Spin Coupling from Porphyrin Metal Centers

Proposed structures for studying coupling in spins from porphyrin metal centers. Left: Coupling paramagnetic metals (Cu) with or across diamagnetic metals (Zn). Right: Coupling various paramagnetic (Cu, Ni) metal centers.

The direct goal of the future work with the porphyrin nanowires is to evaluate the effects of metal centers on spin transport. As discussed previously, it has been computationally shown that different metal centers may have direct impact on the spin transport through the porphyrin backbone.¹⁸ We have shown in this work that changing metal center affects the transport properties of the molecular wires, which gives evidence for the idea that the metals can affect the spin properties of the wire as well. By probing the density of states of these systems, we hope to find different spin dependent states such that spin polarized transport can be realized.

Future work can focus on using the porphyrin wires as molecular switches, altering the spin state of the metal centers from paramagnetic to diamagnetic in similar manner to the valence tautomers and spin crossover compounds studied previously. For example, cobalt (III) porphyrin metal centers, which are diamagnetic based on spin pairing, can be reacted with chlorine or other axial ligands, reducing it to a Co(II) oxidation state which will be paramagnetic. Adding different ligands in general could induce different spin states. Moving up or down the spectrochemical series of ligands can lead to larger or smaller splitting of d-band orbitals, an effect which could cause shifts from high spin to low spin and change the spin state of the system. If the alteration of ligands could be done in a reversible and controllable manner, switch properties could be realized. Or even without ligands, a more direct route that has been shown to be reversible in other systems would be UV-light excitation of metal centers, inducing changes in the reversible redox of Co(III) to Co(II) *via* incident light that would change the spin state of the metal center.³³ Changing oxidation and spin state are expected to change the conductance properties of the porphyrin wires, and perhaps the spin properties as well, and could be used for dynamic systems with controllable properties for molecular electronic applications.

In addition, we've mainly considered metal centers acting individually, but interesting magnetic properties can be had by coupling metal centers, which could lead to interesting spin transport properties. Magnetic interactions of atoms, such as the ferromagnetic coupling of iron particles in a triazine-based organic matrix, have been shown throughout literature.³⁴ Porphyrin arrays have also seen magnetic coupling, more generally antiferromagnetic coupling between chemically bound heterocycle units.³⁵ The advantage to the porphyrin wires studied here is they can be controllably synthesized with different metal centers along the same wire. Though antiferromagnetic coupling has mainly been highlighted so far, discovery of ferromagnetic coupling in the wires could benefit their ability to act as spin polarizers, and also potentially lead to hysteresis effects that could benefit their use in applications such as single molecule transistors toward memory applications.

6.3 Methods

6.3.1 Solvent Assisted Transfer Printing

Gold substrates were prepared on silicon wafers as described previously (see Section 3.2.2). Patterning of bottom substrates was done using MaN-1400 negative photoresist and a custom photomask. After metal evaporation, photoresist was lifted off in acetone. 10 μm circular holes were then defined on the bottom gold substrate using a new photoresist layer and different mask, this layer done with an MaN:MaT (thinner) 1:7 solution, spun cast at 3000 rpm for 30 s and baked at 120 $^{\circ}\text{C}$ for 60 s, exposed for 40 s, and developed in MaD developer for 2 mins. To protect the gold not exposed, remaining photoresist was hard baked at 200 $^{\circ}\text{C}$ for minimum 2 hrs, removing its solubility in common solvents. Substrates were then soaked in monolayers of 1,10-decanedithiol (DDT) were prepared from 30 mM solutions soaked for > 24 hrs.

Donors for transfer printing were evaporated on SiO_x wafers (60 nm gold) through a shadow mask to remove need for liftoff. 4% poly(methyl methacrylate) (PMMA) in anisole was spun cast on gold features on silicon oxide, 4000 rpm for 60 s, then annealed at 150 °C for 3 mins. Features were taped *via* Scotch double-sided tape to polyethylene terephthalate (PET) strips, PMMA side down, and placed in 25% w/w KOH to etch the silicon oxide and release the evaporated gold features. After ~1 hr, silicon oxide wafers fall off or are easily removed. PET strips now containing PMMA/gold features for transfer are cleaned in DI-H₂O for 30 mins, rinsed in H₂O and dried coarsely with N₂ stream, and dried in vacuum overnight.

For solvent assisted transfer, several drops of isopropanol (IPA) are deposited onto DDT functionalized gold substrates, and the PET strip is gently placed with gold features side down onto the transfer substrate (any alignment for location of final features is done here). IPA evaporates over the course of an hour, bringing the gold features into contact with the surface. The substrate is then submerged into acetone to dissolve a small amount of the PMMA, facilitating release of the gold features and allowing the PET/PMMA stack to be peeled away from the transfer substrate, leaving gold features transferred onto the DDT monolayer substrate.

6.4 References

- (1) Chen, K.; Yeh, H.; Chen, H.; Liu, T.; Huang, S.; Wu, P.; Tiu, C. *Adv. Chem. Eng. Sci.* **2013**, *3*, 105–111.
- (2) Chung, S.; Jang, M.; Ji, S.-B.; Im, H.; Seong, N.; Ha, J.; Kwon, S.-K.; Kim, Y.-H.; Yang, H.; Hong, Y. *Adv. Mater.* **2013**, *25*, 4773–4777.
- (3) Love, J. C.; Estroff, L. A.; Kriebel, J. K.; Nuzzo, R. G.; Whitesides, G. M. *Chem. Rev.* **2005**, *105*, 1103–1169.
- (4) Kiguchi, M.; Ohto, T.; Fujii, S.; Sugiyasu, K.; Nakajima, S.; Takeuchi, M.; Nakamura, H. *J. Am. Chem. Soc.* **2014**, *136*, 7327–7332.
- (5) Guédon, C. M.; Valkenier, H.; Markussen, T.; Thygesen, K. S.; Hummelen, J. C.; van der Molen, S. J. *Nat. Nanotechnol.* **2012**, *7*, 305–309.
- (6) Díez-Pérez, I.; Hihath, J.; Lee, Y.; Yu, L.; Adamska, L.; Kozhushner, M. A.; Oleynik, I. I.; Tao, N. *Nat. Chem.* **2009**, *1*, 635–641.
- (7) Wende, H.; Bernien, M.; Luo, J.; Sorg, C.; Ponpandian, N.; Kurde, J.; Miguel, J.; Piantek, M.; Xu, X.; Eckhold, P.; Kuch, W.; Baberschke, K.; Panchmatia, P. M.; Sanyal, B.; Oppeneer, P. M.; Eriksson, O. *Nat. Mater.* **2007**, *6*, 516–520.
- (8) McCreery, R. L. *Chem. Mater.* **2004**, *16*, 4477–4496.
- (9) Kim, B.; Choi, S. H.; Zhu, X.-Y.; Frisbie, C. D. *J. Am. Chem. Soc.* **2011**, *133*, 19864–19877.
- (10) Baghbanzadeh, M.; Simeone, F. C.; Bowers, C. M.; Liao, K.; Thuo, M.; Baghbanzadeh, M.; Miller, M. S.; Carmichael, T. B.; Whitesides, G. M. *J. Am. Chem. Soc.* **2014**, *136*, 16919–16925.
- (11) Schmidt, R. D.; Shultz, D. A.; Martin, J. D.; Boyle, P. D. *J. Am. Chem. Soc.* **2010**, *132*, 6261–6273.
- (12) Niskala, J. R.; Rice, W. C.; Bruce, R. C.; Merkel, T. J.; Tsui, F.; You, W. *J. Am. Chem. Soc.* **2012**, *134*, 12072–12082.
- (13) Castner, D. G.; Hinds, K.; Grainger, D. W. *Langmuir* **1996**, *12*, 5083–5086.
- (14) Cumpson, P. J.; Seah, M. P. *Surf. Interface Anal.* **1997**, *25*, 430–446.
- (15) Wold, D. J.; Haag, R.; Rampi, M. A.; Frisbie, C. D. *J. Phys. Chem. B* **2002**, *106*, 10–13.

- (16) Kronemeijer, A. J.; Huisman, E. H.; Akkerman, H. B.; Goossens, A. M.; Katsouras, I.; van Hal, P. A.; Geuns, T. C. T.; van der Molen, S. J.; Blom, P. W. M.; de Leeuw, D. M. *Appl. Phys. Lett.* **2010**, *97*, 173302.
- (17) Li, Z.; Park, T.-H.; Rawson, J.; Therien, M. J.; Borguet, E. *Nano Lett.* **2012**, *12*, 2722–2727.
- (18) Cho, W. J.; Cho, Y.; Min, S. K.; Kim, W. Y.; Kim, K. S. *J. Am. Chem. Soc.* **2011**, *133*, 9364–9369.
- (19) Park, T.-H.; Therien, M. J. *Org. Lett.* **2007**, *9*, 2779–2782.
- (20) Wang, G.; Na, S.-I.; Kim, T.-W.; Kim, Y.; Park, S.; Lee, T. *Org. Electron.* **2012**, *13*, 771–777.
- (21) Meitl, M. A.; Zhu, Z.-T.; Kumar, V.; Lee, K. J.; Feng, X.; Huang, Y. Y.; Adesida, I.; Nuzzo, R. G.; Rogers, J. A. *Nat. Mater.* **2006**, *5*, 33–38.
- (22) Van 't Erve, O. M. J.; Friedman, A. L.; Cobas, E.; Li, C. H.; Hanbicki, A. T.; McCreary, K. M.; Robinson, J. T.; Jonker, B. T. *J. Appl. Phys.* **2013**, *113*, 17C502.
- (23) Liang, X.; Sperling, B. A.; Calizo, I.; Cheng, G.; Hacker, C. A.; Zhang, Q.; Obeng, Y.; Yan, K.; Peng, H.; Li, Q.; Zhu, X.; Yuan, H.; Walker, A. R. H.; Liu, Z.; Peng, L.-M.; Richter, C. A. *ACS Nano* **2011**, *5*, 9144–9153.
- (24) Dubey, M.; Weidner, T.; Gamble, L. J.; Castner, D. G. *Langmuir* **2010**, *26*, 14747–14754.
- (25) Paniagua, S. A.; Li, E. L.; Marder, S. R. *Phys. Chem. Chem. Phys.* **2014**, *16*, 2874–2881.
- (26) Galbiati, M.; Seneor, P.; Mattana, R.; Tatay, S.; Bouzehouane, K.; Deranlot, C.; Jacquet, E.; Forment-aliaga, A.; Jegou, P. *ACS Nano* **2012**, *6*, 8753–8757.
- (27) Galbiati, M.; Barraud, C.; Tatay, S.; Bouzehouane, K.; Deranlot, C.; Jacquet, E.; Fert, A.; Seneor, P.; Mattana, R.; Petroff, F. *Adv. Mater.* **2012**, *24*, 6429–6432.
- (28) Coll, M.; Gergel-hackett, N.; Richter, C. A.; Hacker, C. A. *J. Phys. Chem. C* **2011**, *115*, 24353–24365.
- (29) Buriak, J. M. *Chem. Commun.* **1999**, 1051–1060.
- (30) Bo, T.; Salomon, A.; Cahen, D.; Gooding, J. J. *Langmuir* **2007**, *23*, 3236–3241.
- (31) Hoffmann, H.; Mayer, U.; Brunner, H.; Krischanitz, A. *Vib. Spectrosc.* **1995**, *8*, 151–157.
- (32) Jeong, H.; Kim, D.; Kim, P.; Rae Cho, M.; Hwang, W.-T.; Jang, Y.; Cho, K.; Min, M.; Xiang, D.; Daniel Park, Y.; Jeong, H.; Lee, T. *Nanotechnology* **2015**, *26*, 025601.

- (33) Kume, S.; Kurihara, M.; Nishihara, H. *Chem. Commun.* **2001**, 6, 1656–1657.
- (34) Umbach, T. R.; Bernien, M.; Hermanns, C. F.; Krüger, A.; Sessi, V.; Fernandez-Torrente, I.; Stoll, P.; Pascual, J. I.; Franke, K. J.; Kuch, W. *Phys. Rev. Lett.* **2012**, 109, 267207.
- (35) Ikeue, T.; Furukawa, K.; Hata, H.; Aratani, N.; Shinokubo, H.; Kato, T.; Osuka, A. *Angew. Chem. Int. Ed.* **2005**, 44, 6899–6901.